Experimental testing and numerical modelling of the tensile and compressiondamage in Ultra-High Performance Concrete under impact loading

Maria Celeste Blasone

THÈSE

Pour obtenir le grade de

DOCTEUR DE L'UNIVERSITE GRENOBLE ALPES

Spécialité : 2MGE : Matériaux, Mécanique, Génie civil, Eletrochimie

Arrêté ministériel : 25 mai 2016

Présentée par

Maria Celeste BLASONE

Thèse dirigée par **Pascal FORQUIN**, Professeur, Université Grenoble Alpes, et
coencadrée par **Dominique SALETTI**, Maître de conférences, Université Grenoble Alpes,
et par **Julien BAROTH**, Maître de conférences, Université Grenoble Alpes

préparée au sein du **Laboratoire Sols, Solides, Structures et Risque**
dans **l'École Doctorale I-MEP2 – Ingénierie – Matériaux, Mécanique, Environnement, Energétique, Procédés, Production**

Etude expérimentale et modélisation numérique du comportement dynamique de bétons à ultra-hautes performances sous chargement d'impact

Experimental testing and numerical modelling of the tensile and compression damage in Ultra-High Performance Concrete under impact loading

Thèse soutenue publiquement le **24 mars 2021**,
devant le jury composé de :

Monsieur François TOUTLEMONDE
Ingénieur Général des Ponts, Université Gustave Eiffel, Président
Monsieur Marco DIPRISCO
Professeur, Politecnico di Milano, Rapporteur
Monsieur Jaap WEERHEIJM
Maître de conférences, TU Delft, Rapporteur
Madame Magali ARLERY
Ingénieur, CEA/DAM, Examinatrice
Monsieur Jean-Luc HANUS
Maître de conférences, INSA Centre Val de Loire, Examinateur
Monsieur Pascal FORQUIN
Professeur, Université Grenoble Alpes, Directeur de thèse
Monsieur Emmanuel BONNET
Ingénieur, LafargeHolcim Innovation Center, Invité

Remerciements

Mes remerciements vont d'abord à mes encadrants Pascal Forquin, Dominique Saletti et Julien Baroth qui m'ont accompagnée et soutenue avec enthousiasme dans la réalisation de mes travaux. Je les remercie pour la confiance et la liberté qu'ils ont su me donner. J'aimerais remercier aussi Emmanuel Bonnet pour tous nos échanges et pour ses messages d'encouragement qui m'ont beaucoup aidé.

Je souhaite également exprimer ma grande reconnaissance à tous les membres de mon jury de thèse, qui m'ont beaucoup apporté. J'ai été honorée que François Toutlemonde, source d'inspiration pendant mes études, ait bien voulu participer à mon évaluation. Je remercie Marco Di Prisco et Jaap Weerheijm pour avoir rapporté ce manuscrit, vos remarques m'ont aidée à réfléchir au mieux pour vous présenter mes travaux. Je remercie également Magali Arlery et Jean-Luc Hanus pour leurs questions passionnantes, et les points de vue enrichissants qu'ils ont partagés avec moi à ma soutenance.

De plus, je souhaite remercier Svatopluk Dobrusky, Caroline De Silva et Xavier Salvador pour leur accueil chaleureux pendant mes missions à Saint Quentin Fallavier. Je remercie M. Mereu pour nos débats constructifs pendant les phases de conception des essais et Dr. Zinszner pour son support pendant l'analyse des données d'interféromètre.

J'aimerais aussi remercier tous les membres du groupe de travail ExperDYN qui ont contribué de près à mes travaux. Je remercie de tout cœur Marielle, Yannick et David pour avoir partagé avec moi les hauts et les bas qui sont inhérents à la réalisation d'une thèse, dans une ambiance qui me manquera. Emile, Wojtek, Ludovic et Jean-Luc, je vous remercie pour votre support technique pendant les campagnes expérimentales et votre amitié. Je remercie aussi Bratislav pour son aide précieuse pendant mes premières campagnes scientifiques.

Je remercie enfin tous les doctorants, les post-docs et les chercheurs du laboratoire 3SR qui ont participé à mon aventure de thèse. Mes remerciements s'adressent également à la direction, aux membres de l'équipe informatique et aux ingénieurs de la plateforme à rayon X.

Merci de tout cœur,

Maria

Résumé

Cette thèse présente des recherches expérimentales et numériques sur les Bétons à Ultra-Hautes Performances (BHUP) en vue de favoriser leur application technique en tant que structures de protection. Le modèle couplé DFHcoh-KST, décrivant à la fois le comportement confiné et l'endommagement en traction, est sélectionné pour simuler un problème d'impact aux éléments finis (FE) Abaqus/Explicit. Les paramètres matériaux sont identifiés pour deux formulations de Ductal® avec fibres utilisant des techniques expérimentales existantes: tels que les essais de compression quasi-oedométrique (Q-OC), les essais de flexion et les essais d'écaillage à la barre de Hopkinson. L'étude du comportement en traction des BUHP est ensuite étendue à des vitesses de déformation de 10^3 à 10^4 s^{-1} grâce à des essais d'impact sur plaque. Une technique expérimentale novatrice utilisant un système de 'pulse-shaping' permettant une vitesse de chargement constante dans l'échantillon est conçue par simulation numérique et expérimentée en utilisant le lanceur à gaz installé au laboratoire 3SR. De plus une modélisation du processus de fragmentation sous chargement de traction dynamique a été développée à l'aide d'approches continue et discrète en se basant sur des analyses par tomographie aux rayons X des distributions des pores des BUHP. Ces travaux de modélisation permettent d'expliciter le rôle de la microstructure sur la sensibilité à la vitesse de déformation de la résistance à la traction et de la densité de fissures générée dans les matériaux étudiés.

Mots clés: Bétons à Ultra-Hautes Performances**,** comportement confiné, résistance à la traction**,** vitesse de chargement, essais d'impact sur plaque**,** distributions des pores.

Résumé détaillé

Cette thèse présente des études expérimentales et numériques sur les bétons à ultra hautes performances (BUHP) pour leur utilisation dans des applications exigeant une résistance aux charges d'impact. Depuis le milieu des années 1970, des modèles «data-driven» ont été développés par data-fitting pour prédire les performances des béton sous impact. Cependant, ces modèles empiriques sont applicables strictement dans les limites du cadre expérimental et ne se généralisent pas facilement. Une stratégie possible pour surmonter ce problème consiste à réaliser des expériences numériques comme approche complémentaire.

Lors d'un impact, le béton est exposé à des pressions de confinement élevées et à des vitesse de chargement de traction élevés, ce qui entraîne des endommagements sévères. En outre, il est bien connu que le comportement mécanique du béton conventionnel est sensible à la pression de confinement appliquée et à la vitesse de chargement. Par conséquent, la modélisation numérique du BUHP doit tenir compte des lois constitutives décrivant les mécanismes activés sous impact pour être précis, tels que la compaction inélastique, la rupture par cisaillement, la fracturation dynamique de mode I et les fragmentations multiples.

1. Notions générales

Les BUHP sont des matériaux cimentaires présentant une résistance à la compression exceptionnelle. Dans leurs formes commerciales, les BUHP sont souvent dotés de courtes fibres d'acier pour obtenir un comportement ductile en flexion. Les bétons utilisés dans cette étude appartiennent à la famille des bétons Ductal® lancés à la fin des années 90 (Dugat & Acker, 1999). Ces bétons sont conçus pour avoir une résistance élevée à la compression simple, ainsi qu’une capacité d'absorption d'énergie élevée, et constituent une solution idéale de protection contre la menace balistique et l’explosion.

En Figure 1(1), nous observons la section de rupture de trois poutres testées en flexion, où l’on peut distinguer dans chaque cas la matrice cémentaire, des macroporosités et les fibres d'acier dans les poutres renforcées. La Figure 1(2) montre la contrainte nominale en fonction du déplacement pour ces trois cas. Nous ne constatons aucun effet des fibres sur la résistance à la première fissuration, probablement contrôlée par les porosités. En revanche, après première fissuration, un comportement variable est observé pour les spécimens renforcés de fibres, probablement en raison d'une orientation différente des fibres dans la section.

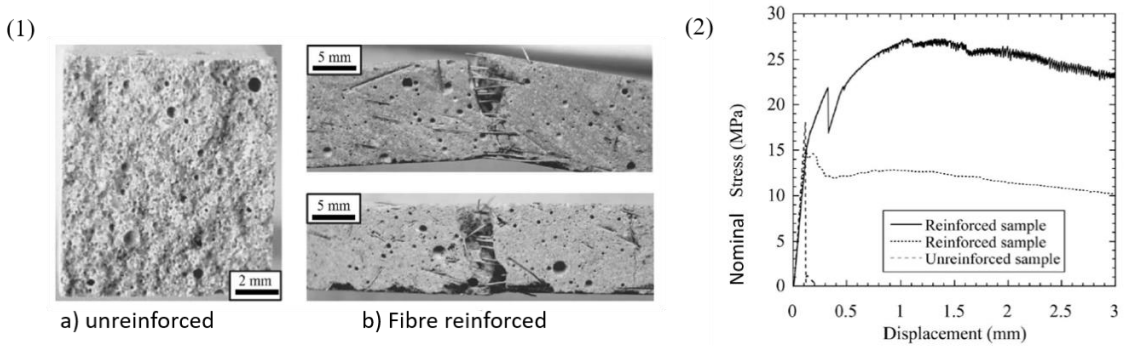

Figure 1 – Réponse quasi-statique des eprouvettes Ductal® en flexion (Forquin, 2003) : (1) section de rupture d'une éprouvette a) sans fibres b) avec fibres ; (2) comportement mécanique macroscopique (résistance à la première fissuration : 15 MPa).

2. L'objectif

Mon travail vise à établir un lien entre les caractéristiques microstructurales du BUHP (pores et fibres) et la réponse mécanique macroscopique du matériau, sous des charges extrêmes comme de grandes pressions de confinement et vitesses de chargement (Figure 2). Pour atteindre cet objectif, je réalise des expériences avec des outils tels que les techniques d'essai d'impact, et j'étudie la microstructure du matériau en tomographie. Finlament, ces données sont utiles pour améliorer le modèle mécanique utilisé pour simuler l'impact balistique. Les activités de recherche développées pendant mon doctorat contribuent également à atteindre les objectifs de la chaire Brittle'S CODEX (Forquin et al., 2020).

3. Structure du manuscrit

Les travaux expérimentaux et numériques que j'ai réalisés et inclus dans le manuscrit sont résumés dans la Figure 3. En particulier, j'ai utilisé le modèle couplé DFHcoh-KST (Forquin et al., 2015, qui décrit le comportement macroscopique à la fois sous confinement et sous tension dynamique) avec une méthode d'éléments finis pour simuler la réponse des cibles en BUHP avec renforcement des fibres à l'impact d'un projectile perforant (vitesse d'impact 950 m/s). Dans le modèle DFHcoh-KST, la pression de confinement influence la déformation volumétrique et la résistance aux charges de cisaillement. Les effets de la vitesse de chargement sont inclus dans la prédiction de l'endommagement en traction à travers une description probabiliste de l'activation et de l'obscuration de défauts pré-existants dans le matériau. Le rôle des fibres intégré à l'aide d'un terme de cohésion qui affecte la résistance résiduelle en traction

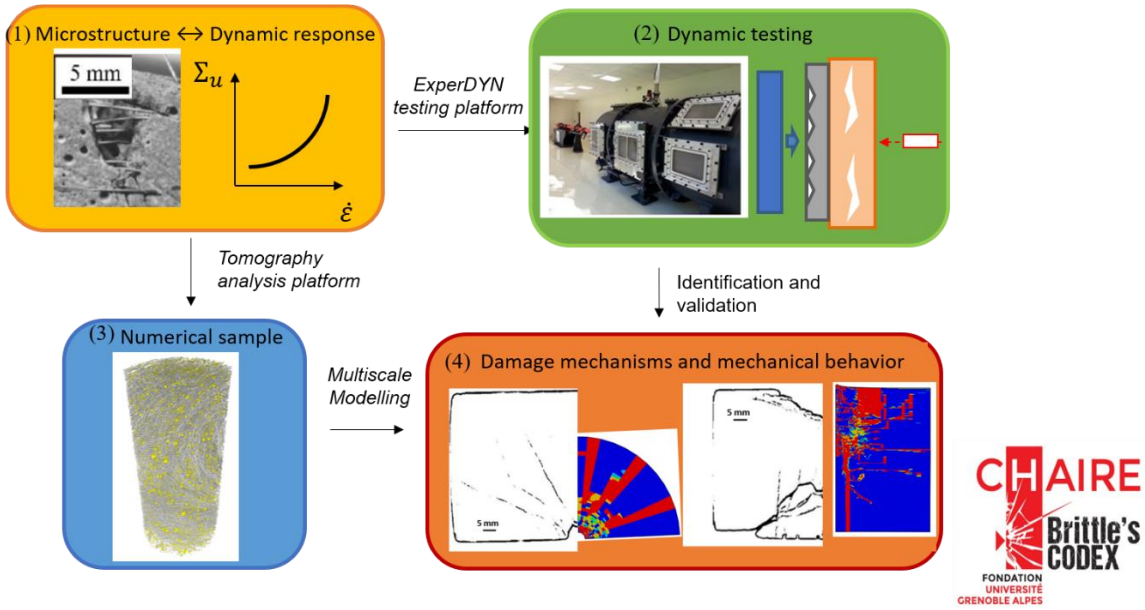

Figure 2 – Objectifs et méthodologie de la chaire *Brittle's CODEX* appliquée au BUHP : (1) Microstructure et réponse dynamique macroscopique ; (2) Échantillon soumis à une expérience d'impact de plaque ; (3) Échantillon vierge scanné par tomographique aux rayons X ; (4) Comparaison des endommagements entre les données expérimentales (analyse tomographique) et la prédiction numérique.

macroscopique après la première fissuration. J'ai identifié les paramètres du modèle DFHcoh-KST pour deux formulations de Ductal® avec fibres, atteignant une résistance à la compression simple de 150 MPa (Ductal® A) et 170 MPa (Ductal® B), en utilisant des techniques expérimentales existantes (essais de compression quasi-oedométrique, essais de flexion et essais d'écaillage à la barre d'Hopkinson) couvrant une pression de confinement allant jusqu'à 500 MPa et une gamme de vitesses de déformation allant de 10^{-5} à 10^{2} s^{-1}.

J'ai étendu pour la première fois le domaine de validité du modèle proposé à des vitesses de déformation très élevés (supérieurs à 10^{3} s^{-1}) en réalisant des essais supplémentaires comme l'étude de la résistance à la traction par écaillage après un impact de plaque. En l'occurrence, j'ai développé une nouvelle technique d'essai, appelée shockless, qui utilise un système de pulse-shaping pour assurer une vitesse de chargement constante dans l'échantillon testé. J'ai développé cette technique à l'aide de simulations numériques et d'expériences menées avec le canon à gaz installé dans le laboratoire 3SR en 2018.

4. Principales réalisations

Je résume ici les différentes conclusions que j'ai pu tirer dans mon manuscrit de thèse.

Les essais de compression quasi-oedométriques définissent partiellement le comportement des

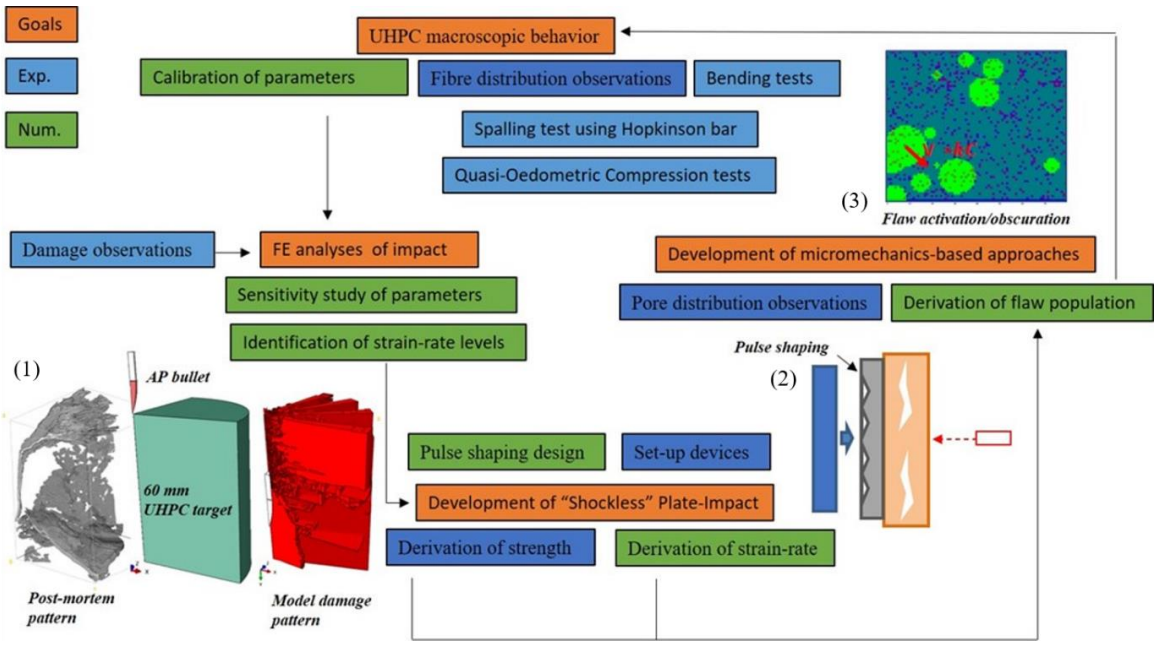

Figure 3 – Organigramme des travaux expérimentaux et numériques : (1) comparaison entre endommagement observé et prédit ; (2) développement d'un système de *pulse shaping* pour les configurations d'impact de plaque ; (3) simulation d'activation et d'obscuration des defauts sous chargements de traction dynamique.

BUHP sous confinement. Les limites de la technique d'essai d'impact de plaque existante sont surmontées par la technique d'impact de plaque shockless développée au cours de ma thèse, basée sur un système de pulse-shaping réalisé à partir d'une plaque volante et une plaque tampon usinée. Les essais de flexion, les essais d'écaillage et les essais d'impacts sur plaque permettent de définir la sensibilité à la vitesse de déformation de la résistance à la première fissuration en traction, couvrant la large gamme de vitesses de déformation accessible lors d'un impact (de 10^{-5} à 10^{4} s^{-1}).

Les simulations par éléments finis de l'impact d'un projectile perforant contre des cibles Ductal® montrent que la prise en compte de la deformation inélastique volumétrique du matériau n'est pas cruciale pour les BUHP. En l'occurrence, les paramètres clés de la stratégie de modélisation sont : le frottement à l'interface projectile-cible, la résistance aux charges de cisaillement des BUHP, la résistance à la première fissuration des BUHP et la résistance résiduelle des BUHP avec fibres.

J'ai dévelopé deux approches (l'une continue, l'autre discrète) décrivant la fragmentation des BUHP sous tension dynamique et basées sur les observations par tomographie à rayons X de la distribution des pores. En supposant que les pores sont les défauts du matériau et qu'ils sont connectés à des cortes fissures de la même la taille que le plus grand agrégat dans les formulations Ductal®, on obtient une famille de défauts qui respectent la résistance à la traction

mesurée dans la gamme de 10^{-5} à 104 s^{-1}.

Les études expérimentales et numériques que j'ai menées sur lese deux formulations de Ductal® ont souvent conduit à un comportement mécanique similaire, sauf en ce qui concerne la résistance aux charges de cisaillement, ce qui peut expliquer les performances balistiques supérieures de Ductal® B par rapport à Ductal® A.

Abstract

This thesis presents experimental and numerical investigations of Ultra-High Performance Concretes (UHPC) in view of intensifying their application as protective structures.

The coupled DFHcoh-KST model, describing both confined behavior and tensile damage, is selected to simulate impact problem using the Finite Element (FE) code Abaqus/Explicit. The material parameters are identified for two Ductal® formulations with fibres using existing experimental techniques: such as Quasi-Oedometric Compression (Q-OC) tests, bending tests and spalling tests at the Hopkinson bar. The investigation of the tensile response of UHPC is then extended at strain rates in the range of 10^3 - 10^4 s^{-1} through plate-impact tests. A new testing technique employing a pulse shaping system to ensure a constant loading rate in the specimen is designed using numerical simulation and experienced using the single-stage gas gun installed in the 3SR laboratory. Finally, the UHPC fragmentation under dynamic tension is simulated with discrete and continuous approaches based on X-ray Computed Tomography (CT) analysis of the UHPC pore distributions. This methodology contributes to understanding the role of the microstructure on the observed strain-rate sensitivity of tensile strength and crack density.

Keywords: Ultra-High Performance Concretes, confined behavior, tensile strength, strain rate sensitivity, plate-impact, pore distributions.

Contents

CHAPTER 1
Introduction

CHAPTER 1

Introduction

Ultra-high-performance concretes (UHPC) are largely employed in applications as bridge components or architectural facades, which mainly benefit from their durability and lightness. Instead, this Ph.D. concerns the unconventional use of UHPC in protective structures such as important infrastructural buildings, nuclear power plants, headquarters and bunkers. These structures have to resist to impact loadings caused by incidental events or attacks.

For the past 20 years, projectile impact experiments have been carried out on UHPC targets to show the abilities of such material in the field. For a given velocity, the penetration depth of the projectile into the target was found to be 50% less than the values measured experimentally for conventional concrete and 30% respect to high strength concrete. Using short steel fibres as disperse micro-reinforcement do not help much on pure penetration if the target thickness is substantially large (O'Neil et al., 1999).

However, concretes with a similar compressive strength can have different ballistic performance. This is due to their mix ingredients. (Dancygier et al.,2007) made some study showing that high quality aggregates and aggregates of larger size are increasing the penetration limit velocity. The fibres are essential to reduce the damage of the impacted elements and the risk of injury caused by concrete fragments (Kravanja et al., 2017). Some tests were performed to investigate which is the effect of the casting procedure but a conclusion in difficult to make (Lovichova et al., 2018).

The development of protective structures made of UHPC is feasible and interesting in both civil and military fields. However, the number of utilizations is still minimal. A well-known use is bearing the date 2005, 100 mm thick precast panels were installed to provide increased security against weapons effects on the roof of the Australian Government building (Cavill et al. 2006). For complete utilization, special knowledge is required.

Many empirical formulas to predict the penetration depth of a rigid projectile in a conventional concrete target already exist since the middle of the 1970s (Kennedy, 1976). Classical and more recent empirical formulae can be found in (Li et al., 2005) and (Baroth et al., 2015). They are applicable strictly within the limits of the tests from which the formula is derived such as projectile geometry, mass and velocity, target geometry, reinforcement, and concrete mechanical properties. Moreover, the range of application does not concern UHPC.

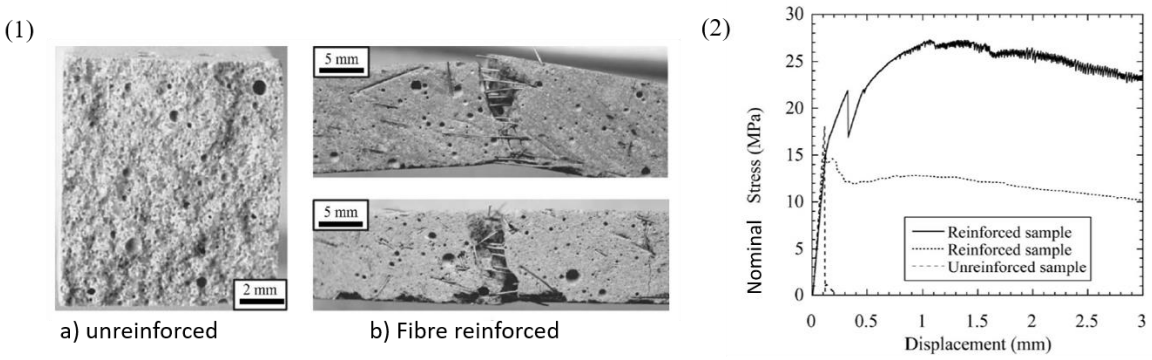

Fig 1.1 – Ductal® quasi-static flexural response (Forquin, 2003): (1) section of failure a) specimen without fibres b) specimen with fibres; (2) Macroscopic mechanical behaviour (fist cracking strength 15MPa).

A complementary approach to predict the penetration resistance is performing a numerical simulation, which requires the development of valid material models. Concrete is a complex material and has been generally accepted as pressure and strain-rate sensitive material (Daudeville and Malécot, 2011) (Buzaud et al., 2013) (Fang and Wu, 2017). Many different concrete models for simulating impact are already available in commercial codes. Researches have shown that a fairly good agreement between the numerical prediction and the experimental result can be achieved through careful parameter calibrations. An open question is if those models can be adapted for concrete, which deviates from the regular concrete material behavior, such as UHPC.

1.1 General notions

UHPCs are cementitious materials exhibiting outstanding compressive strength. In the commercial forms, they contain short steel fibres to achieve ductile behaviour in bending. The concretes used in this study belong to the family of Ductal® concrete launched in the late 90s (Dugat & Acker, 1999) and designed to have high compressive strength combined with high-energy absorption capacity that makes them ideals for protective solutions against ballistic and explosion threats. On the section of failure of the Ductal® beams tested in bending shown in **Fig. 1.1** (11x10x150 mm3), can be distinguished macro porosities and fibres. **Fig. 1.1** - (2) shows the nominal stresses as a function of displacement; no effect of fibres is observed on the first cracking strength, which could be mainly controlled by the porosities; a variable post-peak behaviour is observed for fibre reinforced specimens probably due to a different orientation of fibres in the section of failure.

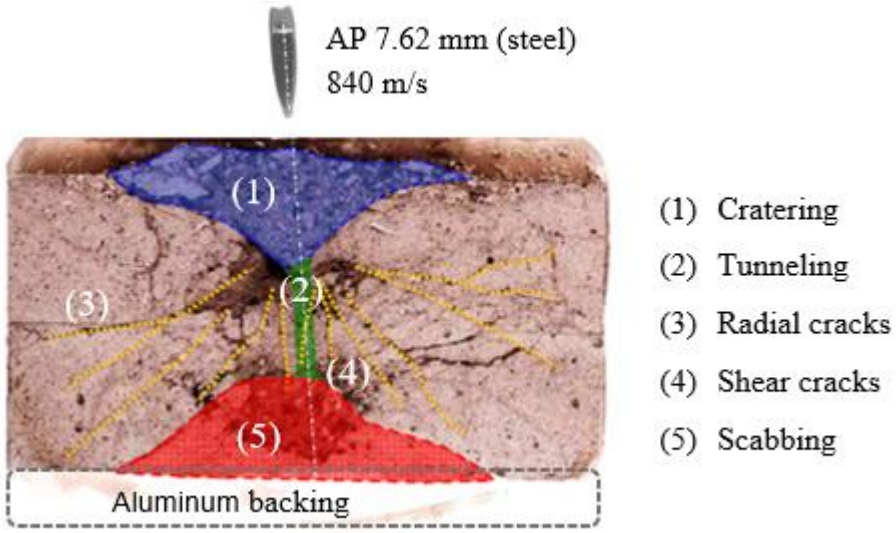

Fig 1.2 - Impact of an armour-piercing projectile AP 7.62 mm (steel core, impact velocity: 840 m/s, final penetration depth: 60 mm) against a bilayered target (60 mm UHPC and 10 mm aluminum backing) (Forquin, 2003)

1.2 Stating the problem

A picture reported in (Forquin, 2003) and (Forquin and Hild, 2010) is shown in **Fig. 1.2** to illustrate the effects of a kinetic striker impacting a concrete target. The striker is a small piercing caliber 7.62×51mm projectile initially fired at 840 m/s. The target is made of a 60-mm-thick UHPC block containing short steel fibres and a 10-mm-thick aluminum backing plate. The projectile is stuck at the concrete-backing interface. (Forquin and Hild, 2010) reported the following distinct phenomenon:

-cratering on the front face due to unconfined compression in the direction orthogonal to the projectile trajectory;

-cracking around the tunnel region due to hoop stresses generated by the swelling of the tunnel during projectile penetration;

-fragmentation of the target made of numerous oriented cracks with respect to the impact point due to tensile hoop stresses induced by the incident compressive wave;

-microcracking parallel to the tunnel due to shear stresses ahead of the projectile (confined compression in front of the projectile);

-scabbing on the rear face due to axial punching of the projectile.

Therefore, the complete damage pattern results from the combination of several dynamic compressive and tensile loadings at different instants and locations after the impact. A similar damage pattern with cratering on the front face and scabbing on the rear face and several radial cracks has been observed in impacted targets of mortars and conventional concretes. Numerical

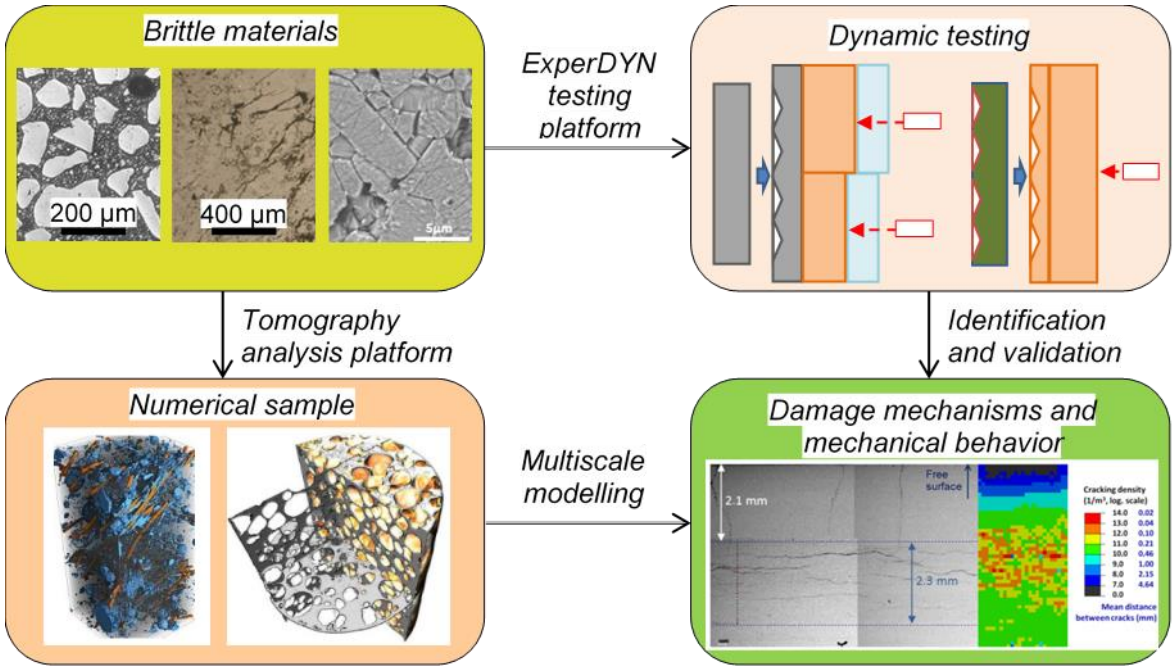

Fig 1.3 – Methodology of the Brittle's CODEX chair: (1) The virgin sample is scanned by X-ray tomography analysis. (2) The sample is subjected to plate-impact experiment. (3) A multiscale modelling of damage is conducted in the numerical sample. (4) A comparison of damage pattern is performed between experimental data (tomography analysis) numerical predictions (Forquin et al., 2020)

simulations have been carried out in literature in order to quantify the loadings generated in the experiment. In these applications, concrete is subjected to confinement pressure of several hundreds of MPa and strain rate from several hundred to thousand s^{-1} (Gran and Frew, 1996) (Forquin et al., 2006) (Erzar, 2010) (Weerheijm, 2013).

1.3 The Brittle'S CODEX chair

The subsequent research activities are performed in the framework of the Brittle'S CODEX chair (Brittle materialS under EXtreme COnDitions) supported by the UGA (Univ. Grenoble Alpes) Foundation and sponsored by the Saint-Gobain and Lafarge-Holcim companies. The chair was established at the Laboratoire 3SR in May 2017, held by Pr. Pascal Forquin with a four-year program and 1 M€ of budget. The program aims at contributing to understanding the behavior under extreme conditions of brittle materials such as rocks, glass, and concrete through: 1) the analysis of the material microstructure 2) the material testing with new experimental techniques able to create controlled dynamic loading condition and 3) the analytical and numerical modelling of the observed damage phenomenon with micromechanics-based approaches. This methodology presented in (Forquin et al., 2020) is summarized in **Fig 1.3** and it has been applied in the framework of this chair to three different

kinds of brittle materials, polycrystalline ices, ceramics and UHPC materials as concern the present thesis.

1.4 Aims of the present work

Under rigid projectile impact, blast loading, or contact detonation, concrete is exposed to extreme loadings such as high confinement stresses and high tensile loading rates, which lead to severe damage modes. These complex events need to be understood and modelled in view of improving the engineering design of UHPC as protective structures. This thesis aims to:

- identify the macroscopic behavior of UHPC materials under high confinement pressure and tensile loading as a function of loading rate and fibre reinforcement;
- develop new experimental techniques able to define the ultimate strength of UHPC at a very high strain rate (above 10^3 s^{-1}) overcoming the limits of the existing techniques;
- improve the modelling and the numerical simulation of the damage processes induced in UHPC at high loading rates, gaining the link with the microstructure.

1.5 Outlines

Chapter 2 contains an extensive literature review on the UHPC material, the experimental techniques available to investigate the response under high pressure and high strain rate, the existing material model already used to simulate UHPC under impact loading.

Chapter 3 proposes an experimental identification of the parameters of a coupled plasticity-damage model to be used to numerically simulate the mechanical behavior of UHPC under impact.

Chapter 4 presents the numerical simulations with the finite element (FE) code Abaqus/Explicit of a ballistic impact of an Armor-Piercing projectile against a concrete using the calibrated model.

Chapter 5 continues the investigation of UHPC behavior at a high strain rate through plate-impact tests. These tests are based on the single-stage gas gun recently installed in the 3SR laboratory.

Chapter 6 presents the modelling of the fragmentation of UHPC under dynamic tension with discrete and continuous approaches based on X-ray Computed Tomography (CT) analysis.

Chapter 7 presents the conclusions of the thesis and the prospects for further research.

CHAPTER 2
STATE OF ART

CHAPTER 2

State of the art

This chapter proposes a state of the art about ultra-high performance concretes (UHPC). The first section presents this concrete: a brief history, the composition, and general characteristics are summarized. Then, the second section provides experimental techniques available to investigate UHPC behavior under high pressure and high strain rate. The third section shows some numerical works taking into account this behavior. Finally, the fourth and last section gives a synthesis of the chapter, justifying the following choices in the thesis.

2.1 Ultra-High Performance Concrete

Ultra-high performance concretes (UHPC) are materials with a cement matrix with quite remarkable mechanical and durability performance. A deep state of the art can be found in the published Proceedings by (Toutlemonde and Resplendino, 2013). In this chapter, the history of their development and the essential elements of their composition are shortly presented.

2.1.1 Brief history

UHPC is still a young material in the history of concrete, although it has been a research topic for over 40 years and in development for approximately 30 years. UHPC was developed in France (Richard and Cheyrezy, 1995) based on early research in Denmark (Bache, 1981). Reactive powder concrete (RPC) was the major milestone for the development of UHPC. The maximum particle size in RPC is limited to approximately 0.6 mm, which means that the material prior to casting appears as a wet powder rather than a wet slurry. RPC design was optimized in the Lagarge research center at l'Isle d'Abeau in partnership with Bouygues and Rhodia to develop Ductal®, the first marketed UHPC, which was launched in the late '90s (Orange, 1999). This technology is now distributed in Western Europe, Asia, Australia, and the United States.

Cor-Tuf is the nomenclature given to a family of RPC developed by the U.S. Army Engineer Research and Development Center to serve as a "laboratory standard" UHPC mixture that can be reproduced for various projects (Williams et al., 2009). Case studies are presented on ongoing research focused on the use of UHPCs for repair and retrofit of armor plate systems in U.S. Army Corps of Engineers (USACE), inland navigation civil works infrastructure, and

ongoing long-term field durability testing at the Treat Island Natural Weathering Station near Eastport, Maine (Green et al., 2014).

2.1.2 Mix formulation

The ratio of water to binder W/B is decreased to below 0.25 to obtain a UHPC (about 0.16 to 0.2). This reduction is possible thanks to the addition of an admixture (superplasticizer), which allows deflocculating binder and cement with minimal amounts of water. The W/B reduction is complemented with an extension of the granular spectrum through ultra-thin micrometer-sized additions, generally consisting of silica fume (5 to 10 times smaller than the size of the cement particles), amounting to about 20% of the cement mass. The aggregate size is strongly reduced compared to ordinary concrete – the largest grain size is of the order of millimeters – and particular attention is given to the nature of the aggregates, which must present sufficient mechanical strength to avoid being the weak points of the mixture.

The resulting material is extraordinarily compact and absent of any capillary porosity. With such a formulation, the compressive strength is generally higher than 120 MPa. Some UHPC may be subject to special treatment at an early age. Thermal treatment, typically 90ºC, applied for approximately 48 hours after the concrete sets, increases the compressive strength from about 170 MPa to the order of 210 MPa. Thermal treatment coupled with pressure treatment sufficient to expel any excess liquids and air from the fresh mixture during the casting operations may produce concrete with a compressive strength higher than 800 MPa (Dugat et al., 1996).

With the increasing compressive strength, the concrete becomes more brittle, which is the major problem for concrete with high strength. Hence, steel fibres are used to restore ductile behavior, about 2 to 3% by volume (160 to 240 kg of steel per cubic meter of concrete). The maximum fibre content is a function of the fibre aspect ratio l/d and fibre shape, and production issues such as workability. The fibres are generally straight and made of very high resistance steel. Their size are in accordance with used aggregates: a length from 12 to 20 mm and a diameter from 0.1 to 0.3 mm. **Table 2.1** depicts the two representative mixture proportions for UHPC in the scientific community.

2.1.3 General characteristic of UHPC

According to recommendations and standards (AFGC2013, prSIA 2052-2016, ACI239-18, CSA A23.1-19), UHPC is defined as concrete with a characteristic compressive strength between 150 and 250 MPa. When compared to conventional concrete, UHPC has higher

UHPC component	Ductal®	Cor-Tuf
Cement	1	1
Silica fume	0.15	0.389
Sand	1.25	0.967
silica four	0.1	0.277
Super plasticizer	0.016	0.017
Water	0.21	0.208
Short strigth steel fibres	0.22 (l/d =70)	0.310 (l/d =54)

Table 2.1 - Two possible UHPC mixture proportions by mass. Ductal® is from (Orange, 1999). Cor-Tuf is from (Williams et al., 2009)

Material characteristic	Conventional concrete	UHPC
Density kg/m3	2300	2300-2800
Compressive strength (MPa)	20-40	150-250
Direct tensile strength (MPa)	1-3	7-15
Elastic modulus (GPa)	25-35	45-65
Fracture energy (kJ/m^2)	0.1	10-40
Water Porosity (%)	15	9-6
Oxygen Permeability (m^2)	10^{-16}	$<10^{-19}$

Table 2.2 - Comparison of conventional concrete and UHPC. (Nf P 18-710, 2016) (ACI 239R, 2018)

strength and elastic modulus. Fibres are added to achieve the ductile behavior under tension, and if possible, to dispense with the use of conventional active or passive reinforcement. **Table 2.2** provides typical ranges for selected mechanical properties of conventional concrete and UHPC.

Under the uniaxial compression, the steel fibre reinforcement only slightly increased the uniaxial compressive strength, but notably improved its resistance capability on the descending branch of the stress-strain curve after the peak (green curve in **Fig 2.1**).

The addition of fibres to the matrix particularly improves the bending behavior of the concrete in the post-first-crack region of the stress deflection curve. The large number of small fibres that cross the path of potential cracks, coupled with the excellent bond between fibres and matrix, provides high resistance to fibre pullout during tensile-cracking and significantly increases the material toughness. The post-cracking resistance depends on the orientation of

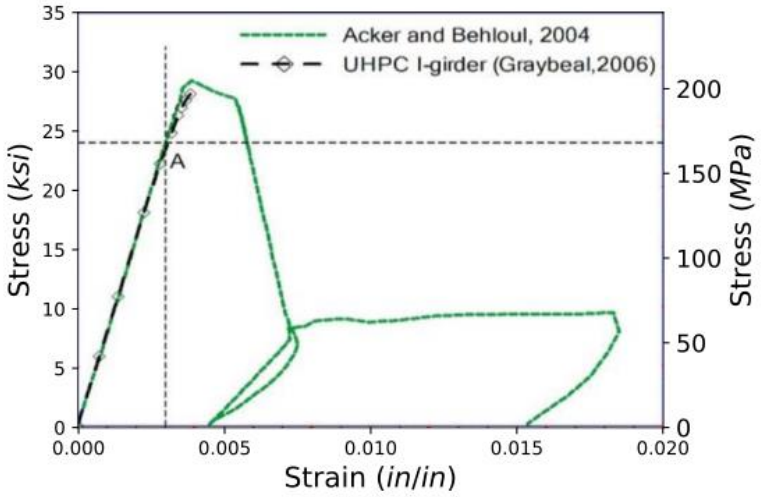

Fig 2.1 - Influence of the fibre reinforcement during uniaxial compression. Figure by (Aaleti, S., B. Peterson, 2013), data of (Acker and Behloul, 2004) and (Graybeal A., 2006)

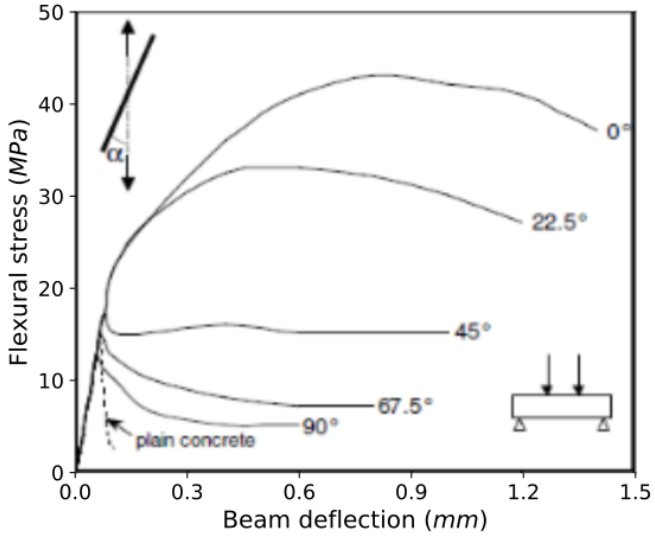

Fig 2.2 - Influence of the fibre orientation on the bending behavior (Behloul, 1996)

fibres (**Fig 2.2**) (Behloul, 1996). The direct tensile strength of the matrix is systematically higher than 6 MPa.

Researches have shown that the permeability coefficient is approximately one to two orders of magnitude lower than conventional concrete due to the discontinuous pore structure (Charron et al., 2007).

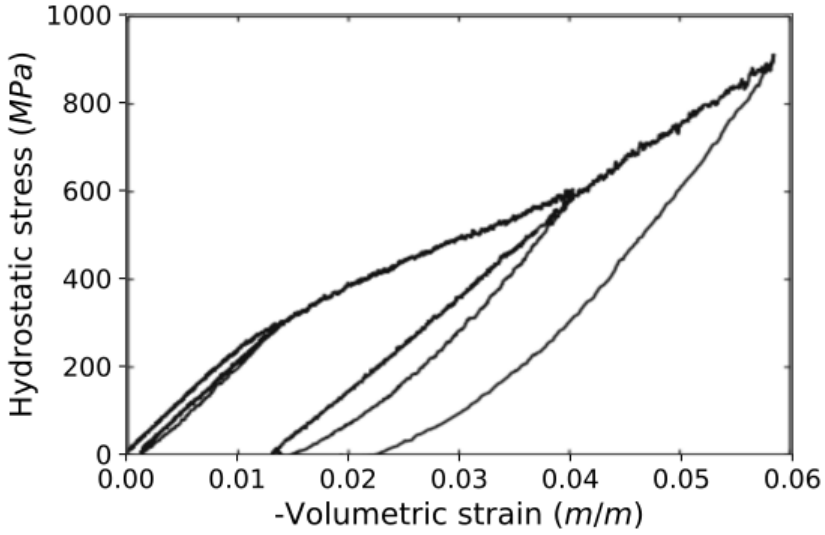

a)

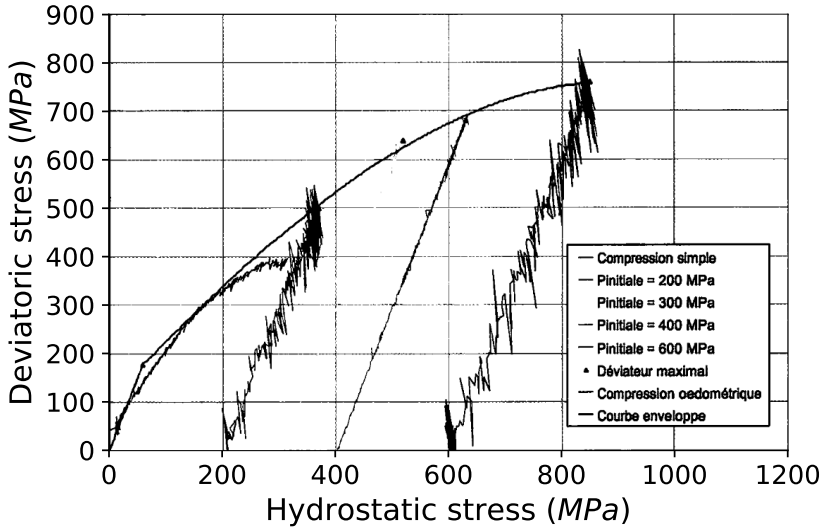

b)

Fig 2.3 - Experimental results of quasi-static tests (Forquin, 2003): a) Compaction curve; b) Deviatoric strength as a function of mean stress for triaxial tests with a fluid pressure pf =0, 200, 300, 400 and 600MPa

2.2 Experimental techniques and results

2.2.1 High confinement in static

Triaxial tests are typically employed to investigate the response under confinement of all types of concrete materials. This test begins with a purely hydrostatic test. Once the desired confinement has been reached, the specimen is axially loaded while holding the confining pressure constant. The deviatoric strength is taken as the maximum stress difference reached

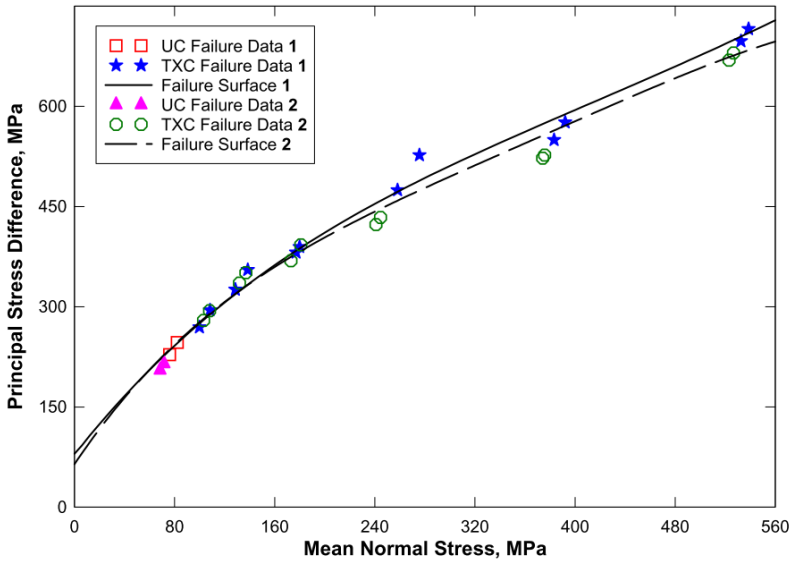

Fig 2.4 - Influence of fibres on confined behavior. Failure Data 1 refers to Cor-Tuf without steel fibres Failure Data 2 refers to Cor-Tuf with steel fibres (Williams et al., 2009)

during the test. The material limit state curve is then deduced from a series of triaxial tests performed at different lateral pressures. **Fig 2.3** by (Forquin, 2003) provides the compaction curve and the limit state curve obtained from four triaxial tests conducted on Ductal® concrete with strength in unconfined compression of 188 MPa. Compared to standard concretes, a very low volumetric strain is observed for the applied level of pressure. The triaxial compression tests exhibited a continuous increase in maximum principal stress difference with increasing confining stress. Data referred to sample without fibre reinforcement. (Williams et al., 2009) defined a failure surface for Cor-Tuf with fibres from test results at six levels of confining pressure (10, 20, 50, 100, 200, and 300 MPa). Overall, the results from all of the compression tests for both Cor-Tuf concrete, with and without steel fibres, were very similar (**Fig 2.4**).

2.2.2 High confinement in dynamic testing

Dynamic axial compression with lateral pressure is not a common experiment, and, to the author's knowledge, UHPC materials have not yet been tested. Ordinary concrete, microconcrete, and high-performance concrete were tested in quasi-static and dynamic QOC (Quasi-Oedometric Compression) tests in (Gatuingt, 1999) (Forquin et al., 2008b) (Safa, 2009) (Forquin et al., 2010) (Piotrowska and Forquin, 2015) (Piotrowska et al., 2016). The principle of this testing technique, the processing method, the validation tools, and the main fundings provided in the literature are summarized in a recent review (Forquin, 2019). The specimens were confined in a metallic ring and loaded employing large-diameter Split-Hopkinson Pressure Bars. The specimen follows an almost uniaxial strain path at a strain rate from 50 to 400 s^{-1}.

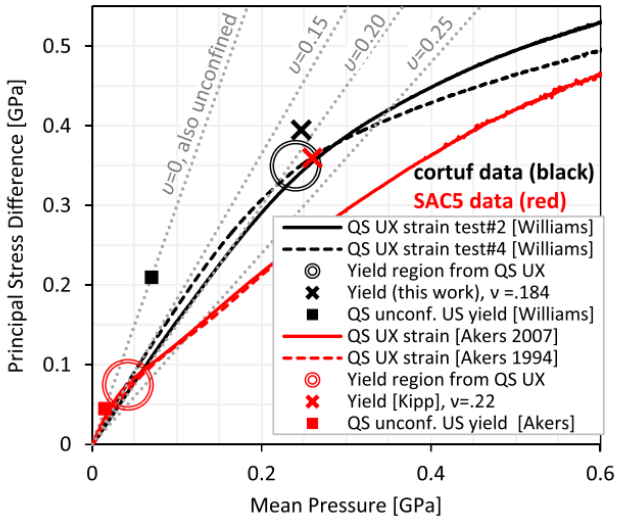

Fig 2.5 - Comparison of dynamic (cross) and Quasi-Static (circle) yield region for Cor-Tuf (UHPC) in black and SAC-5 (ordinary concrete) in red. Data obtained in uniaxial strain conditions except for the points in uniaxial stress (square) corresponding to yield in unconfined. (Neel, 2018)

The data obtained with ordinary concrete and microconcrete showed a quite limited influence of the rate of loading on the strength up to the pressure of 800 MPa (Safa, 2009). For those concrete compositions, the water-pressure plays a significant role inside saturated samples that reduce the shear strength in an amount that seems linked to the initial level of porosity of the specimens (Piotrowska and Forquin, 2015).

Plate impact tests for which the strain rate is in the range of 10^4 – 10^6 s^{-1} can also be used to investigate the effect of the loading rate on the deviatoric strength at high levels of confinement. With this technique, a metallic or polymeric flyer plate hits the concrete target at an impact velocity ranging from a few tens of meters per second to a few thousands of meters per second. The impact generates a planar compressive wave under one-dimensional strain conditions. (Grote et al., 2001) used gauges embedded in the specimen to record the growth of longitudinal and radial stresses in mortar targets. The records are in agreement with the stress levels predicted by the one-dimensional linear elastic stress wave theory for longitudinal stresses lower than a threshold (σ_{HEL}) called the Hugoniot Elastic Limit (HEL). The inability of the material to carry higher deviatoric stress at higher longitudinal stresses suggests then a limited shear resistance. According to the material Poisson's ratio, the elastic loading on the path is:

$$\sigma_{dev} = P\left(\frac{1-2\nu}{1+\nu}\right) (1)$$

The dynamic yield strength Y at the confinement pressure P corresponds to the limit principle stress difference at the HEL, such as:

$$Y = \sigma_{HEL}\left(\frac{1-2\nu}{1-\nu}\right) \ , \ P = \frac{\sigma_{HEL}}{3}\left(\frac{1+\nu}{1-\nu}\right) (2)$$

(Neel, 2018) performed plate-impact tests on Cor-Tuf and estimated σ_{HEL} = 510 MPa. The calculus gives Y= 400 MPa at P = 250 MPa. The pair (P, Y) can be directly compared with the deviatoric stress as a function of mean stress in quasi-static tests. As shown in **Fig 2.5**, (Neel, 2018) compared the dynamic yield point with the path in quasi-static uniaxial strain tests. The strain rate of the plate-impact test was roughly estimated at 10^5 s^{-1}. The strain rate of the quasi-static tests is approximately 10^{-5} s^{-1}. The agreement between both yield strengths at such different loading rates indicates very low strain-rate sensitivity for the yield strength of Cor-Tuf. In the same figure, the data referred to SAC5 ordinary concrete are also reported. It is remarkable that Cor-Tuf, with a static compressive strength approximately five to six times that of the ordinary concretes such as SAC5, yield mainly the same dynamic yield strength. It appears that the strength advantage of UHPC over traditional concretes, at least when loaded in uniaxial strain, declines as the strain rate increases. (Neel, 2018) linked the root of this difference with the fundamental dissimilarities between UHPC and ordinary concrete as the amount of porosity (including capillary porosity) and the strength of the interface transition zone between the cement gel and the aggregates. Moreover, the dynamic experiment subjects the specimen to uniaxial strain at the macro and continuum scale, and voids and heterogeneities alter this condition at the microscale. So the yield strength obtained in this way must be more carefully interpreted for ordinary concrete than UHPC.

2.2.3 Dynamic tension

The concrete behavior under tension is well known to be strain rate sensitive (Rossi and Toutlemonde, 1996) (Forquin et al., 2013). Several experimental techniques exist to quantify the strain rate effect on tensile strength and damage; effects similar to conventional concrete are observed during tests on UHPC and UHPFRC material (Nöldgen et al., 2013) (Thomas and Sorensen, 2017).

2.2.3.1 Low strain rate (10^{-6} to 1 s^{-1})

The corresponding strain rates from 10^{-6} to 1 s^{-1} can be investigated with a servo-controlled uniaxial loading machine (Forquin et al., 2013). The tensile load is applied to the specimens under displacement control by moving the loading frame downward at a constant rate. Since the strain distribution of the specimen is uniform without localization before reaching the maximum strength, it is efficient to express the loading rates with a strain rate. The load acting on the specimen is measured using a load cell.

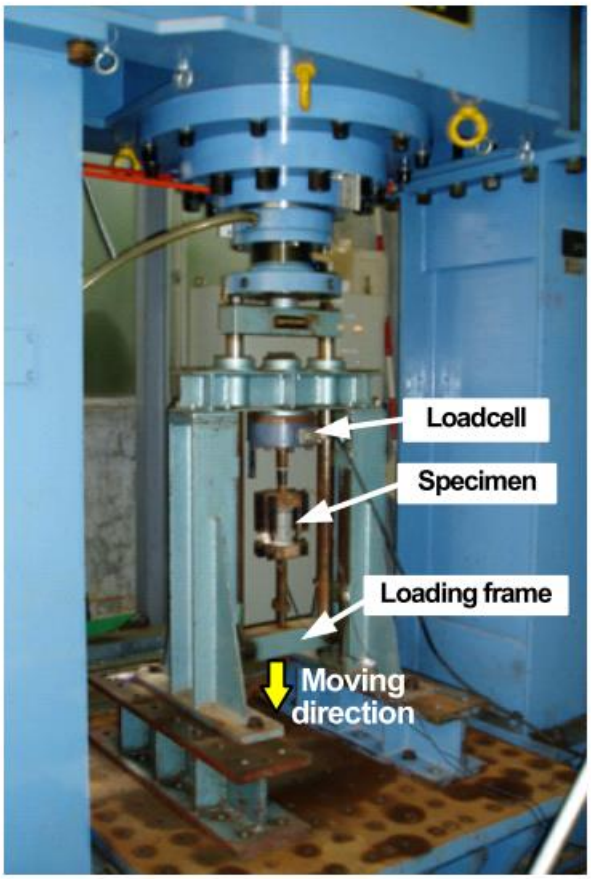

Fig 2.6 - Uniaxial tensile loafing apparatus (Fujikake et al., 2006)

(Fujikake et al., 2006) used the uniaxial loading machine, shown in **Fig 2.6,** on Ductal® notched prismatic specimens (two percent of short straight steel fibres in volume were introduced to the mix) to generate a single fracture rather than multiple cracks. Based on these results, the first cracking strengths increase with increases in the loading rate. The dynamic tensile strength increases by 70% as the strain rate increases from 1.0×10^{-6} to 5.0×10^{-1} s^{-1}, whereas, at the crack opening of 2 mm, the tensile stress is the same at each loading rate.

(Pyo et al., 2015) tested dog-bone specimens of a UHPC (Maximum grain size = 0.8 mm) with different types (twisted and straight) and volume fractions of steel fibres (1-3% by volume). Four strain rates were considered in the tests, ranging from 10^{-5} s^{-1} to 10^{-2} s^{-1}. The strain rate sensitivity of the peak stress is moderate and nearly linear up for all the series. The straight and smooth fibre series (0.2 mm diameter and 25 mm length) shows the lowest rate sensitivity for the post-cracking behavior. The strain rate sensitivity has been found not to depend on fibre volume content, fibre shape and aspect ratio.

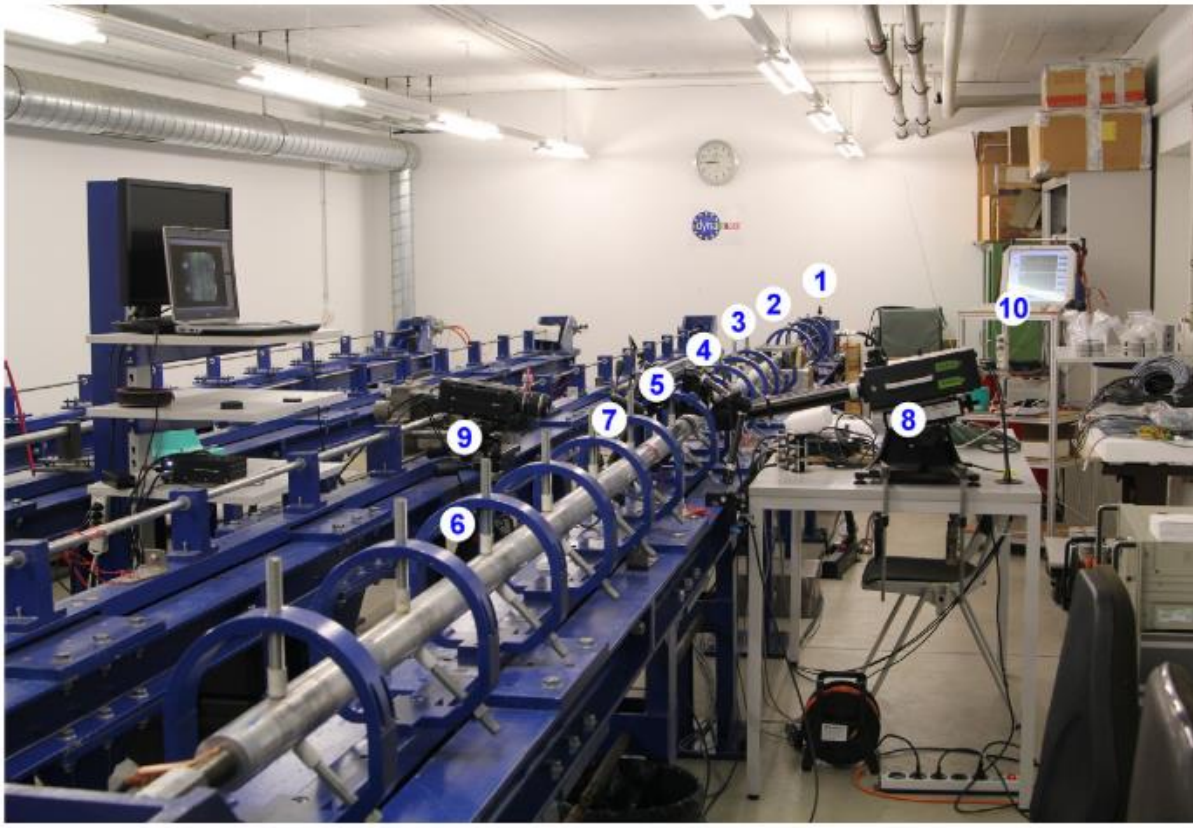

Fig 2.7 - Split Hopkinson Tensile Bar: 1-hydraulic actuator; 2-pretensioned bar; 3-blocking device; 4- input bar; 5-strain gauge station; 6-output bar; 7-specimen; 8-electro-optical extensometer; 9-fast video camera; 10-transient recorder (Cadoni et al., 2019)

2.2.3.2 Medium strain rate (1 to 50 s^{-1})

In the following, the accent is on the experimental methods that reach strain rates up to a few tens s^{-1}. A brief description of the Split Hopkinson Tensile Bar (SHTB) is reported. The specimen is glued between an input and an output bar. A pre-tensioned bar is directly connected to the input bar, used as a pulse generator. A hydraulic actuator pulls one end of the pre-tensioned bar. The force is released through the rupture of a fragile bolt. The amplitude and duration of the stress wave generated in the incident bar are determined by the amplitude of the pretension load and the length of the prestressed bar. The pulse propagates along the input and output bars, leading the specimen to failure.

(Cadoni et al., 2019) used 2 SHTB devices, respectively 20 mm and 60 mm in bar diameter, for testing notched cylinders and dog-bone specimens made of Ductal®. The dog-bone specimens have extremities of diameter as the bars, the gauge length being 30 mm in diameter and 40 mm in length. The input and output bars were instrumented with strain gauges that measured the

incident, reflected, and transmitted pulses (**Fig 2.7** shown the experimental set-up). The signals allow measurement of the stress and strain state in the sample based on the data processing proposed by Kolsky (1949). The strain rate was measured when the maximum value of the strength is reached. The maximum strain rate achieved during the experimental campaign at failure is only 24 s^{-1}. The maximum strain rate is limited by the fact that the balance of input and output forces implies a short round-trip time in the specimen compared to the loading time to failure. The peak stress is double if compared with results with the same material in quasi-static condition. The post-peak behavior seems not to be strain rate sensitive with these fibre volume contents. In the case of the dog-bone specimen, the strength at first cracking is always higher than the post-cracking stresses (first cracking stress = peak stress).

(Caverzan et al., 2015) tested notched cylinders of HPC (the sand used in the material was sieved up to 2 mm) and HPC materials with fibres aligned to the load direction or with a random fibre distribution. Tests were carried out at rates ranging from 0.1 to 150 s^{-1}. Experimental results revealed that the higher the number of fibres, the higher the post-peak stress. The post-peak plateau and the capacity of the material to absorb energy depend on the number and the orientation of the fibres present in the fractured surface.

2.2.3.3 High strain rate (50 to 250 s^{-1})

The so-called spalling technique figures prominently for dynamic tensile loading at a high strain rate (approx. 50-250 s^{-1}) among the existing experimental methods applied to concrete. Based on a Hopkinson bar device, a compressive pulse generated by an impact or blasting is transmitted to one side of the specimen. When this pulse reaches the specimen free-end, a tensile pulse propagates in the opposite direction; the superposition of the signals generates tensile stresses that can lead to the onset, the growth, and the coalescence of cracks. For clarity, the Lagrangian diagram of the propagation of waves is summarized in **Fig 2.8.** The needed instrumentation is also reported in the figure. A strain gauge is used on the bar to observe the incident and reflected pulses. Strain gauges are glued on the specimen; the gauge signals are time-derived to deduce the change of the strain rate. A laser extensometer is used to record the particle velocity. The spall strength is deduced according to the formula introduced by Novikov (1966).

Spalling experiments on UHPFRC (with 1% of fibres) have been conducted by (Millon et al., 2009). The material shows static compression strength up to 180 MPa and static tensile strength up to 9 MPa. Static and dynamic Young's modulus show similar values, a rate dependency was

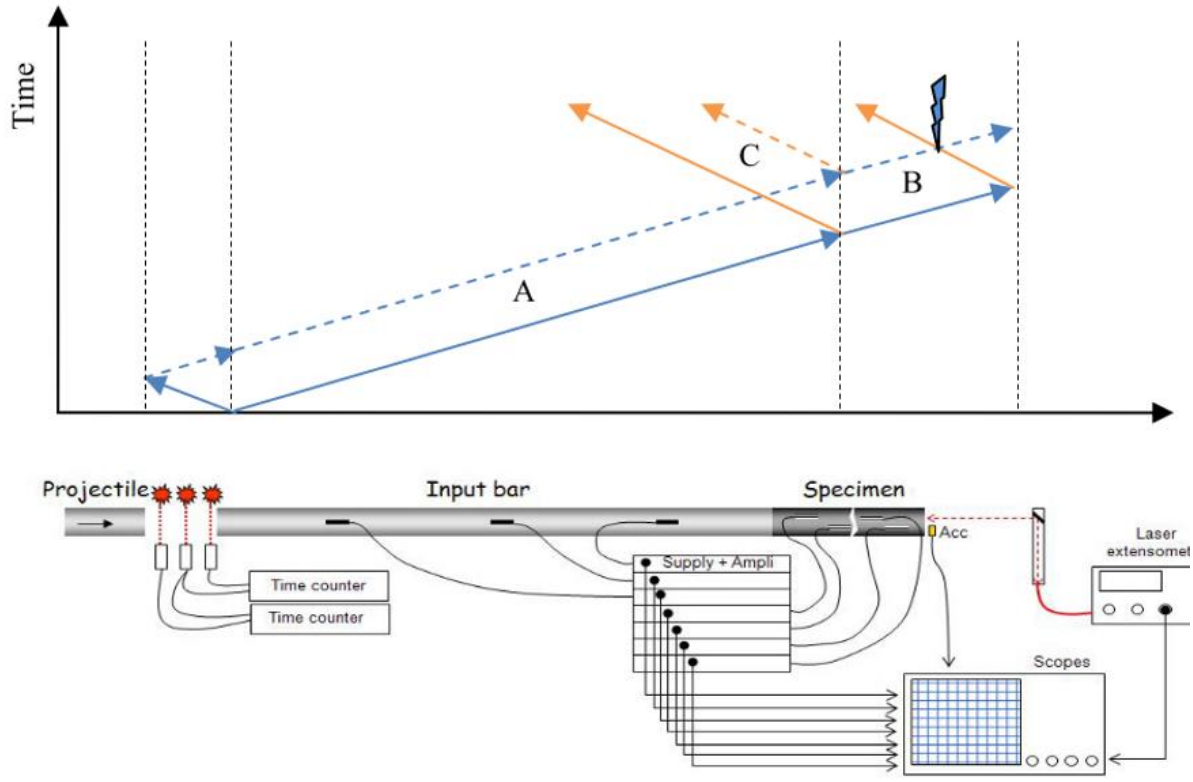

Fig 2.8 - Lagrangian diagram of the propagation of waves in a spalling test involving a Hopkinson bar and description of the instrumentation used (Forquin and Erzar, 2013)

not found. The dynamic tensile strength is of more interest. The tensile strength rises more than by the factor of 2 up to 43 MPa. The fracture energy shows low strain rate effects; the ratio dynamic to quasi-static value is around 1.1

Spalling experiments on UHPC (with 2% of fibres and without) have been conducted by (Forquin and Sallier, 2014) and reported in (Pontiroli et al., 2016) (Forquin et al., 2017) to identify the effect of the strain rate on the tensile strength. A strength three times higher than the static one has been identified at a strain rate from 40 s^{-1} to 140 s^{-1}. Four sets of samples were considered (UHPC without fibres, with randomly oriented fibres, badly oriented fibres, and well-oriented fibers) and subjected to spalling tests. A small influence of fibres and fibre orientation on the peak stress along with a strong influence of fibres and fibre orientation on the post-peak (softening) behavior of UHPC was demonstrated (Forquin et al., 2017).

2.2.3.5 Very-High strain rate (above 10^3 s^{-1})

The plate-impact testing technique is used to generate spalling at higher strain-rates. The impact generates a wave propagating in a one-dimensional strain state in the specimen until reaching the free surface of the specimen. A few hundred nanoseconds later, the tensile stress grows

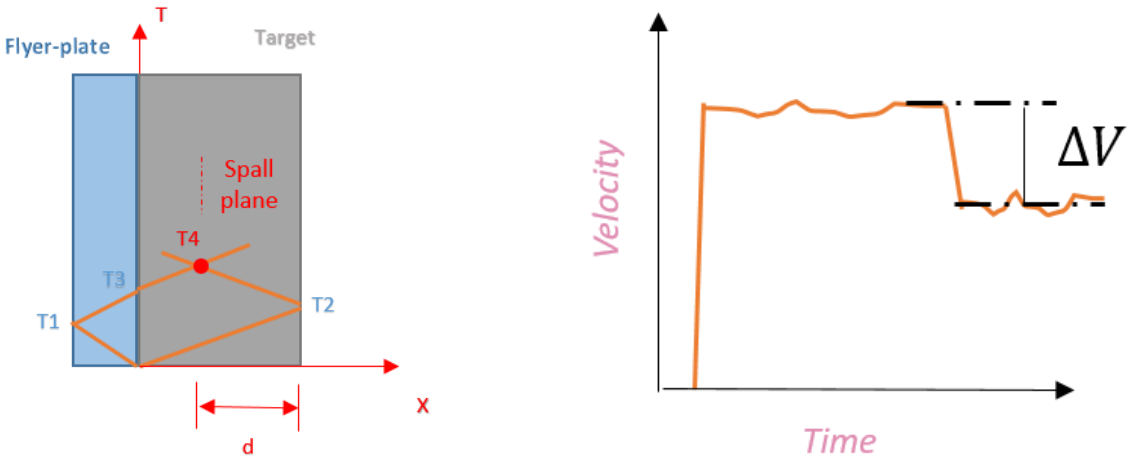

a) b)

Fig. 2.9 - a) Time-distance diagram for a plate-impact experiment b) Particle velocity at the rear face of the specimens versus time

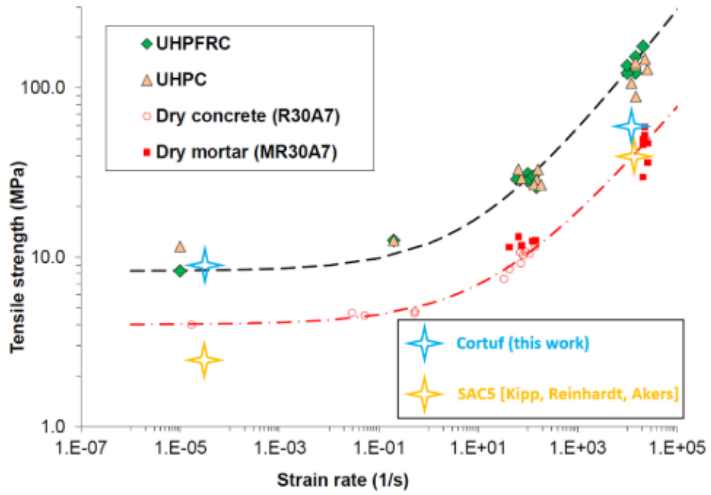

Fig. 2.10 - Strain rate effects on the dynamic tensile strength obtained on concrete, mortar, and on UHPCs with and without fibres (Neel, 2018)

within the core of the tested sample due to the crossing of release waves. If fracture planes develop, the rear part of the pulse encounters a new free surface resulting in a further reflection. Therefore, this last part of the wave appears as a rebound on the free-surface velocity profile. As in the spalling test at the Hopkinson bar, the intensity of the velocity rebound is used to estimate the spall strength (**Fig 2.9**). Regardless, the technique is not extensively diffuse for concrete materials; the data recorded by the interferometer appears difficult to process due to the size of aggregates within the cementitious materials.

(Neel, 2018) reported plate impact experiments on Cor-tuf without fibre reinforcement (quasi-static tensile strength 9 MPa). The impactor was either copper or PMMA, and the window material was either LiF or PMMA, evaporatively coated with a thin (< 1 µm) layer of aluminum

on the surface to be epoxied to the target. The spall strength for Cor-tuf is interpreted as approximately 60 MPa. The strain rate was approximated to 2×10^4 s^{-1} by the author.
(Erzar et al., 2013) used high-pulsed-power technology. They report a spall strength of 45 MPa on a conventional performance (and water-saturated) mortar with quasi-static strength of 3.5 MPa. The experimental configuration used in this campaign allows determining the strain-rate anytime during the test. The GEPI generator is composed of 28 stages able to store 70kJ from a charging voltage of 85kV. The released current rises over about 500 ns to a value of 3.3 MA, converging into the center of the electrodes where a short circuit is ensured. In this region, the intense current and the induced magnetic field generate a compressive wave applied to the internal skin of the electrodes. The same device was used by (Pontiroli et al., 2016) on UHPC (with and without fibre reinforcement). Spall strength was 140 MPa at a strain rate of 1.5×10^4 s^{-1}. The strain-rate has been evaluated numerically at the spall plane when the tensile stress reaches the computed strength, assuming a purely elastic behavior of the specimen until the onset of the fragmentation process. Slight differences have been observed between UHPC with and without reinforcement. The data of Pontiroli for UHPC show a remarkably consistent trend in the spall results with the data for mortars implying that the spall strength is consistently linked to the static tensile strength (**Fig 2.10**). Those values can be compared to Cor-tuf and ordinary concrete. The data for Cor-tuf and SAC5 does not follow the trends as closely as the data of Pontiroli for UHPC and Erzar for MR30A7. In summary, the SAC5 and Cor-tuf spall data indicate that, like the deviatoric strength, the tensile strength advantage of the high-performance formulations mostly disappears at the strain rates associated with the tests. However, the spall strength of both concretes is much higher than the static tensile strength (Neel, 2018).

2.2.3.4 Summary - Low to very high rate

The strain rate effect on the first cracking strength is shown in **Fig 2.11**. There are no significant differences in behavior for strain rates lower than 10 s^{-1}; the real differences in the behavior appear for higher strain rates. A lack of data is evident between 10^2 and 10^4 s^{-1}, and all spall data at a very high strain rate (above 10^4 s^{-1}) are very sparse.

2.2.4 Damage mode

When a concrete structure is subjected to detonation or ballistic impact, several damage modes may be observed as scabbing, spalling, radial cracks, or micro-cracking in the vicinity of the

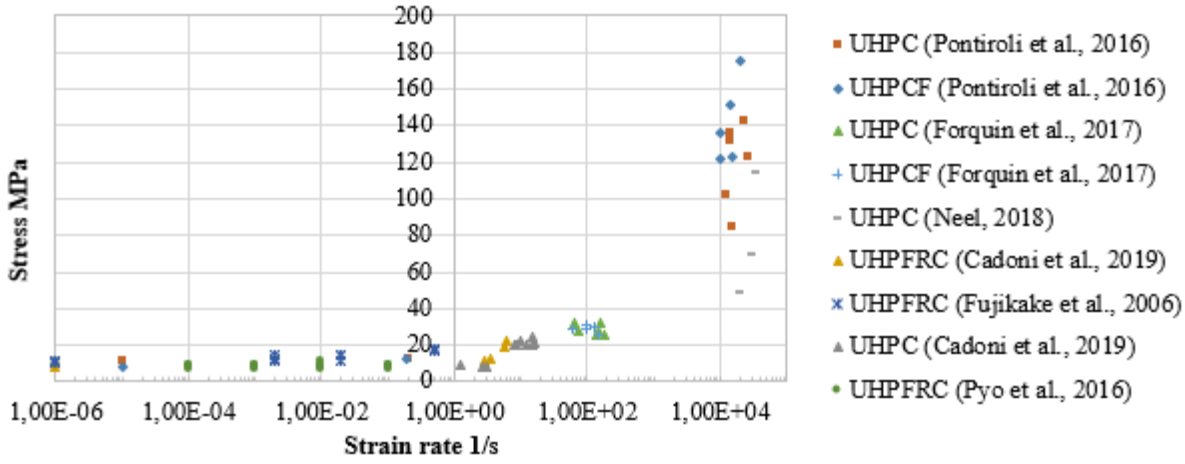

Fig 2.11 - Strain rate effect on first cracking strengths with data for UHPC with and without reinforcement.

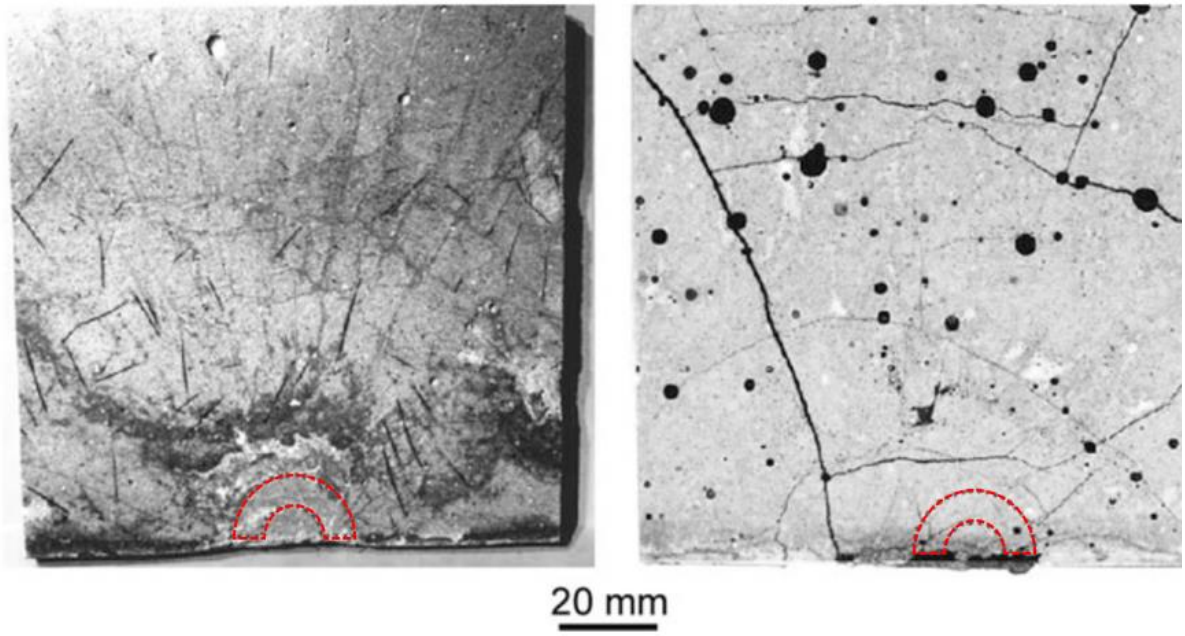

Fig. 2.12 - Edge-on impact experiments performed with Ductal® concrete with and without steel fibre (Forquin, 2015)

localized loading (Li et al., 2005)(Forquin et al., 2008a)(Warren and Forquin, 2016). The edge-on impact test (EOI test) was developed to study the damage mechanisms by Ernst Mach Institute (Germany) (Strassburger et al., 1994), and Centre Technique d'Arcueil (France) (Riou et al., 1998). This experiment aims to produce an equivalent loading to that of a ballistic impact in a two-dimensional configuration to visualize the onset and the expansion of damage in the target using a high-speed camera. UHPC was subjected to the EOI test in (Forquin and Hild, 2008), which shows that despite the intense multiple cracking processes induced in the target due to the impact loading, it retained an excellent cohesion resistance thanks to steel fibres.

A portion of those specimens is shown in **Fig 2.12** tested in the so-called “sarcophagus configuration”. The dotted lines in the figure represent the zone where a dynamic confinement system was applied to avoid that compressive damage in the area of impact restrains the incident wave and thus reduces the tensile loading. Numerous cracks oriented in the radial direction, circular-front cracks centered on the impact point, and spall cracks oriented perpendicularly to the axial direction are visible beyond the area of confinement.

2.3 Numerical modelling in FE code

In the following, a few models use in existing Finite Elements (FE) codes to simulate penetrating impact in concrete structures are detailed. The problem needs a constitutive model describing both confined behavior and tensile damage.

2.3.1 Modelling of UHPC under high confinement

Under impact, a pressure level of several hundreds of MPa can be observed in the vicinity of the projectile nose. Specific phenomena such as pore collapse or increase of shear strength have to be considered (Forquin et al, 2015). A simple plasticity model, Krieg, Swenson and Taylor (KST) was proposed by (Swenson and Taylor, 1983). In this elastic-plastic model, a parabolic relation describes the pressure-dependency of the yield stress in the sense of von Mises plasticity criterion. A piecewise-linear compaction curve describes the pore-collapse phenomenon occurring at high pressure. The elastic behavior becomes more and more nonlinear up to the full consolidation of concrete. At this point, the pore collapse phenomenon is achieved, and the material is considered fully compacted.

The KST model parameters were identified for UHPC at low levels of pressure (up to 1 GPa) through hydrostatic and triaxial tests (Forquin, 2003). (Erzar et al., 2016) extended the validity of the model up to 6 GPa utilizing a series of plate impact experiments. However, the pressure dependency of the deviatoric strength of concrete has not been directly measured for this high pressure. Indeed, specific tests using stress gauges placed to measure the transverse stress have to be conducted to validate the proposed model. Nevertheless, the model appears consistent as it allows getting a good correlation between numerical validations and experimental data (Forquin et al, 2008).

The Johnson–Holmquist Concrete (JHC) model describes the dynamic compressive behavior under large strain and high-pressure conditions (Holmquist et al., 1993). The JHC concrete model contains three essential elements (**Fig. 2.14**): (1) an equation of state (EOS) for the pressure-volume relation that includes the nonlinear effects of compaction, (2) a representation

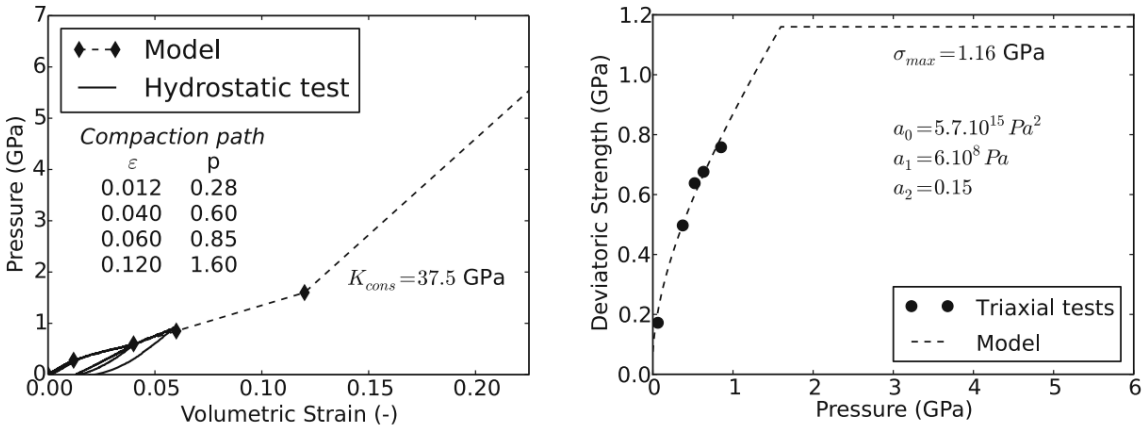

Fig. 2.13 - KST model for the UHPC: a) multi-linear compaction curve, b) plasticity model identified from quasi-static triaxial tests. (Erzar et al., 2016)

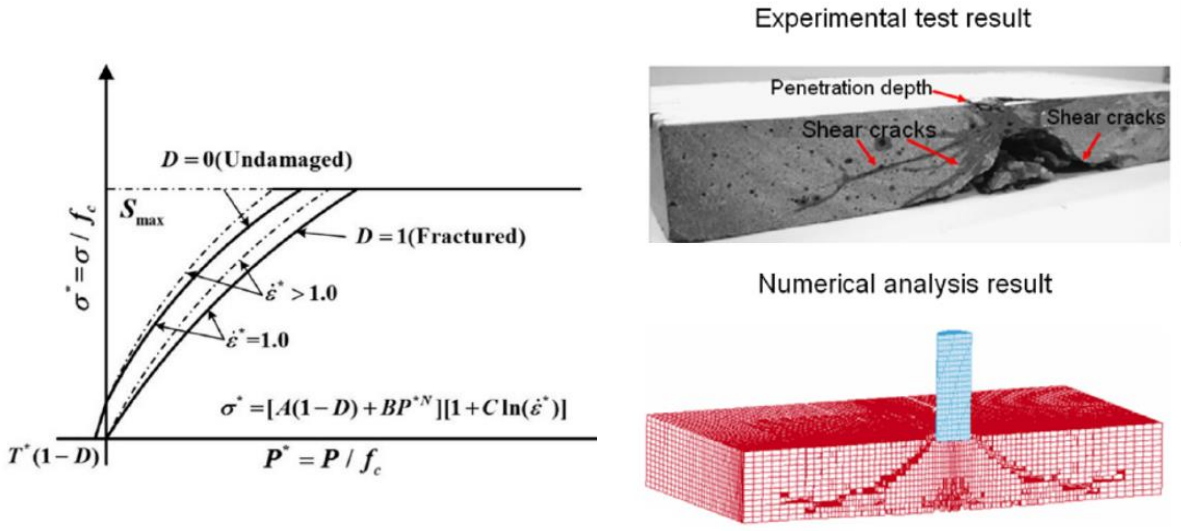

Fig. 2.14 - Normalized deviatoric strength (dividing by quasi-static uniaxial compressive strength) related to hydrostatic pressure, strain rate, and damage parameter (Ren et al., 2017). Comparison of the experimental damage and numerical results (Tai, 2009)

of the deviatoric strength of the intact and fractured material in the form of a pressure-dependent and rate-dependent yield surface, and (3) a damage model that transitions the material from the sound state to the fractured state. The model uses a damage accumulation criterion that includes the equivalent plastic strain and the plastic volumetric strain. A maximal value limits the tensile stresses. In (Tai, 2009), the parameters of the model were adapted to UHPC with fibre fractions of 1.0% and used to model impact experiments with flat-ended projectile up to velocities of 100 m/s (the plate thickness is only two times the projectile diameter). Numerical results (**Fig. 2.14**) correlate well with experimental data defining an erosion algorithm based on the principal tensile strain.

2.3.2 Modelling of UHPC under dynamic tension

A plasticity model is not sufficient for the numerical simulation of impact when damage tension phenomena, i.e., cratering and scabbing, dominate. In this particular case, the model needs to be coupled with a tensile damage model. The Pontiroli-Rouquand-Mazars (PRM) model has been developed in CEA-Gramat to simulate the behavior of concrete under severe loading (Rouquand and Mazars, 2010). This macroscopic model, based on the Mazars's damage model proposed in 1984, includes two scalar damage variables that give the loss of stiffness under pure tensile loading and pure compressive loading. The Hillerborg regularization is included in this model to limit mesh size dependency. The strain rate effects on tensile strength are included in the model by making the initial strain for damage in tension strain rate dependent. The PRM model was then improved in (Erzar et al., 2017) based on characterization tests performed on UHPC specimens with fibre reinforcement. The energy consumed by a crack to propagate through a band of finite elements is made dependent on the fibre length and the volume fraction of fibres participating in the resistance to crack opening.

The PRM model was coupled with the KST model and used to simulate ballistic tests with impact velocities ranging from 233 to 440 ms^{-1}. **Fig 2.15** shows the damage pattern obtained in two-dimensional calculations of a penetration test on a Ductal® slab with and without fibres. The PRM model allowed a good correlation with experimental data for 1% of active fibres.

An anisotropic damage model, the DFH (Denoual-Forquin-Hild) model, was proposed in (Denoual & Hild, 2002; Forquin and Hild, 2010). The model is based on a micromechanical description of crack inception from preexisting defects, crack propagation, and obscuration of defects due to the cracks previously triggered. The phenomenology of the dynamic tensile failure is based on a limited velocity of crack propagation that explains the increase of stress in the material despite existing cracks. Thus, this model allows predicting an increase of strength with the loading rate in dynamic tensile tests and can be applied to materials such as UHPC.

This model was previously used coupled with the KST model to simulate the dynamic fragmentation of Ductal® during the edge-on impact tests in (Forquin and Hild, 2008). The parameters related to crack inception were evaluated under quasi-static loading condition through banding tests. The simulation reproduced reasonably the characteristic time to damage, the orientation of cracking as well as the pattern of crack density even if the crack density was slightly overestimated (**Fig 2.16**). A cohesion law was introduced in the DFH damage model to account for the post-peak dynamic tensile response of concrete in (Erzar and Forquin, 2014). The model, named DFHcoh-KST, was successfully used to numerically simulate the

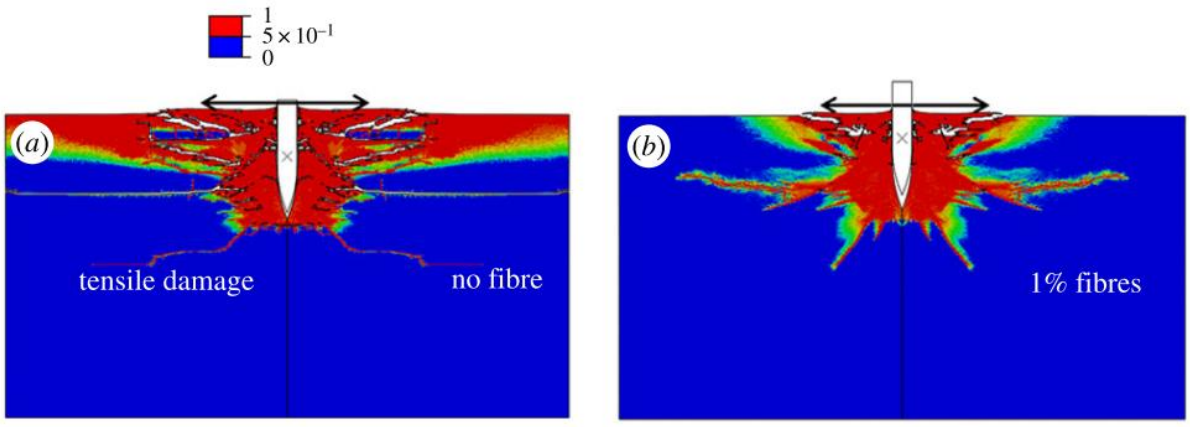

Fig. 2.15 - Penetration of an 8cm-thick UHPC slab at 233 m s^{-1}: damage patterns predicted by numerical simulation with (a) no fibre reinforcement or (b) 1% fibres (Erzar et al., 2017)

penetration of ogive-nosed steel penetrator within plain concrete targets with a thickness of 300 mm or 800 mm in (Forquin et al., 2015). In particular, this numerical work has highlighted the strong influence of free water content in concrete through its confined behavior and tensile strength and the influence of friction at the target-projectile interface.

Another modelling strategy for concrete behavior under dynamic tension is the microplane model where the material response is calculated based on the monitoring of stresses and strains in different pre-defined directions. The model is similar to the discrete models (such as random particle model) with the difference that it is formulated in the framework of continuum. The macroscopic stress tensor is calculated from a known microplane strains and the corresponding microplane constitutive law by integrating the microplane stresses in a thermodynamically consistent way (Ozbolt et al., 2001). Cracking is represented by the localization of strains. When the strains increase, the stress oriented in the same direction (direction of damage) decreases. The strength under dynamic tension is controlled by the rate dependent microplane constitutive law which accounts for the influence of inertia on the growing of cracks at microscale and the effect of the viscous behaviour of the bulk material between the micro-cracks due to the water content. In a number of numerical applications it has been demonstrated that the model is able to realistically predict concrete response under high strain rate (Ožbolt et al., 2014) but has been not yet applied to UHPC behavior.

2.4 Discrete modelling

The DEM is a powerful alternative to the finite element method (FEM) for studying advanced damage states and the failure of concrete. The material is discretized by element particles that interact with neighboring elements according to interaction laws. Although realistic macroscopic brittle behaviors are obtained with these models, a preliminary calibration of the interaction laws is required. Works present analytical expressions that relate continuous parameters to DEM parameters.

DEM method was used to model penetration events on a concrete beam in (Plesha, 2006). Nonlinear compression behavior and strain rate effects were incorporated into the model. Material densification was obtained because of the overlap between DEM elements. It was decided to apply strain rate effects to the material fracture energy since the failure criterion was

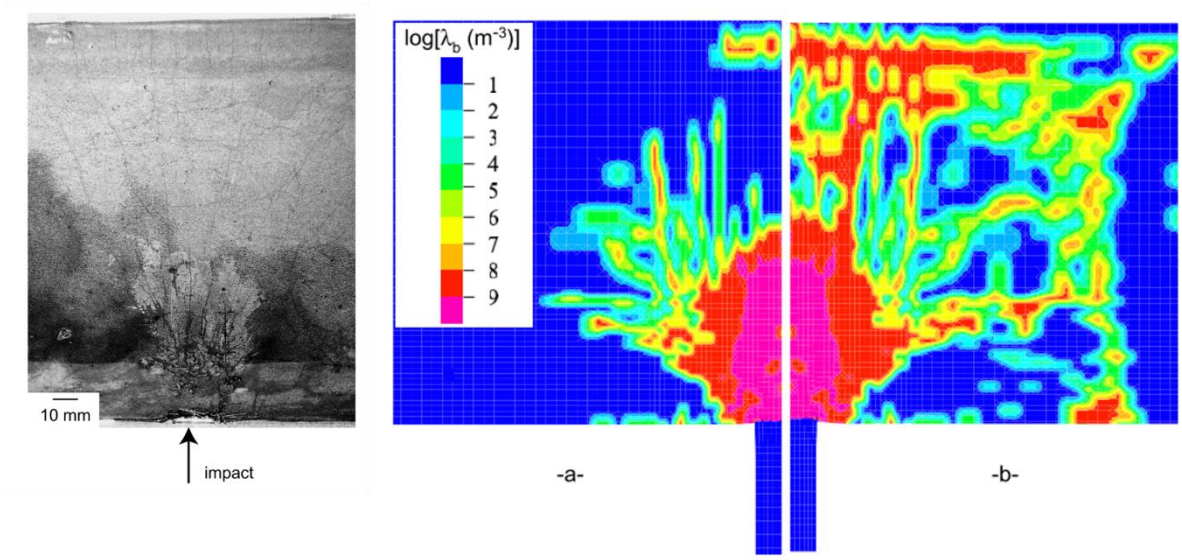

Fig. 2.16 - Post-mortem view of a Ductal® plate impacted at 88 m/s by an aluminum projectile with a confined configuration. The contour of crack density 35 (-a-) and 50 µs (-b-) after the impact (Hild et al., 2008)

primarily based on this quantity. As such, it was assumed that the material dynamic fracture energy changes in the same way as the dynamic tensile strength as a function of strain rate. The limitation of this numerical DEM implementation was that real-life penetration events are three dimensional, whereas the DEM model is presently two-dimension (**Fig 2.17** left).

Also (Daudeville et al., 2019) proposed a DEM modelling for concrete under severe loadings. The concrete structure is modeled by an assembly of rigid spherical elements with different sizes and masses (they do not represent concrete constituents such as aggregates). The nonlinear

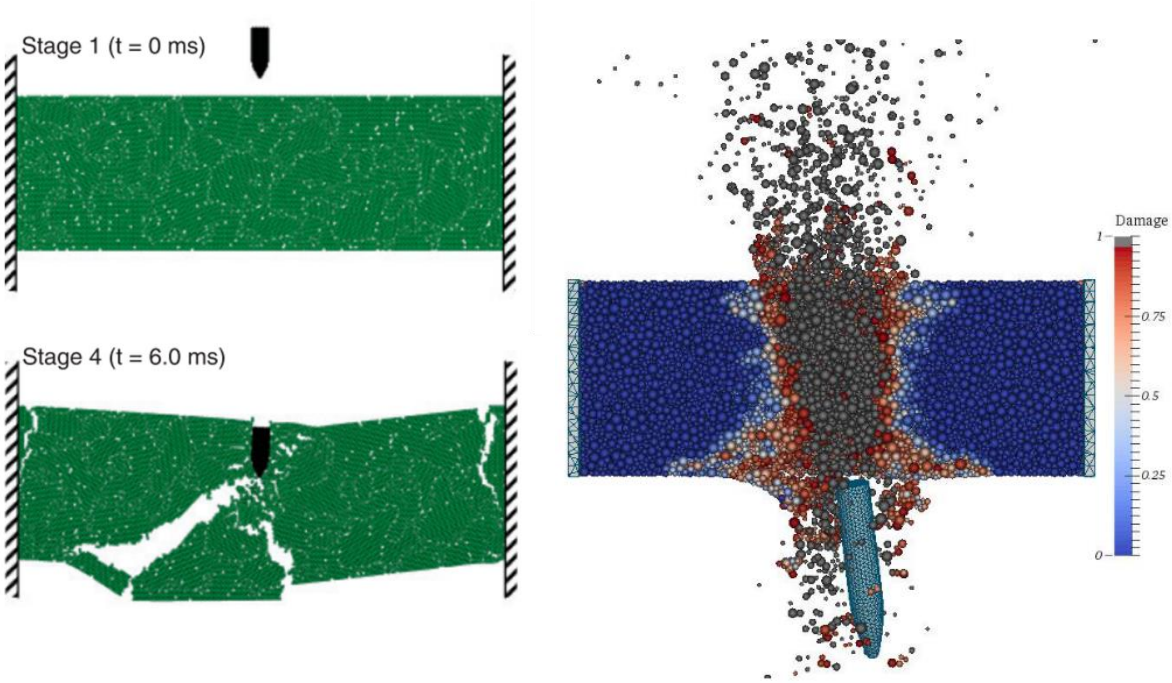

Fig. 2.17 - DEM simulation of projectile penetration into a concrete beam (Federico A. Tavarez‡ and Michael E. Plesha∗, 2007) and a concrete target confined with a thin steel jacket (Antoniou and Antoniou, 2019).

constitutive behavior of concrete is modeled by employing cohesive links between two discrete elements, aiming to reproduce damage and compaction (closure of porosity) of concrete at the macroscopic scale. The cohesive interactions exist even when the elements are not in contact allowing transmitting tensile forces contrarily to contact links that transmit forces in compression. A modified Mohr-Coulomb criterion is used for the modeling of nonlinear behavior. The damage criterion is activated if the normal displacement between two elements is greater than a limit distance associated with the local tensile strength. The increase of strength with strain rate is taken into account only in tension; it is assumed that the increase is applied to the limit distance. The method has not yet been applied to UHPC.

2.5 Synthesis and conclusion

Chapter 2 has presented a state of the art about ultra-high performance concretes (UHPC). It highlights the experimental techniques available to investigate the response under high pressure and high strain rate as well as the existing constitutive models already used to simulate UHPC under impact loading. Although UHPC is still a young material in concrete history, it has been used for various research projects due to its high performances (compression strength, ductility, durability). The mix formulation benefits from low water to binder ratio, ultra-thin additions, and reduced grain size. The resulting compact material exhibits outstanding compressive

strength, but its stress-strain behaviors in compression and tension are brittle after the peaks. Therefore, short steel fibres are added to the formulation to restore a ductile behavior. The fibres notably improved the concrete tensile capacity after cracking. Furthermore, the post-cracking resistance is strongly influenced by the fibre orientation.

The behavior of UHPC becomes less understood when passing to high pressure and high strain rate. UHPC exhibits low volumetric strain under hydrostatic compression and a continuous increase of the deviatoric resistance with increasing confining pressure under triaxial compression. The steel fibre reinforcement seems to have an insignificant effect on the behavior under confined conditions. The influence of the strain rate on the UHPC confined behavior has been poorly investigated. From the experiences in dynamic QOC tests on microconcrete and plate impact tests on Cor-Tuf a low influence of strain rate is expected.

To explore the strain rate effect under tensile loading, servo-controlled uniaxial loading machines are used for low strain rate, Split Hopkinson Tensile Bar are used for intermediate strain rates, and spalling technique are favored for high strain rates are. The strength increase of the peak stress is minimal in the range from 10^{-6} s^{-1} to 10 s^{-1}, then it becomes very significant. The experiences on unnotched specimens highlight that in dynamic condition the fibres play again the primary role only on the post-peak behavior (peak stress coincides with stress at first cracking). At the same time, notched specimens highlight that the endpoint of the softening curve must be reached on the same abscissa of the static experiments. The plate-impact testing technique is used to generate spalling at higher strain-rates without accurate information on the strain rate level reached. Alternately, a pulse generator can be used.

FE method needs a constitutive model for UHPC describing both confined behavior and tensile damage to simulate impact problems. A plasticity model describing the yield strength and irreversible compaction as a function of the applied pressure such as the KST model or a viscoplastic model such as the JHC model describing the loss of yield strength with the increment of equivalent plastic strain may be used to account for the pressure sensitivity of UHPC. However, the role played by the loss of yield strength during the penetration phenomena has not been evidenced in the literature. On the other hand, a continuous damage model may be used to account for the loss of resistance due to fracturing under tensile dynamic loading. In the PRM model, the strain rate effect is integrated as an intrinsic material phenomenon, which means that an empirical law describing the strain rate dependency needs to be defined. An alternative is given by the DFH model that simulates the strain rate effect through a micromechanical description of the inception (linked to the flaw population) and kinetics of fragmentation.

It seems that the coupled plasticity-damage model denoted DFH-KST has already shown its capabilities to model the standard concrete behavior properly under impact; moreover, the more recently introduced cohesive law offers the opportunity for UHPC to integrate the role of the fibres in the modelling strategy. It is why the DFHcoh-KST model is chosen to simulate samples with fibres in Chapter 3.

The model parameters are identified using three existing experimental techniques: the Quasi-Oedometric Compression (Q-OC) test, the bending test, and the spalling test at the Hopkinson bar. The model capabilities to simulate with a finite element (FE) code a ballistic impact on UHPC are then discussed in Chapter 4.

The gas gun recently installed in the 3SR laboratory is used to perform plate-impact tests on UHPC. A new testing technique employing a pulse shaping system to ensure a constant loading rate in the specimen is designed and experienced in Chapter 5.

A attempt in understanding the role of microstructure on the observed strain-rate sensitivity of the UHPC tensile strength is made in Chapter 6, conducting simulations of fragmentation based on X-ray CT (Computed Tomography) analyses of the pore distributions.

CHAPTER 3

Identification of DFHcoh-KST parameters

CHAPTER 3

Identification of DFHcoh-KST parameters

As highlighted in the last chapter, the DFHcoh-KST model seems a good candidate to simulate properly ballistic impact against UHPFRC targets. This chapter is therefore dedicated to the identification of the DFHcoh-KST parameters for UHPFRCs. The first section presents the compositions of the UHPFRC studied in the thesis. Then Krieg, Swenson and Taylor (KST) model parameters are identified in a second section before identifying DFHcoh model parameters in a third section.

3.1 Materials

Two classes of UHPFRCs, with a volumetric dosage of fibres of 2% and achieving the compressive strength of 150 and 170 MPa, are considered for the study. **Table 3.1** shows the mix proportion of the two products of the brand Ductal®, named A-2% and B-2%. The two compressive strengths are obtained using two commercial premixes as powder, both following a mix design with a water to cement ratio of 0.21. The main difference between the premixes is that premix A has no pozzolanic material and premix B uses 150–200 kg per m^3 of silica fume as a replacement for sand. The steel fibres have a length of 14 mm and a diameter of 0.2 mm (strength 2500 MPa).

Table 3.2 collects the quasi-static mechanical properties of Ductal® A-2% and B-2% for standard 28-days curing at 20C° with 100 % relative humidity after demolding. The following properties were obtained at Lafarge-Holcim R&D center according to standard NF P 18-470: the elastic modulus in compression (Ec), the mean compressive strength (fcm), the mean tensile strength in bending already multiplied by the coefficient of reduction (fctm) and the mean tensile post-peak resistance at 0.3 mm crack opening (fctpm). Experiments in compression were performed on at least three samples, whereas experiments in tension were performed on at least six samples. From these results, it is noted that, in quasi-static condition, after the elastic response, Ductal® A-2% is exhibiting a little hardening under direct tension and Ductal® B-2% is exhibiting softening.

Ductal®	A-2%	B-2%
Premix [kg/m3]	2205	2200
Fibres [kg/m3]	155	155
Water [kg/m3]	155	150
Superplasticizer [kg/m3]	25	30
Casting	Mixing procedure used by industry	
Curing	Standard	

Table 3.1 - Mix proportion of the two UHPFRC Ductal® products.

Ductal®	A	B
Density ρ kg/m3	2560[1]	2580[1]
Poisson's ratio v	0.2[2]	0.2[2]
Elastic modulus in compression Ec GPa	55	60
Characteristic compressive strength fcm MPa	150	170
Mean tensile strength fct,m MPa	8.3	11.0
Mean tensile post-cracking strength fctpm MPa	8.9	10.2

Table 3.2 - Quasi-static mechanical properties of the two UHPFRC Ductal® products. [1]average value three specimens [2] value suggest by standard NF P 18-470 for UHPFRC.

3.2 Identification of KST model parameters

The Krieg–Swenson–Taylor model includes an equation of state linking the volumetric strain ε_v to the hydrostatic pressure *P,* which is a piecewise linear curve entered point by point (Swenson and Taylor, 1983):

$$P(\varepsilon_v) = \begin{cases} -K_i\varepsilon_v & \text{if } \varepsilon_v \geq \varepsilon_v^1 \\ P_{i-1}\frac{\varepsilon_v-\varepsilon_v^i}{\epsilon_v^{i-1}-\varepsilon_v^i} + P_i\frac{\varepsilon_v-\varepsilon_v^{i-1}}{\epsilon_v^i-\varepsilon_v^{i-1}} & \text{if } \varepsilon_v^{i-1} > \varepsilon_v > \varepsilon_v^i \\ -K_f\varepsilon_v & \text{if } \varepsilon_v \leq \varepsilon_v^n \end{cases} \quad \textbf{(3.1)}$$

where $-K_i\varepsilon_v^1$ and $-K_f\varepsilon_v^n$ are respectively the pressure at the beginning and the ending of the inelastic compaction. Furthermore, the model accounts for the increase of the yield strength of concrete σ_{eq} with confining pressure in the sense of von Mises plasticity (Swenson and Taylor, 1983):

$$\sigma_{eq}(P) = \sqrt{a_0 + a_1 P + a_2 P^2} \quad \textbf{(3.2)}$$

where a_0, a_1, a_2 are parameters to identify from the experimental data. The KST model parameters for a similar concrete mix design were already identified in (Forquin, 2003) through hydrostatic and triaxial tests. However, the method presents some limitations, which make hydrostatic and triaxial tests costly and difficult to perform (Vu et al., 2013). Indeed, it demands a very high-pressure chamber coupled to a rigid load frame, and it requires a good impermeabilization of the specimen to the fluid that applies the confinement. In the present work, the parameters of both UHPC concretes were identified thanks to Quasi-Oedometric Compression (Q-OC) tests, an attractive alternative to triaxial tests (Forquin, 2019). The method allows more complete instrumentation of the specimen, well-controlled loading paths, and a much more moderate experimental cost. The cylindrical specimen is enclosed in a steel ring and subjected to axial compression. The specimen tends to expand under the effect of the radial swelling and exerts pressure on the ring. The test is called “Quasi”-OC because the sample radial expansion is not nil, but the ring stiffness considerably limits it. A rise of both axial and radial stresses is observed in the specimen during Q-OC, which gives a possible reading of the mean stress difference as a function of the level of applied pressure (the deviatoric behavior) and the diminution of the sample volume with the level of hydrostatic pressure (the compaction law). In the present work, the parameters of both UHPC concretes were identified thanks to Quasi-Oedometric Compression (Q-OC) tests. The tests have been conducted on cylindrical samples without fibres. The steel fibre reinforcement has an insignificant effect on the strength under confined conditions (Williams et al., 2009). Due to the low expected influence of strain rate on concrete confined behavior, tests have been conducted only in quasi-static conditions. The tests have been performed with a constant strain rate of $5\text{x}10^{-5}$ s^{-1}.

3.2.1 Test set-up

The complete set-up is shown in **Fig. 3.1**. The steel ring measures 29.50 mm in inner diameter, 60 mm in outer diameter, and 45 mm in length**.** For this reason, the concrete specimens are 29.20 mm in diameter and 38 mm long. The diameter of the two steel plugs is slightly wider, 29.34 mm. The axial force is generated from the servo-hydraulic jack of the Schenck press with a capacity of 1 MN. The maximum load reached in the confined compression test is about 650 kN. During testing, the load cell of the press measures the axial force applied to the steel plugs, F_0, and three LVDTs attached to the compression platen measure the total axial displacements. Gauges are glued on the outer surface of the ring, recording the hoop strains. Two gauges are

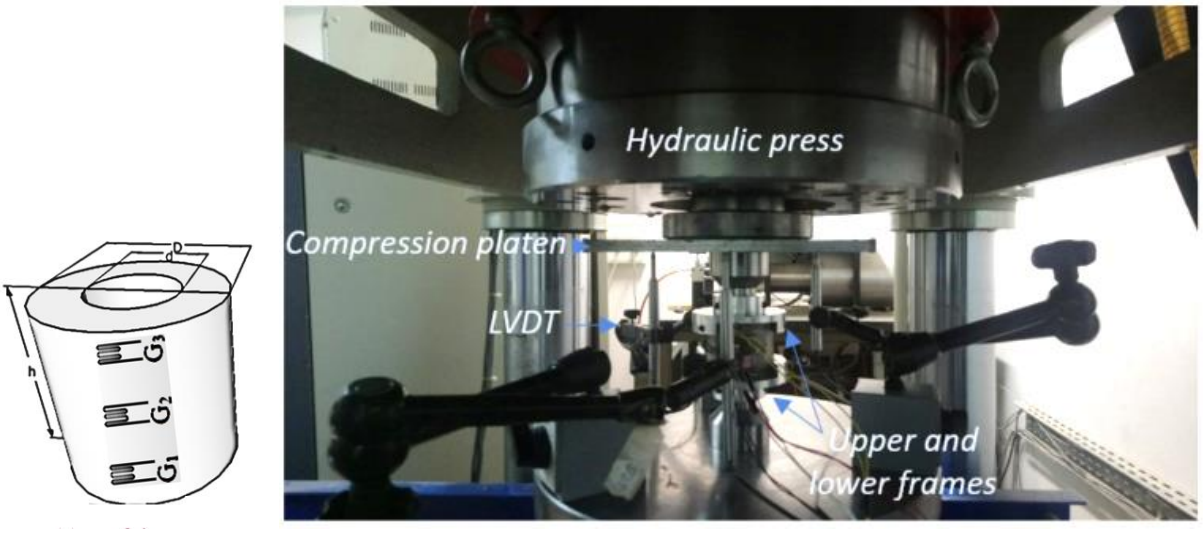

Fig. 3.1 – Set-up of the Quasi-Oedometric Compression (Q-OC) test: hydraulic press, compression platen, three LVDTs, two steel plugs, and two frames

located in the middle of the ring at two diametrically opposed positions, named M2 and M4, and two others, named J1 and J3, are located at a distance from the middle equal to 3/4 of the half-length of the ring. An epoxy resin named Chrysor is used to fill the gap between the sample and the inner surface of the ring. This resin is highly incompressible and has a weak shear strength allowing for relative displacements between the ring and the specimen. The axial centering of the specimen in the ring is made through an aluminum device composed of two identical upper and lower frames. Each frame has six screws that are tightened only during the hardening of the interface product.

3.2.2 Calibration tests

The steel plugs were subjected to simple axial compression to quantify their shortening during the Q-OC test. A polynomial function of order three was used to fit the experimental data. The function gives the axial displacement as a function of the applied force (**Fig. 3.2**) that can be subtracted from the measured axial displacement in QOC tests. The ring alone, already instrumented with the gauges, was subjected to diametral compression, as sketched in **Fig. 3.3**. The test was driven with imposed axial force until 150 kN. During the test, the pressure at the contact points of the ring was limited by placing two aluminum plates between the ring and the platens of the press. The aluminum plates plastified from a moderate applied force (≈ 30 kN), providing a wide area of contact. Two complementary tests were performed; in the second test, the ring was rotated 180 degrees to exclude any dissymmetry of the ring. As shown in the same figure, the two tests give consistent results. A numerical calculation of the test was run with

Length mm	Wide mm	Thickness mm	Modulus of elasticity N/mm^2	Poisson's ratio	Yield stress MPa
45	40	20	7.03 x 10^3	0.3	250

Table 3.3 – Dimensions and mechanical properties of the aluminum plate

Interior Diameter mm	Outer Diameter mm	Length mm	Modulus of Elasticity N/mm^2	Poisson's ratio
29.50	60	45	2.05 x 10^5	0.3

Table 3.4 – Dimensions and mechanical properties of the ring

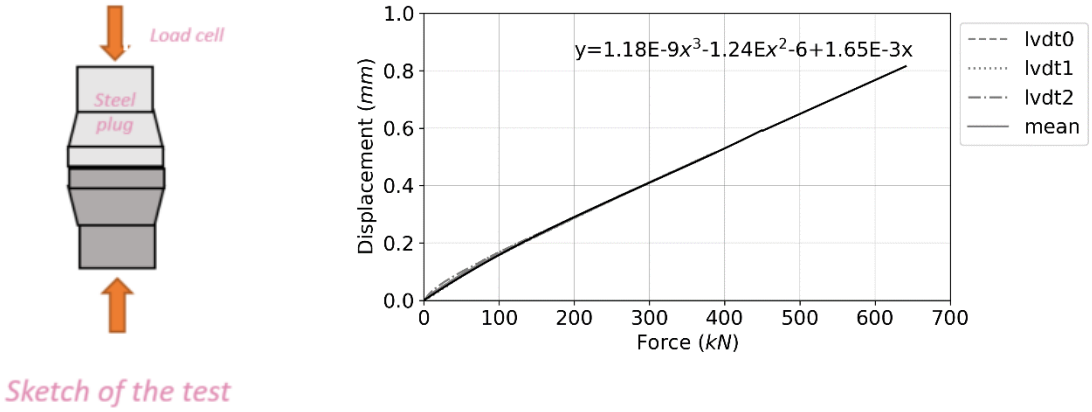

Fig. 3.2 – Axial compression of the steel plugs and identification of the polynomial function fitting the experimental data

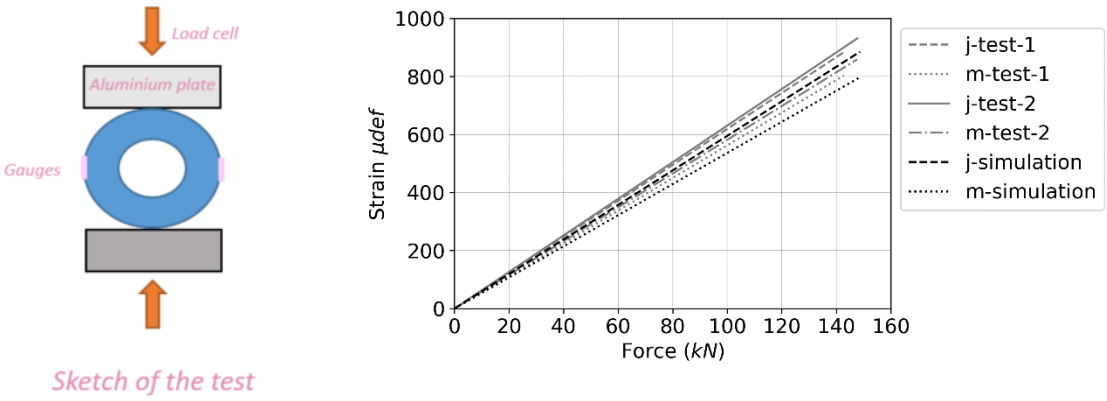

Fig. 3.3 – Comparison between experimental strains during diametral compression of the ring and numerical results obtained assuming the mechanical proprieties of Table 3.4

Abaqus Implicit. The compression platen was not included in the built tridimensional model, and a vertical displacement was directly applied on the upper surface of the aluminum plate. Symmetries, with respect to X, Y, and Z-axis, were taken into account. An elastic-perfectly plastic behavior was assumed for the aluminum plate. Dimensions and mechanical

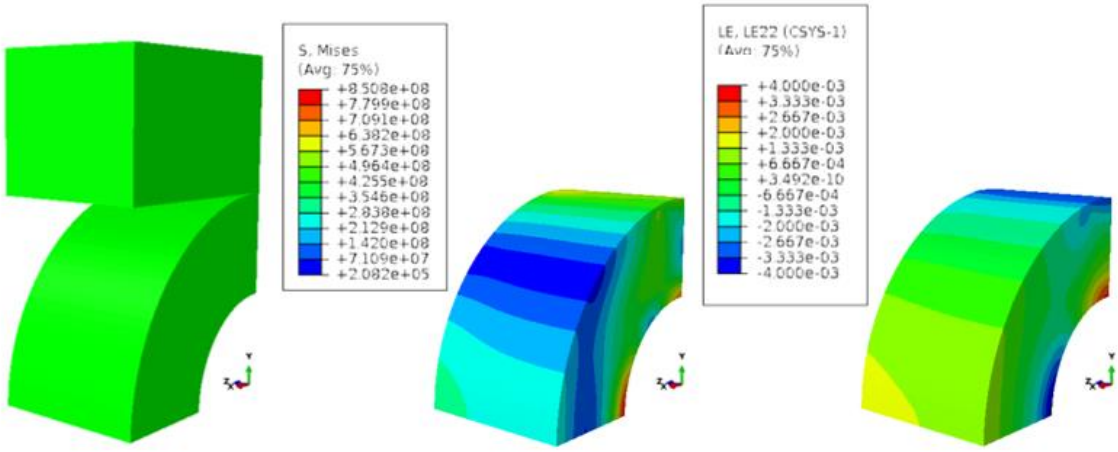

Fig. 3.4 – Modelling of the diametral compression test (Abaqus/Implicit): full model geometry and fields in the ring for the equivalent Mises stress and orthoradial strain

properties of the plates are reported in **Table 3.3**, whereas the mechanical properties given in **Table 3.4** are used for the ring. The equivalent Mises stress and the field of hoop strain in the ring are shown in **Fig 3.4**. The plastification of the ring was successfully prevented during the test. The hoop strains obtained by numerical calculation at the gauge location are also shown in **Fig. 3.4**. The comparison with the strains measured experimentally confirms the validity of the material parameters used to describe the behavior of the ring for the estimation of the inner strain during the Q-OC test.

3.2.3 Method to estimate specimen stress and strain

Since the test is driven only by the axial strain, it provides a single loading path. Although the specimen stress and strain are not homogenous, average stress and strain states are referred to the specimen. The loading path provides $\overline{P^S}$, the average mean pressure, and $\overline{\sigma_{dev}{}^S}$, the average deviatoric stress, such as:

$$\overline{\sigma_{dev}{}^S} = \left|\overline{\sigma_{ax}{}^S} - \overline{\sigma_{rad}{}^S}\right| \quad \textbf{(3.3)}$$

$$\overline{P^S} = -\frac{1}{3}\left(\overline{\sigma_{ax}{}^S} + 2\overline{\sigma_{rad}{}^S}\right) \quad \textbf{(3.4)}$$

with $\overline{\sigma_{ax}{}^S}$ and $\overline{\sigma_{rad}{}^S}$ average axial and radial stresses in the specimen. Similarly, the volumetric strain $\overline{\varepsilon_v{}^S}$ is expressed as a function of $\overline{\varepsilon_{ax}{}^S}$ and $\overline{\varepsilon_{rad}{}^S}$, the average axial and radial strains, hence:

$$\overline{\varepsilon_v{}^S} = \left(1 + \overline{\varepsilon_{ax}{}^S}\right)\left(1 + \overline{\varepsilon_{rad}{}^S}\right)^2 - 1 \textbf{ (3.5)}$$

$\overline{\varepsilon_{ax}{}^S}$ is directly derived by the initial specimen length and the axial displacement (difference between the mean displacement measured by the LVDTs and the elastic shortening of the steel plugs). Whereases, the axial stress is not directly derived by the force F_0 but it also accounts

for the force induced by friction mechanisms. Indeed, the specimen length varies during the test so that friction forces appear at the specimen/ring interface. $\overline{\sigma_{ax}{}^{S}}$ is then:

$$\overline{\sigma_{ax}{}^{S}} = \frac{F_0}{\pi\left[R_{int}\left(1+\overline{\varepsilon_{rad}{}^{S}}\right)\right]^2} - \frac{3}{4}\frac{f\,\overline{\sigma_{rad}{}^{S}}}{R_{int}\left(1+\overline{\varepsilon_{rad}{}^{S}}\right)}\frac{h}{2} \quad \textbf{(3.6)}$$

with R_{int} the initial specimen radius, f the friction coefficient at specimen/ring interface, and h the actual length of the specimen. The expression accounts for the lateral expansion of the specimen as $R_{int}\left(1+\overline{\varepsilon_{rad}{}^{S}}\right)$ represents the equivalent specimen radius. The factor $\frac{3}{4}$ is a factor calibrated through numerical calculations to correct the second term valid only for constant lateral pressure.

The radial strain and the lateral pressure are deduced from the hoop strains measured on the outer surface of the ring, according to the method proposed in (Forquin et al., 2007):

$$\overline{\sigma_{rad}{}^{S}} = f\left(\varepsilon_{\theta\theta_{(M)}}{}^{ext}, \varepsilon_{\theta\theta_{(J)}}{}^{ext}, h, f\right) \quad \textbf{(3.7)}$$

$$\overline{\varepsilon_{rad}{}^{S}} = g\left(\varepsilon_{\theta\theta_{(M)}}{}^{ext}, \varepsilon_{\theta\theta_{(J)}}{}^{ext}, h, f\right) \quad \textbf{(3.8)}$$

being $\varepsilon_{\theta\theta_{(M)}}{}^{ext}$ and $\varepsilon_{\theta\theta_{(j)}}{}^{ext}$ the average strains between the locations M2-M4 and J1-J3. The functions f and g are estimated through numerical calculations of the ring subjected simultaneously to a uniform internal pressure and shear stresses applied on the ring's inner surface for the length h representing the specimen length (**Fig. 3.5**).

3.2.3.1 Numerical calculations of the ring only

The numerical simulations are carried out using Abaqus Implicit. The axial-symmetric model is built for half of the ring (4-node axisymmetric elements). The dimensions and mechanical properties of the ring are listed in **Table 3.4.** The behavior of the ring is purely-elastic. Different friction coefficients are considered. The friction coefficients are set to be equal to 0.2-0.3-0.4, corresponding to shear stresses equal to 20-30-40% of the normal stress. The shear stresses are imposed via nodal forces, so the force direction does not change with the ring deformation. Four strains are extracted from each calculation:

-$\varepsilon_{\theta\theta_{(M,P)}}{}^{ext}$, the orthoradial outer strain at the gauge location M;

-$\varepsilon_{\theta\theta_{(j,P)}}{}^{ext}$, the orthoradial outer strain at the gauge location J;

-$\varepsilon_{\theta\theta_{(z=0,P)}}{}^{int}$, the orthoradial inner strain at the half-length of the ring;

-$\varepsilon_{\theta\theta_{(z=\frac{h}{2},P)}}{}^{int}$, the orthoradial inner strain at the extremity of the loading (representing the specimen end).

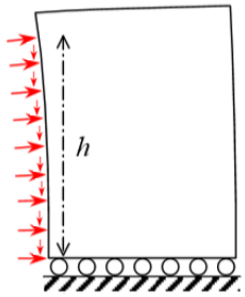

Fig. 3.5 – Sketch of the ring under internal pressure and shear

f	0.2	0.3	0.4
${\varepsilon_{rad}}_{(M)}^{int}$	1.02E-02	1.06E-02	1.11E-02
${\varepsilon_{rad}}_{(M)}^{ext}$	3.44E-03	3.64E-03	3.84E-03
${\varepsilon_{rad}}_{(j)}^{int}$	5.19E-03	4.91E-03	4.63E-03
${\varepsilon_{rad}}_{(j)}^{ext}$	2.21E-03	1.80E-03	1.72E-03
$\frac{{\varepsilon_{rad}}_{(j)}^{ext}}{{\varepsilon_{rad}}_{(M)}^{ext}}$	6.42E-01	4.93E-01	4.47E-01

Table 3.5 – Numerical simulation of the ring under uniform internal pressure of 1 GPa and different friction coefficient. Height of the loaded area: 36 mm.

For example, the strains for the ring subjected to a uniform internal pressure of 1 GPa for a length h = 36 mm are listed in **Table 3.5**. An increase in the difference between ${\varepsilon_{\theta\theta}}_{(z=0)}^{int}$ and ${\varepsilon_{\theta\theta}}_{(z=\frac{h}{2})}^{int}$, i.e., an increase of the ring barreling, it is observed, increasing the friction coefficient. Furthermore, the friction modifies the value of the outer strains ${\varepsilon_{\theta\theta}}_{(M)}^{ext}$ and ${\varepsilon_{\theta\theta}}_{(j)}^{ext}$ from which the internal pressure and radial expansion are calculated. That is why it is important to evaluate the friction coefficient in the experimental data. Once f is quantified, by assuming the radial stress homogeneous in the sample, **Eqs. 3.7** is converted into the following linear equation:

$$\overline{{\sigma_{rad}}^{S}} = \left[\frac{h-h_1}{h_0-h_1}\left(\frac{P}{{\varepsilon_{\theta\theta}}_{(M,P)}^{ext}}\right)_{h_0} + \frac{h-h_0}{h_1-h_0}\left(\frac{P}{{\varepsilon_{\theta\theta}}_{(M,P)}^{ext}}\right)_{h_1}\right]{\varepsilon_{\theta\theta}}_{(M)}^{ext} \quad \textbf{(3.9)}$$

where h_0 and h_1 are the initial and the final specimen length, respectively. Similarly, by assuming the continuity of the hoop strain between the specimen and the ring, **Eqs. 3.8** became:

$$\overline{{\varepsilon_{rad}}^{S}} = \frac{2}{3}{\varepsilon_{\theta\theta}}_{(z=0)}^{int} + \frac{1}{3}{\varepsilon_{\theta\theta}}_{(z=\frac{h}{2})}^{int} \quad \textbf{(3.10)}$$

with

$${\varepsilon_{\theta\theta}}_{(z=0)}^{int} = \left[\frac{h-h_1}{h_0-h_1}\left(\frac{{\varepsilon_{\theta\theta}}_{(z=0,P)}^{int}}{{\varepsilon_{\theta\theta}}_{(M,P)}^{ext}}\right)_{h_0} + \frac{h-h_0}{h_1-h_0}\left(\frac{{\varepsilon_{\theta\theta}}_{(z=0,P)}^{int}}{{\varepsilon_{\theta\theta}}_{(M,P)}^{ext}}\right)_{h_1}\right]{\varepsilon_{\theta\theta}}_{(M)}^{ext} \quad \textbf{(3.11)}$$

$${\varepsilon_{\theta\theta}}_{(z=\frac{h}{2})}^{int} = \left[\frac{h-h_1}{h_0-h_1}\left(\frac{{\varepsilon_{\theta\theta}}_{(z=\frac{h}{2},P)}^{int}}{{\varepsilon_{\theta\theta}}_{(j,P)}^{ext}}\right)_{h_0} + \frac{h-h_0}{h_1-h_0}\left(\frac{{\varepsilon_{\theta\theta}}_{(z=\frac{h}{2},P)}^{int}}{{\varepsilon_{\theta\theta}}_{(j,P)}^{ext}}\right)_{h_1}\right]{\varepsilon_{\theta\theta}}_{(j)}^{ext} \quad \textbf{(3.12)}$$

According to **Eqs. 3.9-10,** the specimen radial stress and strain are corrected for the actual length h of the specimen, besides the radial strain accounts for the ring barrel.

Density, elastic constants	$(\mathrm{kg/m3}), E(\mathrm{GPa}), \nu$	2500,60, 0.2
Initial and final bulk moduli	$K_i(\mathrm{GPa}), K_f(\mathrm{GPa})$	33.3,36.1
Compaction curve	$P_i(\mathrm{MPa}), \varepsilon_v^i$	337,-0.011 778,-0.04
Coefficient of the elliptic equation	a_0, a_1, a_2	1 10^{10}, 307 10^6, 0.4375
Maximum equivalent stresses	${\sigma_{eq}}^{max}(\mathrm{MPa})$	750

Table 3.6 - Parameters of the Krieg, Swenson and Taylor model used in the numerical simulations

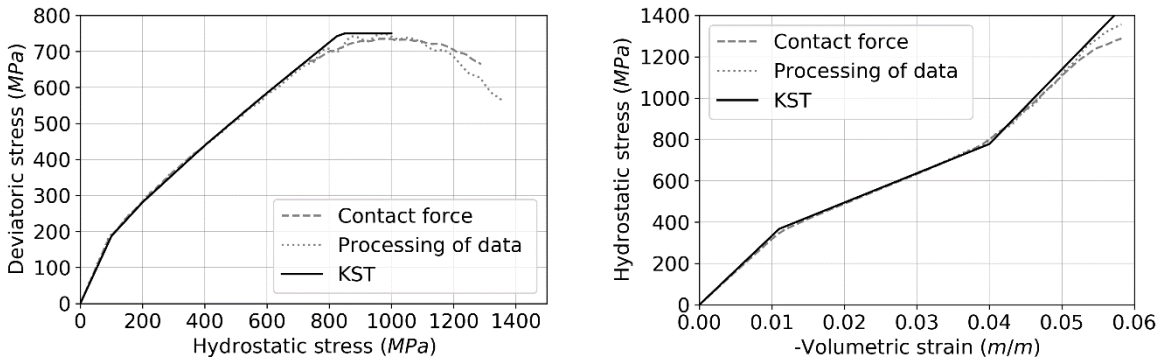

Fig. 3.6 – Processing of data of the numerical simulation (friction coefficient = 0.3 at contact specimen /ring)

3.2.3.2 Validation of the processing method

The methodology of processing the data is validated through numerical simulation of the Q-OC test conducted with the Abaqus-Explicit FE code. Half of the specimen is compressed between the steel plug and the symmetry plane. 4-node axisymmetric elements with reduced integration are used. An axial velocity, slow enough to do not influence the result, is imposed on the plug's upper surface. The specimen material behavior is modelled with the KST parameter of **Table 3.6**. The loading is applied until the equivalent Mises stress reaches its maximum level throughout the specimen. The curves that correspond to the KST model are compared to the curve obtained with the method that is used to process experimental data in **Fig. 3.6**. No difference is observed between the "KST" curve (imposed material behavior) and the curve from data processing. Furthermore, the numerical simulations also provided the contact force specimen/ring. This force is used to directly computed the mean radial strain from the heterogeneous stress field in the sample.

3.2.4 Experimental data

Four tests have been performed in total: two tests on Ductal® A, specimen BC1, and BC5, and two tests on Ductal® B, specimen AC1, and AC4. The axial displacement measured by the LVDTs and deduced after subtracting the elastic shortening of the steel plugs are shown in

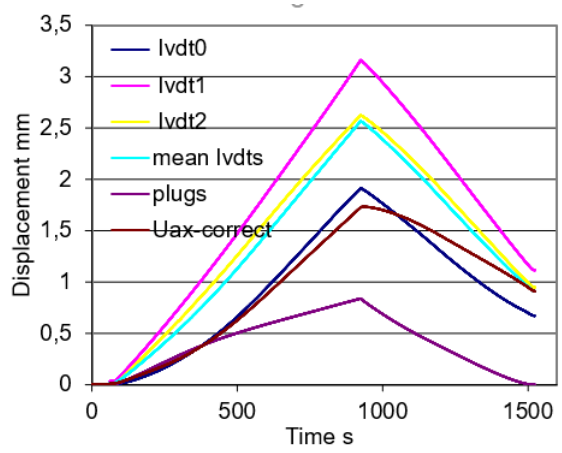

a Evolution of axial displacement

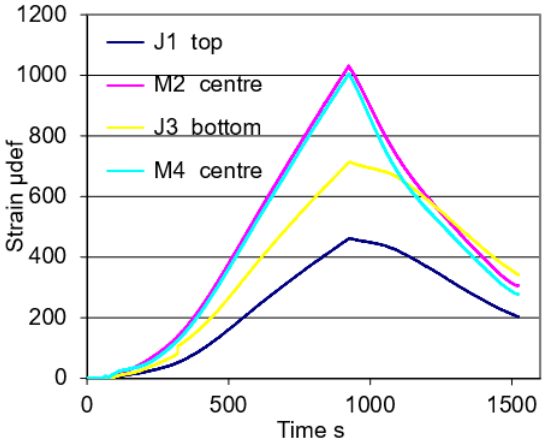

b Evolution of the external orthoradial strains

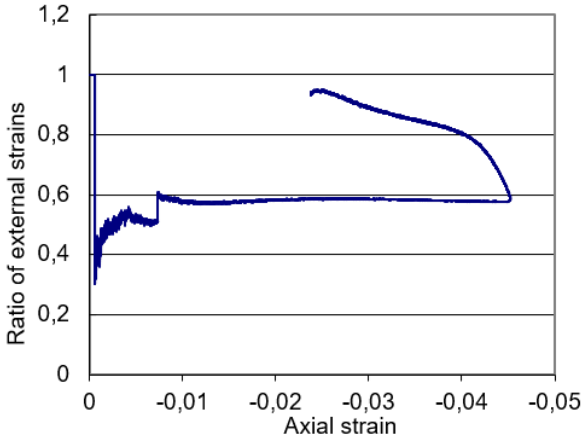

c Ratio of external hoop strains $(\varepsilon_{\theta\theta(J)}{}^{ext}/\varepsilon_{\theta\theta(M)}{}^{ext})$

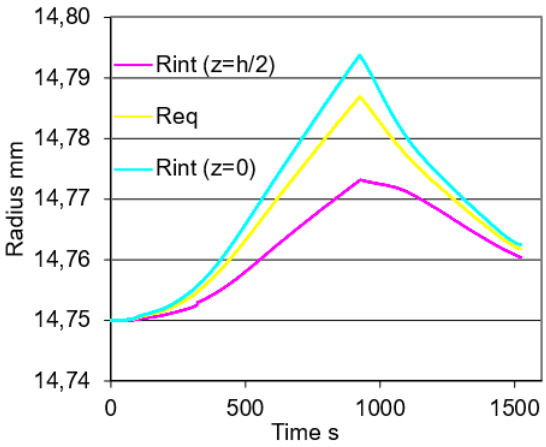

d Evolution of specimen radius

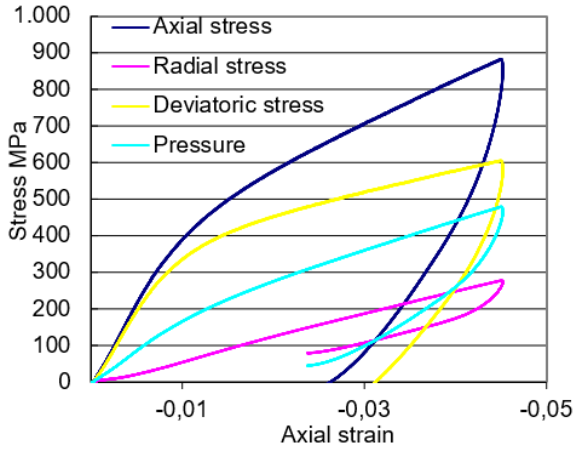

e Evolution of stresses

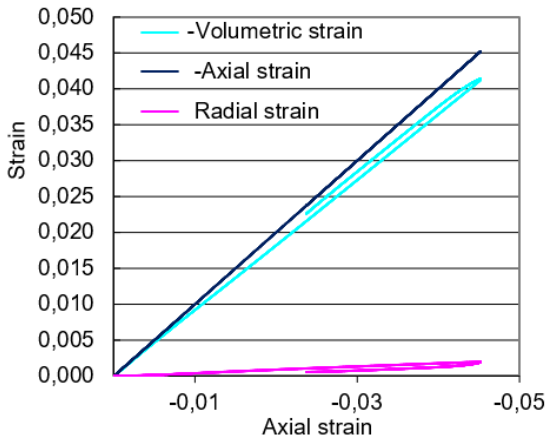

f Evolution of strains

Fig. 3.7 – Post-processing test performed on specimen BC1

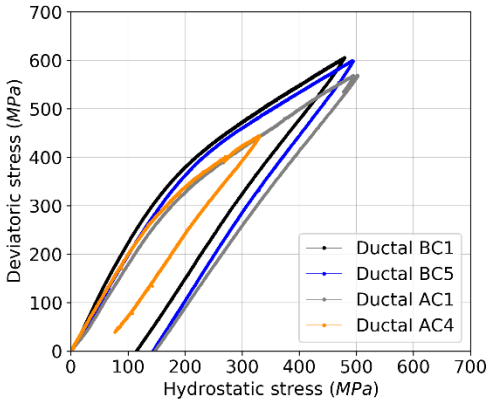

Fig. 3.8a – Evolution of deviatoric stress Vs. hydrostatic pressure

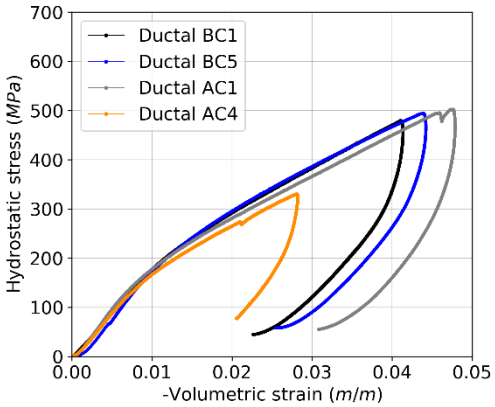

Fig. 3.8b – Evolution of hydrostatic pressure Vs. volumetric strain

Fig. 3.7a for the test performed on specimen BC1. **Fig. 3.7b** shows the external hoop strains measured by the strain gauges. As expected, the deformation of the ring is not homogeneous. The external strains at the center are higher than those at the extremities. This is in agreement with the results of the numerical simulations. The difference between J1 and J2 is due to an imperfect axial centering of the specimen in the ring (a defect of symmetry of 2 mm was measured post-testing). The ratio between the mean values of ${\varepsilon_{\theta\theta}}_{(J)}^{ext}/{\varepsilon_{\theta\theta}}_{(M)}^{ext}$ is plotted in **Fig. 3.7c** as a function of the nominal axial strain. It is equal to 0.58 as the strain reaches -1% and then remains constant along with all the loading (maximum axial strain –4.5%). This ratio is compared with the one estimated using a finite element model in the case the ring is subjected to a homogeneous pressure (**Table 3.5**). In the present test, it indicates that the friction coefficient is closer to 0.3. Specimen stresses and strains were estimated, as previously mentioned, accounting for the influence of friction. The outer strains were used to obtain the average radial confinement (**Eqs. 3.10**). The inner strains were calculated using **Eqs. 3.11-12.** The corresponding specimen radius at the half-length ($z = 0$) and end ($z = \frac{h}{2}$) of the specimen are plotted in **Fig. 3.7d.** as a function of time. The equivalent radius was used to derive the axial stress (**Eqs. 3.6**). The evolution of stresses is shown in **Fig. 3.9e**. At the beginning of the test, the deviatoric stress is close to the axial stress as in a simple compression test. Later, the deviatoric stress increases slower than the axial stress due to linear increases of radial stress. The evolution of strains is shown in **Fig. 3.9f**. The radial strain remains small, so the volumetric strain is very close to the axial strain; the test is proved to be a "quasi-oedometric" compression. All specimens were subjected to an axial compression up to 900 MPa, leading to confinement pressure up to 450 MPa. The deviatoric behavior (evolution of deviatoric stress Vs. hydrostatic

Ductal		A	B
Initial and final bulk moduli	$K_i(\text{GPa}), K_f(\text{GPa})$	30.6, 34.3	33.3, 37.5
Compaction curve	$P_i(\text{MPa}), \varepsilon_v^i$	130,0.0425 500,0.0460 800,0.0633	140,0.0420 500,0.0405 800,0.0560

Table 3.7 - Parameters of the hydrostatic behavior for A and B concrete.

Ductal		A	B
Coefficient of the elliptic equation	a_0, a_1, a_2	3.0 10^{15}, 5.02 10^{8}, 0.310	6.4 10^{15}, 7.06 10^{8}, 0.109
Maximum and minimum stresses	${\sigma_{eq}}^{max}, {\sigma_{eq}}^{min}$	150,780	170,800

Table 3.8 - Parameters of the deviatoric behavior for A and B concrete

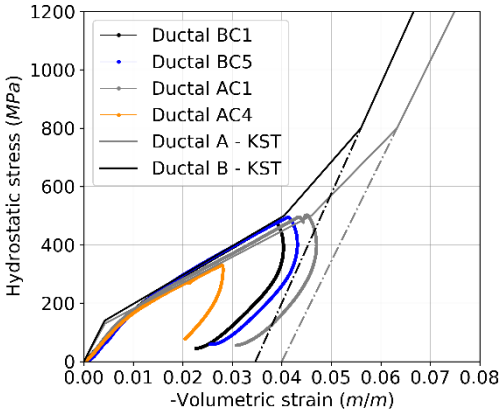

Fig. 3.9 – KST material compaction of Ductal A and Ductal B

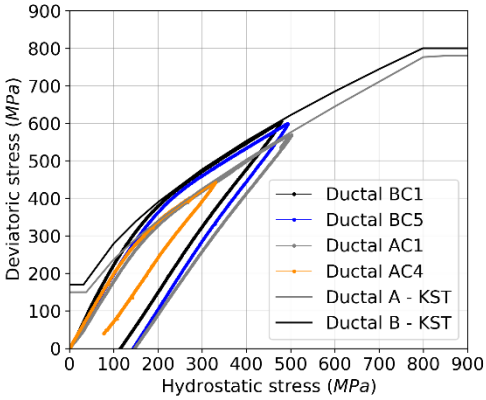

Fig. 3.10 – KST envelope for the deviatoric response of Ductal A and Ductal B

pressure) and the compaction law (evolution of hydrostatic pressure Vs. volumetric strain) are shown in **Fig. 3.8a-b.** A notable increase in strength occurred with the hydrostatic pressure, whatever the concrete. Under a hydrostatic pressure of 450 MPa, the strength reaches 550 MPa for Ductal® A and 600 MPa Ductal® B to be compared with the strength under simple compression 150 and 170 MPa, respectively, for Ductal® A and Ductal® B. All specimens began to exhibit inelastic strains at a pressure level of approximately 200 MPa and a volumetric strain of approximately -1.2%. Those are the pressure and the strain level at which the response began to soften appreciably. Then, the volume reduction of Ductal® B is slightly lower.

3.2.5 KST parameters

The KST model parameters were identified for Ductal® A and Ductal® B based on the data from Q-OC tests. The parameters for the hydrostatic and deviatoric responses are listed in **Table 3.7** and **Table 3.8**. The descriptions of the material model compaction are plotted in **Fig. 3.9**. The

initial bulk moduli are set equal to the theoretical values considering the elastic parameters E and v. The theoretical elastic bulk modulus reads:

$$K_i = \frac{E}{3(1-2v)} \textbf{ (3.13)}$$

The resulting K_i for Ductal® A and Ductal® B are respectively 30.6 and 33.3 GPa. Then, the responses follow the quasi-oedometric softening up to the highest experimental hydrostatic pressure. It is reasonable to assume that the collapse of porosities was not completed during Q-OC. Therefore, the responses for Ductal® A and Ductal® B were extrapolated for higher pressures. The assumed final bulk moduli K_f are respectively 34.3 and 37.5 GPa. The ending of the inelastic compaction corresponds to the residual volumetric strains of respectively -4% and -3.5%. The envelopes for the deviatoric response are shown in **Fig. 3.10**. The yield stresses follow the experimental results; besides, a limit to the increase of the strength was set at pressures higher than 800 MPa. By lack of experimental data, it is assumed arbitrarily that the materials stop to gain strength when all the porosities are crushed out as in (Forquin, 2003).

3.3 Identification of DFHcoh model parameters

In brittle materials, cracks propagate from activated preexisting defects. When cracking is in mode I (opening mode), the local stress state around the crack is modified by a complex stress release wave. The area affected by the stress relief is named here 'obscuration zone' because the initiation of defects is prevented in this zone. The phenomenology of the cracking process corresponds then to the competition between the activation of defects in non-obscured zones and the growth of obscuration zones along with the crack propagation. According to DFH (Denoual-Forquin-Hild) model (Denoual & Hild, 2000; Forquin & Hild, 2010) the non-obscuration probability of a point *M* at time *T* is defined as the condition that none critical defect is activated in the horizon of (*M,T*). In a case of multiple fragmentation process the obscuration probability can be used to define a damage variable in the framework of Continuum Damage Mechanics. An anisotropic damage model operates with three damage variables D_i which are used to describe the cracking associated with each principal orthogonal direction, thus:

$$\Sigma_i = (1 - D_i)\sigma_i = (1 - P_{oi})\sigma_i \text{ (Denoual and Hild, 2002) } \textbf{(3.14a)}$$

$$\Sigma_i = (1 - D_i)\sigma_i = (1 - P_{oi})\sigma_i + P_{oi}\,\sigma_i^{coh} \text{ (Erzar and Forquin, 2014) } \textbf{(3.14b)}$$

where P_{oi} is the obscuration probability associated to each principal direction. In non-obscured zones, the microscopic stress components σ_i are used, whereas nil stress (**Eq. 3.14a**) or a

cohesion strength σ_i^{coh} (**Eq. 3.14b**) is set in the obscured zones. Thus, the ultimate (maximum) macroscopic strength can be deduced, such as:

$$\Sigma_{iu} = \max \Sigma_i(t) = \Sigma_i(t_u) \; with \; \frac{d\Sigma_i}{dt}(t_u) = 0 \quad \textbf{(3.15)}$$

P_{oi} is calculated according to the following differential equation:

$$\frac{d^2}{dt^2}\left(\frac{1}{1-P_{oi}}\frac{dP_{oi}}{dt}\right) = 6\lambda_t(\sigma_i)S(k\mathrm{C})^3 \text{ when } \frac{d\sigma_i}{dt} > 0 \text{ and } \sigma_i > 0 \quad \textbf{(3.16)}$$

where *S* is a shape parameter related to the size of the obscuration zones and λ_t is the density of critical defects, i.e., the average number of activated defects within the considered volume, when the tensile stress exceeds a stress generated randomly for each finite element in a preliminary step. *E* and ρ are, respectively, the Young's modulus and the mass density. In this description, each obscured zone is centered on the point of crack initiation and grows in a self-similar way with a diameter proportional to the size of the crack, so *S* = 3.74 for a non-spherical volume (Denoual and Hild, 2002). The term kC corresponds to the speed of the obscured zone growth and it is assumed to be constant and proportional to C, the 1D elastic wave speed. It has been considered that k = 0.38 as in the energy-based analytical solution of (Kanninen et al., 1986) for the speed of crack propagation and $C = \sqrt{\frac{E}{\rho}}$.

The amount of cracks is expressed as a crack density λ_{crack} and its increment is assumed to be proportional to the increment of critical defects weighted by the fraction of non-obscured zones (new cracks develop only in the partial area that is not obscured). Therefore this fraction is assumed to be comparable to the probability of non-obscuration $(1 - P_{oi})$ leading to :

$$\lambda_{crack}(T) = \int_0^T \frac{d\lambda_{crack}(t)}{dt}\,dt = \int_0^T (1 - P_{oi})\frac{d\lambda_t}{dt}\,dt \qquad \textbf{(3.17)}$$

According to Weibull's model, the density of critical defects λ_t is expressed as a power-law function of the applied stress:

$$\lambda_t = \lambda_0 \left(\frac{\langle\sigma_i\rangle}{\sigma_0}\right)^m \qquad \textbf{(3.18)}$$

where the exponent *m* is the Weibull modulus, σ_0 is the stress relative to a reference density λ_0 and <·> are the Macauley brackets (i.e., the positive part of '·'). The constant $\frac{\lambda_0}{{\sigma_0}^m}$ is commonly named Weibull scale parameter.

3.3.1 Quasi-Static and dynamic predictions from DFH model

Under quasi-static loading condition, there is a sudden change between the virgin material (i.e., $D = 0$) and a fully broken material (i.e., $D = 1$). An ad-hoc formula describes this single fragmentation process. According to the next equation (which respects the weakest-link hypothesis), ${\Sigma_u}^{QS}$ is defined proportional to the volume of the domain *Z* raised to the power -1/ *m*:

$$ {\Sigma_u}^{QS} = \mathrm{Z}^{-1/m} * \frac{\sigma_0}{{\lambda_0}^{1/m}} * \Gamma\left(\frac{m+1}{m}\right) \qquad \textbf{(3.19)} $$

where Γ is the Euler function of the second kind (Abramowitz and Stegun 1965). No stress rate effect is obtained when sub-critical crack grown does not occur (stress rate-indipendent). Under dynamic condition, a multiple-fragmentation process occurs, and the ultimate strength starts to be stress-rate sensitive. By combining the solution of P_o and **Eqs. 3.14a-15** Σ_u is derived for a structure Ω of volume *Z* loaded in tension with a constant stress rate $(\dot{\sigma})$ and assuming λ_t given by **Eq. 3.18.** The ultimate strength ${\Sigma_u}^{Dyn}$ reads:

$$ {\Sigma_u}^{Dyn} = (\dot{\sigma})^{\frac{m}{m+3}} \times \left(\frac{\lambda_0}{{\sigma_0}^m}\right)^{-\frac{1}{m+3}} \times (S(kC)^3)^{-\frac{1}{m+3}} \times \left(\frac{(m+1)(m+2)}{6 \times \exp(1)}\right)^{\frac{1}{m+3}} \qquad \textbf{(3.20)} $$

Eq. 3.20 shows that ${\Sigma_u}^{Dyn}$ depends on three types of parameters. The first term highlights the influence of the loading rate; the second corresponds to parameters related to crack initiation, whereas the third term corresponds to the parameters associated with the crack propagation. The limited crack speed kC explains the increase of strength with the stress-rate despite the triggering of a more significant number of defects.

One may define a transition criterion between 'quasi-static' (single fragmentation) and 'dynamic' response (multiple fragmentation), such as:

$$ \frac{{\Sigma_u}^{Dyn}}{{\Sigma_u}^{QS}} = 1 \textbf{ (3.21)} $$

The transition defined by **Eq. 3.9** leads to the following inequality (Hild et al., 2008):

$$ \Sigma_u = \begin{cases} {\Sigma_u}^{QS} \; if \; \dot{\sigma} < \dot{\sigma}_t & quasi - static \; response \\ {\Sigma_u}^{Dyn} if \; \dot{\sigma} \geq \dot{\sigma}_t & dynamic \; response \end{cases} \qquad \textbf{(3.22)} $$

with

$$ \dot{\sigma}_t = (Z)^{\frac{m+3}{3m}} * \left(\frac{\lambda_0}{{\sigma_0}^m}\right)^{-\frac{1}{m}} * S^{\frac{1}{3}}(kC) * \left[\frac{6 \times \exp(1)}{(m+1)(m+2)} \Gamma^{m+3}\left(\frac{m+1}{m}\right)\right]^{\frac{1}{3}} \qquad \textbf{(3.23)} $$

This transition does not only depend on material parameters, but also involves the considered volume Z. The response of a large structure can be considered as 'dynamic' for low-stress rates in a large-enough volume, whereas the material can experience a single fragmentation process

(i.e. following the weakest link hypothesis) for the same loading-rate applied to a smaller domain. $\dot{\sigma}_t$ is used as transition criteria between a strain rate dependent response (high-stress rate) and a stress rate-independent and volume size-dependent response (low-stress rate).

3.3.2 Identification of Weibull parameters

As mentioned before, in the DFH model, the density of critical defects is described by a power-law function of the applied stress, whose exponent is the Weibull modulus *m* (Weibull, 1939). *m* represents the scatter in the failure stresses obtained during quasi-static tensile testing (the lower *m*, the higher the scatter). The scale parameter $\frac{\lambda_0}{{\sigma_0}^m}$ in **Eq. 3.18** can be derived from **Eq. 3.19,** substituting ${\Sigma_u}^{QS}$ by σ_w , the mean tensile failure stress in bending, and Z by Z_{eff}, the effective volume of the bending sample of height *h*, of width *w* and of span length *l*, such as:

$$\frac{\sigma_0}{{\lambda_0}^{1/m}} = \sigma_w * {Z_{eff}}^{1/m} * \Gamma^{-1}\left(\frac{m+1}{m}\right) \; with \; Z_{eff} = \frac{whl}{2(m+1)^2} \quad \textbf{(3.24)}$$

Three-point flexural experiments were performed on specimens of Ductal® A and Ductal® B without fibre reinforcement of dimensions 12×16×100 mm^3 (Height × width × span) to identify their Weibull parameters. More than 24 experiments were performed for each concrete material. A servo-hydraulic Instron testing machine with 100 kN load capacity was used (**Fig 3.11**). The evolution displaying force vs. displacement is shown for two tests in **Fig 3.12** (left). The failure stress was directly derived from the maximum force. The stress rate was estimated from the derivative of the applied load; levels of stress rate of about 0.2-0.3 MPa/s are reported. The crack initiation (defined as the start of the stress-rate fall) and the maximum sustained stress coincide, which underlines the very brittle response of the matrix without the fibre reinforcement **Fig 3.12** (right). The tensile failure stresses of Ductal® A and Ductal® B sorted in increasing order of stress are plotted in **Fig 3.15**. The failure probability of the *i*-th test is defined as:

$$P_F = \frac{i-0.5}{n} \qquad \textbf{(3.25)}$$

with *n* the total number of experiments. The points expressed in the form of Ln(-Ln(1- P_F)) versus Ln(σ) are interpolated by a linear function, the slope of which is *m*. For the two mixes A and B, the Weibull's moduli are found around 10.4 and 8.9, respectively. These values can be considered in the same order, given the uncertainty regarding the Weibull modulus estimated greater than 10%. Further, average failure stresses of 19.3 MPa and 20.9 MPa are calculated with **Eq 3.19** when referred to the same effective volume of 53 mm^3. These values refer to a

strain rate of about $5x10^{-6}$ s^{-1}. The experimental data are summarised in **Table 3.9** and compared with the ones used in (Forquin and Hild, 2008).

Fig 3.11 – Experimental set-up: Instron 100 kN

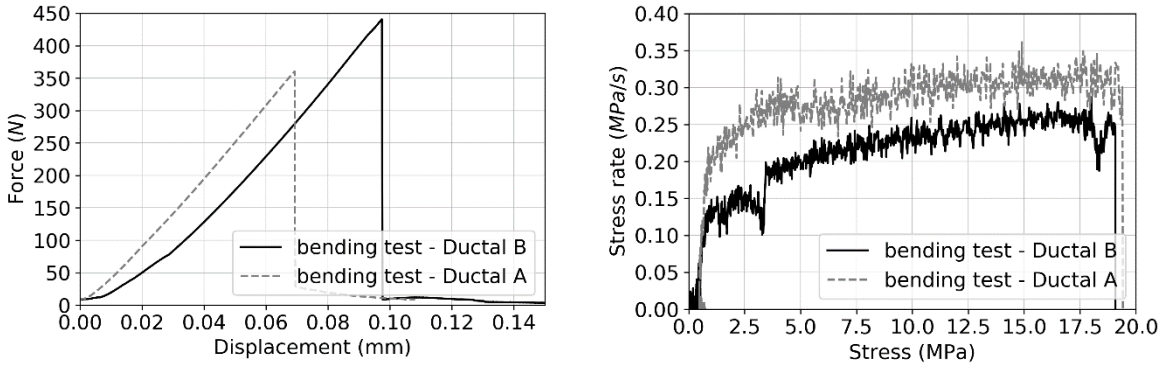

Fig 3.12 – Experimental data of two bending tests: Force vs. Displacement (left) and Stress rate vs. Stress (right)

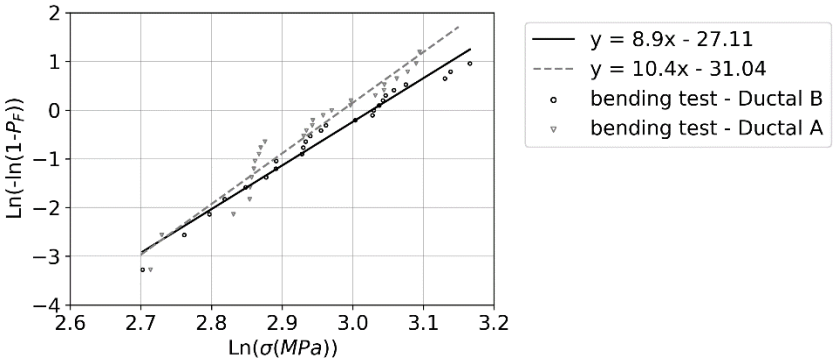

Fig 3.13 – Identification of Ductal® Weibull modulus from the failure stresses of a bending test

Ductal	A	B	FM	FM-2%
References			(Forquin, 2003)	
Higth x width x span mm^3	12x16x100		11x10x130	
Number of tests	26	24	18	9
Mean tensile failure stress MPa $\sigma_w(V_{eff})$	18.90	19.42	22	17
Effective volume mm^3	64	100	53	30
Weibull modulus m	10.4	8.9	11	14.6
Size effect moduli -1/m	-0.096	-0.112	-0.091	-0.068
Ref. effective volume (V_{eff}^{ref}) mm^3	53			
Mean tensile failure stress MPa $\sigma_w\left(V_{eff}^{ref}\right)$	19.3	20.9	22	17.8

Table 3.9 - Experimental data from bending tests ($\dot{\varepsilon}$ =5x10^{-6} s^{-1}).

Ductal		A-2%	B-2%
Density, elastic parameters	$\rho\left(\frac{\text{kg}}{m^3}\right), E(\text{GPa}), v$	2560, 55, 0.2	2580, 60, 0.2
Cracks propagation parameters	$S,\ k$	3.74, 0.38	
Cracks initiation parameters	$V_{eff}(\text{mm}^3)$, $\sigma_w(\text{MPa})$, m	64, 18.90, 10.39	98, 19.42, 8.95

Table 3.10 - Parameters of the DFH model for A-2% and B-2% concrete.

3.3.3 Quasi-static – Dynamic transition

In the following, the predictive capability of the DFH model to reproduce the response of UHPFRCs is discussed. Once the elastic properties and the Weibull parameters are known, the model has no other parameter to tune apart from the crack propagation velocity. The velocity of a single crack is assumed to be 1761 m/s for concrete A-2% and 1832 m/s for concrete B-2% (0.38 multiply by the theoretical elastic wave speed). The identified model parameters for the two UHPFRC materials are collected in **Table 3.10**. One may be questioned on the reason why the bending data referred to UHPCs without fibre reinforcement has been used to assign

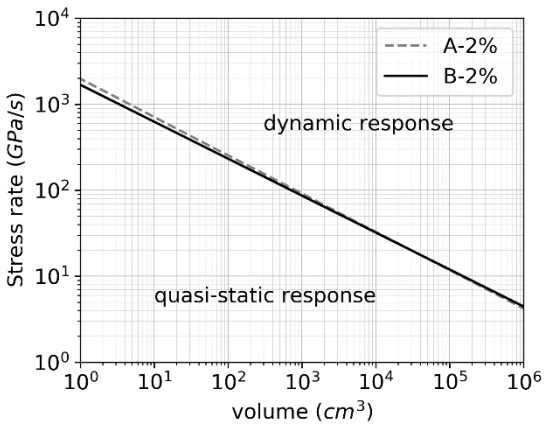

Fig 3.14a – Quasi-static – dynamic stress rate transition as a function of the volume whithout quasi-static increase factor

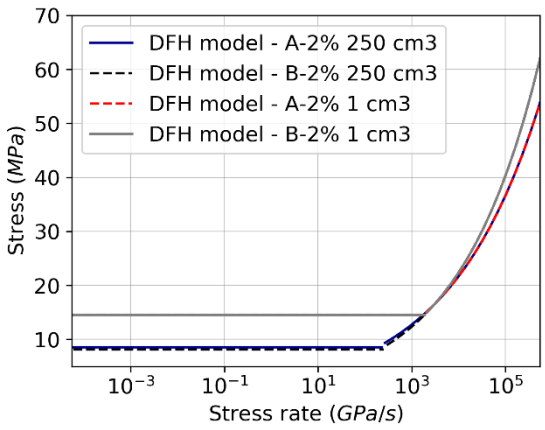

Fig 3.14b – DFH model predictions for the evolution of ultimate strength whithout quasi-static increase factor

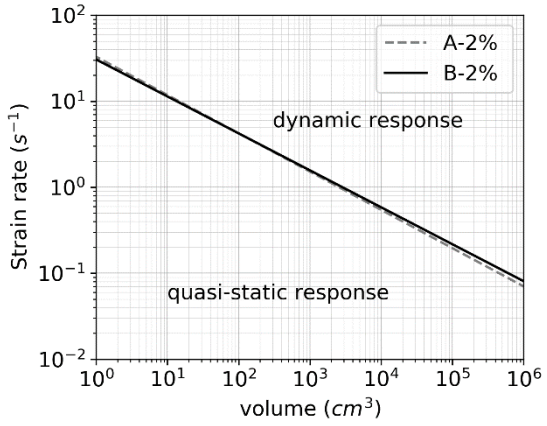

Fig 3.14c – Quasi-static – dynamic transition converted in strain rate for a volume loaded in direct tension whithout quasi-static increase factor

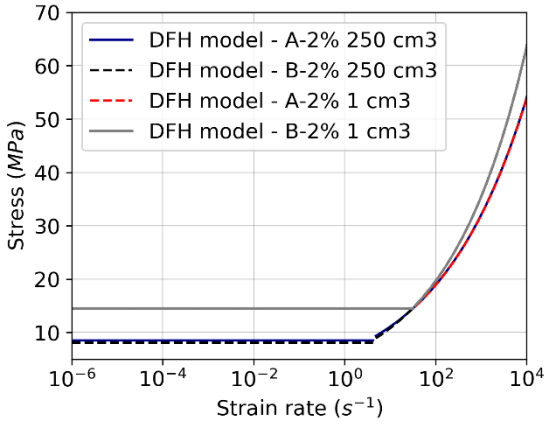

Fig 3.14d – DFH model predictions for the evolution of ultimate strength converted in strain rate for a volume loaded in direct tension whithout quasi-static increase factor

the parameter of crack initiation for UHPFRC materials. It has to be kept in mind that, even if those were the only data available, the hypothesis that fibres do not affect the first cracking strength is made along with the whole study.

First, $\dot{\sigma}_t$ is plotted as a function of the loaded volume *Z* in **Fig 3.14a** to know whether a 'quasi-static' or 'dynamic' response is expected. Then, the analytical solutions of ${\Sigma_u}^{QS}$ and ${\Sigma_u}^{Dyn}$ are plotted in **Fig 3.14b** depending on the stress rate for two selected volumes: 1 cm^3 and 250 cm^3 (a prismatic specimen 50x50x100 mm^3 subjected to a direct tensile test). As established by **Eq. 3.23,** a higher $\dot{\sigma}_t$ is obtained for the smaller volume. If the volume is considered loaded in direct tension, it is possible to express Σ_u as a function of the strain rate such as $\dot{\varepsilon} = \dot{\sigma}/\mathrm{E}$, the transition

Ductal	A-2%	B-2%	A-2%	B-2%
Z (cm^3)	1		250	
$\dot{\varepsilon}_t$ (s^{-1})	≈30		≈3	
$\Sigma_u{}^{QS}$(Z) (MPa)	14.51	15.01	8.53	8.10
$\Sigma_u{}^{Dyn}$ ($\dot{\varepsilon} =$ 100 s^{-1}) (MPa)	18.93	19.85	18.93	19.85
$\Sigma_u{}^{Dyn}$ ($\dot{\varepsilon} =$ 1000 s^{-1}) (MPa)	31.71	35.39	31.71	35.39

Table 3.11 - DFH model prediction for A-2% and B-2% concrete without quasi-static increase factor.

strain rate $\dot{\varepsilon}_t$ for the selected volumes are respectively ≈3 s^{-1} and ≈30 s^{-1} (**Fig 3.14c-d**). The model prediction is summarized in **Table 3.11**. As expected, the DFH model allows predicting an increase of the ultimate strength with the loading rate for a 'dynamic' response. Still, it cannot explain the rate-effect observed in concrete materials up to ≈1 s^{-1} and attributed to the viscous fluid (residual water) in the pores of the concrete, which puts up considerable opposition to imposed deformation of the skeleton (Rossi and Toutlemonde, 1996). This strength enhancement named here 'quasi-static increase factor' is included in the model in the next section.

3.3.4 Quasi-static increase factor

The simplified empirical description, which applies to all concretes and can be transposed to UHPCs, corresponds to a linear increase of the logarithmic tensile strength versus the logarithmic loading rate (considered to be constant in the identification tests), such as:

$$\Sigma_u{}^{QS}(\dot{\varepsilon}) = \Sigma_u{}^{QS}(\dot{\varepsilon}_0)\left(\frac{\dot{\varepsilon}}{\dot{\varepsilon}_0}\right)^{n^{qs}} \qquad \textbf{(3.26)}$$

Eq. 3.26 is used to correct the 'quasi-static' response of the DFH model (correction of the predicted ultimate strength for $\dot{\varepsilon} < \dot{\varepsilon}_t$).

Furthermore, one may assume that the "quasi-static increase factor" defined for quasi-static loading applies to the parameter σ_w related to crack initiation in a case of 'dynamic' response. Note that this parameter (in **Table 3.10**) have been identified through the mean tensile failure stress in bending at $\dot{\varepsilon} = 5\text{x}10^{-6}$ s^{-1}. The best choice would be to make the identification of the Weibull parameters in **Table 3.9** over a wide range of strain rate. Here, the literature has been used to extrapolate the data from $\dot{\varepsilon} = 5\text{x}10^{-6}$ s^{-1} to higher strain rate due to the absence of an appropriate experimental device available.

(Fujikake et al., 2006) used a servo-controlled uniaxial loading machine for testing in direct tension Ductal® specimens with fibres within a range of strain rate from 10-6 to 10 s−1. Based on these results, the ultimate strength increase with an increase in the loading rate with a factor n^{qs} of 0.03. The same factor n^{qs} was applied for concrete A-2% and concrete B-2% in this study. The new model parameters are reported in **Table 3.12.** where σ_w is strain rate sensitive fallowing **Eq. 3.26**. The model prediction, in terms of ultimate strength, is shown in **Table 3.13.** In **Fig 3.15** the model is compared with the experimental results of (Cadoni et al., 2019) that report several dynamic tensile tests on dog-bone specimens of Ductal® A- 2% and B-2% at a stress rate of ≈ 330 MPa.s−1. The loaded volume was Z= 28 cm^3 considering the full gauge length of the specimens, whereas the strain rate corresponds to ≈ 5 s^{-1}**.**

Ductal		A-2%	B-2%
Density, elastic parameters	$\rho\left(\frac{\text{kg}}{\text{m}^3}\right), E(\text{GPa}), v$	2560, 55, 0.2	2580, 60, 0.2
Cracks propagation parameters	S, k	3.74,0.38	
Quasi-static increase factor	n^{qs} , $\dot{\varepsilon}_0$ (s^{-1})	0.03, $5x10^{-6}$	
Cracks initiation parameters ($\dot{\varepsilon} =$ 5 s^{-1})	$V_{eff}(mm^3)$, σ_w(MPa), m	64, 18.90 ($\dot{\varepsilon}$ =5x10^{-6} s^{-1}), 10.4	98, 19.42 ($\dot{\varepsilon}$ =5x10^{-6} s^{-1}), 8.9

Table 3.12 - Parameters of the DFH model for A-2% and B-2% concretes.

Ductal	A-2%	B-2%
Z (cm^3)	28	
$\dot{\varepsilon}_t$ (s^{-1})	≈15	
$\Sigma_u{}^{QS}$ ($\dot{\varepsilon} =$ 5x10^{-6} s^{-1}) (MPa)	10.52	10.34
$\Sigma_u{}^{QS}$ ($\dot{\varepsilon} =$ 15 s^{-1}) (MPa)	22.09	18.38
$\Sigma_u{}^{Dyn}$ ($\dot{\varepsilon} =$ 100 s^{-1}) (MPa)	31.71	31.20
$\Sigma_u{}^{Dyn}$ ($\dot{\varepsilon} =$ 1000 s^{-1}) (MPa)	56.60	55.61

Table 3.13 - DFH model prediction for A-2% and B-2% concretes.

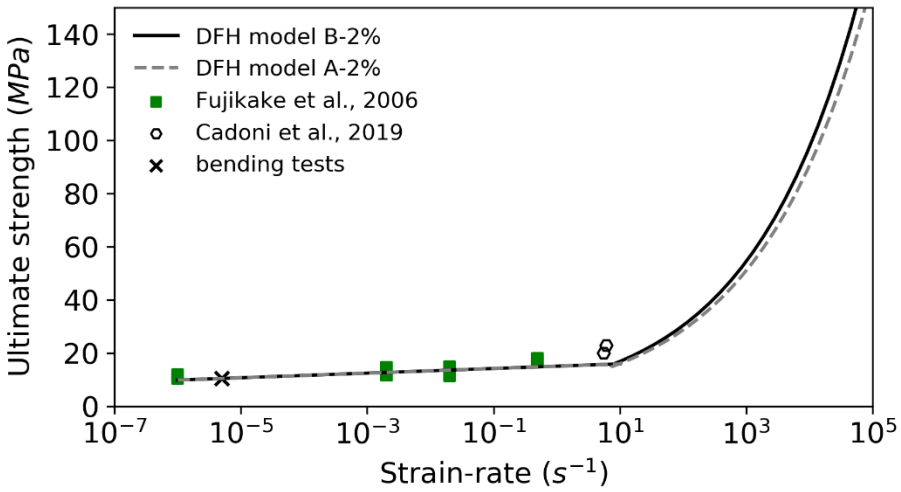

Fig 3.15 - Corrected 'quasi-static' strength for $\dot{\varepsilon}$ up to $\dot{\varepsilon}_t$ (right part of the plot); and prediction of the dynamic response considering the set of Weibull parameters extrapolate from 5x10-6 s-1 to higher strain rate (left part of the plot) $Z = 28$ cm^3

3.3.5 Validation of the dynamic response through the spalling test

Spalling tests were conducted to evaluate the capability of the model to predict the tensile strength of UHPFRCs at strain rates higher than $\dot{\varepsilon}_t$. The Hopkinson bar device of the 3SR laboratory has been used. The arrangement used for the tests is shown in **Fig 3.16**. The test configuration is the same as previous works (Erzar and Forquin, 2010): a compressive pulse is generated by the impact of a hemispheric smooth-end striker against the Hopkinson bar.

The striker and the bar are made of aluminum alloy (having mechanical impedance very close to concrete one) and have the same diameter of 45 mm. They are 65 mm and 1200 mm long, respectively. The radius 1.69 m of the hemispheric surface of the striker leads to almost constant strain rates during the tensile load phase. A strain gauge (G-bar) is glued at the middle of the bar to record the incident and reflected pulses. Three strain gauges, each 20 mm in length, are glued on the specimen located at 20 mm from the bar-specimen interface (G-120) and at 60 mm and 40 mm from the free-end (named G-60 and G-40, respectively). A laser extensometer is used to record the particle velocity on the rear free surface. The laser is directed towards a reflector (thin paper sheet) glued against the specimen free end located at a distance of R/2 from the axis.

The cylindrical specimens, 46 mm in diameter and 140 mm in length, with and without fibre reinforcement, were drilled from large blocks 270x270x170 mm^3. Mainly attention was made

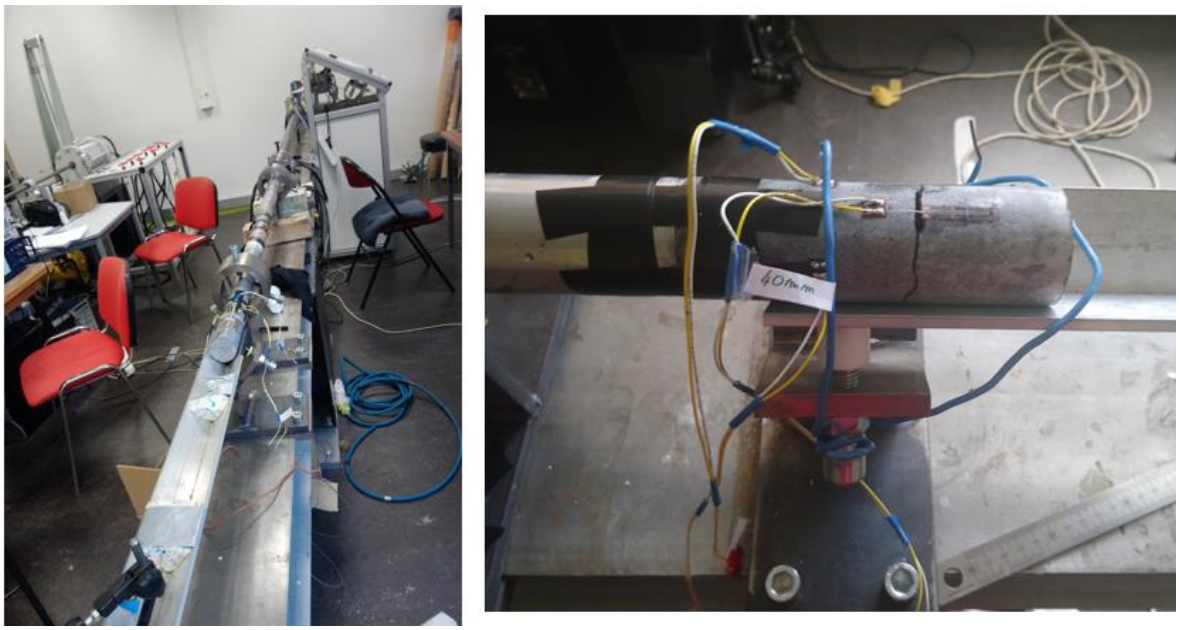

Fig 3.16 – Experimental device and instrumentation (left), tested specimen (right)

during the UHPFRC specimen's preparation: cylinders were cored out from the block parallel to the direction of flow during casting and far from the pouring point, leaving a space of at least 20 mm (fibre length) from the block edges to avoid wall-effect and fibre segregation (Leal et al., 2017) (Wang et al., 2018). A turning machine was used to perform the rectification of the samples in order to obtain good parallelism between the upper and lower surfaces, considering a tolerance of ±0.1 mm.

3.3.5.1 Experimental results obtained in spalling tests

The measured free surface velocity at the end of the specimen is used to determine the tensile strength (Schuler et al., 2006). The spall strength, according to the formula introduced by Novikov (1966), reads:

$$\sigma_{spall} = \frac{1}{2}\rho C V_{pb} \quad (3.27)$$

where ρ is the specimen density (kg/m^3), C is the elastic wave speed (m/s, assumed constant) and V_{pb} is the pull-back velocity (m/s) that corresponds to the difference between the maximum particle velocity and the rebound velocity, both measured on the measured velocity profile. This formula is assuming that we have an elastic behaviour for UHPC before failure.

The densities are determined before testing by measuring the mass and the dimensions of each specimen. The wave speed is calculated by measuring the travel time of the incident pulse through the whole specimen length. The signals G-bar and at the specimen free-end has been

Sample	Density (kg/m^3)	Wave speed (m/s)	Dynamic Young's modulus (GPa)	Pull back velocity (m/s)	Dynamic tensile strength (MPa)	Strain rate min-max (s^{-1})
A76	2433	4392	46.93	6.01	32.12	90-106
A74	2437	4605	51.67	7.04	39.49	123-169
A75	2424	4517	49.44	6.91	37.83	180-212
A2	2456	4765	54.51	5.49	31.48	81-139
A3	2407	4972	59.51	6.06	36.18	156-193
A30P1 (2%)	2556	4602	54.3	5.72	33.62	111-200
A30P4 (2%)	2554	4779	58.54	5.85	35.84	158-195

Table 3.14 – Test results for Ductal® A with and without fibre reinforcement

Sample	Density (kg/m^3)	Wave speed (m/s)	Dynamic Young's modulus (GPa)	Pull back velocity (m/s)	Dynamic tensile strength (MPa)	Strain rate min-max (s^{-1})
B347	2464	4471	49.24	5.61	30.897	63-111
B341	2451	4495	49.52	4.77	26.274	13-79
B342	2466	4580	51.72	5.97	33.713	101-132
B343	2461	4457	48.89	6.70	36.751	200-232
B348	2463	4729	53.19	6.70	39.024	160-195
B346	2463	4729	55.07	8.30	48.330	149-239
B32P1 (2%)	2615	4663	57.06	5.90	35.977	221-236
B32P4 (2%)	2549	4663	55.43	7.37	43.807	155-207

Table 3.15 – Test results for Ductal® B with and without fibre reinforcement

used for the calculus. The Dynamic Young's Modulus E_{dyn} is estimated from C using the following relationship, valid for a uniaxial stress state, based on the theory of one-dimensional elastic wave-propagation in homogenous materials:

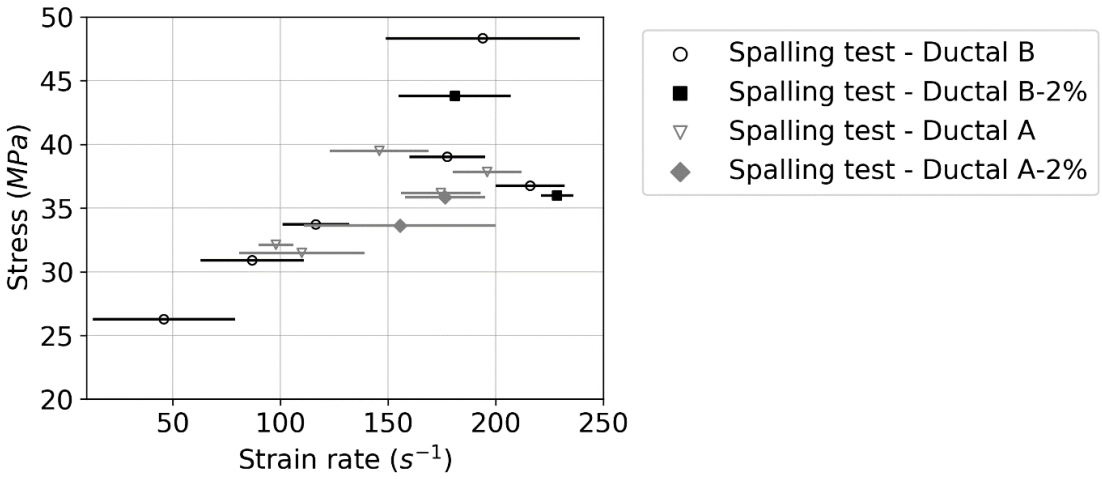

Fig 3.17 – Strain rate effect on the dynamic tensile strength obtained on Ductal® A and B with and without fibres

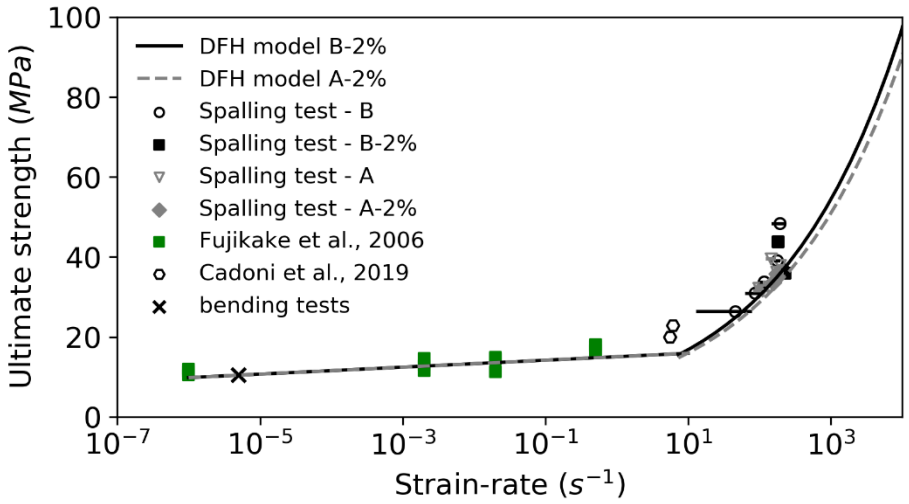

Fig 3.18 – Comparison of spall strength with the ultimate strength considering the strength enrichment at low strain rate (range 5x10^{-6} s^{-1} to 5 s^{-1})

$$C = \sqrt{E_{dyn}/\rho} \quad \rightarrow \quad E_{dyn} = C^2\rho \quad (3.28)$$

The spalling tests were conducted on specimens made of the two mixes (Ductal® A and Ductal® B with and without fibre reinforcement). All specimens were tested in dry condition at 28 days, after minimum 24 hours of drying in the laboratory environment. The tests were performed with impact velocities between 9 and 16 m/s. Higher striker impact velocity leads to a higher peak of the compressive wave but also a higher strain rate in the specimen. For the maximum measured strain rate, around 230 s^{-1}, the maximum compressive stress reached in the specimen,

-120 MPa, didn't exceed the quasi-static compressive strength of the studied concrete materials, so it can be excluded any effect of the compressive loading on the tensile failure.

The strain-rate history is deduced by averaging the time-derivates of the signals near the fracture planes (G-60 and G-40). The test results are given in **Tables 3.14-15**. The table indicates the density, the measured wave speed, and the pull-back velocity for each test.

Additionally, the spall strength and the minimum and maximum values of strain-rate during the tensile phase are given. **Fig 3.17** shows the tensile strength trends as a function of strain rate, with data for Ductal® A and Ductal® B, with and without fibre reinforcement. Even if tensile strength for Ductal® A-2% and Ductal® B-2% differs slightly in quasi-static loading conditions (8.3 and 11 MPa in direct tension), no clear differences can be observed in the range of strain rate investigated through the spalling tests. The higher performance of Ductal® B-2% with respect to A-2% in quasi-static compression loading does not lead in the studied case to higher performance regarding the dynamic tensile loading. For both mixes, the fibre reinforcement did not raise the ultimate strength.

In terms of ultimate strength, the model predictions are compared to the experimental results of the spalling tests on the plot of **Fig 3.18**. For both concrete, the increase of dynamic strength with the strain rate is quite well predicted once that the parameters related to crack inception are extrapolated to the strain rate of transition between quasi-static and dynamic response.

3.3.6 Introduction of the cohesion strength

Fibres seem not to affect the spalling strength, whereas they play a significant role in the residual velocity. In **Fig 3.19,** the velocity profiles recorded at the specimen free-end for two samples made of Ductal® A and B with fibres are compared with the velocity profile obtained for two samples without fibre reinforcement. The selected couples of tests were subjected to the same dynamic loading, in fact, a similar maximum particle velocity was reached. The residual velocities for the samples with fibres are below the signal measured for the samples without the fibres. As noted in (Forquin et al, 2017) this difference would be due to a difference of post-peak tensile strength of concrete with and without fibres.

Before the spalling test, UHPFRC specimens were analyzed using X-ray Computed-Tomography at the resolution of 85 μm. In the 3D reconstruction of the specimen in grey values, the brightness allows to distinguish the fibre phase from the concrete matrix. The objective is to use the 3D reconstruction in grey values to estimate the fibre orientation in the tested specimen with respect to the loading direction, which corresponds to the longitudinal axis of

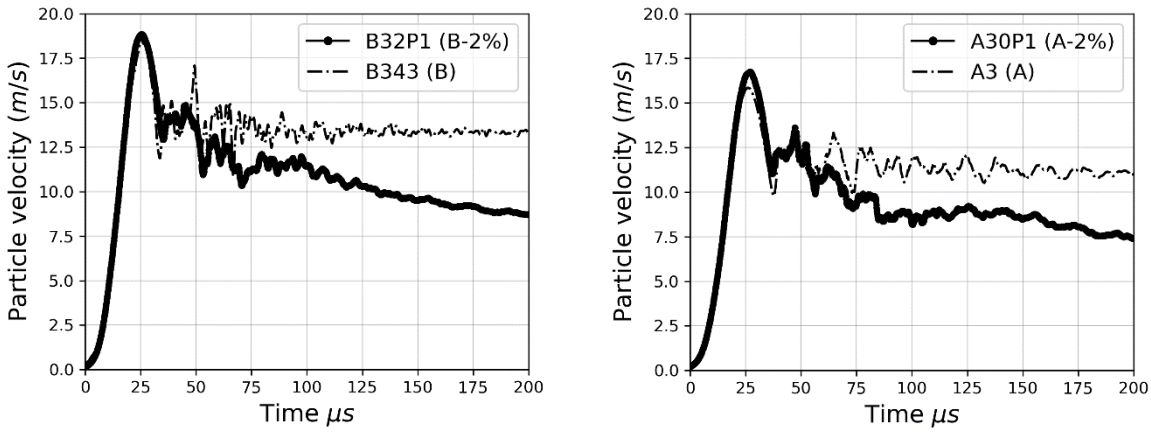

Fig 3.19 – Comparison of the velocity profiles during spalling tests for Ductal® A and B with and without fibres

the cylindrical specimen and the Z-axis of the 3D image, whereas the plane XY is orthogonal to the loading direction of the spalling test.

A method based on the Hessian matrix was used to find the orientation of the fibres in each voxel included in the fibre phase. The Hessian eigenvalues represent the magnitude of the local contrast changes in the three orthogonal principal directions. Once the eigenvalues and eigenvectors were calculated, the fibre orientation was defined as the eigenvector corresponding to the third eigenvalue. This vector indicates the direction in which there is the least variation in the gray value. The approval of this eigenvector as the fibre orientation is based on the fact that moving along the longitudinal axis of a fibre does not produce a substantial change in gray value being the fibre diameter only 2.5 pixels. This method based on the work of Krause et al. (2009), Lorenz (1997), and Nagel (2006) was already applied to measure the fibre orientation distribution in UHPFRC beam subjected to three-point bending tests by (Trainor et al., 2013).

In this study, stereoplots were used to visualize the 3D vectors in a 2D plot. The eigenvectors are all transposed at the origin of a unit sphere. For each vector, a point is designed on the surface of the sphere based on the orientation of the vector. The sphere is then cut into a hemisphere using the plane XY. This hemisphere is observed from the positive-z part of the sphere. The negative-z part of the sphere is also considered flipping every component of the vectors pointed on the negative half of the sphere. The points on the hemisphere are then projected onto the plane XY. In **Fig 3.20,** the "Lambert equal-area projection" is used, which means that an isotropic distribution of angles is projected as equally filling the projected space. A fibre pointing on the z-axis represents a point in the middle of the circle, and a fibre orthogonal to the z-axis represents a point on the perimeter of the circle. The intermediate angles are uniformly distributed along the radius. In the figure, the projected space is divided into bins,

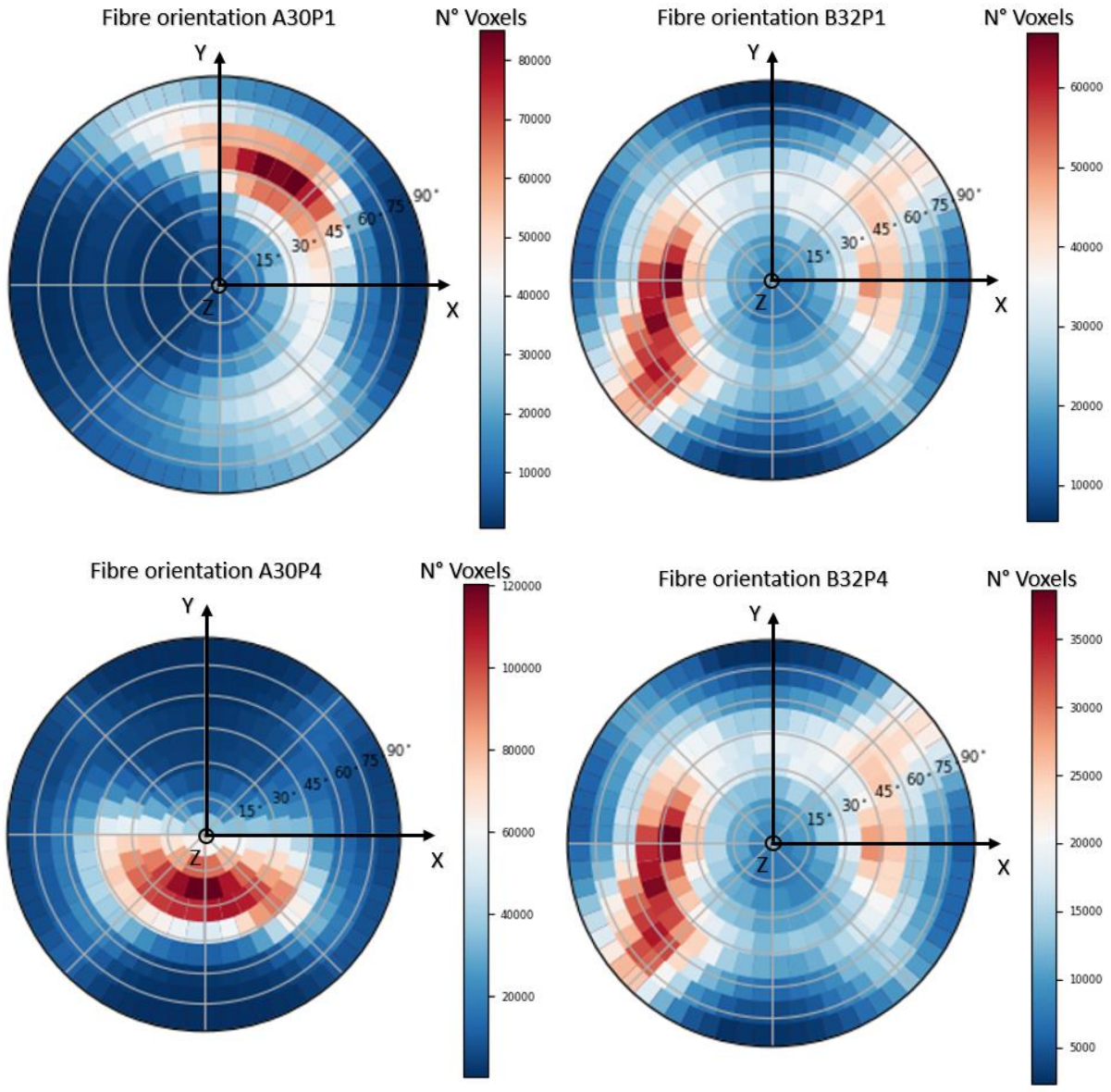

Fig 3.20 – Stereoplot (Lambert equal-area projection method) of the fibre orientation in the tested specimens: the angles are referred to the longitudinal axis of the specimen, i.e., the axis of loading during the spalling test

and the counts are given through a color bar expressing the total number of voxels for each bin (the extremities of the color bar represent the minimum and the maximum bin counts in each specimen). From the plot, it can be concluded that the fibres for all the four specimens are mainly oriented at about 30-45° with respect to the axis of loading. This fibre orientation will establish the post-cracking resistance.

The DFH model with cohesion has been considered to take into account in the softening behaviour the effect provided by the fibres in the damaged zone due to bridging phenomena that counters the opening of cracks. The term $\sigma_i{}^{coh}$, i.e., the cohesion strength set in the

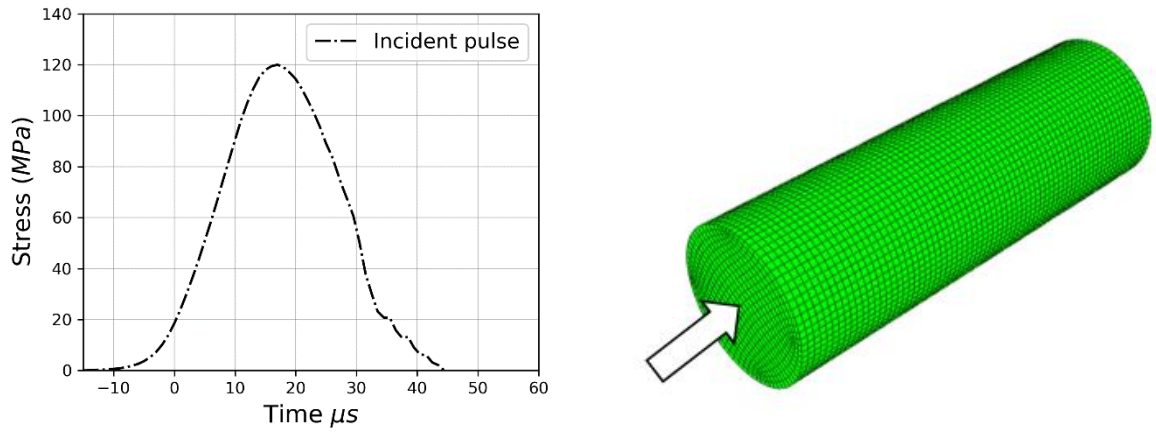

Fig 3.21 – Experimental incident compressive pulse and 3Dmesh for the FE model of the spalling test

obscured zones, is only a function of the applied strain and no strain rate dependency is considered. It is expressed as (Erzar and Forquin, 2014):

$$\sigma^{coh} = {\sigma_0}^{coh} \exp\left(-\left(\frac{\varepsilon}{{\varepsilon_0}^{coh}}\right)\right) \textbf{(3.29)}$$

where ${\sigma_0}^{coh}$, ${\varepsilon_0}^{coh}$ are parameters to be derived from experimental data. The identification of the cohesion strength parameters is made by inverse method comparing the velocity profiles measured on the rear face of the spalled samples to the numerical modeling predictions. The numerical simulations of the spalling test were performed with the Finite Element code Abaqus/Explicit. The specimens were thinly meshed by 3D elements of size 0.2 mm and loaded by the compression pulses measured in the experiments (the signal G-bar was used to reconstruct the experimental pulse)(**Fig. 3.21**). As shown in **Fig. 3.22a-b**, for both Ductal® A-2% and B-2%, the experimental particle velocities and the velocities estimated in the numerical simulation using the DFHcoh model are in good agreement. In contrast, the model predictions neglecting the cohesion strength give residual particle velocities above the experimental ones. The complete model parameters for the two UHPFRC materials are given in **Table 3.16**. Note that the same cohesion strength parameters have been assigned to Ductal® A-2% and Ductal® B-2%.

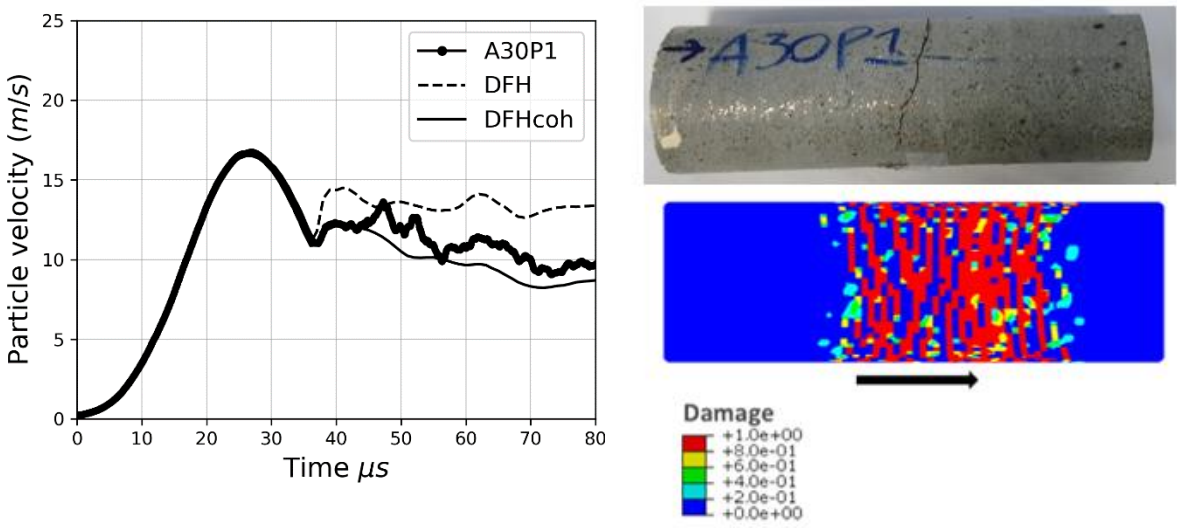

Fig. 3.22a – Velocity profile measured on the rear face of one A-2% sample during the spalling test compared to numerical modelling with and without cohesion (left) and post-mortem study comparison of damage (right)

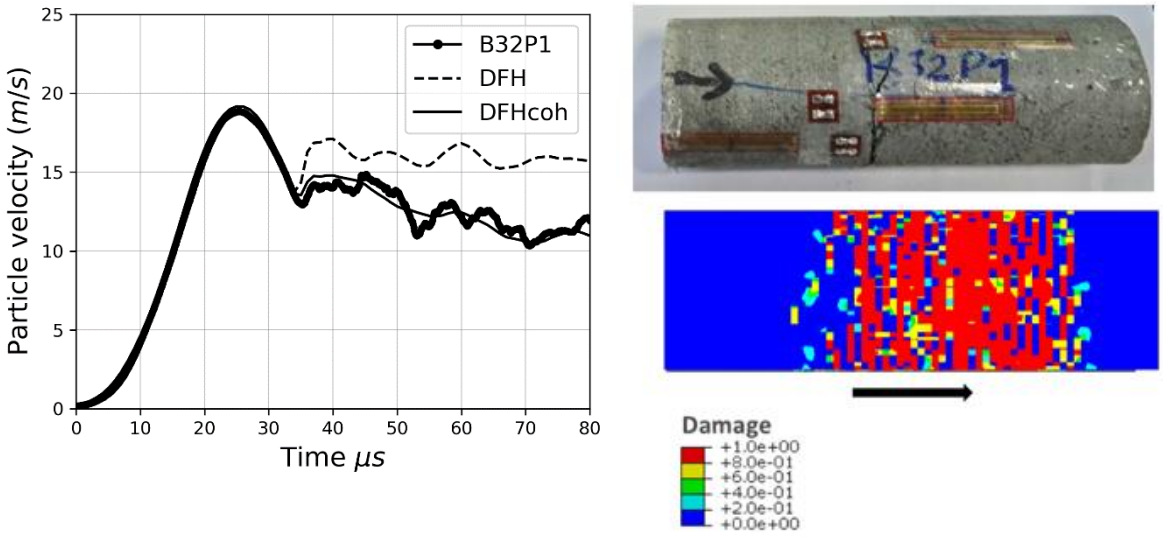

Fig. 3.22b – Velocity profile measured on the rear face of one B-2% sample during the spalling test compared to numerical modelling with and without cohesion (left) and post-mortem study comparison of damage (right)

Parameters	Symbol (Unit)	Ductal A	Ductal B
Density, elastic parameters	$\rho(\mathrm{kg/m3}), E(\mathrm{GPa}), v$	2500, 55, 0.2	2500, 60, 0.2
	Parameters of the hydrostatic behaviour		
Initial and final bulk moduli	$K_i(\mathrm{GPa}), K_f(\mathrm{GPa})$	30.6, 34.3	33.3, 37.5
Compaction curve	$P_i(\mathrm{MPa}), -\varepsilon_v^i$	130,0.0425 500,0.0460 800,0.0633	140,0.0420 500,0.0405 800,0.0560
	Parameters of the deviatoric behaviour		
Coefficient of the elliptic equation	$a_0(\mathrm{Pa}), a_1(\mathrm{Pa}),$ a_2	3.0 10^{15}, 5.02 10^{8}, 0.310	6.4 10^{15}, 7.06 10^{8}, 0.109
Maximum and minimum stresses	${\sigma_{eq}}^{max}(\mathrm{MPa}),$ ${\sigma_{eq}}^{min}(\mathrm{MPa})$	150,780	170,800
	Parameters of the fragmentation model		
Quasi-static increase factor	$\mathrm{n}^{qs}, \dot{\varepsilon_0}(s^{-1})$	0.03, 5x10^{-6}	0.03, 5x10^{-6}
Cracks initiation parameters	$\mathrm{V}_{eff}(\mathrm{mm3}),$ $\sigma_w(\mathrm{MPa}),$ m	64, 18.90 ($\dot{\varepsilon}$ =5x10^{-6} s^{-1}), 10.4	98, 19.42 ($\dot{\varepsilon}$ =5x10^{-6} s^{-1}), 8.9
Cohesive law parameters	${\sigma_0}^{coh}(\mathrm{MPa}), {\varepsilon_0}^{coh}$	20, 0.015	20, 0.015

Table 3.16 - The KST-DFHcoh model Parameters.

3.4 Conclusion

In the present chapter, an experimental identification of the DFHcoh-KST parameters is proposed to simulate the mechanical behavior of UHPFRC targets under impact using the coupled model. The identification of the Krieg, Swenson and Taylor (KST) model parameters first consisted of conducting quasi-oedometric compression (Q-OC) tests on cylindrical specimens (29.2x38mm) enclosed in a strain gauge-instrumented steel ring with well-known mechanical properties. The average radial strain and stress within the specimens were estimated

using the strain measured on the outer surface of the ring with a processing method numerically validated with a finite element model. The curves describing material compaction and yield strength respect the experimental results. The identified UHPC behavior under confinement is surely valid up to the hydrostatic pressure of 500 MPa.

On the other hand, the identification of the Denoual-Forquin-Hild (DFH) model parameters required results from different testing techniques. The DFH parameters responsible for the crack initiations were chosen, combining the experimental results from dozen of bending tests performed on 11x16x100mm^3 UHPC beams and dynamic direct tension tests from literature covering a strain-rate range from 10^{-6} to 10 s^{-1}. The resulting model predictions have been validated up to strain rate of 10^2 s^{-1} through spalling tests on samples with and without fibres. The other parameters, particularly the cohesion strength has been identified based on the particle velocity profile during spalling tests by resorting to an inverse method. Fibre orientation at about 30-45° with respect to the axis of loading have also been observed in the samples.

The objective of the next chapter is to use the calibrated model to simulate a ballistic impact test.

CHAPTER 4
Simulation of impact

CHAPTER 4

Simulation of impact

As described in the previous chapter, in the DFHcoh-KST model, a parabolic relation describes the pressure dependency of yield stresses (in the sense of Von Mises plasticity), and an anisotropic damage model (accounting for strain rate effect and fibre crack bridging action) is used to simulate the tensile failure of Ultra-High Performance Fibre Reinforced Concrete. The model parameters were identified for two commercial UHPFRCs of the brand Ductal® belonging to two different classes of strength thanks to laboratory tests under different loading conditions employing quasi-oedometric compression tests, bending tests, and spalling tests.
In the present chapter, the DFHcoh-KST model implemented in the Finite Element (FE) code Abaqus is used to simulate the ballistic impact of an AP (Armour-Piercing) projectile against Ductal® panels. The influences of yield strength, material compaction, strain rate effect, and tensile damage are pointed out to evaluate the key parameters of the behavior of UHPFRCs responsible for their excellent ballistic performance.

4.1 Ballistic tests

400mm x 400mm panels of Ductal® A-2% and B-2% with various thicknesses (from 60 mm to 100 mm) were subjected to ballistic impact experiments with pointed small-caliber projectiles in (Dobruský et al., 2018). The standard for the ballistic protective material EN 1532 was followed for the testing procedure. The 5.56×45mm and 7.62×51mm calibers were used, corresponding to the standard protection level labelled FB5 and FB7. The 5.56×45mm bullet has a steel penetrator (4.8 mm in diameter and 8 mm in length) and a soft lead core with a brass jacket. The total weight is 4.0 g, and the average shooting velocity is 950 m/s. The 7.62×51mm bullet has a complete hard steel core (6.2 mm in diameter and 23 mm in length) and a brass jacket. The total weight is 9.8 g, and the average shooting velocity is 820 m/s. The panels were subjected to three consecutive shots with a spacing of 120 mm. The distance to the panels was 10 m. Table 3.3 summarizes the results of the experimental campaign. All panels withstood the impact loading without perforation. The bullet velocity was measured 2.5 m ahead of the panel by a 10GHz Doppler radar. The penetration depth was measured from a surface to the rear part of the bullet and then increased by an estimation of the post-impact size of steel penetrator (5 mm for 5.56×45mm and 10 mm for 7.62×51mm). It was observed that there is no increase in

	Thickness mm	Caliber	Velocity m/s	Penetration mm	Crater equivalent diameter mm	Scabbing rear face
Ductal A-2%	100	7.62×51mm	814	37	56	No
Ductal A-2%	80	7.62×51mm	837	38	60	No
Ductal B-2%	80	7.62×51mm	816	32	58	Yes
Ductal B-2%	60	5.56×45mm	957	34	48	Yes

Table 4.1 – Ballistic performance of the two UHPFRC Ductal® products (average value of three consecutive shots)

the penetration depth with the three consecutive shots. Only a 80 mm thick panel was tested for both Ductal® A-2% and B-2% with the same caliber, i.e., 7.62×51mm. The average value of penetration of the three shots is respectively 38 and 32 mm. This means an average difference of 6 mm for the penetration depth between Ductal® A-2% and B-2%.

4.2 FE analyses

This section deals with Finite Element (FE) analyses of a ballistic impact of a small-caliber projectile, 5.56×45 mm, launched at the speed of 950 m/s against a 60 mm-thick UHPFRC panel. Before the modelling phase, post-mortem observations are made on an available impacted target of Ductal® B-2% to help in the discretization of the problem. Important information summarized hereafter are derived from the observations that simplified the modelling regarding the bullet trajectory and the extension of the area to simulate. Moreover, they help in the selection of the constitutive models to consider for each material involved.
The program Abaqus/Explicit is used to conduct the calculation. First, as in the real experiment, a UHPFRC panel made of Ductal® B-2% is considered for the FE analyses. This calculation is used to determine additional numerical parameters introduced in the FE analysis to avoid huge element distortion. Then numerical calculations of impact against panels of Ductal® A-2% and B-2% are compared.

4.2.1 The Ductal® B-2% target

A ballistic test was performed upon a 60 mm-thick panel made of Ductal® B-2% with a pointed bullet, 5.56×45mm caliber (reference FB5), launched at an impact speed of 950 ±10 m/s. The bullet is composed of a hard steel penetrator and a soft lead core, both encapsulated in a pointed jacket of full brass (total mass 4 g). The panel withstood the impact without perforation. A

Fig 4.1 – Views of the impacted target of Ductal® B-2% (60x60x95 mm) and recovered parts of the bullet after impact: penetrator 4.8 mm in diameter, 10 mm in length, soft core 4.1 mm in diameter and 8 mm in length (final dimensions)

crater of irregular shape, about 20 mm in average radius, formed on the front side and additional damage was visible on the rear side (scabbing). On both sides, fragments were kept in place thanks to the steel fibres. The 60x60x95 mm^3 target shown in **Fig 4.1**, including half of the front crater, is extracted from the tested panel. The penetration depth into the target is, including the residual bullet length, 43 mm. The penetration channel created by the bullet is straight and at the right angle to the impacted surface, so it can be concluded that the trajectory of the bullet was steady during the penetration process.

The steel penetrator is recovered practically intact after the impact, 4.8 mm in diameter and 8 mm in length are measured as the initial dimensions. In addition, the lead core is recovered almost intact, the diameter is reduced from 4.8 to 4.1 mm, and the length remains unchanged at 10 mm. The diameter of the penetration channel is about the penetrator diameter, so it is reasonable that the lead was supported in the radial direction by the walls of the penetration channel during its penetration process. The jacket of the bullet is very soft, and it is not recovered after the impact; it might have been entirely consumed, or it might be stripped away from the core during penetration.

4.2.2 The FE model

The graphical environment Abaqus CAE is used to create the 3D quarter-symmetry model of the problem. The jacket of the bullet is not included in the numerical model. The lead core and the steel penetrator are modeled as two separated parts. An initial velocity of 950 m/s is

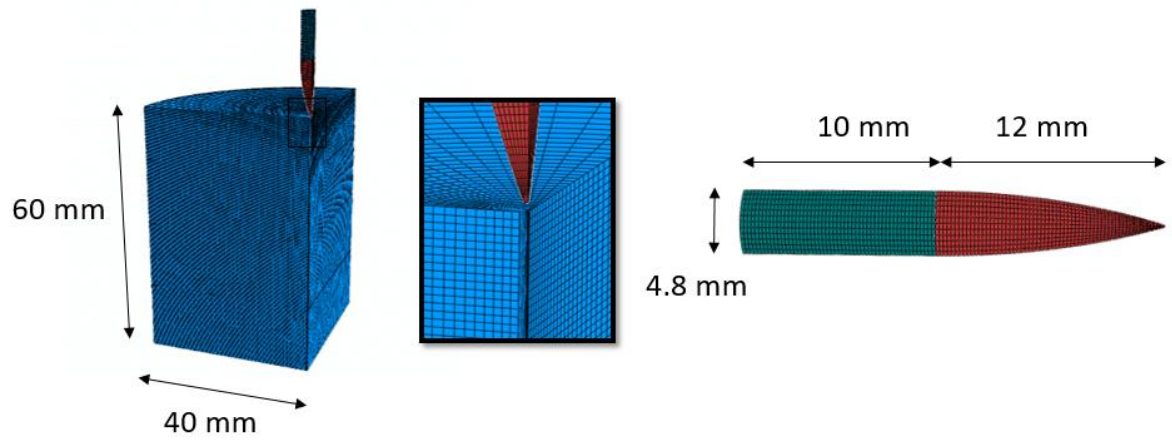

Fig 4.2 - Complete Mesh (left), details of the tunnel and bullet (steel in red, lead in green, and UHPFRC in blu)

assigned to both the lead and the steel part. Based on the post-mortem observation, the trajectory of the bullet is considered normal to the concrete panel. A cylindrical target of radius 40 mm is considered for the UHPFRC panel, i.e., two times the experimental average crater radius.

The tunnelling and erosion methods are both used for the UHPFRC panel to overcome the enormous element distortions of FE simulations. The tunnelling method consists of meshing a small diameter tunnel compared to the projectile diameter along the expected projectile path. As shown in **Fig. 4.2** (right), the nose of the steel penetrator was falsely made pointed to enlarge the tunnel during the penetration process easily.

The second method, known as the erosion method, consists in eliminating each finite-element reaching a specific criterion defined in terms of maximum equivalent plastic strain. The erosion criterion was applied only to the UHPFRC materials. The equivalent plastic strain is defined as $\varepsilon_p=(2/3\ \varepsilon_{ij}^p\ \varepsilon_{ij}^p)^{1/2}$.

The three elements (panel, lead core and penetrator) were discretized with hexahedral elements with reduced-integration, referenced C3D8R in Abaqus (an 8-node brick with 1 integration point in the middle of the element). A mesh of increasing size from the impact point, from 0.2 mm to 2 mm, is used for the panel, whereas the two parts of the bullet have an equivalent mesh size of 0.2 mm. The complete mesh used in the calculations had 203424 FE and 226258 nodes. The contact between the panel, the lead core, and the penetrator is modelled using the general contact algorithm implemented in Abaqus, i.e., an hard contact in the normal direction combined with a friction coefficient in the tangential direction. Note that because element erosion is possible for the UHPFRC panel, its interior elements must be included in the surface of the contact definition.

	Density, Young's modulus, Poisson's ratio $\rho\left(\frac{\mathrm{kg}}{m^3}\right), E(\mathrm{GPa}), v$	Yield stress
steel	7800, 210, 0.3	2 GPa (Forquin et al., 2015)
lead	11340, 15, 0.3	-

Table 4.2 - Material parameters considered for the bullet

4.2.3 Impact against Ductal® B-2% panel

FE analyses are conducted with version 6.13-2 of Abaqus/Explicit. The DFHcoh-KST coupled model used for the UHPFRC panel was implemented as a VUMAT user-defined subroutine. The parameters identified for Ductal® B-2% in the previous section are used. A simple elastic-perfectly plastic behavior is considered for the steel penetrator as the ballistic tests had shown that the penetrator did not deform or fracture. The behavior of the lead is considered elastic as the ballistic tests had shown that the core did not present enormous plastic deformation. This questionable choice is made as the FE method was producing incorrect results for the lead response when elastic plastic behavior and erosion were considered without restraining the lateral displacement of the lead core. The assumption solves in a practical way the discrepancy with the experimental result as the correct definition of the constitutive behavior of the lead is out from the aims of this study. The material parameters considered for the bullet are reported in **Table 4.2**.

4.2.3.1 Influence of tunnel radius, friction and erosion criterion

A series of calculations are performed to investigate the influence of the tunnel radius (TR), the friction coefficient (FC), and the erosion criterion (EC) considered in the FE analysis on the bullet deceleration and penetration depth. The influence on the bullet deceleration is investigated by plotting the velocity profiles in the FE analysis calculated as the average velocity as a function of time for three nodes of the steel penetrator on the penetration axis (**Fig. 4.3)**. Simultaneously, the final penetration depth is calculated as the integral of the plot (**Table 4.3**). Four tunnel radiuses (TR) are considered respectively of 0.2 mm, 0.4 mm, 0.6 mm, and 0.8 mm, corresponding to a ratio between the tunnel and the bullet radiuses of 1/12, 1/6, 1/4, and 1/3. As shown in **Fig. 4.3a**, the tunnel radius seems not to have a strong influence on the bullet deceleration until a tunnel radius of 0.6 mm, i.e., a tunnel to bullet ratio of radius equal

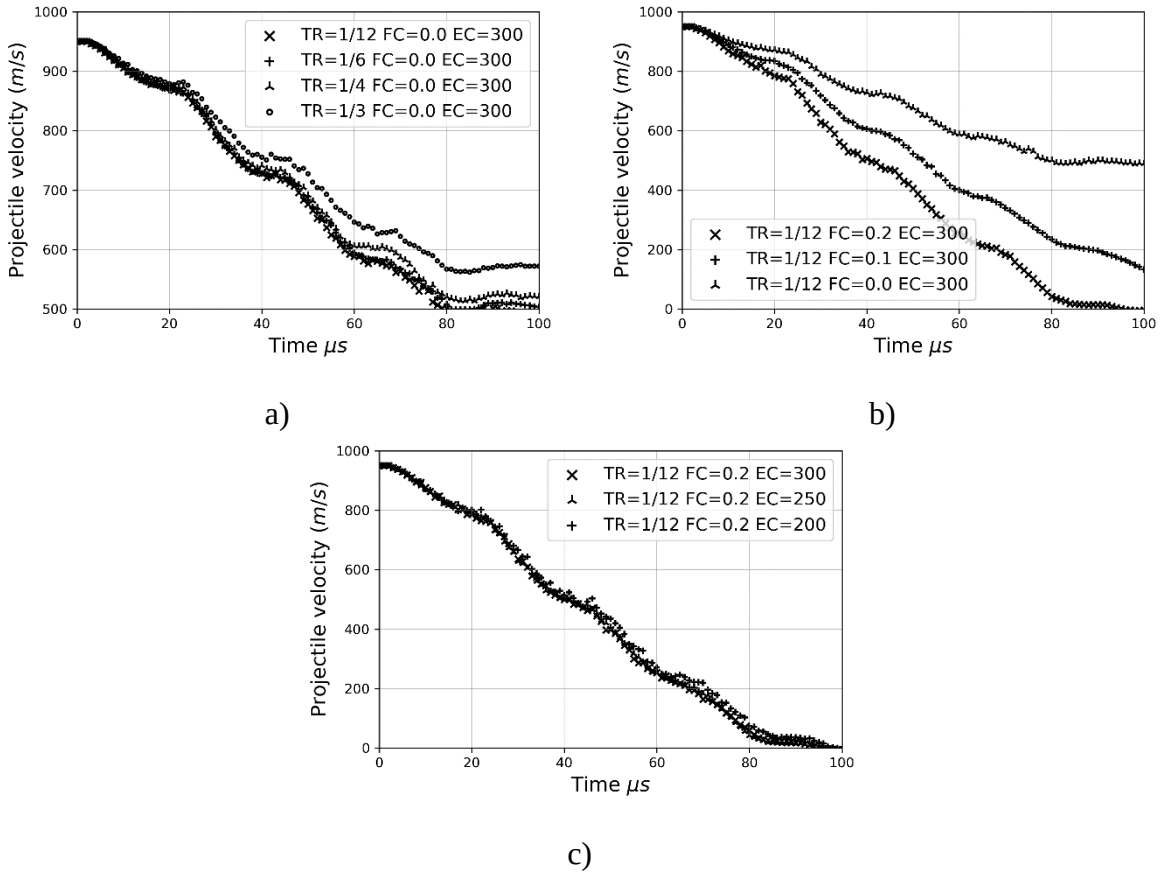

Fig. 4.3 – Velocity profiles for the steel penetrator: a) Influence of the tunnel radius (TR); b) Influence of erosion criterion (EC); c) Influence of friction coefficient (FC).

to 1/4. These calculations are performed without friction at the bullet–panel interface, leading to a marked underestimation of projectile deceleration.

The previous FE analyses lead to the panel perforation in all the cases. Thus, the influence of friction is investigated for a tunnel radius of 0.2 mm, considering three values of the friction coefficient (FC = 0.0, FC = 0.1, and FC = 0.2).

The projectile velocity profiles are compared in **Fig. 4.3b**. A marked influence of the friction coefficient is visible on both the velocity profile and the depth of penetration. As reported in **Table 4.3,** a relevant variation of the penetration depth is obtained, changing the friction coefficient from 0.0 to 0.2.

All these calculations are then taken into account to select the values of the tunnel radius, the friction coefficient and the maximum equivalent plastic strain to be set as reference values for further analyses. Even if the profile of the velocity during the ballistic test is unknown, the calculation for a UHPFRC panel with a tunnel radius of 0.2 mm, and equivalent plastic strain and friction coefficient set to 300 % and 0.2 provides the experimental penetration depth. The penetration depth versus time is also shown in **Fig. 4.5a.**

Tunnel radius (mm) TR (with FC = 0.0 & EC = 300) 0.2, 0.4, 0.6, 0.8	Final depth of penetration (mm) perforation all cases
Friction coefficient FC (with TR = 0.2 & EC = 300) 0.0, 0.1, 0.2	Final depth of penetration (mm) perforation, perforation, 41.90
Erosion criteria EC (%) (with TR = 0.2 & FC = 0.2) 200, 250, 300	Final depth of penetration (mm) 43.6, 42.0, 41.90

Table 4.3 - Influence of the tunnel radius (TR), friction coefficient (FC), and erosion criterion (EC) on the final penetration depth

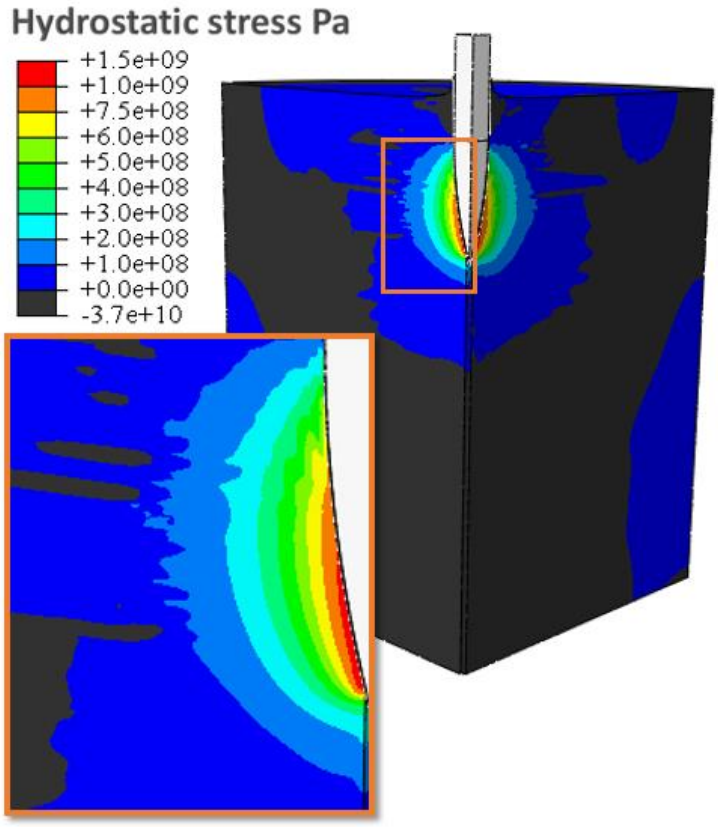

Fig. 4.4 – Isocontours of hydrostatic stress at 20 μs

4.2.3.2 Pressure field and hoop strain rate

The pressure field generated in the FE calculation is used to discuss the level of confinement pressure reached in the panel during the penetration phenomena. Confining pressures up to 1 GPa develop in the vicinity of the projectile. In **Fig. 4.4.**, an onion-shaped zone exhibiting high hydrostatic stress ranging from 100 MPa to 1.5 GPa surrounding the steel penetrator is shown at 20 microseconds. The radius of the bulb is ≈4 times the bullet radius; the stress exceeds values of 500 MPa within a radius ≈2 times the bullet radius.

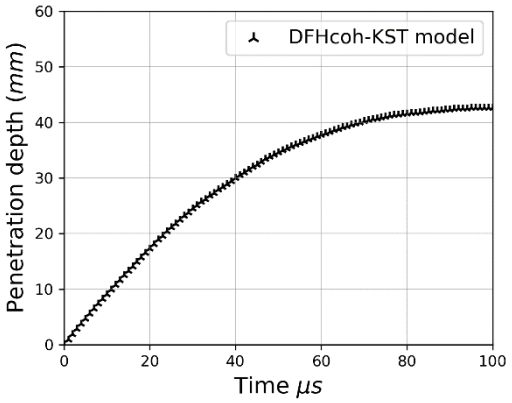

Fig. 4.5a – Penetration depth versus time

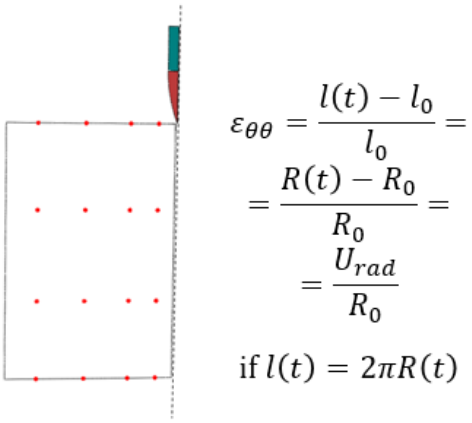

Fig. 4.5b – Nodes used in the hoop strain estimation

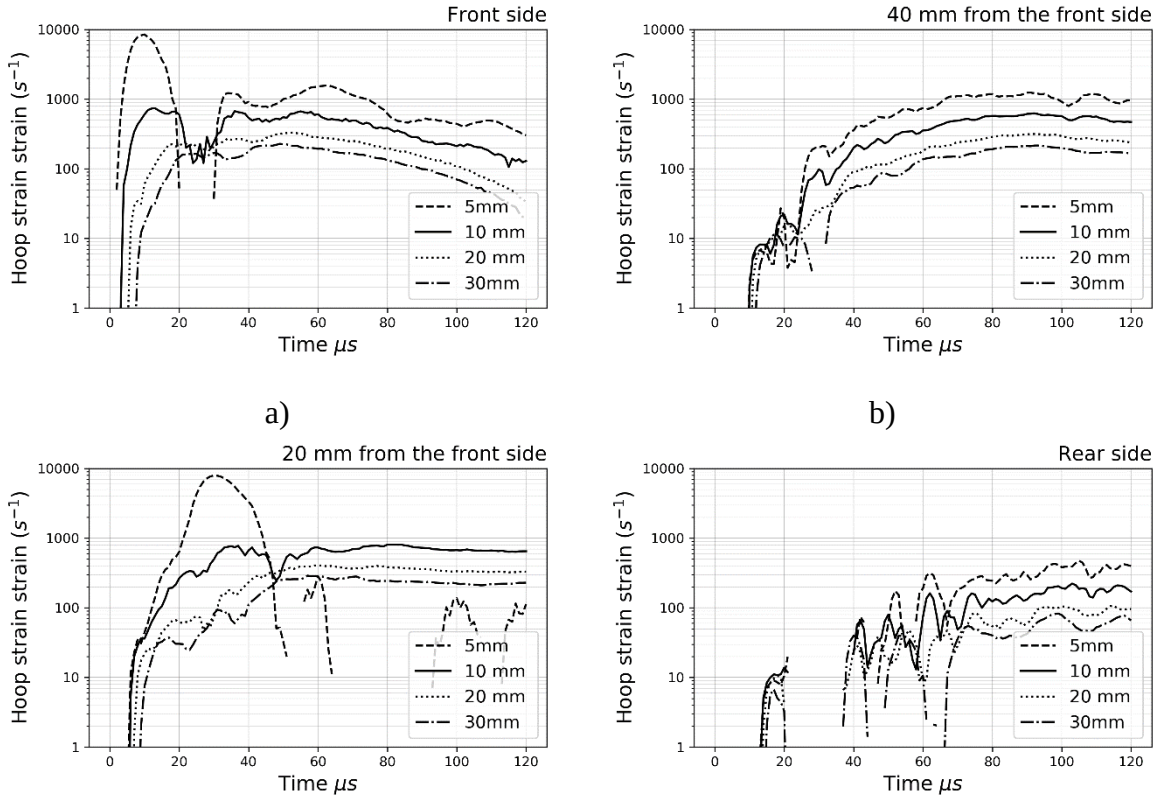

Fig. 4.6 – Hoop strain rates at four distances from the axis of penetration: a) at the front side; b) 20 mm from the front side; c) 40 mm from the front side; c) at the rear side;

A numerical analysis is made for a rough estimation of the tensile strain rate levels reaching by the UHPFRC panel during the bullet penetration. For this purpose, the radial displacement history output of distinct nodes of the FE mesh was stored and processed. The penetration of the bullet into the panel imposes a radial extension that is responsible for the radial cracking through the UHPFRC panel. A nominal hoop strain (orthoradial strain) is defined as:

$$\varepsilon_{\theta\theta} = \frac{R(t)-R_0}{R_0} = \frac{U_{rad}}{R_0} \textbf{ (4.1)}$$

with U_{rad} the radial displacement of the node and R_0 its distance from the axis of penetration. The related hoop strain rates are plotted as functions of time in **Fig. 4.6** for nodes located on the front face, at 20 mm from the front face, at 40 mm from the front face, and on the rear face. Moreover, four different distances from the axis of penetration are considered, respectively 5 mm (≈ 2 times the bullet radius), 10 mm (≈ 4 times the bullet radius), 20 mm (≈ 8 times the bullet radius), and 30 mm (≈ 12 times the bullet radius). The penetration depth versus time is also shown, in **Fig. 4.5,** to help in the interpretation of the analysis. As expected, the spherical wave generated at the impact point arrives at the panel rear face in about 12 μs and leads suddenly to hoop tensile strain rates of tens s^{-1} through all the panel thickness. Then, the hoop tensile strain rate related to the radial extension that grows with the bullet's penetration reaches several hundred s^{-1} through all the panel thickness. At 5 mm from the penetration axis, they even exceed 10^3 s^{-1}. Then, the hoop strain rate decreases of about one order of magnitude, from 5 to 30 mm distance from the penetration axis.

4.2.4 Impact against Ductal® A-2% and B-2% panels

Once the tunnel radius, the friction coefficient, and the maximum equivalent plastic strain are defined, the results obtained by numerical calculations using the material parameters of Ductal® A-2% and B-2% are compared. The velocity profiles and the final penetration depths for the steel penetrator are shown in **Fig. 4.7.** Ductal B-2% provides more penetration resistance than Ductal A-2%. The bullet stops respectively after 100 and 180 μs. The penetration depths, including the bullet, are 41.90 and 53.84 mm, so a difference of ≈10 mm between the A-2% and B-2% panels is obtained.

In both panels, the penetration phenomenon causes the onset and growth of tensile damage. In the first 20-30 microseconds, damage initiates at the periphery of the zone (bulb) under high confinement. Two main damage structures develop: cracks orthogonal to the axis of penetration, shaped like discs, propagating parallel to the impacted surface; and cracks radial to the penetration axis propagating through the panel thickness. At 40-50 microseconds, the orthogonal cracks, with the bullet indentation, turn and propagate toward the front side (saucer-like fashion) that cause the removal of material in the experiment, i.e., the cratering phenomena. New radial cracks initiate, this time below the nose of the bullet, and propagate toward the rear side. Those cracks can converge with the previous radial cracks. At 60-90 microseconds, inclined cracks, in the form of a conical frustum, form below the bullet and propagate close to

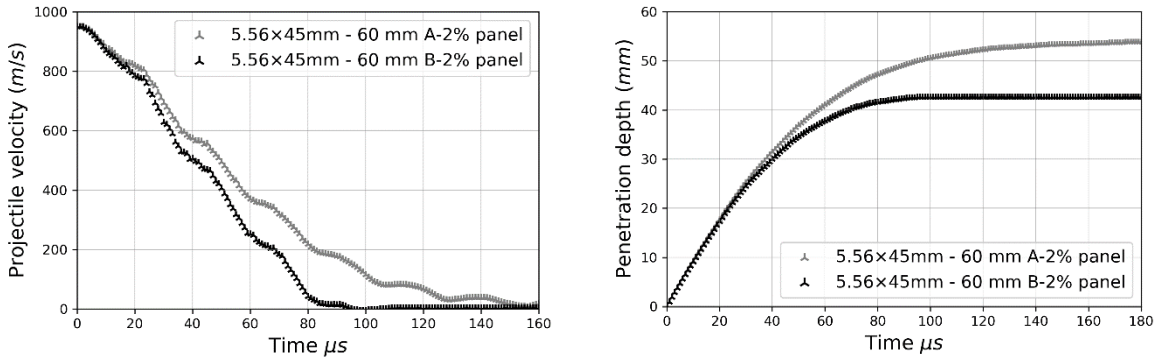

Fig. 4.7 – Velocity profile (left) and final penetration depth (right) for the steel penetrator

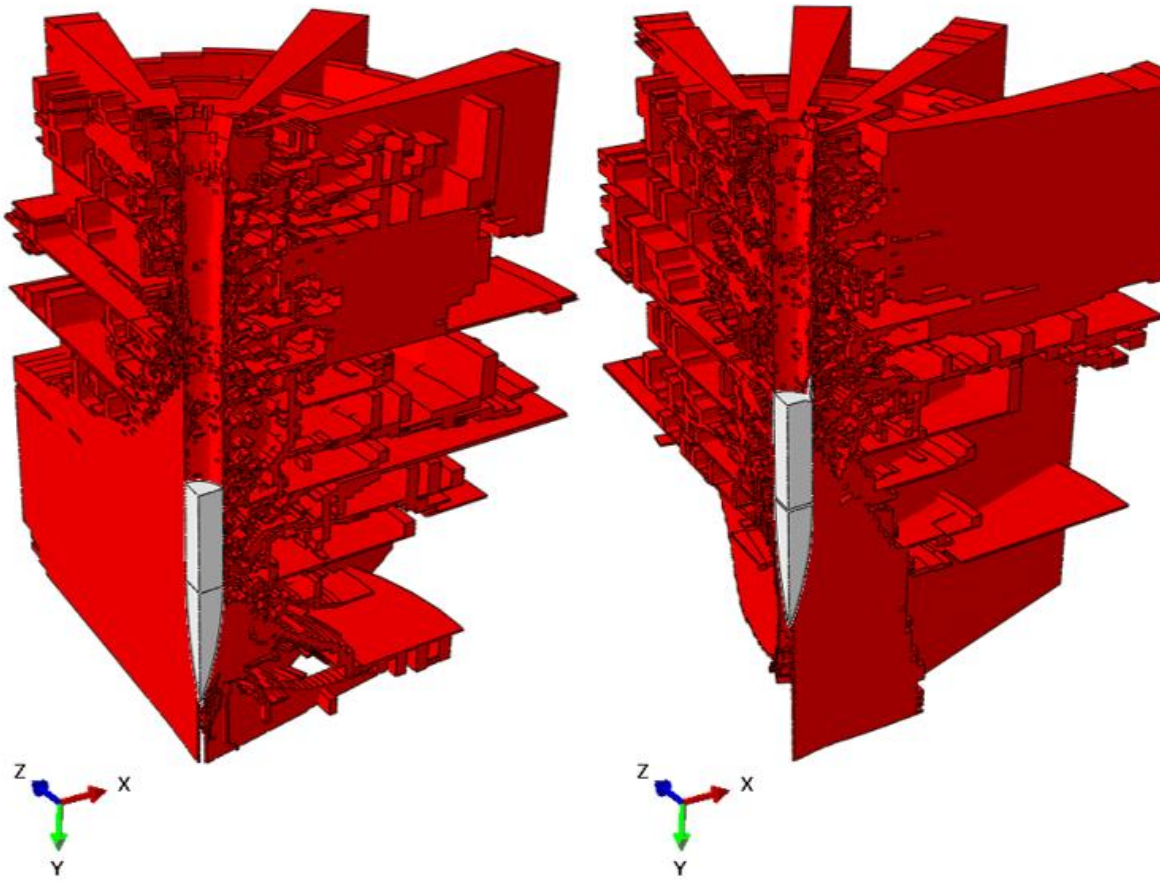

Fig. 4.8 - 3D Damage pattern in 60 mm-thick panels: Ductal A-2% (right) and Ductal B-2% (left)

the rear side. Those cracks are responsible for the scabbing phenomenon. The damage phenomena end (cracks end the propagation) about when the bullet stops. **Fig. 4.8** shows the tridimensional damage pattern for panel A-2% and B-2% after the entire event is ended (elements reaching D=1 in the principal stress direction have been extracted). The estimation of the extension of cratering and scabbing in the numerical simulation is not obvious. The crater and scabbing radius have been measured considering the damage structures tapping the front and rear sides. For panel B-2%, they measure respectively 19.20 and 8.7 mm, whereas they

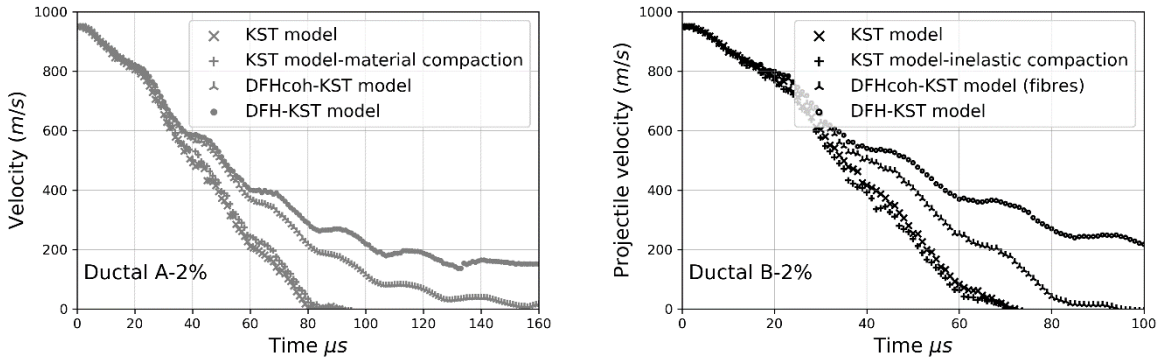

Fig. 4.9 – Influence of the UHPFRC constitutive behaviour on the velocity profile of the steel penetrator

	A-2%	B-2%
Panel behavior	Final depth of penetration (mm)	Final depth of penetration (mm)
KST model	41.81	33.20
KST model (no material compaction)	40.29	33.70
DFHcoh-KST coupled model	53.84	41.90
DFH-KST coupled model (no cohesion strength)	perforation	perforation

Table 4.4 - Influence of UHPFRC behavior on the final penetration depth: KST model, KST model (material compaction), DFHcoh-KST coupled model, DFH-KST coupled model

measure 16.29 and 19.70 mm for panel A-2%. No difference is observed in the cratering phenomenon. The scabbing in panel A-2% is more pronounced than in panel B-2%. When the frustum-of-cone formed in panel A-2%, the bullet has residual kinetic energy to extend the damage zone.

4.2.5 Influence of the panel model

Two additional calculations for the two Ductal® materials were conducted considering only the KST plasticity model for the behavior of the panels. The velocity profiles are shown in **Fig. 4.9.** and the final penetration depths for the steel penetrator are given in **Table 4.4.**

In the KST model, the tensile stresses are only limited by a negative minimum value of hydrostatic pressure (P_{cut}) set to -8.3 MPa for Ductal® A-2% and -11 MPa for Ductal® B-2% (as the mean tensile strength in quasi-static tension). Neither damage nor strain rate dependency is taken into account in that case. The first calculation uses the full set of material parameters

identified for Ductal® A-2% and B-2% under confinement. This numerical calculation predicts a penetration depth of 41.81 mm for Ductal A-2% and 36.68 mm for Ductal® B-2%, so penetration depths much less than the DFHcoh-KST model. In the second numerical simulation, a linear equation replaces the compaction law, and the constant bulk modulus is set equal to the initial elastic bulk modulus. This numerical calculation predicts a penetration depth of 40.29 mm for Ductal® A-2% and 35.20 mm for Ductal® B-2%, which is almost the same depth as the previous calculus. Moreover, if the penetration depths obtained with the KST model for Ductal® A-2% and B-2% are compared, in this case, the difference is reduced by half (≈5 mm).

One additional numerical simulation was conducted for the two Ductal® materials neglecting in the DFHcoh-KST model the effect of the fibre reinforcement on the softening post-peak tensile behavior by setting the parameter $\sigma_0{}^{coh}$ to zero (nil cohesion in the obscuration zone). This assumption leads for both Ductal® materials to drastically decrease the bullet deceleration until the full perforation of the panels.

4.3 Discussion and conclusion

The DFHcoh-KST model implemented in the Finite Element (FE) code Abaqus was used to simulate the ballistic impact of an Armour-Piercing projectile launched at the speed of 950 m/s against a 60 mm-thick panel.

One Ductal B-2% numerical sample has been subjected to a ballistic test. The influence of tunnel radius, friction and erosion criterion on the projectile deceleration and depth of penetration was investigated. On the one hand, numerical simulations indicated that the friction had a marked influence. On the other hand, as long as the ratio of tunnel radius to projectile radius is below 1/4, the tunnel radius has an insignificant influence on projectile deceleration. In the same way, if the limit equivalent plastic strain (erosion criteria) is above 200%, its influence became insignificant.

Two UHPFRC numerical samples have been subjected to a ballistic test. It was observed that Ductal B-2%, stronger under confining pressure, provides more penetration resistance than Ductal A-2%. Additional numerical simulations have been launched for the panels of Ductal A-2% and B-2% to evaluate the influence of tensile damage and material compaction on the ballistic performance of the panels. Neglecting the material compaction under hydrostatic compression shows that the modelling of the inelastic compaction is not crucial for UHPFRC. Considering only the KST model for the panels pointed out the importance of considering a constitutive model in which the loss of resistance due to fracturing under tensile loading is taken into account. The calculations without the effect of the cohesion strength underline the

importance of correctly representing the tensile softening response of UHPFRC in the constitutive model.

The level of confinement pressures and tensile strain rate were also discussed. According to this numerical study, during the impact, confining pressures up to 1.5 GPa develop in the panel in the vicinity of the projectile nose. The hydrostatic and deviatoric behavior of UHPC needs to be validated for pressures higher than 500 MPa. Strain rates about few hundreds of s^{-1} are reached in the whole target, whereas strain-rates exceeding 10^3 s^{-1} are noted around the tunnel. The tensile behavior of UHPC needs to be validated for strain rates up to 10^2 s^{-1} .

CHAPTER 5
Spalling through Plate-Impact

CHAPTER 5

Spalling through Plate-Impact

The numerical simulations of impact in the previous chapter pointed out that the behavior of concrete needs to be investigated over a wide range of strain rates. A strain rate exceeding 10^3 s^{-1} has been estimated around the tunnel region in the target. This level of strain rate is out of the range investigated through the spalling technique conducted with the Hopkinson bar.
Spalling at a high strain rate can be produced during a Plate-Impact experiment. However, the method suffers from a substantial limitation: the level of strain-rate is challenging to estimate and to control. Indeed, the strain rate within a target subjected to Plate-Impact is not constant during the experiment. This is due to the shape of the compressive pulse generated with the impact. It can be considered as a trapezoidal shape with sharp rising and descending edges. Consequently, the loading rate in the impacted target is not constant and can reach very high values (strain rate above 10^5 s^{-1}), and it cannot be adjusted by changing the speed of the flyer plate. Furthermore, the speed of the flyer plate is bounded by a lower limit to ensure the spalling and by an upper limit to avoid any material damage in compression before that the spall occurs. Recently (Forquin and Zinszner, 2017) proposed to use a machined plate to produce a smooth compression in plate-impact experiments on ceramics. By means of numerical simulations, they proved that machined contact surfaces provide an easy way to modify the rising time of the pulse generated by the impact. The plate-impact testing technique is used in this chapter to investigate the tensile behavior of UHPC materials without fibre reinforcement at very high strain-rates, above 10^3 s^{-1}. New experimental configurations based on machined flyer-plate combined with a buffer are developed to adjust the loading rate in the target.

5.1 Material

The investigations are conducted with the two commercial premixes of the brand Ductal® A and B presented in the previous chapter. This time the fibre reinforcement is not included in the mixture. The average mechanical properties are reported in **Table 5.1**. The density ρ referred to the mean value of six cylindrical specimens (46 mm diameter - 140 mm length). The elastic modulus is replaced by the average Dynamic Young's modulus measured in compression in the spalling experiment performed with the Hopkinson bar on specimens of Ductal® A and Ductal®

Ductal®	A	B
Density ρ kg/m3	2420±13[1]	2458±8[1]
Poisson's ratio v	0.2[2]	0.2[2]
Dynamic Elastic modulus in compression E_{dyn} GPa	52.41±3.7[1]	51.27±2[1]

Table 5.1 – Elastic mechanical properties of the two Ductal® products without fibre reinforcement. [1]average value specimens tested in spalling at the Hopkinson bar [2] value by standard NF P 18-470 for UHPFRC

B (E_{dym}). For both the material, v is set equal to the value suggested by standard NF P 18-470 for UHPFRC.

5.2 Pulse shaping concept

Tensile stress in the target is generated when the incident compressive wave reflects back at the free surface of the target as a tensile wave that exceeds in amplitude the incident compressive wave. However, the resulting tensile stress profile in the specimen is determined by the overlap between both the incident and reflected waves. **Fig. 5.1** presents a diagram of the wave overlap in a target (with a linear elastic material response) for three shapes of simple triangular pulse. For each pulse shape, the interaction of the waves is shown at the times T1 (target still under compression) and T2 (tension stresses are developed). The origin of the Cartesian axes is defined at the free surface. The incident and reflected waves are represented respectively in blue and red. At the same time, the resulting overlap is shown in yellow. In the case of a compressive pulse with right-angled rising-edge and smooth descending-edge the interaction between incident and reflected waves leads to a discontinuity of stress state in the target. In the same way, a discontinuity is noted with of a compressive pulse made of smooth rising-edge and right-angled descending-edge. On the contrary, in the case of compressive pulse composed of smooth rising-edge and descending-edge the interaction between incident and reflected waves prevent any discontinuity of stress. However, both rising and descending edges have to present linear stress profiles to maintain a constant strain rate. Moreover, if the rising and descending edges carry exactly opposite slopes as for an isosceles triangular wave, uniform tensile stress is held in a portion of the target. The pulse shaping that fits our case of study is carefully designed in the next part.

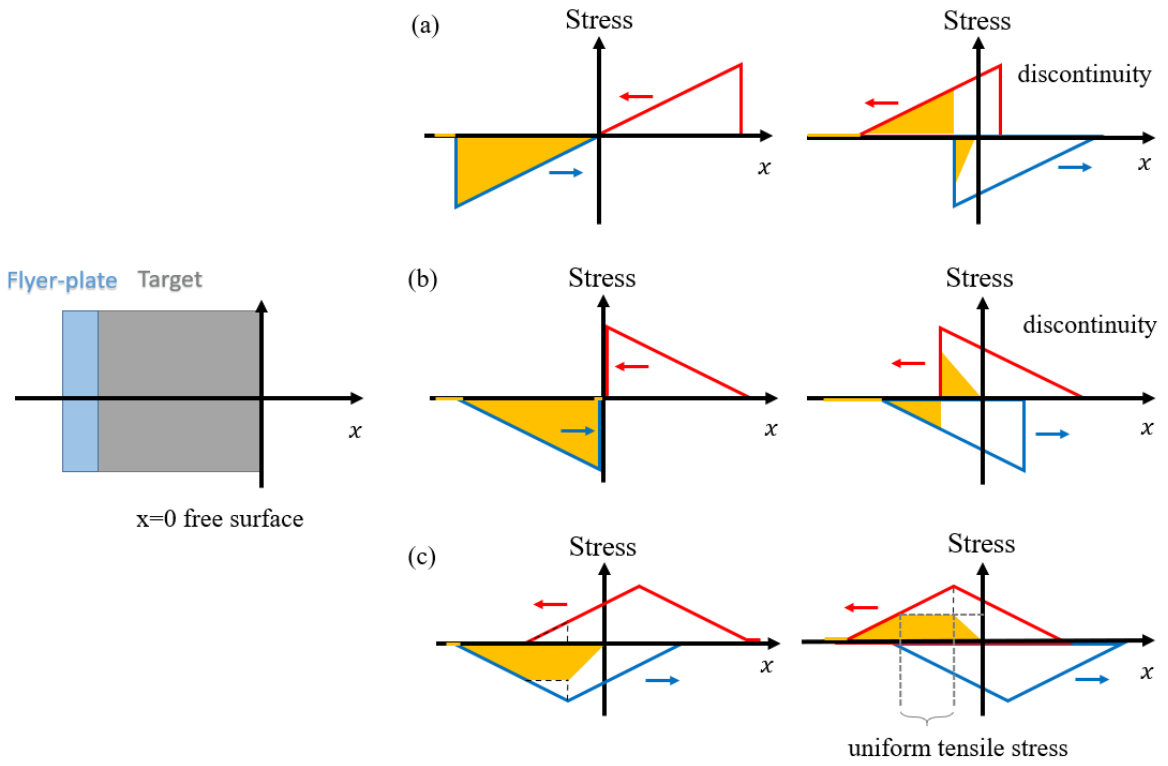

Fig 5.1 - Stress wave reflection and overlap in the target a) through the interaction of two right-angled triangular waves – smooth rising edge b) through the interaction of two right-angled triangular waves - smooth descending edge c) through the interaction of two isosceles triangular waves

material	Density (g/cm^{-3})	Elastic properties		Plastic yield strength	
		E (GPa)	ν	σ_y (MPa)	ε_p
6061-T6	2700	68.9	0.33	270	0
Ductal®	2420	52	0.2		

Table 5.2 – Material parameters used in the Abaqus/Explicit numerical simulation

5.3 Numerical design

5.3.1 1D Model

The objective of this section is to quantify the strain rate during a traditional plate-impact experiment on a UHPC material at the spall location. This aim in view, 1-D strain calculations have been conducted using the explicit transient dynamic finite-element (FE) code Abaqus/Explicit. For the standard plate impact configuration, a 5-mm-thick 6061-T6 Aluminum striker impacting a 10-mm-thick Ductal target is considered (**Fig. 5.2a**). A linear elastic – perfectly plastic behavior is assumed for the striker, whereas an elastic behavior is used for the target. The material parameters are reported in **Table 5.2**.

After impact, compressive axial stress developed first, and the tensile load arises second. The spalling is expected to occur almost in the middle part of the target between 60-100 MPa. The axial stress versus strain rate curves is plotted in **Fig. 5.2b** at different locations from the free surface, distance 3.9, 4.0 and 4.1 mm. The level of strain-rate is in the order of a few 10^4 s^{-1}, and it is heterogeneous during the tensile loading. As expected, by increasing the striker speed, the strain rate level increases, but the strain rate heterogeneity increases too (as it is noted comparing the stress at 3.9, 4.0 and 4.1 mm). This simple calculation underlines that the standard plate impact configuration is not adapted to discuss the strain-rate effect on the spall strength of UHPC. A second calculation was performed considering a 1-D strain state and a pressure pulse directly applied to the target. Two triangular pulses were selected with the same peak axial stress in compression (**Fig. 5.2c**). In this second case, the level of strain rate is noted to be perfectly constant during the development of the tensile stresses from 0 to 100 MPa (**Fig. 5.2d**). It demonstrates that, if they can be generated, triangular-shaped compression pulses can bring a real improvement to investigate the strain-rate sensitivity of concrete with the plate-

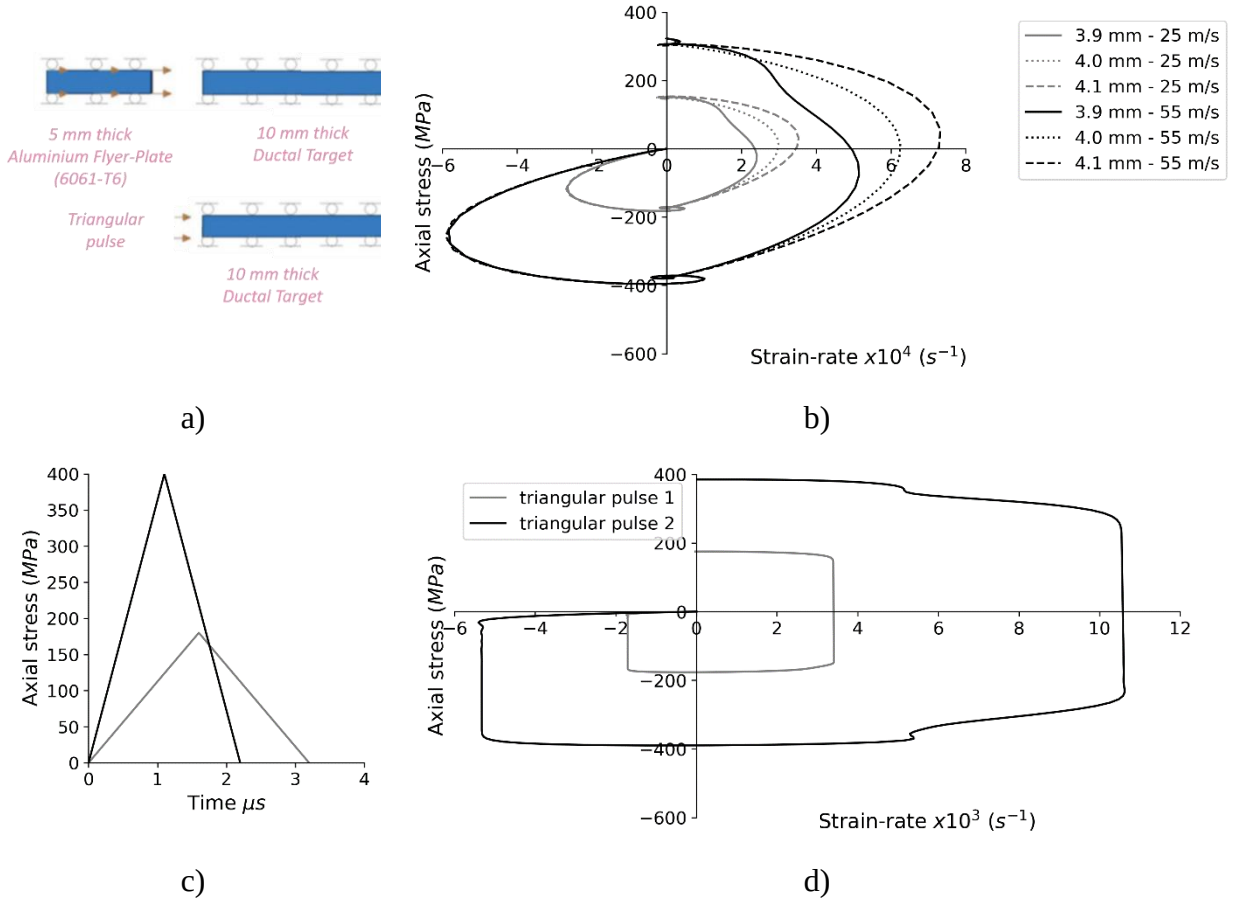

Fig 5.2 - 1-D strain calculations of plate-impact: a) Scheme of configurations, b) Axial stress Vs strain rate at the spalled plane for the classical configuration, c) Ideal incident waves, d) Axial stress Vs strain rate generated by triangular waves

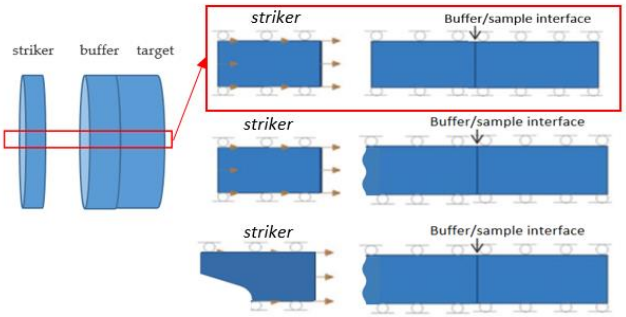

Fig 5.3 - Description of the three configurations: a) classical striker and buffer; b) classical striker and "wavy" buffer; c) "toothed" striker and "wavy" buffer

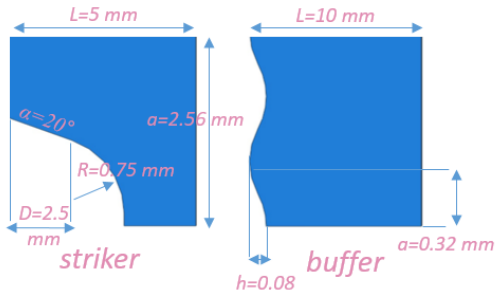

Fig 5.4 - Dimensions adopted in the 2-D strain calculations for the tooth of the striker and the wave of the buffer

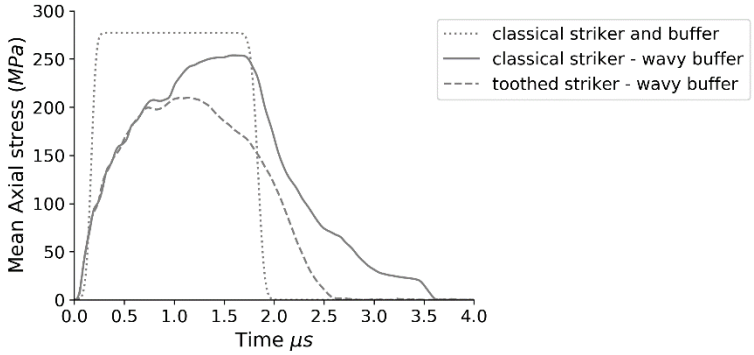

Fig 5.5 - Mean axial stress versus time at the buffer/sample interface for the three configurations obtained by 2D simulations considering the tooth half period and the initial striker velocity of 40 m/s

impact technique. The strain rate generated is then related to the slop of the edges of the triangular pulse.

5.3.2 2D Model

The objective of this section is to design a plate-impact experiment producing a compressive pulse approximating a triangular pulse employing chip-forming machined plates with "toothed" and "wavy" shape surfaces. The proposed testing configuration is composed of a 5-mm-thick Aluminum flyer-plate and a 10-mm-thick ductal plate. A 5-mm-thick aluminum buffer is placed between the impactor and the target to homogenize the stress field along the vertical (transverse) direction. The calculations are made considering a single half-period of the tooth of the flyer plate (**Fig. 5.3-4**). The normal displacement is set to zero on the top and bottom surfaces to model the corresponding symmetry planes. A frictionless surface-to-surface contact algorithm was used to describe the contact between each component of the systems. An initial axial velocity of 40 m/s was set for the strikers, whereas the buffer and the target are initially in

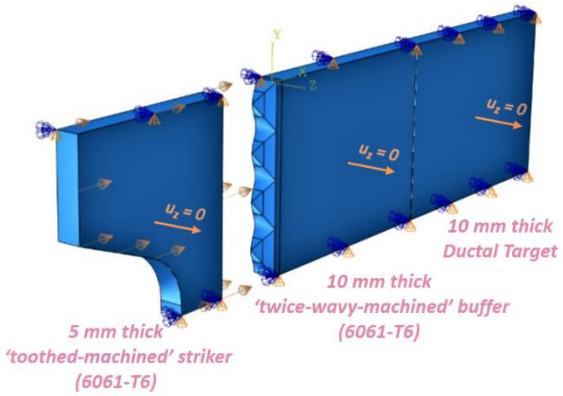

Fig 5.6 a - Scheme of the 3D simulation considering the tooth half period in the vertical direction and the wave half period in the transversal one

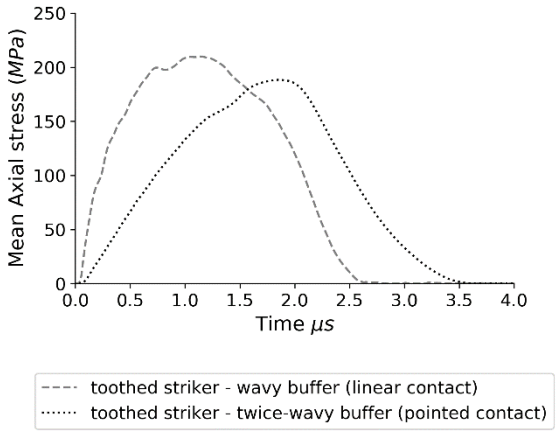

Fig 5.6 b - Mean axial stress versus time at the buffer/sample interface

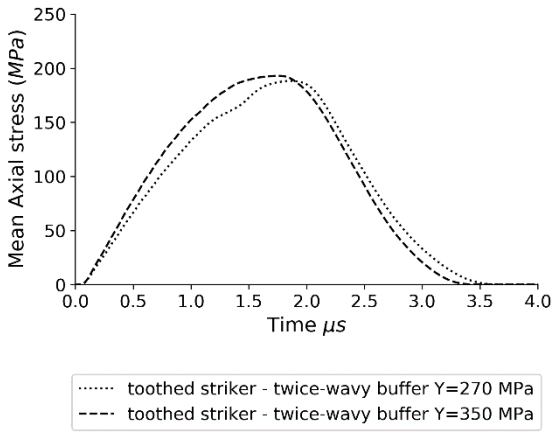

Fig 5.7 a – Effect of aluminum yield strength

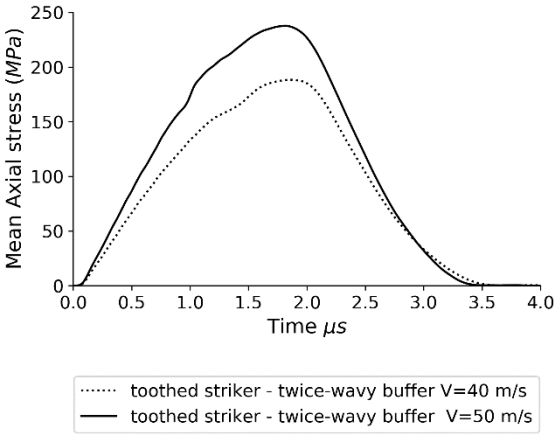

Fig 5.7 b – Effect of the impact velocity

contact. **Fig. 5.5** provides the mean axial stress (axial force divided by the vertical cross-section) versus time at the buffer/sample interface for three different configurations: classical striker and buffer; classical striker and "wavy" buffer; and "toothed" striker and "wavy" buffer. It is shown that the "wavy-shape" of the impacted surface of the buffer provides smooth rising and descending edges, whereas the "toothed-shape" of the rear surface of the flyer plate provides a smoother descending edge and does not affect at all the rising edge.

5.3.3 3D Model

In the following testing configuration, a “toothed” striker, a “twice-wavy” buffer (machined plate along with two orthogonal directions) and a Ductal® target were considered. Numerical simulations were conducted with Abaqus/Explicit FE code and a 3D model made of C3D8R elements (eight-node hexahedral reduced integration elements). The out-of-plane displacement is set to zero on all the nodes of the top and lateral surfaces (**Fig. 5.6a**). The compression pulse at the buffer/sample interface for an impact velocity of 40 m/s is plotted in **Fig. 5.6b**, and it is compared with the pulse obtained by a “once-wavy” buffer. It is shown that a pointed contact between striker and buffer generates rising and descending edge less bent compared to a linear contact. **Fig. 5.7a** demonstrated that a possible variability of the 6061-T6 aluminum yield strength would have a marginal effect on the pulse shaping. Moreover, **Fig. 5.7b** shows that the impact velocity affects not only the maximum axial stress, as in a traditional impact configuration, but it also affects the slope of the rising edge, which means that an ideal velocity can be assigned to the designed pulse shaping system to generate an approximated isosceles triangular pulse.

5.3.4 Final test configurations

The final configurations selected for impact testing are presented in this section. The diameter of striker, buffer and target is set to 70 mm. The combination “toothed” striker -“twice-wavy” buffer is maintained to generate a compressive pulse approaching a triangular shape. Two configurations are designed with two different striker velocities employing striker and buffer of different dimensions in view of generating different tensile strain-rate in the target. The configurations are titled Conf. 1 and Conf. 2. The main details are reported in **Table 5.3**. The compressive pulse transferred to the target for the two configurations is presented in **Fig. 5.8.** The pulses are extracted in 3D calculations considering the full radius of the striker, buffer, and target. For Conf 1, the pulse is compared with the one obtained with the 3D reduced model of the previous section. Note that stresses are averaged over the same area, and identical mesh sizes are used in the calculations. The effect of using a reduced model is considered insignificant.

For Conf. 1 and Conf. 2, the duration of the pulse is respectively 2.5 and 3.5 μs. The ratio between the maximum axial stress reached in the two configurations is 1/2 for the proposed impact velocities. **Fig. 5.9** shows the axial stresses for the two configurations as a function of the strain rates in the spalled section. During the development of the tensile stress (0-100 MPa)

Configuration	Striker velocity m/s	Dimension mm	"toothed" striker	"twice-wavy" buffer	target
Conf 1	40	thickness (*L*)	5	12	10
		half period (*a*)	2.56	0.32	-
		depth (D tooth) (h wave)	2.76	0.08	-
Conf 2	80	thickness (*L*)	3.5	10	10
		half period (*a*)	1.92	0.32	-
		depth (D tooth) (h wave)	2.26	0.08	-

Table 5.3 – Details of the two final test configurations. The notation *L*, *a*, *D* and *h* refer to the sketch of Fig 5.4

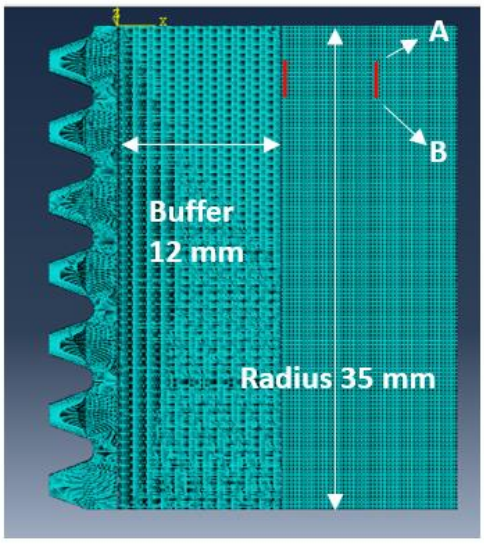

Fig 5.8a – 3D model considering the full plate radius in the vertical direction

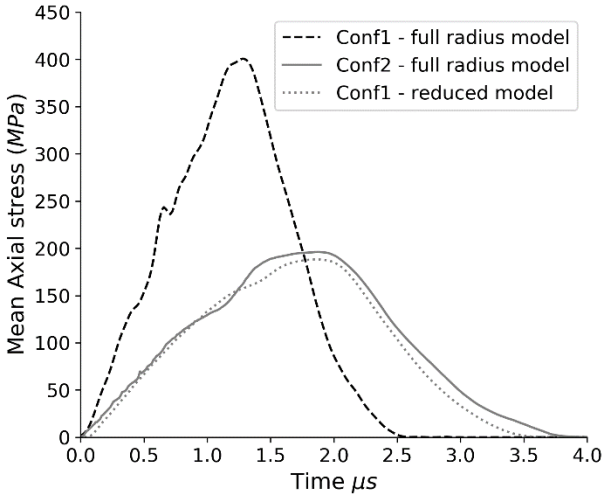

Fig 5.8b – Evolution of the mean axial stress in the target near the buffer/sample interface for the two designed configurations: stresses are averaged over the same area as the reduced 3D model

the strain rates are respectively $4x10^3$ and $12x10^3$ s^{-1} (ratio 1/3) for both configurations. For Conf. 1, the figure contains the plot for two different locations referred at the points A and B located at the beginning and end of the half period of the tooth. It is demonstrated that the stress and strain fields in the target are homogeneous along the vertical direction, so the buffer is thick enough compared to the period of the tooth shape.

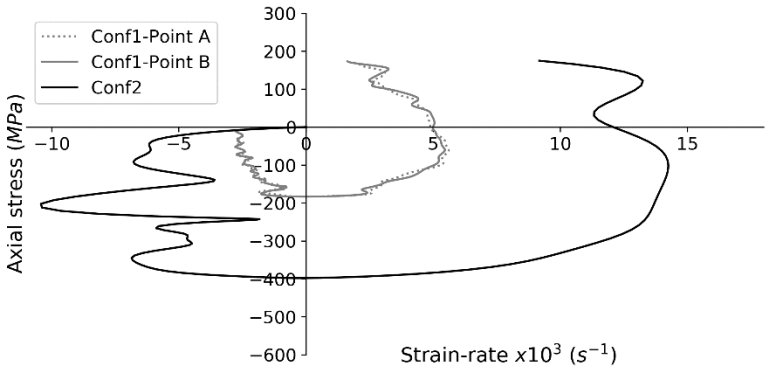

Fig 5.9 – Axial stress Vs. strain rate at the spalled plane for the two design configurations

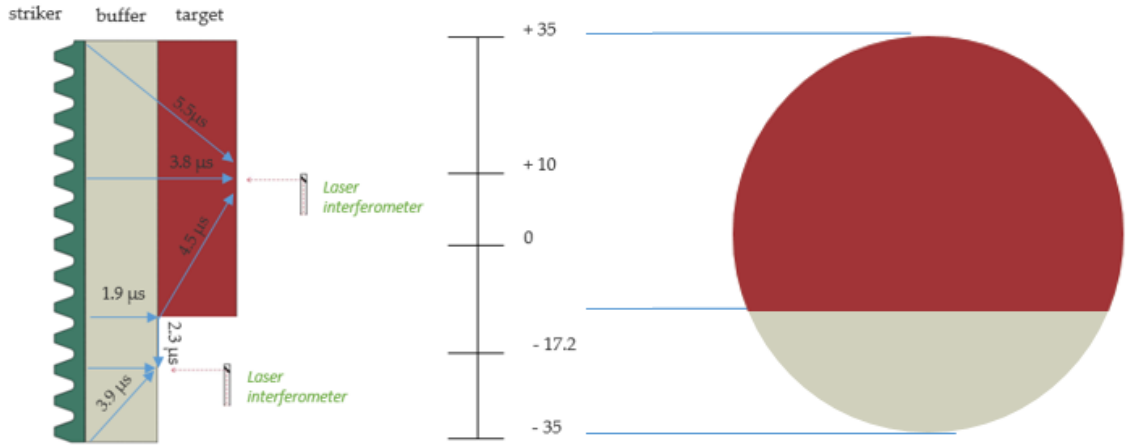

Fig 5.10 – Experimental set-up with two laser interferometers

5.4 Experiments

The spalling experiments through plate-impact have been carried out on samples without fibre reinforcement of Ductal® A and Ductal® B. The specimens were obtained by cutting a cylindrical core 70 mm in diameter drilled from large concrete blocks. They were rectified by a turning machine enclosed in a protective aluminum ring. This leads to a parallelism between the faces of ±0.025 mm. A milling machine with Computer Numerical Control (CNC) manufactured the patterns of strikers and buffers. The cutter tool (hemispherical-end mil) passed over the surfaces milling along the paths specified by a Stereo Lithography file (.STL). The maximum imposed scallop height (i.e., the size of the ridge formed by the residual material between two successive courses of the tool) was 0.005 mm.

During the impact test, the particle velocity at one point of the rear surface of both target and buffer were measured simultaneously by two laser interferometers. That is why the concrete plates were cut at 45 mm in one transversal direction, as presented in **Fig. 5.10**. The laser spots

were located at +10 mm and -17.2 mm from the center of the circle to ensure 1D strain condition throughout the time required for the measurement. The optimal spot locations were selected considering the arrival times of the longitudinal waves and the waves originating from the lateral boundaries. Aluminum was sprayed on the rear face of the concrete specimen to increase the laser reflection. Note that the buffer and the specimen are glued together with a low viscosity epoxy (AY103-1 Araldite combined with HY951 hardener), which needs the assembly to be oven-dried at 45 °C for 24 hours. So, the residual water in the concrete specimen could be considered expended.

5.4.1 Plate-impact facility

Experiments are carried out on the single-stage gas gun installed in the 3SR laboratory and designed by THIOT Ingénierie (Puybrun, France). The facility has three interconnected parts: a gas reservoir or breech, a gun tube or barrel, and a target chamber. The principle is that the gas, initially stored at high pressure in the reservoir, is suddenly released, so it acts on the rear face of the projectile enclosed inside the barrel. The gas pressure difference on both sides of the projectile causes its acceleration along the barrel until emerging into the target chamber.

The reservoir holds light gas, such as helium and nitrogen, at pressures until 400 bars. The facility, with a 6 m long gun barrel and interchangeable calibers (D25, D80, D100, D120 mm), is capable of projectile velocities from a few tens of meters per second to 1000 m/s. The air in the target chamber and gun barrel is evacuated prior to the test using a vacuum pump to a pressure of approximately 15 mbar; this prevents the formation of an air cushion between target and striker at impact. The velocity of the striker is determined from the transit time between two pins at the exit of the gun barrel 30 mm distant from each other.

The 80 mm diameter barrel was used for the experimental campaign. The reservoir was filled with nitrogen at 6 bars. The projectile was carried in the gas gun in a plastic sabot (polycarbonate) and located approximately 4 m away from the reservoir to reach moderate velocity in the range of 40 to 90 m/s (**Fig. 4.11b**). The striker's velocity at the impact is affected by the total mass of the striker + sabot, the pressure of reservoir and target chamber, its initial location in the barrel, and the friction between the sabot and the barrel tube.

5.4.2 Additional devices

The target chamber was equipped with a special mounting system (**Fig. 5.11**). The holder (which has a machined cavity in the center) carries the target backed by a foam material to achieve wave release. The target is optically aligned to the gun barrel using a collimated laser

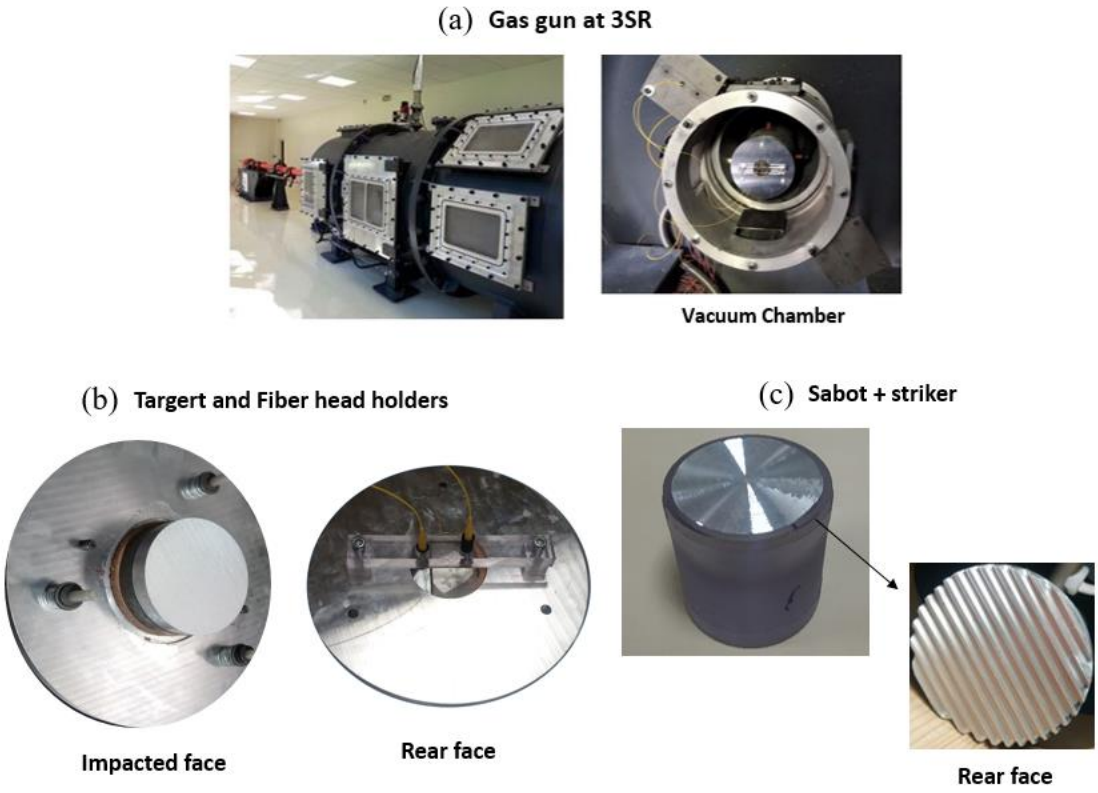

Fig 5.11 – Experimental devices: a) single-stage gus gun b) target and fiber holders with alignment screws c) sabot of polycarbonate

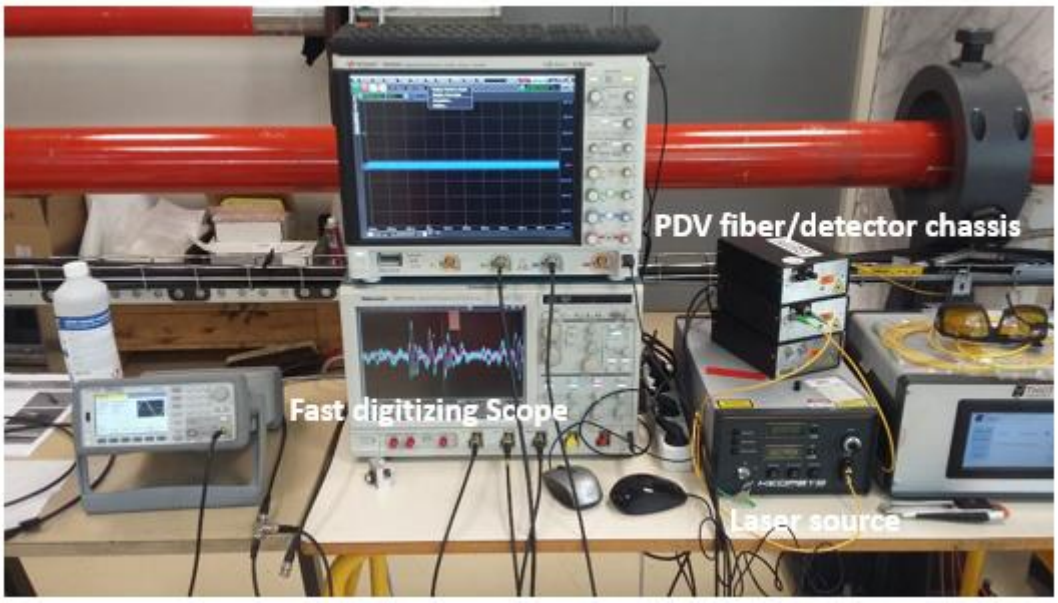

Fig 5.12 – Installation of the Heterodyne PDV system, using 1550 nm laser source, 2-channel PDV optic/detector box, and fast digitizing scope

beam to eliminate relative tilt at the instant of impact. The position of the laser beam, reflected from the front surface of the target plate, is monitored on a stationary screen roughly 8 m away.

The screws on the target holder are employed to drive the target at the normal angle. A maximum angular misalignment of 1 mrad was tolerated.

A Heterodyne Photon Doppler Velocimetry (Heterodyne - PDV) system was set up to measure the particle velocity on the target rear face (**Fig. 5.12**). The system uses a 1550 nm light source to illuminate the target and buffer rear surfaces using optical fibers. The reflected light frequency is changed slightly by the Doppler's effect when the surface is moving. The system uses the same optical fiber for both transmit and receive signals. The optic fibers are fixed on the ad-hoc support made of polycarbonate. The reflected light is sent to the PDV optic/detector box, producing two-channel output 90° out of phase. The box contains all the splitters, circulators, and power meters used in a PDV system. Two digital scopes record the interferometer traces with a sampling rate of 2.5 Giga samples per second.

5.4.3 Surface Velocity Measurements

Two main methods exist to process the interferometer traces. The first one is based on the fact that the particle velocity of the pointed surface is directly proportional to the Doppler frequency of the recorded signals. The method is named Sliding Fast Fourier Transform (SFFT) analysis and uses a window of adaptive size to extract the frequencies of the traces (one-channel output is sufficient for the analysis). The second one is based on the fact that the displacement of the pointed surface is proportional to the phase angle between the two 90° out of phase signals. It is named Quadrature analysis and calculates the velocity with a numerical derivative of the phase angle measured through Lissajous curves.

The post-processing of the signals was made here through the application WAVE (WAves data processing for photonic doppler VElocimetry) developed by CEA DAM Gramat, DEA, STEX and LRME. The equations already implemented in the code are detailed in **Appendix 4**. Although the quadrature analysis requires more steps to obtain the velocity from the row data (the phase angle is measured over signal sub-sections), it was observed that the two methods give practically complementary velocity profiles. An example is given in the following**.** The SFFT method is applied for the row signal CH1 in **Fig. 5.13a**, whereas the row signals CH1 and CH2 (90° out of phase signals) are analyzed with the quadrature method. The velocities profiles in **Fig. 5.13b**, obtained with the SFFT and the quadrature methods, diverge only in the range between 0 and 5 m/s. The SFFT method failed exclusively for low velocities due to the low-frequency noise of the signal. That is why, for the whole processing of the data of the experimental campaign, the SFFT method was preferred, whereases the quadrature method was mainly applied to derive the beginning and end slope of the experimental pluses.

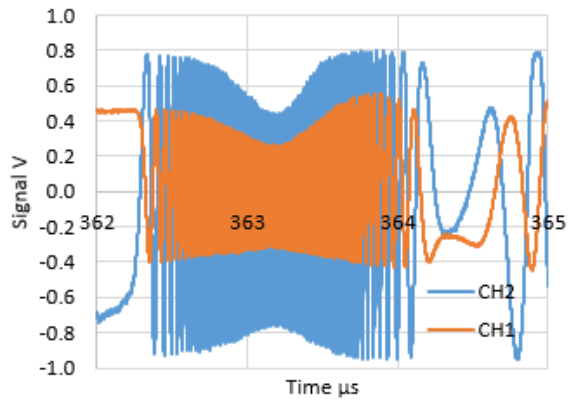

Fig 5.13 – Row two-channel output signals raw for experimental data. First motion occurs at t = 362.2 µs

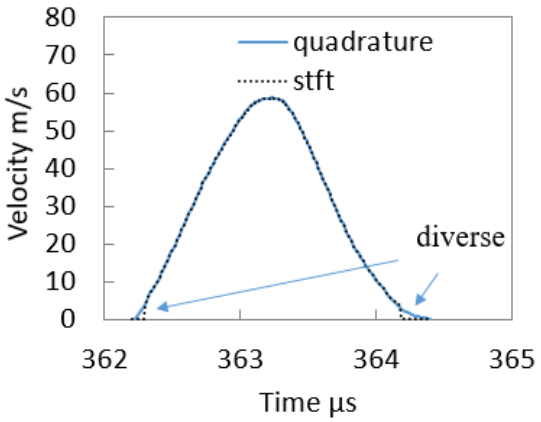

Fig 5.14 – Direct comparison of quadrature (solid black line) and SFFT (dash blu line) methods for experimental data.

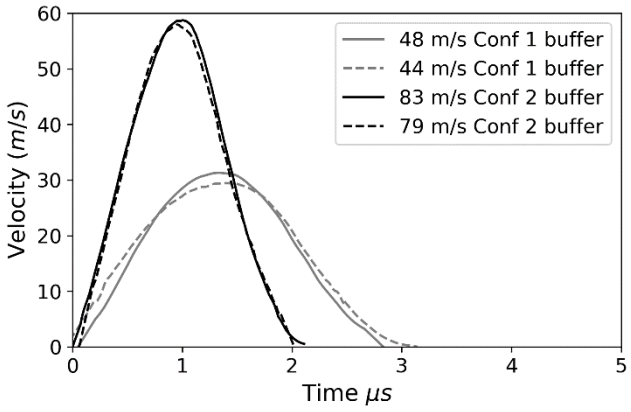

Fig 5.15 – Measured particle velocities at the buffer rear surface

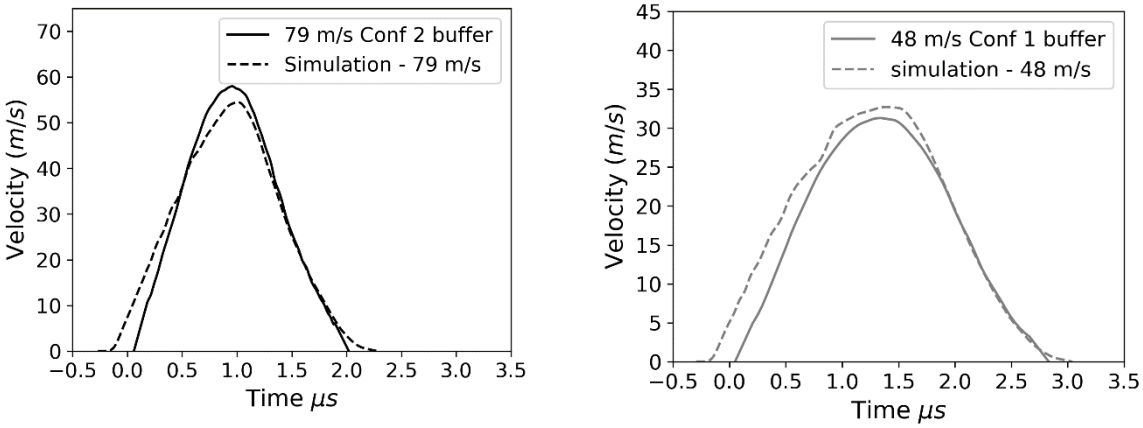

Fig 5.16 – Comparison of particle velocities at the buffer rear surface: measurements versus numerical simulation (maximum velocity difference +3.49 m/s and -1.5 m/s)

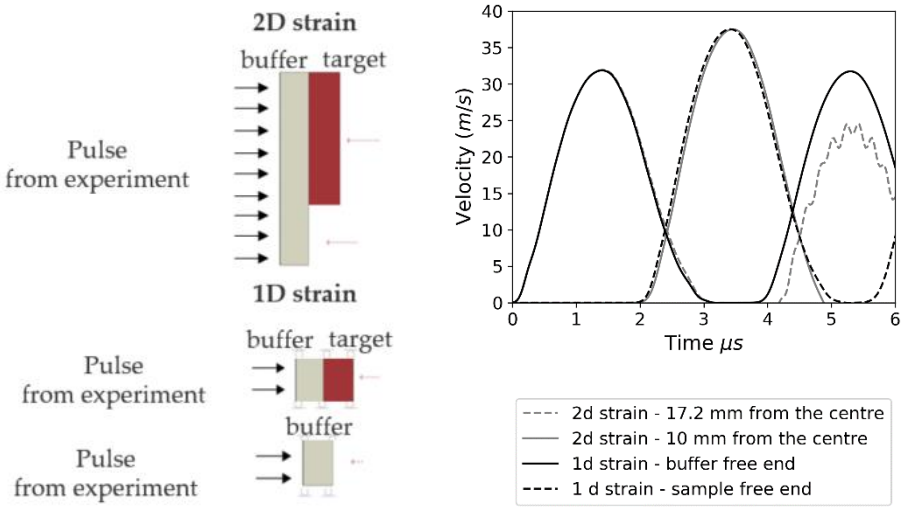

Fig 5.17 – Comparison of numerical particle velocities at the buffer and target rear surface: 1D calculation versus 2D calculation

5.4.4 Pulse-shaping validation

The measured particle velocities at the rear surface of the buffer for Conf. 1 and Conf. 2 are reported in **Fig. 5.15**. It is worthy to note that the same pulse is obtained with two tests performed at almost the same striker velocity, which validates the method reproducibility. Moreover, the comparison between the experimental particle velocities and the ones predicted by the numerical calculation is shown in **Fig. 5.16**. It has been demonstrated that assuming a simple elastoplastic behavior with strain-rate independent parameters for the aluminum striker and buffer is realistic and sufficient for a preliminary design.

Another important factor in the design of the experimental configuration is to ensure one-dimensional motion throughout the time period required for the measurements. In **Fig. 5.17**, the experimental pulse is used to numerically simulate in 2D the effect of the waves generated at the boundaries. The velocity profiles for the rear surface of the buffer and the target at the location of the laser spots are extracted from the 2D simulation. Then a 1D calculation is used to verify that the velocity profiles have not been modified compared to 2D simulation.

5.4.5 Test analysis

Plate impact tests have been performed with both pulse shaping systems: six tests on Ductal® A (3 Conf1 + 3 Conf2), and four tests on Ductal® B (2 Conf1 + 2 Conf2). The experimental striker velocities are given in **Table 5.4**. Note that they differ from the striker velocities set in the design stage in section **5.3.4** for Conf1 and Conf2 (respectively 40 and 80 m/s). This did not

Sample	Configuration	Impact velocity m/s	N° laser interferometer
A0	**flat striker**	**51 m/s**	1*
A2	**conf1**	**48 m/s**	2
A5	**conf1**	**68 m/s**	2
A3	**conf1**	**99 m/s**	2
A1	**conf2**	**57 m/s**	1*
A4	**conf2**	**79 m/s**	2
A6	**conf2**	**85 m/s**	2
B2	**conf1**	**48 m/s**	2
B5	**conf1**	**44 m/s**	2
B1	**conf2**	**57 m/s**	1*
B3	**conf2**	**83 m/s**	2

Table 5.4 – Test information: sample ID, striker-buffer configuration, measured impact velocity, number of laser interferometers. *target rear face

preclude the test processing. In the same table, the number of recorded signals at the free surface is reported. The particle velocities are shown in **Appendix A5.** One should be aware, however, that the accuracy of the processing methods introduced in section **5.4.3** may depend on the quality of the acquired signals that vary between the test.

5.4.5.1 Quality indicator

According to the elastic wave propagation theory, in the case of a change of sonic impedance, assuming that the contact is perfect between the buffer and the specimen, the ratio between the incident and the transmitted particle velocities at the buffer/sample interface read:

$$\frac{V_t}{V_i} = \frac{2\rho_b C_{Lb}}{\rho_b C_{Lb} + \rho_T C_{LT}} \quad (5.1)$$

$\rho_b C_{Lb}$ and $\rho_T C_{LT}$ are respectively the sonic impedances of buffer and target. The theoretical value of the longitudinal wave speeds C_{Lb} and C_{LT} can be expressed as function of the density ρ, the poisson ratio v, and the Young's modulus E, such as:

$$C_L = \sqrt{\frac{(1-v)}{(1+v)(1-2v)} * \frac{E}{\rho}} \quad (5.2)$$

The parameters of Ductal® A and B, in **Table 5.1**, and the parameter of the buffer, in **Table 5.2**, has been used to estimate a theoretical value of the ratio V_t/V_i equal respectively to 1.166 for

concrete A and 1.167 for concrete B. An experimental value for the ratio V_t/V_i is calculated for each test as the ratio between the maximum particle velocity measured at the rear face of the concrete target and the maximum particle velocity measured at the rear face of the buffer. The experimental ratios are given in **Table 5.5.** For most of the tests, the experimental ratio is between the range of 0.98-1.18. The fact that the experimental ratios approach the theoretical value is a positive test quality indicator. For the two tests, A3-conf1 and A6-conf2, strongly low particle velocity has been measured at the target rear surface compared to the buffer rear surface. It was concluded that this was due to damage in compression before loading the sample in tension, so these tests were excluded for the estimation of the spalling strength. For the test A1-conf2 and B1-conf2, the particle velocity on the buffer rear face was not measured, so the ratio is estimated replacing the maximum particle velocity with the value predicted by a numerical calculation of the test. The 3D reduced model of the buffer and striker geometry of Conf2 was used (V = 57 m/s).

5.4.5.2 The longitudinal wave speed and spall strength

Eq. 5.2 gives C_L equal to 4905 m/s for concrete A and 4814 m/s for concrete B. An experimental longitudinal wave speed ${C_L}^{exp}$ was calculated from the difference in time between the arrivals of the incident waves at the rear surfaces of buffer and target. Therefore the value is averaged over the specimen length. The values are given in **Table 5.6.** Unfortunately, it was impossible to assign an experimental value for the test A2-conf1 and B2-conf1 due to an error in the recording system of the signals, so only two measures for concrete composition are available. The mean values are equal to 4889 m/s for concrete A and 4708 m/s for concrete B (difference of ≈3%). The acoustic approximation of Novikov gives the sample spall strength assuming an elastic behavior prior failure (Novikov et al., 1966):

$$\sigma_{spall} = \frac{1}{2}\rho C_L V_{pb} \quad (5.3)$$

The density ρ is determined before testing by measuring the mass and the dimensions of each concrete target. The longitudinal wave speed C_L is calculated according to **Eq. 5.2**. The pull-back velocity V_{pb} is determined as the difference between the maximum particle velocity and the rebound velocity. The resulting spalling strength is given in **Table 5.6**. The results are in the order of 80 MPa. For A5-conf1 and B3-conf2, using ${C_L}^{exp}$ in the estimation of the strength lead to a lower value of 6% (≈4 MPa).

Sample	Max particle velocity buffer m/s	Max particle velocity target m/s	$\frac{V_t}{V_i}$
A-flat striker 51 m/s	-	56.19	-
A2-conf1 48 m/s	31.29	36.9	1.18
A5-conf1 68 m/s	48.86	51.41	1.05
A3-conf1 99 m/s	84.19	61.86	0.73
A1-conf2 57 m/s	-	41.31	1.19*
A4-conf2 79 m/s	58.65	60.83	1.04
A6-conf1 85 m/s	59.13	18.74	0.32
B2-conf1 48 m/s	26.28	25.68	0.98
B5-conf1 44 m/s	29.42	31.05	1.06
B1-conf2 57 m/s	-	34.91	1.00*
B3-conf2 83 m/s	58.71	67.64	1.15

Table 5.5 – Maximum particle velocity measured at the rear face of buffer and target and the experimental ratio between the incident and the transmitted particle velocities at the buffer/sample interface. *particle velocity at the rear face of buffer derived by numerical calculation

5.4.5.3 The strain rate estimation and sensitivity

Thanks to the experimental configuration with two laser measurements, the loading rate can be determined at any time at any point in the following way. The strain-rate has been evaluated numerically (1-D strain calculations in Abaqus/Explicit of the target which front face is loaded with the experimental compressive pulse), assuming a purely elastic behavior of the specimen before the spall, and considering the section reaching first the measured spall strength.

The minimum and maximum values of strain-rate in the target during the tensile phase in the numerical calculation are given in **Table 5.6**. The strain rate sensitivity of Ductal® A and Ductal® B is summarized in **Fig 5.18**. The two test configurations allowed obtaining data for strain-rates ranging from 3.5×10^3 s^{-1} to 1.5×10^4 s^{-1}. It is difficult to deduce if there is a real strength enrichment with increasing the strain rate in the tested range. It is sure that it has been measured failure stresses higher of factor 2 than the ones in spalling at the Hopkinson bar (50-250 s^{-1}) and factor 7 compared to those in a quasi-static direct tension test (10^{-5} s^{-1}).

Sample	Density (kg/m3)	Wave speed (m/s)	Pull back velocity (m/s)	Dynamic tensile strength (MPa)	Strain rate (1/s) min-max
A-flat striker 51 m/s	2407	-	13.01	77.01	≈10000[1]
A2-conf1 48 m/s	2399	nan	11.86	70.09	7272-7656
A5-conf1 68 m/s	2400	4646	13.01	76.90	7232-7807
A1-conf2 57 m/s	2398	-	11.20	66.18	8616-9649*
A4-conf2 79 m/s	2423	5133	14.19	84.28	14818-15633
B2-conf1 48 m/s	2422	nan	10.48	61.55	3124-3930
B5-conf1 44 m/s	2440	4795	12.86	75.81	4296-5325
B1-conf2 57 m/s	2472	-	13.96	82.83	5942-7143*
B3-conf2 83 m/s	2436	4622	14.84	87.41	15615-16944

Table 5.6 – Dynamic tensile strength by Novikov formula and strain rates by numerical simulations. [1] strain rate estimated by formula [*]incident pulse estimated by numerical calculation

5.4.5.4 The standard plate-impact test

In addition, a standard plate-impact test was performed with a flat aluminum flyer plate 5-mm-thick and a target 10-mm-thick made of Ductal® A. The Aluminum plate impacted the target's front surface at the velocity of V = 51 m/s. This time, the transmitted particle velocity reads:

$$V_t = \frac{\rho_s C_{Ls}}{\rho_s C_{Ls} + \rho_t C_{Lt}} V \quad (5.4)$$

where $\rho_s C_{Ls}$ and $\rho_T C_{LT}$ are the sonic impedances of impactor and target, respectively. **Eq. 5.2,** using once again the parameters of Ductal® A in **Table 5.1** and the parameters of the aluminum in **Table 5.2**, leads to a theoretical value of V_t equal to 29.73 m/s. Consequently, the expected maximal particle velocity at the rear face of the target is 59.47 m/s (2*V_t). The particle velocity at the rear face of the target was derived from the interferometric signal. The maximal velocity measured in the target was 56.19 m/s compared to the 59.47 m/s given by the theoretical formula; this is a positive test quality indicator.

Eq. 5.3 gives a spalling strength of 77.01 MPa. This time the strain rate history is unknown, and a formula that provides an approximated value has been reprised from literature as in (Neel, 2018). It reads:

$$\dot{\varepsilon} = V_{pb} / C_L \Delta t \quad (5.5)$$

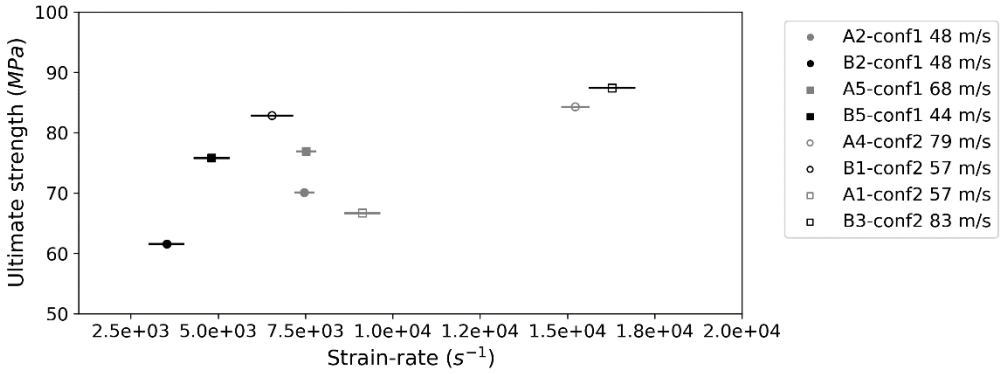

Fig 5.18 — Strain rate sensitivity of spall strength Ductal® B and Ductal® A. The horizontal intervals correspond to the minimum and maximum values of strain-rate obtained by numerical simulation assuming an elastic behavior prior failure

where Δt is the time between the maximum particle velocity and the rebound velocity. The formula gives an average strain rate during the development of tensile stresses in the target, assuming a compressive pulse with symmetric edges. **Eq. 5.5** gives for the standard plate-impact a strain rate of 10^4 s^{-1}.

5.4.6 Numerical simulation with DFH model

Numerical simulations of four experiments were conducted with Abaqus/Explicit FE code (B3-conf2 83 m/s, A4-conf2 79 m/s, B5-conf1 44 m/s, A2-conf1 48 m/s). In these calculations, only the central part of the target in 1D strain condition is considered. The calculation is made with a 3D mesh discretizing a parallelepiped having the same length as the specimen and section 20x20 mm^2. The finite elements have a size of 0.2 mm (**Fig 5.20**). The normal displacement is set to zero on the lateral surfaces, and the front face is loaded with the experimental compression pulse. The experimental pulse has the same shape as the velocity profile measured at the buffer rear surface. The maximum pulse stress is derived by the maximum particle velocity measured at the rear face of the target. In detail, an adimensional experimental pulse is obtained by dividing the complete velocity profile at the buffer rear face with its maximum. Then, the maximum pulse stress is calculated as $\sigma_{max} = \frac{1}{2}\rho C_L V_{max}$.

The DFH model is used to simulate the behavior of Ductal® A and B. The parameters for the two concrete without fibre reinforcement are shown in **Table 5.7.** The parameters take into account the strength enrichment at low strain rate (range 5x10^{-6} s^{-1} to 5 s^{-1}). **Fig 5.19** presents the comparison between the experimental free-end velocity profiles and the numerically obtained velocities. A good correlation between experimental and numerical velocities is observed. Specimens are not recovered post-testing, so the simulation is used to verify that the

Ductal		A	B
Elastic parameters	$E(\mathrm{GPa}), v$	52.41, 0.2	51.27, 0.2
Cracks propagation parameters	S, k	3.74,0.38	
Quasi-static increase factor	n^{qs} , $\dot{\varepsilon}_0$ (s^{-1})	0.03, $5\mathrm{x}10^{-6}$	
Cracks initiation parameters	$\mathrm{V}_{eff}(\mathrm{mm3})$, $\sigma_w(\mathrm{MPa})$, m	64, 18.90 ($\dot{\varepsilon}$ =5x10^{-6} s^{-1}), 10.4	98, 19.42 ($\dot{\varepsilon}$ =5x10^{-6} s^{-1}), 8.9

Table 5.7 - Parameters of the DFH model for A and B concretes.

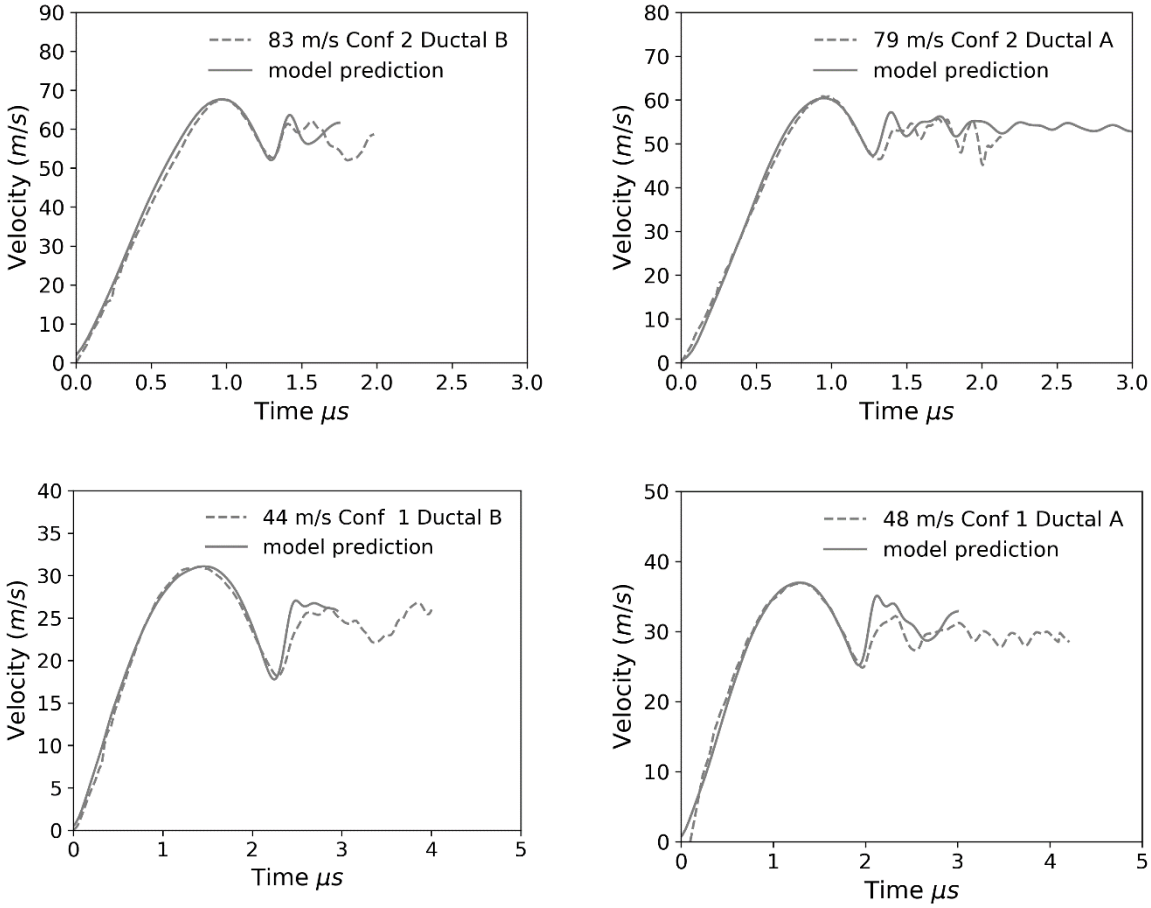

Fig 5.19 – Experimental particle velocities and numerical results

	Specimen length (mm)	Section strain-rate (mm)	Section damage (mm)
A2-conf1 48 m/s	9.79	3.9	4
A4-conf2 79 m/s	10.37	2.6	1.45
B5-conf1 44 m/s	9.59	4.5	4.2
B3-conf2 83 m/s	10.40	2.1	2.2

Table 5.8 – Distance from the free end of the specimen.

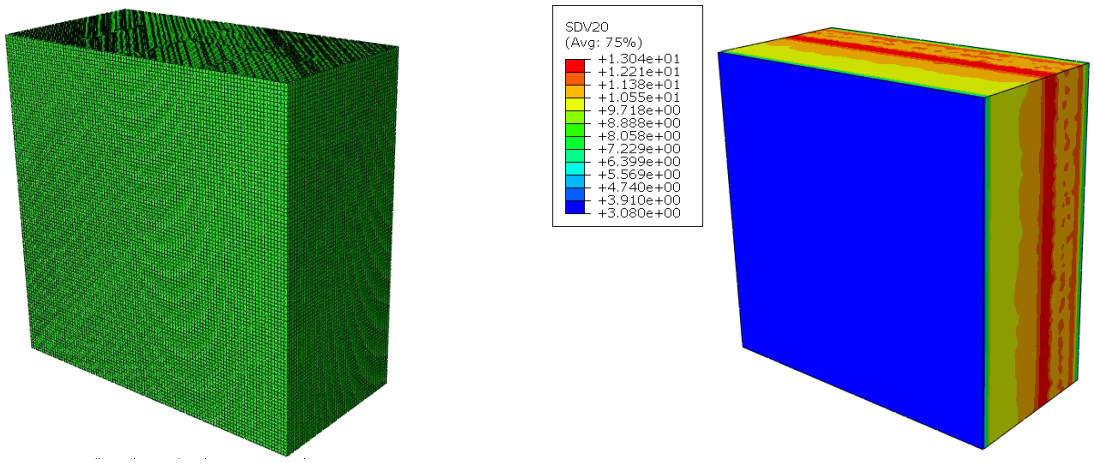

Fig 5.20 - A4-conf2 79 m/s –mesh and Log of crack density

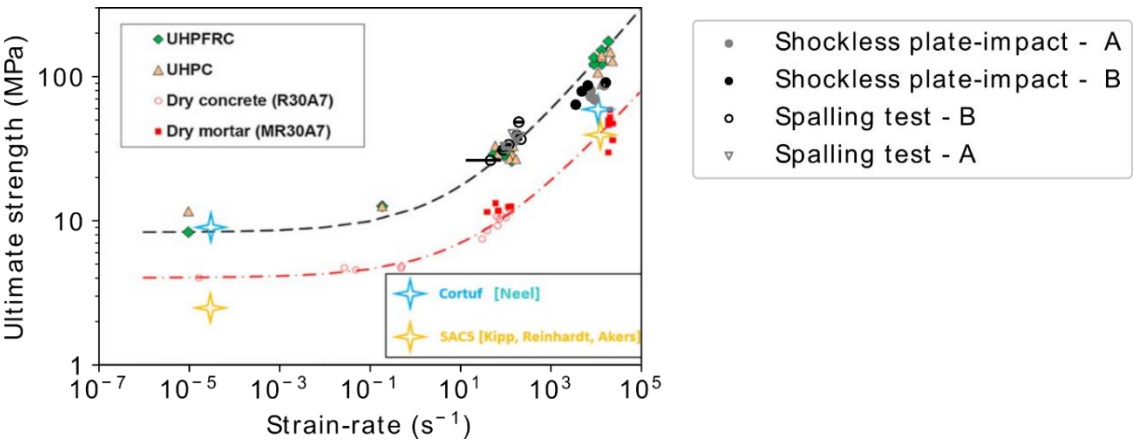

Fig 5.21 – Comparison with traditional plate impact on concrete and UHPC by (Neel, 2018b) ; Comparison with Shockless plate impact concrete and mortar by (Erzar et al., 2013), UHPC and UHPFRC by (Pontiroli et al., 2016)

location of the damage initiation corresponds with the section used to compute the strain rate in the elastic calculation in section **5.4.5.3**. The distances from the free-end are compared in **Table 5.8.** The two methods predict the spalling plane at an equivalent location.

Moreover, the logarithmic of the predicted crack density is shown in **Fig 5.20** and corresponds to density in the order of 10^{12} cracks per m^3.

5.5 Comparison with literature

The experimental results of both spalling and plate impact tests obtained in this study are compared with the experimental results in literature commented in Chapter 2 in this section. **Fig. 5.21**. by (Neel, 2018b) was already commented in section **2.2.3.5**. In addition, it is observed a perfect match in the spall results at the Hopkinson bar with the data reported in (Pontiroli et al., 2016). Instead, the plate impact tests with pulse shaping are light below the trend obtained with the GEPI generator.

5.6 Synthesis and conclusion

This chapter has presented a plate-impact test. It has been prepared using 1D, 2D and 3D numerical models. Simple 1-D calculations underline that classical plate impact test configuration is not adapted to discuss the strain-rate effect on spall strength. Then, a new plate-impact testing technique based on machined flyer-plate combined with a buffer was developed. The 2D calculations pointed out that the "wavy-shape" of the buffer provides a smooth rising-edge of the pulse whereas the "toothed-shape" of the rear surface of the striker provides a smooth descending-edge of the pulse. The 3D calculations allowed the design of a test configuration, "toothed" striker - "twice-wavy" buffer – flat sample, to investigate the spall strength at the wanted order of strain rate. Test configuration with two laser interferometers has given access to the shape and intensity of the incident loading pulse without any effect of the boundary.

First experimental results validate the pulse shaping system; the experimental pulses were reproductive and match the numerical design. The technique was used to investigate the tensile behavior of the two concrete materials without fibre reinforcement at very high strain-rates. The spalling strength of the order of 75 MPa has been estimated for both concrete formulations and numerical calculations allow estimating strain-rates in the range from 3.5×10^3 s^{-1} to 1.5×10^4 s^{-1}. The measured tensile strengths are higher than the one observed in spalling at the Hopkinson bar (50-250 s^{-1}), confirming that the gain of resistance with the strain rate continues at a very high strain rate.

The numerical simulation of the plate impact tests with the DFH damage model showed the good capability of the numerical tool to reproduce the experimental velocity profiles. However, the predicted crack density corresponds to thousands of cracks per mm^3 i.e., a crack density in the order of 10^{12} cracks per m^3. Consequently, the activated defects at such elevated strain-rates should be defects distributed at a much smaller scale than the effective volume of quasi-static

bending tests used to calibrate the DFH model parameters (Weibull parameters). Indeed, the effective volume of bending tests is a few tens of mm^3. It is not small enough to be representative of the density of flaws activated in plate-impact simulation.

In Chapter 6, a modelling of the dynamic fragmentation process under dynamic tension is proposed based on X-ray CT (Computed Tomography) observations of the microstructure of UHPC expressed as distribution of pores. In this approach, pores are considered as the defects responsible for crack inception.

CHAPTER 6

Modelling based on X-ray CT analysis

CHAPTER 6

Modelling based on X-ray CT analysis

As mentioned before, in the DFH model, the density of critical defects is described by a power-law function of the applied stress, whose exponent is the Weibull modulus *m*. This chapter aims to overcome the limitation of the DFH model of considering a Weibull distribution of flaws, which restrains the validity of the predicted tensile strength and crack density under dynamic tension to the range of strain rate that agrees with the flaw population activated in quasi-static bending tests. In the framework of the Brittle's CODEX chair project (Forquin et al., 2019)(Forquin et al., 2020), X-ray CT (Computed Tomography) analyses are conducted to investigate the UHPC flaw population and verify if the Weibull law fits the pore distribution. The X-ray CT analysis is applied to the two UHPC materials studied experimentally (Ductal® A and Ductal® B) with and without fibre reinforcement. So, four different flaw populations are initially investigated. These data are then used as an input of modelling based on continuous and discrete approaches.

6.1 X-ray scan

Cylindrical specimens (with and without fibre reinforcement) of different dimensions were scanned using the X-ray source in Laboratoire 3SR. The source operated at 150 kV and 300 μA, and the beam was passed through a 1.0 mm copper filter to reduce the beam hardening. The sample was placed on the stage rotating around the vertical axis to make radiographs of many different angles. Then, the software XAct was used to build the 3D image from the acquired radiographs. The specimen dimensions are given in **Table 6.1.** However, the 3D reconstructions of the specimens have different voxel sizes: 85 μm for specimens 46 mm in diameter and 140 mm in length; 30 μm for specimens 50 mm in diameter and 100 mm in length; and 20 μm for specimens 29 mm in diameter and 38 mm in length. The number of scans made for each studied concrete material and each voxel size is reported in **Table 6.2**.

6.2 Pores distribution investigated through X-ray CT

One cross-section of 600 x 800 pixels from the 3D reconstruction of the cylindrical sample of Ductal® A-2%, 30 μm in voxel size, is shown in **Fig. 6.1a**. Here, the brightness is proportional to the material density, so fibres are white, the concrete matrix appears in grey, whereas pores

Specimen diameter (mm)	Specimen length (mm)	Voxel size (µm)	Cropped volume (mm^3)	Crop dimensions (mm)
46	140	85	84000	25x28x120
50	100	30	84000	30x28x100
29	38	20	14000	20x20x35

Table 6.1 – Specimen dimensions and voxel sizes

Voxel size (µm)	Ductal A	Ductal A-2%	Ductal B	Ductal B-2%
85	3	2	3	2
30	-	1	-	-
20	2	-	2	-

Table 6.2 – Number of specimens scanned

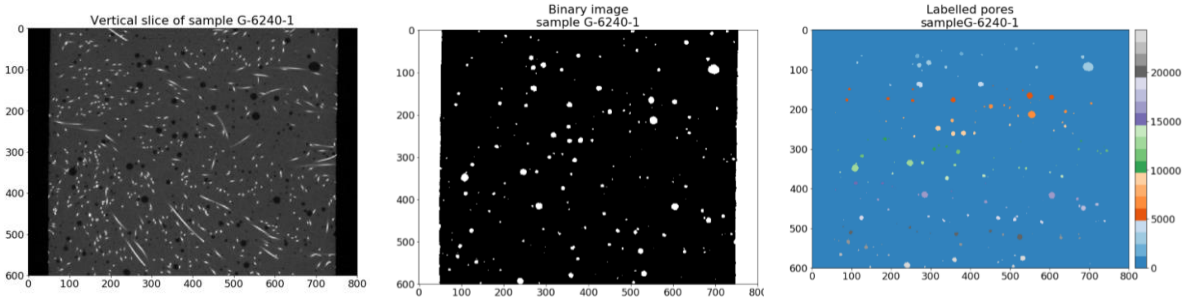

a) b) c)

Fig 6.1 —Section of 600 x 800 pixels from a 3D reconstruction (85 µm.px^{-1}) in grey values, binarized image by thresholding and labeling of porosities

are black. The brightness alone is sufficient to distinguish the pores, the fibres and the concrete matrices unambiguously. Consequently, the 3D image is binarized, fixing a grey level as a threshold (**Fig. 6.2b**). Note that the grey values of all images are normalized before thresholding in such a way that the peak value of pores in the histogram stands at 0.2, and the peak value of the matrix stands at 0.75. So, the same threshold of 0.5 has been used for each reconstruction, even if they have different voxel sizes.The isolated groups of voxels, identified as porosity, are labeled using the multi-dimensional image processing package of python named scipy.ndimage (Weaver, 1985) (**Fig. 6.1c**), whereas the label toolkit of the package SPAM (Software for the Practical Analysis of Materials) (Stamati et al., 2020) is used to evaluate for each pore its volume and the coordinate of the center of mass of the ideal ellipsoids fitting the pore (Ikeda et al. 2000). Noise limits the ability to reliably identify pores smaller than a threshold size (Gualda

and Rivers, 2006; Tammas-Williams et al., 2015). The lower limit of neighboring voxels required to represent a single pore is fixed at 65 pixels. This is ≈ 5 pixels in equivalent diameter Deq i.e., the diameter for a sphere having the same volume; the pores smaller than this limit were eliminated from the analysis.

6.3 Cumulative flaw densities

The cumulative flaw densities of prismatic volumes of different sizes Z cropped out from the 3D reconstruction of the scanned specimens are calculated in the following. The dimensions of the volume crop are given in **Table 6.1**. For each considered volume, pores are classified from the bigger to the smaller equivalent diameter Deq, and the density is calculated as the cumulative number of pores N divided by the volume. Note that the coordinates of the mass centers the ideal ellipsoid fitting the pore as defined in (Ikeda et al. 2000) are used for tracking, so only pores for which centers drop in the volume are taken into account.

Figs. 6.2a-b show the flaw densities as a function of Deq referred to 84 cm^3 cropped out from the 3D reconstruction of the specimens without fibre (three specimens) and with fibre reinforcement (two specimens) with a resolution of 85 μm. Note that the smaller Deq counted up at such resolution is 0.426 mm. Differences between the analyzed specimens are observed comparing each other the flaws densities of the two matrices without fibres, even if the three samples were cored out from the same concrete block (270x270x170 mm^3); moreover, Ductal® B seems to have a population of pores more variable than Ductal® A.

The flaws densities of the two matrices with fibres are reported in the same figures. It is observed that fibres densify the pore population, and the effect seems more pronounced for Ductal A, probably because of the good repeatability of the analyzed specimens.

Summing up the volumes of the same concrete matrix, the flaw densities averaged over 84x3 = 252 cm^3 are obtained for A and B concretes, and the flaw densities averaged over 84x2 = 168 cm^3 are obtained for A and B concretes with fibre reinforcement. As shown in **Fig. 6.2c**, pores density is clearly lower for Ductal® B (with and without fibres). For both the matrices, now it is clear that fibres densify the pore population.

Further analyses were done at a higher resolution to get pores with a size less than 0.426 mm in equivalent diameter. X-ray CTs were conducted with two samples for each concrete matrix without fibres with a resolution of 20 μm, leading to the minimum pore size of 0.1 mm. However, at this resolution, the size of the analyzed volume is only 28 cm^3. The flaw densities are plotted in **Fig. 6.3a.** The matrix B has a reduced number of pores with respect to matrix A

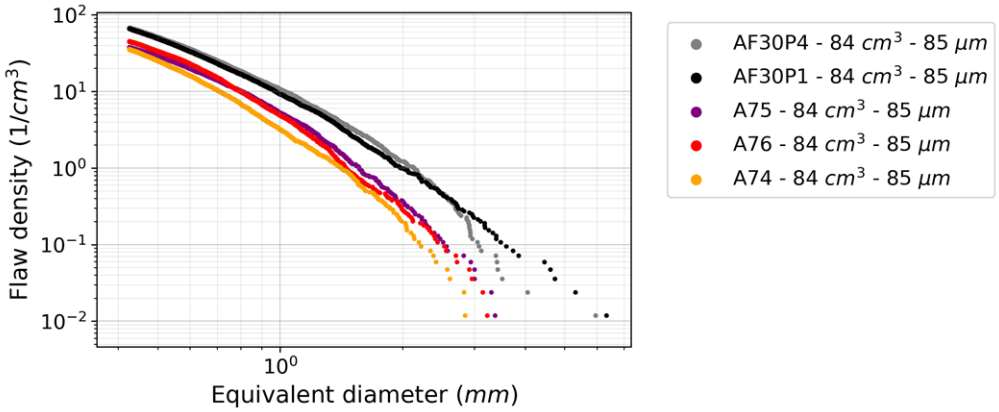

Fig 6.2a —Flaw densities as a function of pore diameter considering a volume of V=84 cm³ from several specimens of Ductal A with and without fibre reinforcement

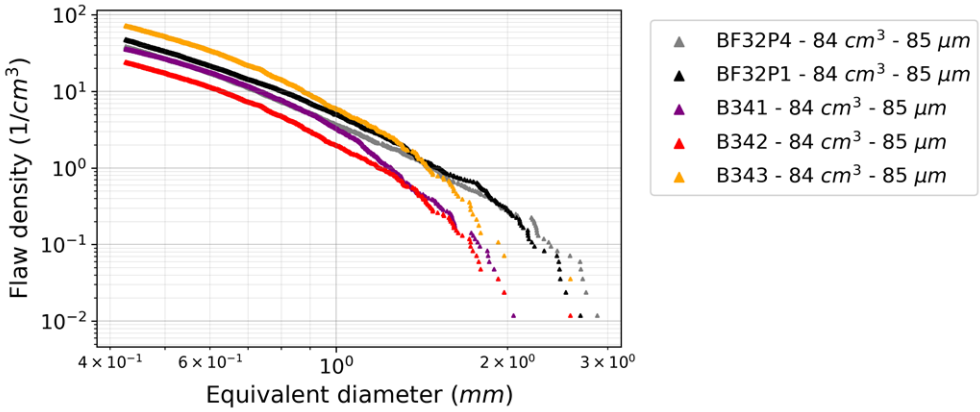

Fig 6.2b —Flaw densities as a function of pore diameter considering a volume of V=84 cm³ from several specimens of Ductal B with and without fibre reinforcement

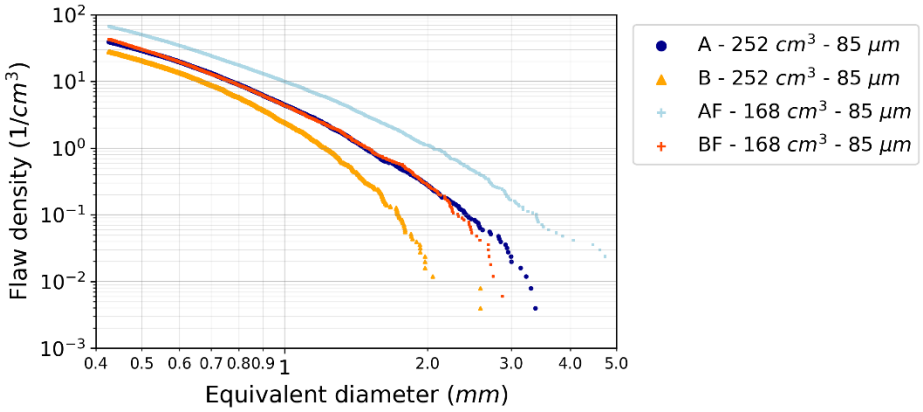

Fig 6.2c — Averaged flaw densities as a function of pore diameter for Ductal A and B with and without fibre reinforcement

considering equivalent pore diameters < 0.426 mm, whereas the flaws densities of A and B are almost conflated considering equivalent pore diameters > 0.426 mm. Only Ductal® A with fibre was analyzed at high resolution. The flaw density of Ductal® A with fibre was extracted

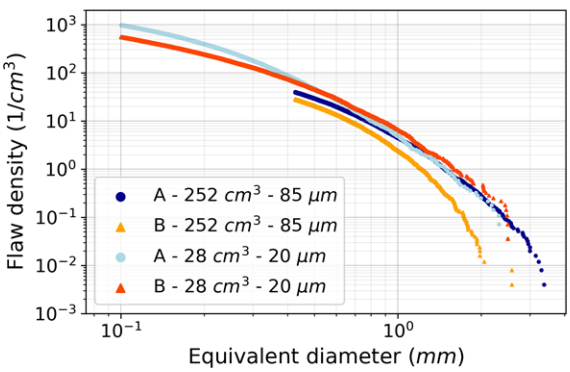

Fig 6.3a—Comparison of flaw densities referred to the larger available volume obtained at a different resolution for Ductal® A and B

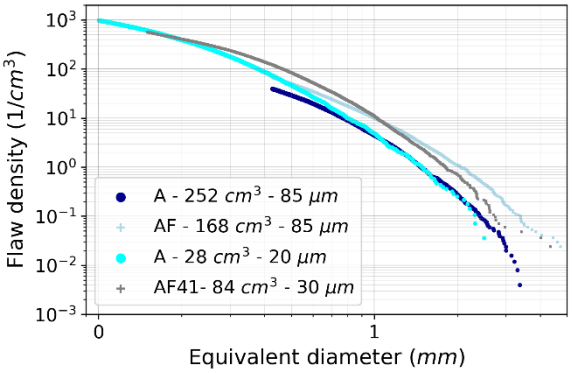

Fig6.3b—Comparison of flaw densities referred to the larger available volume obtained at a different resolution for Ductal® A and B with fibre

considering a volume *Z*= 84 cm^3 through an X-ray CT at 30 μm resolution and is compared in **Fig. 6.3b** to the curves referred to the same matrix without fibres at 20 μm resolution. The effect of fibres on the density of pores seems to disappear at the pore diameter of 0.2 mm.

6.4 Effect of X-ray CT resolution

Aiming to identify a characteristic flaw density for each studied material from the plots in **Fig. 6.3** (matrix A, B and A with fibres), the adopted strategy will be that the characteristic curve follows the flaws density obtained at the higher resolution for the smallest pore sizes and the flaws density obtained averaging over the largest scanned volume for the largest pore sizes. Consequently, a pore size of transition has to be selected.

To do so, the flaw densities at high resolution (20 and 30 μm), presented in section **6.3**, are compared with the flaw densities derived by the low resolution X-ray CT (85 μm), this time, averaging over the same limited volume. In **Figs. 6.4a-b**, the flaws densities of Ductal® A and B, taken out at the two resolutions of 20 and 85 μm, are averaged over Z = 28 cm^3. On the other hand, in **Fig. 6.4c** the flaws densities of Ductal® A with fibres, taken out at the resolutions of 30 and 85 μm, are averaged over Z = 84 cm^3. As expected, for large pore diameters, the curves are not uniques for each considered material because the volume is not representative. But, these comparisons give an idea of the effect of the X-ray CT resolution. The flaw density at low resolution is underestimated for Ductal® B. However, the high and low resolution curves do not meet, once again, due to the variability in the analyzed specimens. For Ductal® A, with and without fibres, the curves at different resolutions meet at the pore diameter of about 1 mm. The flaw density at low resolution is underestimated for pore diameters smaller than 1 mm. That is why the pore diameter of 1 mm is selected as the point of transition.

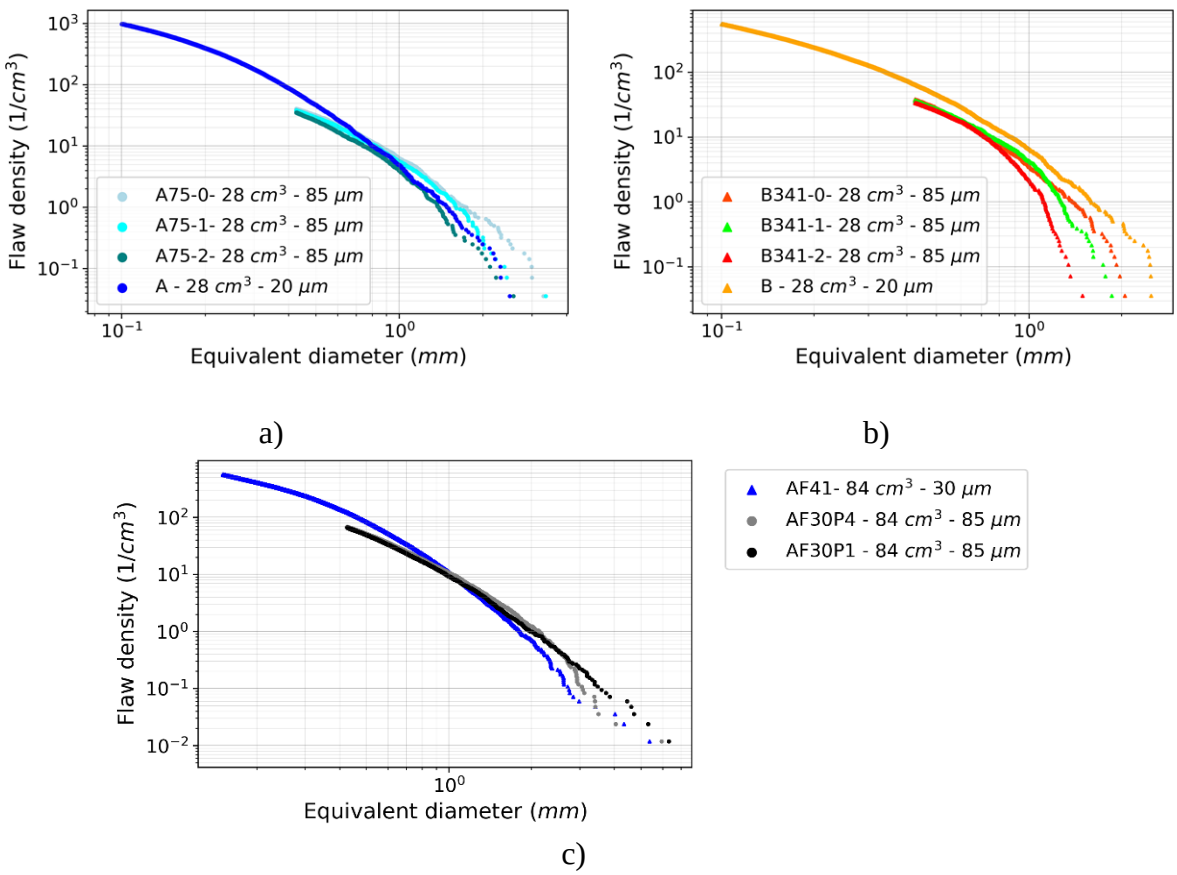

Fig 6.4—Comparison of flaw densities referred to the same size in volumes and obtained at different resolution: a) Ductal A; b) Ductal B; c) Ductal A with fibre reinforcement; a) Ductal A;

The characteristic flaw density assigned to matrix A and B fallows the flaws density obtained at 20 µm averaging over 28 cm^3 for Deq < 1 mm, whereas it fallows the flaws density obtained at 85 µm averaging over 252 cm^3 for Deq > 1 mm. The characteristic flaw density assigned to matrix A with fibres fallows the flaws density obtained at 30 µm averaging over 84 cm^3 for Deq < 1 mm, whereas it fallows the flaws density obtained at 85 µm averaging over 168 cm^3 for Deq > 1 mm.

6.5 Use of LEFM to get the distribution of inception stresses

The characteristic cumulative flaw densities need to be linked to the applied stress to be used in the DFH model. The Linear Elastic Fracture Mechanics (LEFM) theory relates the size of a crack to its inception stress (Jayatilaca A. D. S., Trustmm K., 1977). According to this theory, the stress σ_c to trigger a preexisted crack of size $2a$ is given by:

$$\sigma_c = \frac{K_{IC}}{Y\sqrt{\pi a}} \quad \textbf{(6.1)}$$

where K_{IC} the critical stress intensity factor of the considered material and Y is a dimensionless correction factor linked to the crack geometry, often referred to as the geometric shape factor.

For example, in the case of a straight crack of length $2a$, oriented perpendicularly to the loading direction in an infinite plate subject to a uniform stress field, this correction factor is $Y = 1$, whereas, in the case of a penny-shaped crack of radius a in an infinite domain under uniaxial tension, the geometric shape factor value is $Y = 2/\pi$. Here, a stress of inception is assigned to each pore equivalent diameter by replacing in **eq. 6.1** the size of the initial crack $2a$ with D_{eq}, such as:

$$\sigma_c(Deq, \dot{\varepsilon}) = \frac{K_{IC}}{Y\sqrt{\pi\frac{Deq}{2}}} \text{ x } \left(\frac{\dot{\varepsilon}}{\dot{\varepsilon}_0}\right)^{n_0} \quad \textbf{(6.2)}$$

where n_0 corresponds to an exponent traducing the strain-rate sensitivity in the "quasi-static" regime and $\dot{\varepsilon}_0$ is a reference strain-rate (**Table 6.3**). At the applied stress $\sigma = \sigma_c(\overline{Deq}, \bar{\dot{\varepsilon}})$ all the pores having an equivalent diameter $Deq \geq \overline{Deq}$ are considered as critical defects at $\dot{\varepsilon} = \bar{\dot{\varepsilon}}$. The two parameters K_{IC} and Y need to be fixed for using the distribution of flaws identified by X-ray CT.

The critical stress intensity factor K_{IC} (0.627 $MPa\sqrt{m}$) is deduced from a Single-Edge Notched Bending (SENB) test performed by (Forquin, 2003) with a Ductal® notched sample of dimensions 5×3×20 mm3 (h×w×L, with L the span length). Given the initial notch length a of 1.3 mm ($\alpha = a/h$) and F the peak force reached in the test (24.2 N), the critical stress intensity factor K_{Ic} is estimated with the following formula (ASTM D5045-14, 2014):

$$K_1 = \left(\frac{FL}{wh^{1.5}}\right) f(\alpha), f(\alpha) = 1.5\frac{\alpha^{0.5}[1.99-\alpha(1-\alpha)(2.15-3.93\alpha+2.7\alpha^2)]}{(1+2\alpha)(1-\alpha)^{1.5}} \quad \textbf{(6.3)}$$

Note that the composition of the tested concrete to estimate K_{IC} should be very close to Ductal® *B*, but the same value is used for both concretes A and B. The remaining unknown in **Eq. 6.2** is *Y*. Moreover, a method to estimate the values of Y, leading to stresses of inception for the porosities equivalent to the one assumed in the classical DFH model, is proposed in the next section.

6.6 The continuous approach - Explicit $\boldsymbol{\lambda_t}$ function

According to the Weibull law, the density of critical defects versus the applied stress yields a straight line in a log-log space. A new function for λ_t is defined in the same space, which interpolates the discrete points of the flaw densities of section **6.3**. expressed as a function of the stress of inception of **Eq. 6.2**. Here, Y is supposed to be a constant for the given materials, and for concrete A and B it is estimated by matching $\lambda_t(\dot{\varepsilon})$ to the Weibull law at the stress $\sigma_w(\dot{\varepsilon})$, i.e., the DFH model parameter recalled in **Table 6.3**. The same Y is used for the matrix A with and without fibres as the same crack initiation parameters were used for concrete A and

Ductal		A	A-2%	B
Elastic parameters	$\rho\left(\frac{\text{kg}}{\text{m}^3}\right), E(\text{GPa})$ v	2420, 52.4, 0.2	2560, 55, 0.2	2460, 51.27, 0.2
Cracks propagation parameters	S, k	3.74, 0.38		
Quasi-static increase factor	$\text{n}^{qs}, \dot{\varepsilon_0}\ (\text{s}^{-1})$	0.03, $5\text{x}10^{-6}$		
Cracks initiation parameters $(\dot{\varepsilon} = 5\ \text{s}^{-1})$	$V_{eff}(\text{mm3})$, $\sigma_w(\text{MPa})$, m	64, 18.90 ($\dot{\varepsilon}$ =5x10^{-6} s^{-1}), 10.4		98, 19.42 ($\dot{\varepsilon}$ =5x10^{-6} s^{-1}), 8.9

Table 6.3 - Parameters of the DFH model for A and B concretes

A-2% in the DFH model. Note that the estimation of *Y* employing an already calibrated parameter compensates for the uncertainty associated with the critical stress intensity factor. The proposed interpolation function is a piece-wise function with two breakpoints, such as:

$$\begin{cases} X \le X_1 \rightarrow Y = f_1(X) \\ X_1 < X \le X_2 \rightarrow Y = \dfrac{f_1(X) f_2(X)}{(f_1(X)^q + f_2(X)^q)^{\frac{1}{q}}} \\ X > X_2 \rightarrow Y = f_2(X) \end{cases} \quad \textbf{(6.4)}$$

$$with\ Y = Log(\lambda_t)$$
$$X = Log(\sigma)$$
$$f_i(X) = a_i(X - X_i) + Y_i \quad i = 1,2$$

The function parameters for Ductal® A (with and without fibres) and B (without fibres) are reported in **Table 6.4,** and a plot for Ductal® B is shown in **Figs 6.5.** The piece-wise function, for $\dot{\varepsilon}$ =5x10^{-6} s^{-1} and $\dot{\varepsilon}$ =100 s^{-1}, fits the characteristic flaw density derived by the tomography analyses (with Y=0.83) quite well. Furthermore, it is interesting to note that the slope of the tangent to the function is close to m precisely at the point of intersection with the Weibull law. The three interpolation functions are compared in **Fig. 6.6** for $\dot{\varepsilon}$ =5x10^{-6} s^{-1}. This time, the horizontal axis is not on a logarithmic scale to show off the microscopic stresses that can activate the porosities at the selected strain rate. Functions A and B meet at 30 and 60 MPa. The gap between the function A and A-2% is extinguished for stresses of 70 MPa.

Material	K_{IC} $(MPa\sqrt{m})$	Y	Function parameters
A	0.627 (Forquin, 2003)	0.80	$\begin{cases} X_1 = 7.40log\left(\frac{\dot{\varepsilon}}{\dot{\varepsilon}_0}\right)^{n_0}, Y_1 = 5.42, a_1 = 8, q = 18 \\ X_2 = 8.15log\left(\frac{\dot{\varepsilon}}{\dot{\varepsilon}_0}\right)^{n_0}, Y_2 = 9.23, a_2 = 2.5 \end{cases}$
A-2%		0.80	$\begin{cases} X_1 = 7.44log\left(\frac{\dot{\varepsilon}}{\dot{\varepsilon}_0}\right)^{n_0}, Y_1 = 6.32, a_1 = 9, q = 14 \\ X_2 = 8.15log\left(\frac{\dot{\varepsilon}}{\dot{\varepsilon}_0}\right)^{n_0}, Y_2 = 9.23, a_2 = 2.5 \end{cases}$
B		0.83	$\begin{cases} X_1 = 7.172log\left(\frac{\dot{\varepsilon}}{\dot{\varepsilon}_0}\right)^{n_0}, Y_1 = 5.90, a_1 = 8, q = 15 \\ X_2 = 7.672log\left(\frac{\dot{\varepsilon}}{\dot{\varepsilon}_0}\right)^{n_0}, Y_2 = 8.53, a_2 = 1.8 \end{cases}$

Table 6.4 – Estimated geometric shape factors and parameters of the interpolation function.

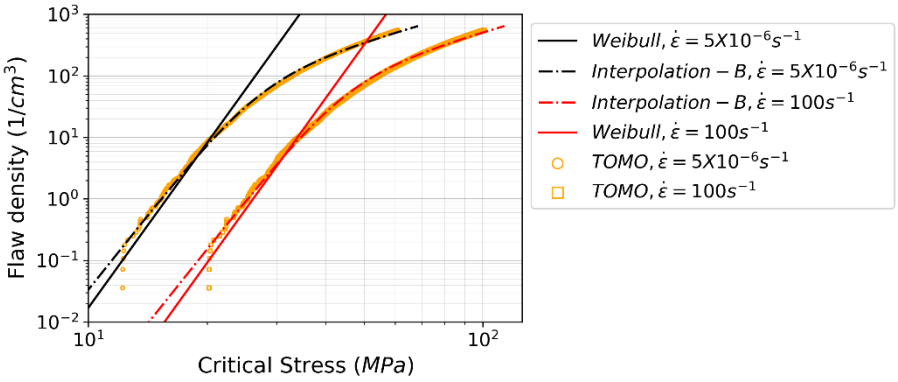

Fig 6.5—Density of critical defects as a function of the applied stress for Ductal B ($\dot{\varepsilon}$ =5x10^{-6} s^{-1}in black, $\dot{\varepsilon} = 100$ s^{-1} in red).

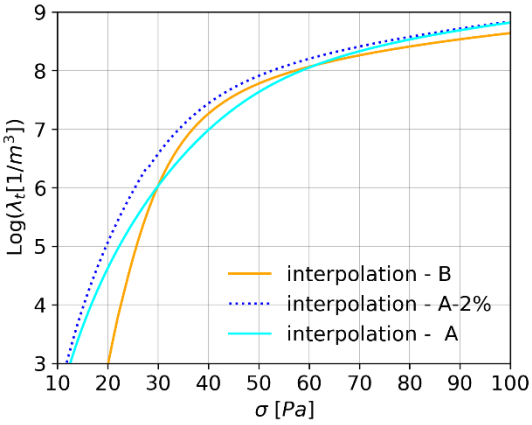

Fig 6.6—Comparison between the densities of critical defects at $\dot{\varepsilon}$ =5x10-6 s^{-1}

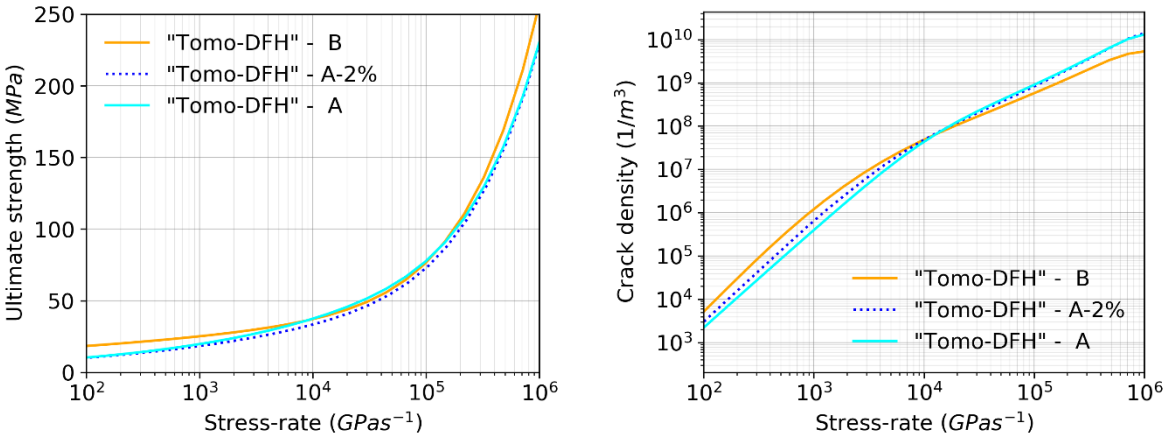

Fig 6.7—Predictions of the macroscopic strength (right) and final crack density (left) with the stress rate considering λ_t as interpolated piece-wise function

6.6.1 Predictions of the continuous approach

The ultimate macroscopic strength Σ_{max} and the final crack density $\lambda_{crack}(T_{end})$ predicted by the "Tomo-DFH" model, which assumes λ_t as **Eq. 6.4** are discussed in this section. The material is supposed to be loaded at a uniform stress rate. Note that only the stress rates predicting a 'multiple fragmentation' are considered in the following.

The obscuration probability $P_o(t)$ (i.e., $\mathrm{D}(t)$) is calculated by triple integration of **Eq. 3.16**, so the macroscopic stress $\Sigma(t)$ is provided according to **Eq. 3.15** and $\lambda_{crack}(T_{end})$ is obtained by integrating **Eq. 3.17**. The obtained Σ_{max} and $\lambda_{crack}(T_{end})$ for a large range of stress-rates with the three concrete materials A, A-2% and B are shown in **Fig. 6.7**. The evolutions of Σ_{max} and $\lambda_{crack}(T_{end})$ are rather similar even if the three populations of defects are not the same. A slight difference in Σ_{max} is observed between concrete A and B. Concrete B has a non-negligible higher strength only for the lowest and the highest stress-rates considered in the figure. The differences in $\lambda_{crack}(T_{end})$ are more pronounced, even if the curves representing the evolution of the crack density with the stress-rate cross each other at $\dot{\sigma}$=10^4 GPa s^{-1}. For both Σ_{max} and $\lambda_{crack}(T_{end})$ the effect of the fibres is imperceptible. Note the cohesive strength has been omitted in this analysis.

The results are compared in **Fig. 6.8** with the ones given by the "Weibull-DFH" model**.** The predictions of Σ_{max} diverge only from considerable stress rates, of the order of ≈3x10^4 GPa s^{-1},

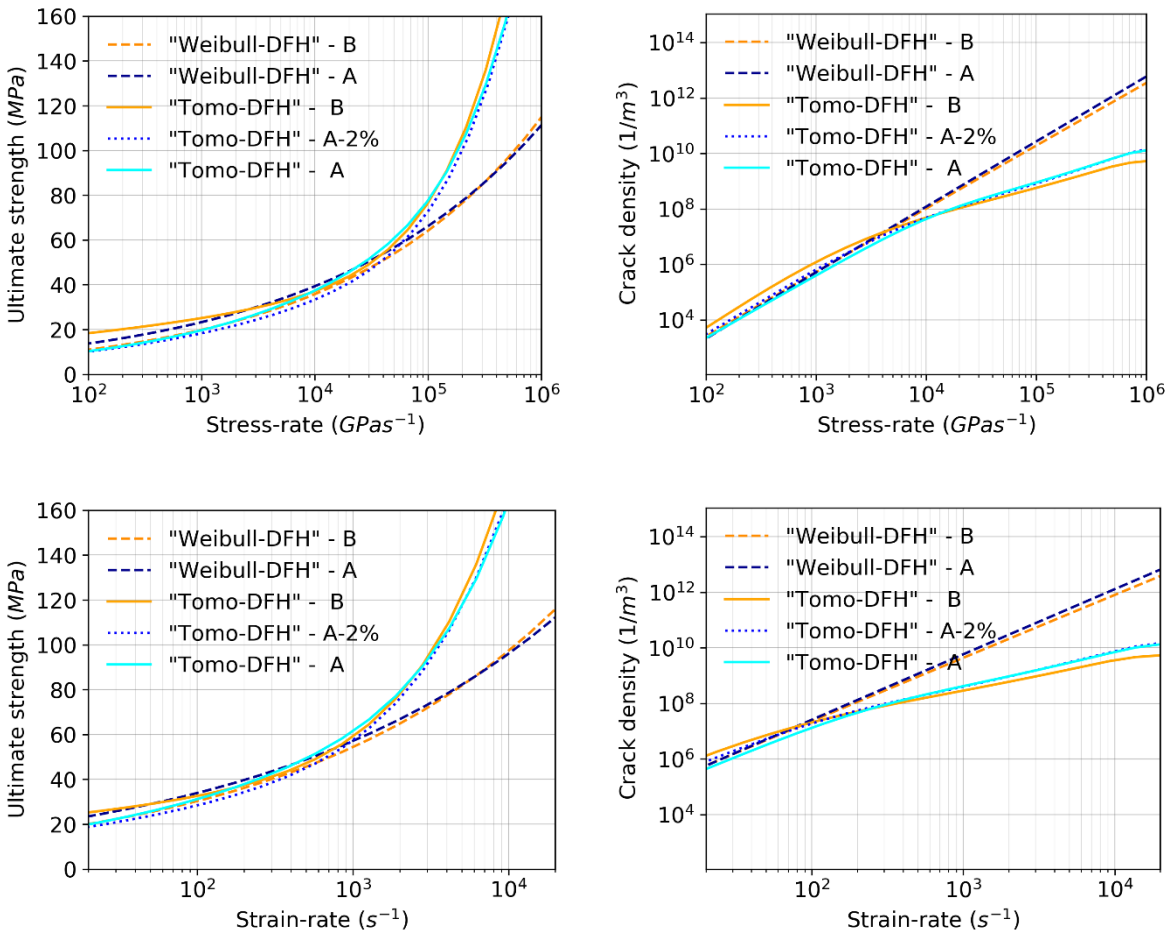

Fig 6.8—Comparison between predictions of the macroscopic strength (right) and final crack density (left) with the stress and strain rate considering λ_t as interpolated piece-wise functions or using the linear relationship

i.e., $\dot{\varepsilon} \approx$ 550 s^{-1}, whereas the predictions of $\lambda_{crack}(T_{end})$ diverge already at stress $\approx$ 2x10^3 GPa s^{-1}, i.e., $\dot{\varepsilon} \approx$ 100 s^{-1}.

6.8 The discrete approach - Pore location

In this section, the simultaneous inception and growth of individual obscuration volumes are numerically simulated considering the real location of each pore and its stress of activation. The approach, named discrete, has been developed using the programming language Python. The routine is composed of the following steps. First, a parallelepiped of centimeter size is defined, and a three-dimensional mesh of the domain is created considering elementary cubic elements of homogeneous size. Second, a scanned volume of the same size as the domain is considered. The coordinates of each pore are assimilated to the center of mass of the ideal ellipsoid fitting the pore, and a critical stress is attributed to each pore based on its equivalent diameter according to **eq. 6.2.** Then, the porosities belonging to each elementary element are listed, and

Parameters	A	B
Cube size (mm)	35x40x20	35x40x20
Element size (mm)	0.5	0.5
Number of elements	224000	224000
Pores	26090	15082

Table 6.5 – Parameters used for the discrete numerical simulations

the critical stress of the weakest pore is attributed to this element according to **eq. 6.2** (the critical stress is strain rate dependent).

A constant stress-rate is homogenously applied to the domain. The stress increases linearly as long as none of the critical stresses is reached. Once the applied stress reaches the critical stress of one element, a spherical obscuration volume centered on it starts to grow with a radius proportional to the constant speed kC. The stress is set to zero in all the elements that belong to the obscured volume. It means that the neighboring elements reached by this growing spherical volume cannot be activated anymore even if the stress exceeds their activation stress. The stress continues to increase linearly in the elements that don't belong to any obscuration volume. The discrete numerical simulation ends when the whole volume is obscured. The macroscopic stress is calculated by averaging the stresses in all the elements of the domain, and the ultimate macroscopic strength is defined as the maximum value of the macroscopic stress. The crack density is calculated as the number of elements that reached their critical stress without being obscured divided by the total volume.

6.8.1 The discrete approach applied to concretes A and B

A 3D volume 35x40x20 mm^3 was considered for both concretes A and B, respectively, named domains A and B. Those dimensions were defined as the largest provided by the tomographic scans at 20 μm. The geometric shape factors of **Table 6.4** have been used to calculate the critical stress of each extracted pore. A mesh element size of 0.5 mm was chosen as a compromise to capture the smallest pore sizes providing a reasonable calculation time. This mesh size is much smaller than the average distance between the centers of mass of the pores. 26090 critical stresses were placed in domain A against the 15082 critical stresses of domain B. One cross-section of those domains is shown in **Fig. 6.9** for $\dot{\varepsilon} = 10\ s^{-1}$**.** Note that no critical stress is assigned in the elements that do not interest the center of mass of a pore. From the figure, the reduced number of porosity of domain B can be appreciated. For each domain, the initial features are detailed in **Table 6.5.**

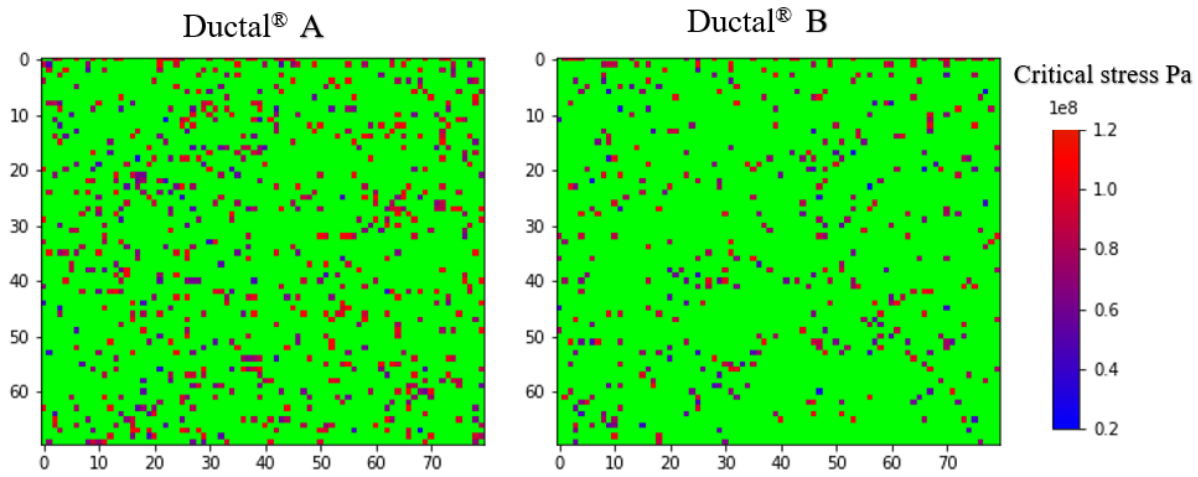

Fig 6.9 —Critical stresses for one cross-section (70 x 80 elements) at $\dot{\varepsilon}$ =10 $s^{-1}$of the domain considered for concrete A and B. No critical stress is assigned to the elements in green

A constant stress-rate is homogenously applied to domains A and B. The algorithm was applied, considering a large number of stress-rates in between 10^2 GPa s^{-1} and 10^5 GPa s^{-1} (≈ 2 s^{-1} and 2 10^3 s^{-1}). The time step was kept constant to 1 ns for every stress-rate applied as, with this value, the total number of time increments was pertinent to describe the growth of the obscured zone in the domain accurately. The results in terms of ultimate strength Σ_{max}, n° number of activated elements at $T_{\Sigma_{max}}$ and T_{end}, and densities of cracks $\lambda_{crack}(T_{\Sigma_{max}})$ and $\lambda_{crack}(T_{end})$ are detailed in **Table 6.6.**

As shown in **Fig. 6.10** for both concretes A and B**,** a good match is observed between the predictions provided by the continuous and discrete approaches in terms of dynamic strength for stress rate in between 10^3 GPa s^{-1} and 10^5 GPa s^{-1} (≈ 20 s^{-1} and 2 10^3 s^{-1}). This confirms that the continuous function, identified in **Table 6.4**, properly describes the flaw population of Ductal A and B detected by tomography. Even if the continuous approach does not consider the exact position of the pores, it leads to quasi-equivalent results to the one obtained with the discrete approach. For stress rates lower than 200 GPa s^{-1} (≈4 s^{-1}), the discrete approach predicts a stress rate independent ultimate strength, which depends only on the weakest defect in the volume 28 cm^3 resulting in a unique crack density and a higher ultimate strength than in the continuous approach for concrete A. This phenomenon is not captured in the continuous approach as this approach does not involve the size of the considered volume.

Moreover, above $\dot{\sigma}$=10^5 GPa s^{-1}, it is observed that the cracking density predicted by the two continuous and discrete approaches start to diverge. This is due to the limited resolution of the scan and size of the smallest pores (0.1 mm corresponding to the critical stress of 113.54 MPa for concrete A and 106.29 MPa for concrete B) that are considered in the discrete approach.

	A					
$\dot{\sigma}$	$\dot{\varepsilon}$	Σ_{max}		$\lambda_c(T_{\Sigma_{max}})$		$\lambda_c(T_{end})$
Gpa/s	1/s	Mpa	N°	1/m3	N°	1/m3
1.00E+02	1.91E+00	22.74	2	7.14E+04	2	7.14E+04
1.77E+02	3.38E+00	22.74	2	7.14E+04	2	7.14E+04
3.16E+02	6.03E+00	23.14	4	1.43E+05	6	2.14E+05
5.62E+02	1.07E+01	23.72	7	2.50E+05	12	4.29E+05
1.00E+03	1.91E+01	24.74	10	3.57E+05	26	9.29E+05
1.77E+03	3.38E+01	26.28	20	7.14E+05	52	1.86E+06
3.16E+03	6.03E+01	28.72	49	1.75E+06	143	5.11E+06
5.62E+03	1.07E+02	32.02	128	4.57E+06	378	1.35E+07
1.00E+04	1.91E+02	36.47	305	1.09E+07	953	3.40E+07
1.77E+04	3.38E+02	42.16	876	3.13E+07	2420	8.64E+07
3.16E+04	6.03E+02	49.61	2147	7.67E+07	5793	2.07E+08
5.62E+04	1.07E+03	58.93	5627	2.01E+08	11842	4.23E+08
1.00E+05	1.91E+03	71.02	11372	4.06E+08	20662	7.38E+08
1.77E+05	3.38E+03	87.07	21560	7.70E+08	25528	9.12E+08
3.16E+05	6.03E+03	116.83	26090	9.32E+08	26090	9.32E+08
5.62E+05	1.07E+04	171.72	26090	9.32E+08	26090	9.32E+08
1.00E+06	1.91E+04	271.81	26090	9.32E+08	26090	9.32E+08

Table 6.6 – Results of discrete numerical simulation concrete A

	B					
$\dot{\sigma}$	$\dot{\varepsilon}$	Σ_{max}		$\lambda_c(T_{\Sigma_{max}})$		$\lambda_c(T_{end})$
Gpa/s	1/s	Mpa	N°	1/m3	N°	1/m3
1.00E+02	1.95E+00	21.32	4	1.43E+05	4	1.43E+05
1.77E+02	3.45E+00	21.32	6	2.14E+05	6	2.14E+05
3.16E+02	6.16E+00	21.84	6	2.14E+05	8	2.86E+05
5.62E+02	1.10E+01	22.21	8	2.86E+05	15	5.36E+05
1.00E+03	1.95E+01	22.57	12	4.29E+05	24	8.57E+05
1.77E+03	3.45E+01	23.84	23	8.21E+05	66	2.36E+06
3.16E+03	6.16E+01	26.08	58	2.07E+06	163	5.82E+06
5.62E+03	1.10E+02	29.29	154	5.50E+06	416	1.49E+07
1.00E+04	1.95E+02	33.59	332	1.19E+07	937	3.35E+07
1.77E+04	3.45E+02	39.04	898	3.21E+07	2002	7.15E+07
3.16E+04	6.16E+02	46.51	2033	7.26E+07	4219	1.51E+08
5.62E+04	1.10E+03	56.41	4082	1.46E+08	8173	2.92E+08
1.00E+05	1.95E+03	69.80	8156	2.91E+08	13029	4.65E+08
1.77E+05	3.45E+03	88.92	14659	5.24E+08	14906	5.32E+08
3.16E+05	6.16E+03	123.63	15082	5.39E+08	15082	5.39E+08
5.62E+05	1.10E+04	179.79	15082	5.39E+08	15082	5.39E+08
1.00E+06	1.95E+04	284.20	15082	5.39E+08	15082	5.39E+08

Table 6.7 – Results of discrete numerical simulation concrete B

In contrast, in the continuous approach, the pore distribution is extrapolated above this threshold. Therefore whereas the continuous approach predicts an increasing number of cracks thanks to an extrapolation of the pore distribution, the discrete approach reaches a plateau. It results in an estimation of the ultimate strength subsequently higher than the ultimate strength predicted by the continuous approach at $\dot{\sigma}$=10^6 GPa s^{-1}.

Finally, according to the discrete simulations, the reduced quantity of the smallest porosity of concrete B does not give higher ultimate strength in the range of loading-rate between 10^3 GPa s^{-1} and 10^5 GPa $s^{-1,}$ and no conclusion can be made above $\dot{\sigma}$=10^5 GPa s^{-1} because, at this loading rate, all the defects considered are already activated.

Moreover, above $\dot{\sigma}$=10^5 GPa s^{-1}, it is observed that the cracking density predicted by the two continuous and discrete approaches start to diverge. This is due to the limited resolution of the scan and size of the smallest pores (0.1 mm corresponding to the critical stress of 113.54 MPa for concrete A and 106.29 MPa for concrete B) that are considered in the discrete approach.

In contrast, in the continuous approach, the pore distribution is extrapolated above this threshold. Therefore whereas the continuous approach predicts an increasing number of cracks thanks to an extrapolation of the pore distribution, the discrete approach reaches a plateau. It results in an estimation of the ultimate strength subsequently higher than the ultimate strength predicted by the continuous approach at $\dot{\sigma}$=10^6 GPa s^{-1}.

Finally, according to the discrete simulations, the reduced quantity of the smallest porosity of concrete B does not give higher ultimate strength in the range of loading-rate between 10^3 GPa s^{-1} and 10^5 GPa $s^{-1,}$ and no conclusion can be made above $\dot{\sigma}$=10^5 GPa s^{-1} because, at this loading rate, all the defects considered are already activated.

6.10 Comparison with the experimental data

The predictions are overlapped with the experimental results. Both the spalling and the plate impact tests are reported in **Fig. 6.11**. For the loading rates reached in the spalling tests at the Hopkinson bar, considering the porosities extracted by X-ray CT analysis or the critical defects based on the Weibull model, the predicted ultimate tensile strengths are in agreement with the experiments. This is happening as the calibration of the geometric shape factors is based on the classical Weibull model already adjusted to fit the experimental data.

Anyways, the assumption seems to not stand up anymore at the loading rates reached by the plate impact tests. In fact, at these extreme loading rates, new physical phenomena could be

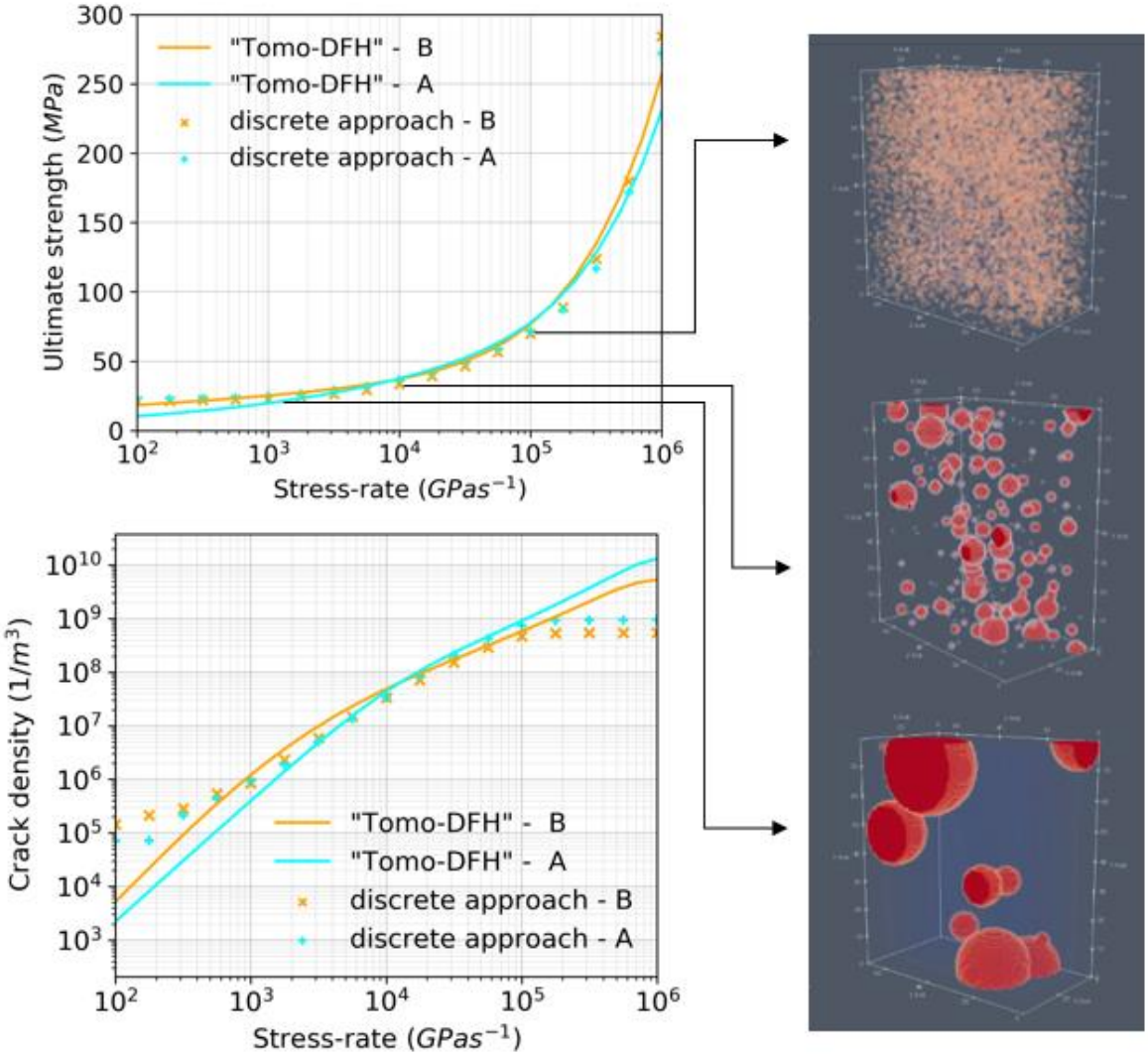

Fig 6.10 —Comparison between the continuous and discrete approaches in terms of macroscopic strength and final crack density (right) and pictures of the obscured volumes at 10^3 $GPas^{-1}$, 10^4 $GPas^{-1}$, 10^5 $GPas^{-1}$ for concrete B (left)

involved in the response. As a possible explanation, the considered porosities could not be the only location where the crack initiate. Other physical phenomena may occur.

In the applied continuous and discrete methods, the only flaws considered in the matrix are macropores of mm scale that correspond to the entrapped air during the casting process. Other types of porosity exit in a concrete matrix as capillary pores at μm scale and gel-pores at the nm scale. UHPCs are well-known to have reduced capillary pores with respect to the standard concrete. The presence of nanoscale particles as silica fume in the mix composition likely decreases the gel-pores, but the exact effect is still an active research topic.

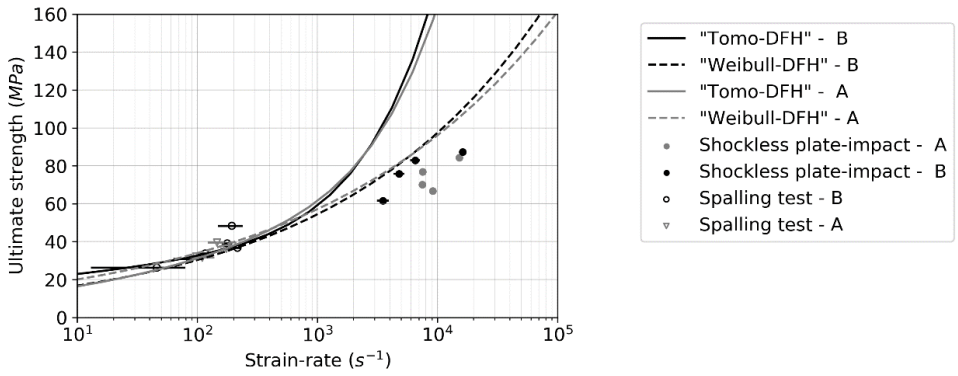

Fig 6.11 - Comparison of the experimental tensile strength with the ultimate strength considering the strength enrichment at low strain rate (range 5x10-6 s-1 to 10 s-1)

Flaws can also be micro-cracks that develop during the hydration of cement from autogenous shrinkage. For example, (Scheydt and Muller, 2012), using the ESEM technique (Enviromental Scanning Electron Microscope), detect in a UHPC with a maximum aggregate size of 8 mm micro-cracks with a crack width between 0.5 µm and 2 µm. The crack length is not measured, but the cracks were mainly running alongside the sand grains. Adding this new category of flaw in the approach could impact the predicted strength and could explain why the modeling overestimates the tensile strength at a very high loading rate.

6.11 Case of micro-cracks connected to pores

If those micro-cracks exist in the studied matrices, they are impossible to be detected by X-ray CT analysis as they are closed. In the next, the continuous approach is used to determine the distribution of critical defects that fit the experimental results at a very high strain rate by an inverse method. Again the porosities extracted by the X-ray scans are used, but a defect is now made of the spherical pore and wing-end cracks of unknown length δ. The critical stress given to the defect is defined by replacing in **eq. 6.2** the size of the initial crack 2a with Deq+2δ, such as:

$$\sigma_c(Deq, \dot{\varepsilon}) = \frac{K_{IC}}{Y\sqrt{\pi\frac{Deq+2\delta}{2}}} \text{ x } \left(\frac{\dot{\varepsilon}}{\dot{\varepsilon}_0}\right)^{n_0} \quad \textbf{(6.5)}$$

Three crack lengths have been considered, respectively, of 0.1, 0.2, and 0.3 mm. For concrete A and B, Y is still estimated by matching λ_t to the linear relationship at the stress σ_w in **Table 6.3.** For each δ, the parameters of the interpolation function **eq. 6.4** are given in **Table 6.7.**

Material	δ	Y	Function parameters
A	0.1	0.78	$\begin{cases} X_1 = 7.3\left(\frac{\dot{\varepsilon}}{\dot{\varepsilon}_0}\right)^{n_0}, Y_1 = 3.5, a_1 = 18, q = 5 \\ X_2 = 7.82\left(\frac{\dot{\varepsilon}}{\dot{\varepsilon}_0}\right)^{n_0}, Y_2 = 8.85, a_2 = 6 \end{cases}$
A	0.2	0.75	$\begin{cases} X_1 = 7.35\left(\frac{\dot{\varepsilon}}{\dot{\varepsilon}_0}\right)^{n_0}, Y_1 = 3.56, a_1 = 21, q = 10 \\ X_2 = 7.8\left(\frac{\dot{\varepsilon}}{\dot{\varepsilon}_0}\right)^{n_0}, Y_2 = 8.96, a_2 = 10 \end{cases}$
A	0.3	0.72	$\begin{cases} X_1 = 7.35\left(\frac{\dot{\varepsilon}}{\dot{\varepsilon}_0}\right)^{n_0}, Y_1 = 3.59, a_1 = 21, q = 20 \\ X_2 = 7.74\left(\frac{\dot{\varepsilon}}{\dot{\varepsilon}_0}\right)^{n_0}, Y_2 = 8.89, a_2 = 13 \end{cases}$
B	0.1	0.80	$\begin{cases} X_1 = 7.36\left(\frac{\dot{\varepsilon}}{\dot{\varepsilon}_0}\right)^{n_0}, Y_1 = 3.95, a_1 = 20, q = 10 \\ X_2 = 7.48\left(\frac{\dot{\varepsilon}}{\dot{\varepsilon}_0}\right)^{n_0}, Y_2 = 6.80, a_2 = 6 \end{cases}$
B	0.2	0.79	$\begin{cases} X_1 = 7.38\left(\frac{\dot{\varepsilon}}{\dot{\varepsilon}_0}\right)^{n_0}, Y_1 = 3.95, a_1 = 19, q = 30 \\ X_2 = 7.48\left(\frac{\dot{\varepsilon}}{\dot{\varepsilon}_0}\right)^{n_0}, Y_2 = 6.45, a_2 = 8.5 \end{cases}$
B	0.3	0.76	$\begin{cases} X_1 = 7.38\left(\frac{\dot{\varepsilon}}{\dot{\varepsilon}_0}\right)^{n_0}, Y_1 = 3.95, a_1 = 18, q = 30 \\ X_2 = 7.48\left(\frac{\dot{\varepsilon}}{\dot{\varepsilon}_0}\right)^{n_0}, Y_2 = 6.30, a_2 = 11 \end{cases}$

Table 6.7 – Estimated of geometric shape factors and parameters of the interpolation function for different lengths of the wing-end cracks.

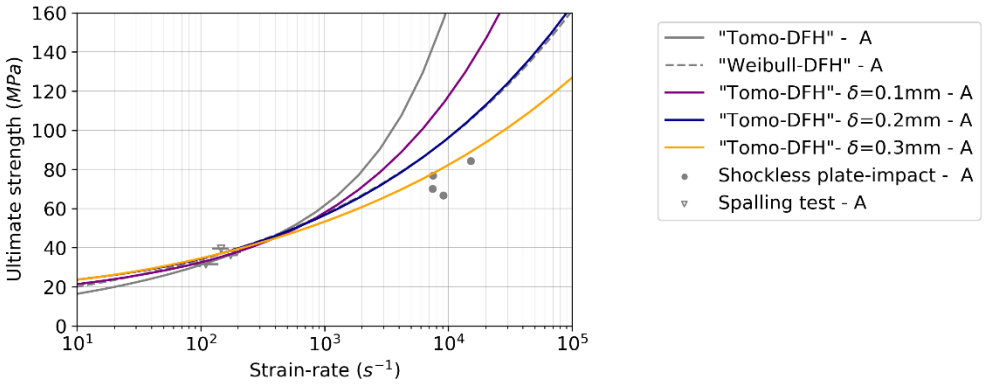

Fig 6.12a Ultimate strength considering pores and wing-end cracks concrete A

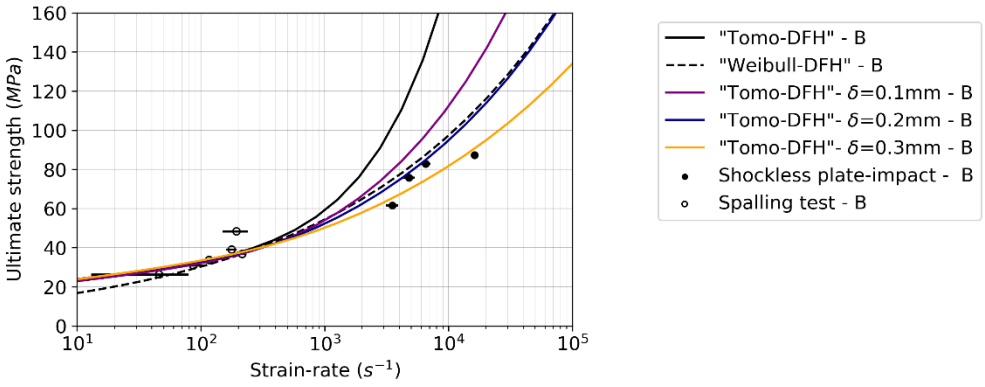

Fig 6.12b Ultimate strength considering pores and wing-end cracks concrete B

Figs. 6.12 show the predicted ultimate strengths as a function of the strain rate. For both the studied UHPC, the new assumption is not modifying the strength at the loading rate of the spalling test at the Hopkinson bar. The length of the wing-end crack that fits the plate impact data is 0.3 mm, which is about the size of the largest aggregate in the concretes formulation of Ductal®.

6.12 Synthesis and conclusion

An X-ray computed micro-tomography (CT) analysis has been presented in this chapter. After specifying the set-up and UHFRPC samples, pore distributions have been investigated until a minimum pore size of 0.1 mm, plotting cumulative densities for prismatic volumes of different sizes. A sensitivity analysis allowed checking the influence of the X-ray CT resolution and the studied volume. The pore equivalent diameter of 1 mm was selected as the point of transition of reliability between high and low resolution. Ductal® B seems to have a population of pores more variable than Ductal® A. Summing up the analyzed volumes of the same concrete matrix, the pore density seems lower for Ductal® B. Fibres increase the number of pores, and this effect seems to disappear for pore smaller than 0.2 mm.

The linear Fracture Mechanics (LEFM) allowed linking the cumulative flaw densities to the applied stress to be used as input in the modelling. Then, two equivalent approaches were developed. In the continuous approach, a piece-wise function interpolates the critical flaw densities as function of the applied stress, and the differential equation of the obscuration probability is integrated as in the DFH model. In the discrete approach, a prismatic finite volume is considered, and the growth of obscuration zones is numerically simulated considering the individual pore locations.

The two approaches gave equivalent results in term of tensile strength and crack density. They diverge from the “Weibull-DFH” model at high strain-rates as the critical defect densities based on the X-ray CT analysis diverge from the Weibull law at the highest stress levels. For concrete A, B and A with fibres, similar responses are predicted. By comparing the model prediction of ultimate strength vs. strain rate with experimental data from spalling and plate-impact tests, it is observed that continuous and discrete approaches overestimate the tensile strength at very high loading rate for both concretes A and B. Resorting to an inverse method, it is observed that a good fit of the experimental results can be obtained assuming that pores are connected to wing-end cracks about the size of the largest aggregate in the concretes formulation of Ductal®.

CHAPTER 7

General conclusion and perspectives

This thesis has presented experimental and numerical investigations on Ultra-High Performance Concretes (UHPC) in view of intensifying their use in application demanding resistance to impact loadings. Under impact, concrete is exposed to high confinement stresses and high tensile loading rates, leading to severe damage modes affecting ballistic performance. Consequently, the DFHcoh-KST model, describing the behavior under confinement and dynamic tension, has been chosen to simulate with a Finite Element (FE) code the response of UHPC targets with fibre reinforcement under impact. In the coupled model, the confining pressure is influencing the volumetric strain and the deviatoric strength. The strain rate effects are included in the probabilistic description of the tensile damage variable based on the activation and obscuration of a Weibull distribution of flaws. The roles of the fibre content and orientation are integrated, introducing the term cohesion strength.

The DFHcoh-KST model parameters were identified for two Ductal® formulations with fibres achieving the compressive strength of 150 MPa (Ductal® A) and 170 MPa (Ductal® B) through an experimental characterization based on existing techniques. The quasi-oedometric compression (Q-OC) tests depicted the behaviors under confinement up to the hydrostatic pressure of 500 MPa. The bending tests and the spalling tests allowed to define the tensile behaviors, covering a range of strain rates from 10^{-5} to 10^{2} s^{-1}. The finite element simulations of the ballistic impact of an AP (Armor-Piercing) projectile against Ductal® panels showed that accounting for inelastic compaction with the applied pressure is not crucial for UHPC. The friction at the projectile-panel interface, the UHPC deviatoric strength, the UHPC tensile peak strength and softening are the key-parameters in the modelling strategy.

Nevertheless, the same simulations showed that confinement pressures up to 1.5 GPa and strain rates above 10^{3} s^{-1} arise in the panels during the projectile penetration. The validity domain of the proposed model was extended by performing additional tests investigating the tensile response of UHPC at very-high strain rates (above 10^{3} s^{-1}). A real effort was made to overcome the limits of plate-impact tests and pave the way for a new experimental technique. The proposed pulse shaping system, based on machined flyer-plate and buffer, successfully allowed the UHPC specimens to be subject to a controlled strain rate in the range of 10^{3} - 10^{4} s^{-1}.

	Experimental	Numerical
chapter 3	Sample manufacturing and metrology Set-up adaptation and execution of Q-OC tests Preparation and execution of bending and spalling tests X-ray CT observations	Setting and validation of Q-OC processing method Post-processing experimental data Identification of KST, DFH and cohesion models parameters Fibre distributions analyses
chapter 4		FE modelling of ballistic impact Sensitivity study Identification of pressure and strain-rate levels
chapter 5	Sample manufacturing and metrology Alignment of striker-target-optical fibre Installation of recording system	Pulse shaping design (material and geometry for striker and buffer, impact velocity) Post-processing of PDV signals Reconstruction of experimental pulse Strain rate estimation by FE numerical simulation
chapter 6	X-ray CT observations	Pore distribution analyses Continuous and discrete modelling of fragmentation process and predictions over a large range of strain-rates

Table 7.1 – Experimental and numerical works per chapter

Two equivalent approaches were developped to overcome the limitation of the DFH model of considering a Weibull distribution of flaws. The UHPC fragmentation under dynamic tension was simulated with the discrete and continuous approaches based on X-ray Computed Tomography (CT) observations of the microstructure of UHPC expressed as distribution of pores. Assuming that the size of the pore is related to the stress of activation and that pores are connected to wing-end cracks about the size of the largest aggregate in the concrete formulations of Ductal® led to a flaw population that correctly described the observed tensile strength above 10^3 s^{-1}.

All experimental and numerical works managed in this thesis are summarized in **Table 7.1**.

To conclude, all these experimental and numerical investigations applied to the two Ductal® formulations often led to similar mechanical behavior except regarding the deviatoric strength, which may explain the higher penetration resistance of Ductal® B with respect to A.

Eventually, these new experimental and numerical studies could be completed by tests showing the UHPC behavior under confinement pressure above 500 MPa. This could be done with an adapted triaxial or Q-OC device; or instead, plate-impact tests. Moreover, additional shockless plate-impact configuration for spalling could be experienced by testing new geometries and materials for striker and buffer to attempt to enlarge the range of accessible strain rates. It is clear since the beginning of this study that there is a marked difference between the strain rate reached using the Hopkinson bar device and the plate-impact facility; completely new experimental techniques should be practiced to close this gap. Moreover, the origin of the scatter in the experimental data during the dynamic tension is not investigated in the manuscript. Additional tests should be performed to make this type of analysis.

For the modelling of the UHPC behavior under dynamic tension, the parameters of the DFH model, responsible of the strain rate sensitivity of the ultimate strength in quasi static tensile regime, could be validated with additional experimental techniques at strain rate around 10 s^{-1}. The parameters controlling the post peak behaviour in the proposed model should be validated with additional tests on fibred specimens in both static and dynamic conditions trying to cover a large range of strain rate .

Finally, the X-ray CT analyses of pore distributions might be extended to further lower pore size, and these new information could be coupled to observations of defects of lower size with a Scanning Electron Microscope aiming to validate the existence of the micro-cracks assumed to correctly predict the dynamic strength of UHPC at very-high strain rates in the continuous and discrete approaches. Furthermore, a validation of the predicted crack density in the models should be attempt through experimental data. Plate impact tests where it is possible to recover the target post-testing could be envisaged by the design of new experimental configurations where the target is artificially confined in a “sarcophagus”.

Appendix

Appendix A1

Comparison to Giga test

The results are compared with hydrostatic tests and triaxial tests on Ductal® A and Ductal® B with fibre reinforcement performed by Forquin and Zingg (2019). The specimens were 50 mm in diameter and 100 mm long. The tests were carried out employing the hydraulic press named GIGA (jack with 13 MN of capacity). Hydrostatic pressures, up to 600 MPa and 440 MPa were applied to Ductal® B and Ductal® A, respectively as shown in **Fig. A1.1**. The compressibility from the purely hydrostatic tests is only slightly higher than the one deduced with Q-OC tests, which demonstrates a poor influence of the loading path on the compaction behavior of UHPC material. The compaction of more porous concretes is known to be loading path depended (Burlion et al., 2017). A pronounced difference was observed, for example, in ordinary concrete (Piotrowska, 2015). In the studied case, the deviatoric stress developed during Q-OC seems not to modify strongly how porosities are crashed. The triaxial tests at three levels of initial confining pressure (100, 200 e 400 MPa) and a simple compression test are shown for Ductal® A and Ductal® B in **Fig. A1.2**. Triaxial tests were done without measured the hoop strain, so the specimen's radial expansion was estimated assuming the volume constant during the deviatoric loading. The oedometric stress path is placed slightly above the maximum stress difference reached during the triaxial tests.

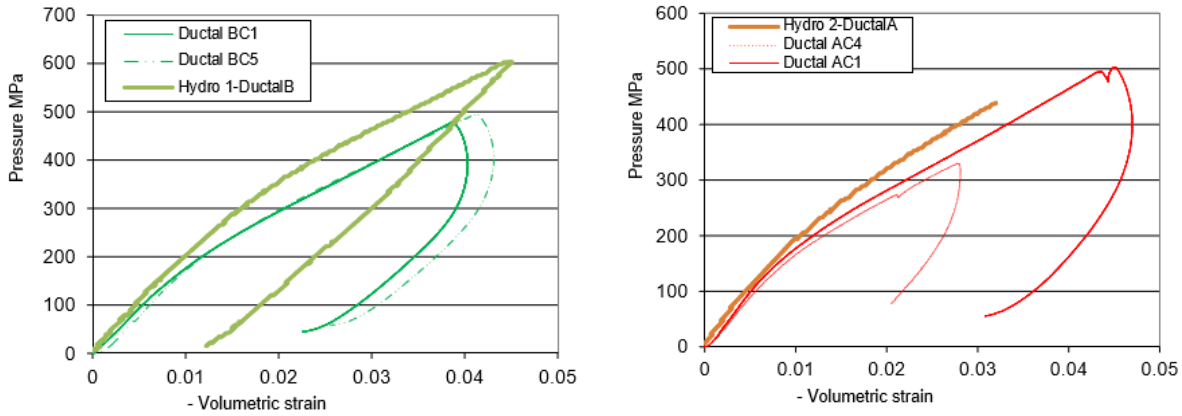

Fig. A1.1 Experimental hydrostatic and Q-OC tests results

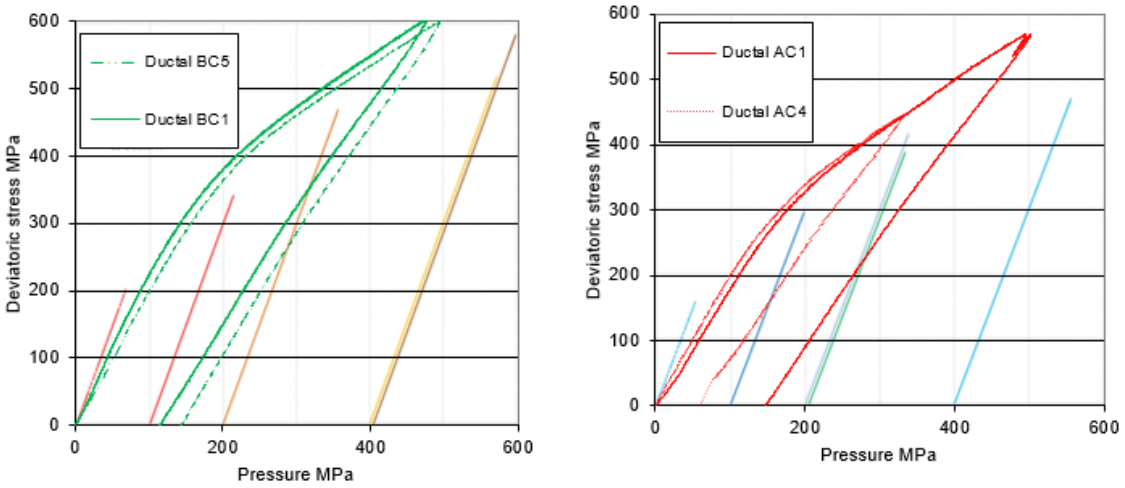

Fig. A1.2 Experimental triaxial and Q-OC tests results

Appendix A2

Post-mortem X-ray Computed Tomography analysis

The Ductal® B-2% target, dimensions 60x60x95 mm3, was fully scanned using the X-ray source in 3SR Laboratory (**Fig. A2.1**). The acquired radiographs were used to reconstruct the 3D image of the target with a voxel size of 90 μm. Image processing techniques were applied to the 3D image with the aim of extract the damage pattern. The 3D multiscale Hessian filter proposed by (Voorn et al., 2013) to extract narrow fractures in cylindrical samples of dolomite has been tested. Two orthogonal cross-sections of the 3D reconstruction are shown before and after the filter has been applied. The filter detected fractures minimum of 3 pixels wide; however, the fibres strongly affected the efficiency of the filter. Even if they were masked before the filter was applied, the fibres created numerous holes. A further algorithm should be developed to reconstruct the whole fracture planes. So, the extracted pattern was not used for quantitative analyses of the damage. Nonetheless, the study pointed out the cracking radiating from the point of impact and saucer-shaped cracking all around the crater obtained in the numerical calculations. A good correlation is obtained between the post-mortem observations and the numerical damage pattern in terms of crater extension and inclination of the rear cone (**Fig. A2.2**).

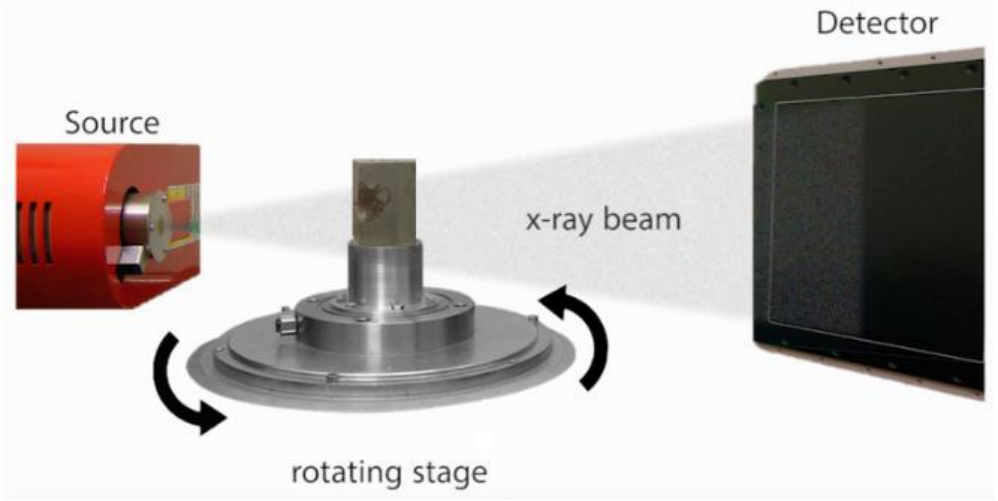

Fig. A2.1 X-ray tomography system in 3SR Lab: source at 150 kV - 400 μA, beam filtered with 1.0 mm copper, detector 1536×1920 pixels (0.127×0.127 mm^2), source-detector distance 767 mm

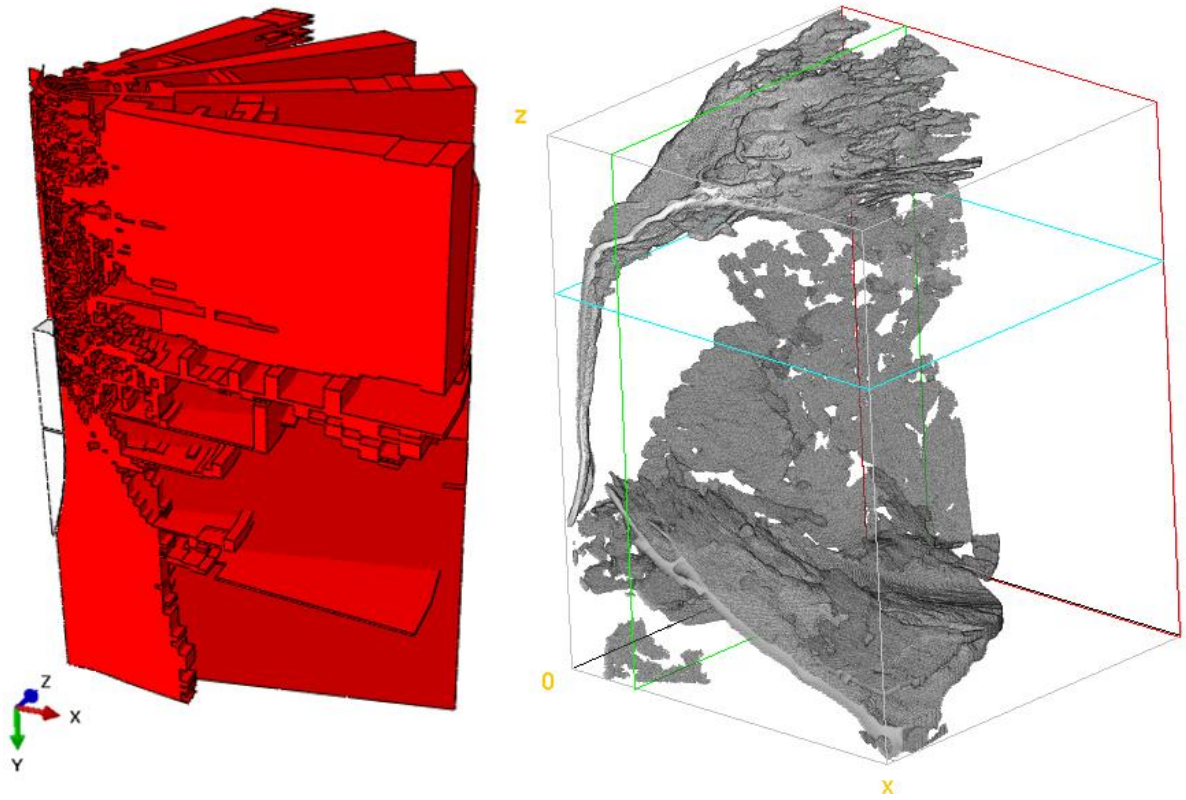

Fig. A2.1 Damage pattern by modelling vs post-mortem observation by 3D image analysis techniques: a quarter-symmetry FE model with a 40 mm radius (right) and equivalent size crop into the 60 mm-thick B-2% impacted panel (left)

Appendix A3

7.62×51mm caliber against 80 mm-thick Ductal® A-2% and B-2% panels

FE simulation of the impact of the 7.62×51mm bullet against an 80 mm-thick panel is made in Abaqus/Explicit. The model is made of a quarter of the panel with a 53 mm radius and the steel penetrator of the bullet (**Fig. A3.1**). The tunnel to bullet ratio of radius is equal to 1/6, and the minimum mesh size is 0.26 mm. The penetrator has an elastic-perfectly plastic behavior, and the panel follows the DFHcoh-KST model. The materials parameter of Ductal® A-2% and B-2% are considered. The equivalent plastic strain and the friction coefficient are 300 % and 0.2. The initial velocity of the penetrator is 820 m/s. Once again, orthogonal, radial and conical cracks are initiated and propagate along with the bullet indentation. The bullet stops penetrating the panel A-2% in 74 µs and the panel B-2% in 65 µs (**Fig. A3.2**), while the tensile damage is still under development. In both the calculation, one radial crack propagates through the whole thickness. A spall crack develops 13 mm from the rear side in panel A-2% at 100 µs, and a spall crack develops 16 mm from the rear side in panel B-2% at 60 µs. In both the calculation, the damage phenomena end at 120 µs (**Fig. A3.3**). The penetration depths, including the bullet, are respectively 31.18 and 28.01 mm.

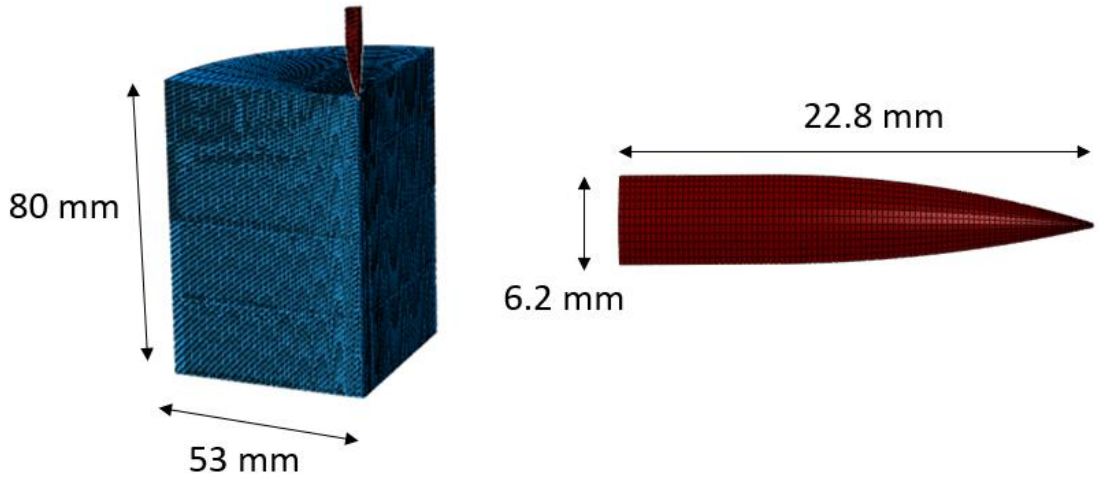

Fig. A3.1 Mesh and details of the bullet (steel in red and UHPFRC in blue)

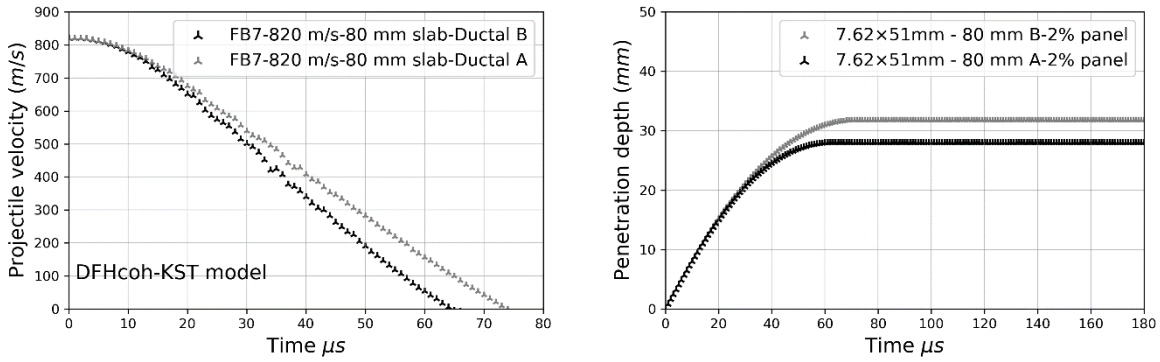

Fig. A3.2 Velocity profile (left) and final penetration depth (right) for the steel penetrator

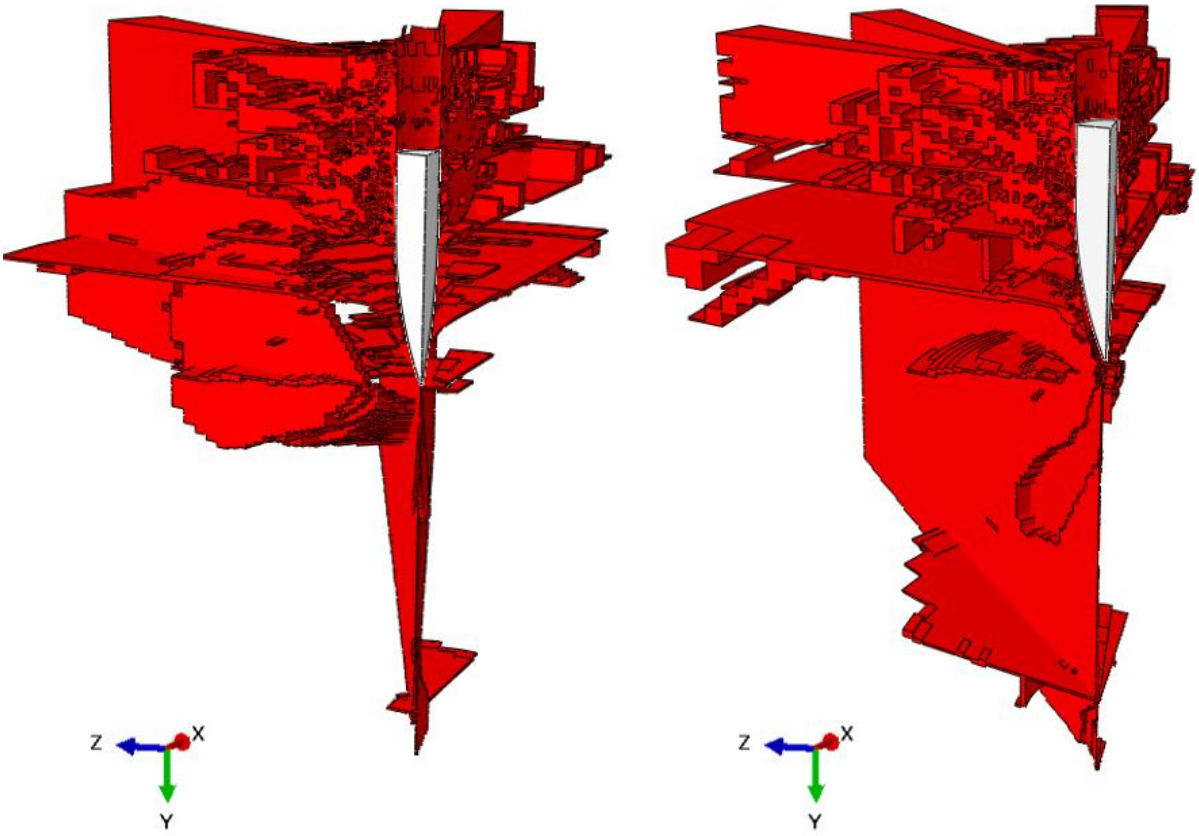

Fig. A3.3 3D final damage pattern in 80 mm-thick panels: Ductal A-2% (right) and Ductal B-2% (left)

Appendix A4

Sliding Fast Fourier Transform

The equation used to derive the surface velocity is:

$$v(t) = \frac{\lambda}{2}.f(t) \quad (1)$$

where λ is the original wavelength of the laser light and $f(t)$ is the time-varying frequency content of the raw signal. Time-frequency bin sizes are determined from the period, or total length, of the Gaussian window according to the relations:

$$\Delta t = \frac{T}{2\sqrt{\pi}} \quad (2)$$

and

$$\Delta f = \frac{1}{2T\sqrt{\pi}} \quad (3)$$

Quadrature or displacement methods

The equation used to derive the surface displacement is:

$$S(t) = \frac{\lambda}{2}.F(t) \quad (1)$$

where λ is the original wavelength of the laser light and $F(t)$ is the fringe count given by:

$$F(t) = \varphi(t) - \varphi^0(t) \quad (2)$$

The two-channel output amplitudes, $A_1(t)$ and $A_2(t)$, are sinusoidal functions of the fringe count:

$$A_1(t) = {A_1}^0\big(cos\big(2\pi F(t)\big) + \delta_1\big) \quad (3)$$

$$A_2(t) = {A_2}^0\big(cos\big(2\pi F(t)\big) + \delta_2\big) \quad (3)$$

where ${A_1}^0$ and δ_1 are the initial amplitude and phase angle. The Lissajous curves lie on the ellipse written as:

$$\left(\frac{A_1(t) - {A_1}^0\delta_1}{{A_1}^0}\right)^2 + \left(\frac{A_2(t) - {A_2}^0\delta_2}{{A_2}^0}\right)^2 = 1 \quad (4)$$

Appendix A5

Experimental Particle Velocities

The particle velocities obtained by SFFT method or both SFFT/quadrature methods (as indicated in **Table A5.1**) are shown in **Figs. A5.1-3**. The particle velocities obtained by the SFFT method or both SFFT/quadrature methods, as indicated in Table A5.1, are shown in Figs. A5.1-3. The profiles recorded at the rear buffer face were available for the tests: B3-conf2 83 m/s, A4-conf2 79 m/s, B5-conf1 44 m/s, A2-conf1 48 m/s, B2-conf1 48 m/s, A5-conf1 68 m/s. For all tests, the profiles recorded at the target rear face show a rebound. For test A5-conf1 68 m/s, the signal 68 m/s Conf1 Ductal A differs from all the others. This may indicate that the target exhibited a non-linear behavior before the rebound of the curve.

Sample	Configuration	Impact velocity m/s	N° laser interferometer	Processing Method
A0	**flat striker**	**51 m/s**	1*	SFFT
A2	**conf1**	**48 m/s**	2	SFFT
A5	**conf1**	**68 m/s**	2	SFFT quadrature
A1	**conf2**	**57 m/s**	1*	SFFT
A4	**conf2**	**79 m/s**	2	SFFT quadrature
B2	**conf1**	**48 m/s**	2	SFFT
B5	**conf1**	**44 m/s**	2	SFFT quadrature
B1	**conf2**	**57 m/s**	1*	SFFT
B3	**conf2**	**83 m/s**	2	SFFT quadrature

Table A5.1 – Test information: sample ID, striker-buffer configuration, measured impact velocity, number of laser interferometers, processing method. *target rear face

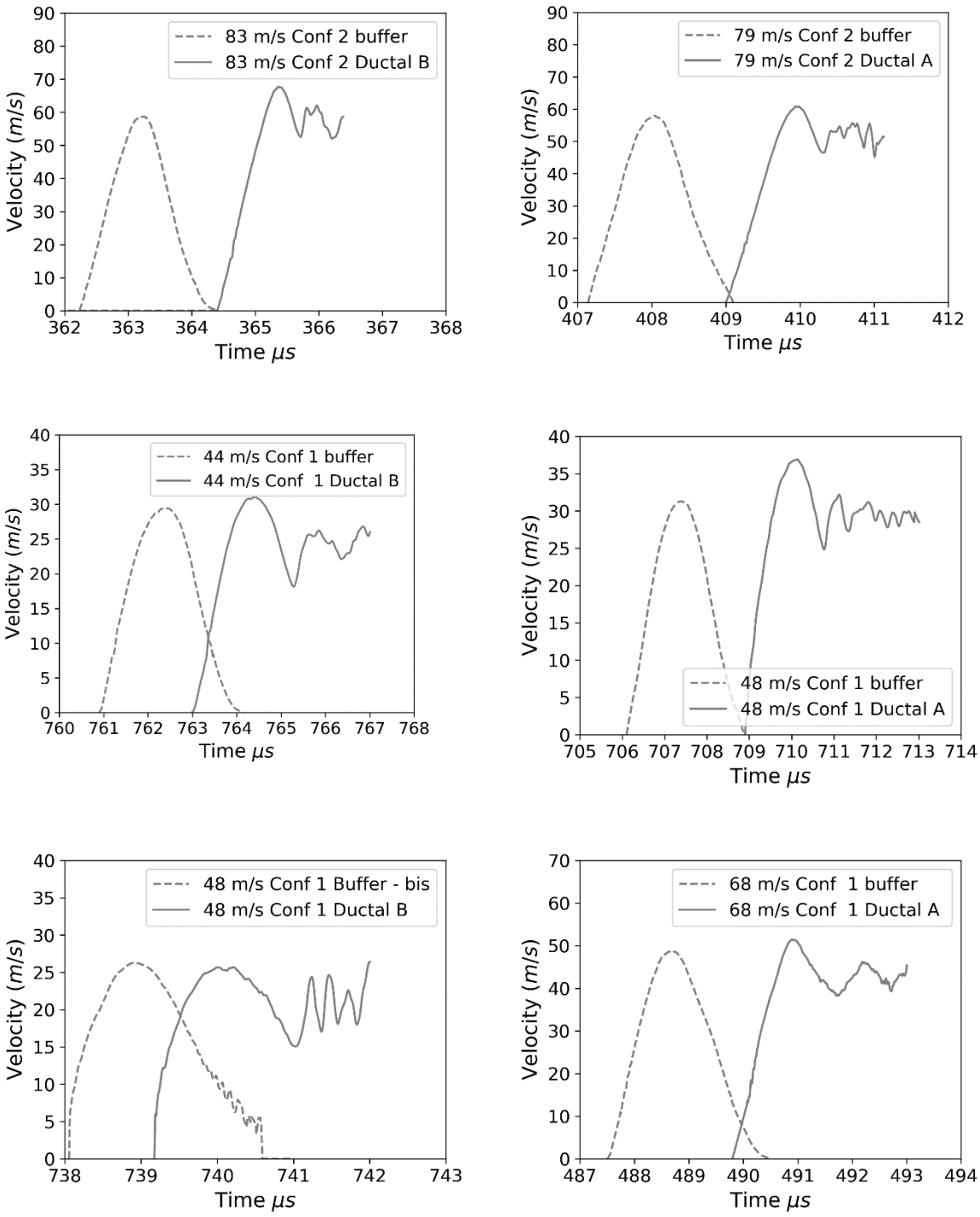

Fig. A5.1 Experiments with two laser interferometers: **B3-conf2 83 m/s, A4-conf2 79 m/s, B5-conf1 44 m/s, A2-conf1 48 m/s, B2-conf1 48 m/s, A5-conf1 68 m/s**

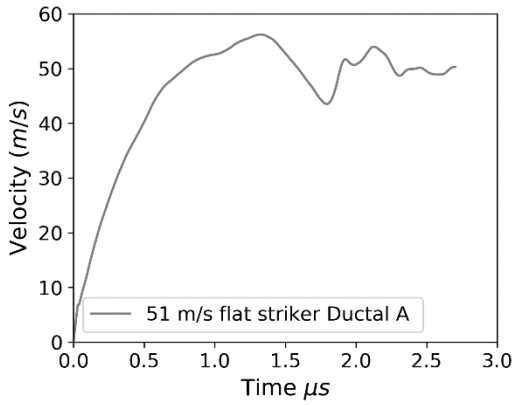

1 Fig. A5.2 Experiment with classical configuration (**A-flat striker 51 m/s)**

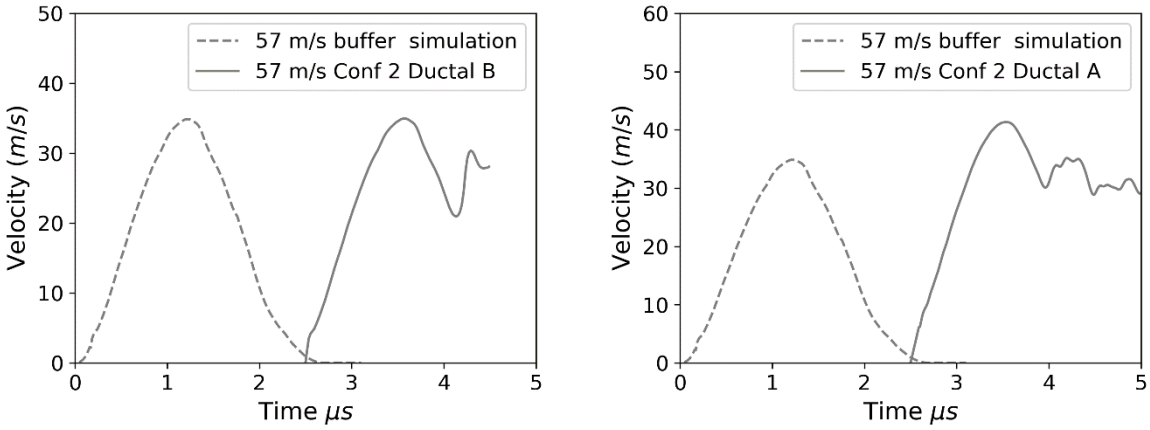

Fig. A5.3 Experiments with one laser interferometer: **B1-conf2 57 m/s, A1-conf2 57 m/s**

REFERENCES

Aaleti, S., B. Peterson, and S.S., 2013. Design Guide for Precast UHPC Waffle Deck Panel System, Including Connections.

Abramowitz, M., Stegun, I.A., 1965. Handbook ofMathematical Functions, Dover Publications, Inc., New York (USA).

ACI 239R, 2018. Ultra-high-performance concrete: An emerging technology report. Am. Concr. Inst. ACI 239.

Acker, P., Behloul, M., 2004. Ductal Technology: a Large Spectrum of Properties, a wide range of applications, in: Proceedings of the Fib Symposium 2004 - Concrete Structures: The Challenge of Creativity.

Antoniou, A., Antoniou, A., 2019. Discrete element modeling of concrete structures under impact To cite this version : HAL Id : tel-01990419 Modélisation aux éléments discrets des Discrete element modelling of concrete.

Bache, H.H., 1981. Densified Cement/Ultrafine Particle-Based Materials, in: Proceedings of 2nd International Conference on Su- Perplasticizers in Concrete, Ottawa, Canada. p. 33.

Behloul, M., 1996. Analyse et modélisation du comportement d'un matériau à matrice cimentaire fibrée à ultra hautes performances : du matériau à la structure. Cachan, France, École Normale Supérieure de Cachan.

Burlion, N., Pijaudier-cabot, G., Dahan, N., Burlion, N., Pijaudier-cabot, G., Dahan, N., 2017. Experimental analysis of compaction of concrete and mortar To cite this version : HAL Id : hal-01006829.

Buzaud, E., Ionescu I, Voyiadjis G, 2013. Materials under Extreme Loadings, Materials under Extreme Loadings. https://doi.org/10.1002/9781118622612

Cadoni, E., Forni, D., Bonnet, E., Dobrusky, S., 2019. Experimental study on direct tensile behaviour of UHPFRC under high strain-rates. Constr. Build. Mater. 218, 667–680. https://doi.org/10.1016/j.conbuildmat.2019.05.152

Charron, J.P., Denarié, E., Brühwiler, E., 2007. Permeability of ultra high performance fiber reinforced concretes (UHPFRC) under high stresses. Mater. Struct. Constr. 40, 269–277. https://doi.org/10.1617/s11527-006-9105-0

Daudeville, L., Antoniou, A., Omar, A., Marin, P., Potapov, S., & Pontiroli, C., 2019. Discrete Element Analysis to Predict Penetration and Perforation of Concrete Targets Struck by

Rigid Projectiles, in: In Dynamic Damage and Fragmentation. John Wiley & Sons, Inc. pp. 297–314. https://doi.org/https://doi.org/10.1002/9781119579311.ch9

Daudeville, L., Malécot, Y., 2011. Concrete structures under impact. Eur. J. Environ. Civ. Eng. 15, 101–140. https://doi.org/10.1080/19648189.2011.9695306

Denoual, C., Hild, F., 2002. Dynamic fragmentation of brittle solids: A multi-scale model. Eur. J. Mech. A/Solids 21, 105–120. https://doi.org/10.1016/S0997-7538(01)01187-1

Dobruský, S., Bonnet, E., Sebastien, B., Jacomo, D., 2018. Ballistic resistance of Ductal® Ultra-High Performance Fiber-Reinforced Concrete (UHPFRC), in: ICPS5, Poznan, Poland.

Dugat, J., Roux, N., Bernier, G., 1996. Mechanical properties of reactive powder concretes. Mater. Struct. Constr. 29, 233–240. https://doi.org/10.1007/bf02485945

Erzar, B., 2010. Ecaillage, cratérisation et comportement en traction dynamique de bétons sous impact : approches expérimentales et modélisation. Thèse présentée par.

Erzar, B., Buzaud, E., Chanal, P.Y., 2013. Dynamic tensile fracture of mortar at ultra-high strain-rates. J. Appl. Phys. 114. https://doi.org/10.1063/1.4852935

Erzar, B., Forquin, P., 2014. Analysis and modelling of the cohesion strength of concrete at high strain-rates. Int. J. Solids Struct. 51, 2559–2574. https://doi.org/10.1016/j.ijsolstr.2014.01.023

Erzar, B., Forquin, P., 2010. An Experimental Method to Determine the Tensile Strength of Concrete at High Rates of Strain. Exp. Mech. 50, 941–955. https://doi.org/10.1007/s11340-009-9284-z

Erzar, B., Pontiroli, C., Buzaud, E., 2017. Ultra-high performance fibre-reinforced concrete under impact: Experimental analysis of the mechanical response in extreme conditions and modelling using the Pontiroli, Rouquand and Mazars model. Philos. Trans. R. Soc. A Math. Phys. Eng. Sci. 375. https://doi.org/10.1098/rsta.2016.0173

Erzar, B., Pontiroli, C., Buzaud, E., 2016. Shock characterization of an ultra-high strength concrete. Eur. Phys. J. Spec. Top. 225, 355–361. https://doi.org/10.1140/epjst/e2016-02637-4

Fang, Q., Wu, H., 2017. Concrete structures under projectile impact, Concrete Structures under Projectile Impact. https://doi.org/10.1007/978-981-10-3620-0

Federico A. Tavarez‡ and Michael E. Plesha∗, † Department, 2007. Discrete element method for modelling solid and particulate materials. International 1102–1119.

https://doi.org/10.1002/nme

Forquin, P., 2019. Investigation of the Quasi-Static and Dynamic Confined Strength of Concretes by Means of Quasi-Oedometric Compression Tests. Compressive Strength Concr. Pavlo Kryvenko, IntechOpen.

Forquin, P., 2015. On the Damage Mechanisms Involved in Different Geomaterials Subjected to Edge-on Impact Experiments, in: Dynamic Behavior of Materials, Volume 1.

Forquin, P., 2003. Endommagement et fissuration de matériaux fragiles sous impact balistique, rôle de la microstructure. Thèse Dr. Ec. Norm. Supérieure Cachan.

Forquin, P., Arias, A., Zaera, R., 2008a. Role of porosity in controlling the mechanical and impact behaviours of cement-based materials. Int. J. Impact Eng. 35, 133–146. https://doi.org/10.1016/j.ijimpeng.2007.01.002

Forquin, P., Arias, A., Zaera, R., 2007. An experimental method of measuring the confined compression strength of geomaterials. Int. J. Solids Struct. 44, 4291–4317. https://doi.org/10.1016/j.ijsolstr.2006.11.022

Forquin, P., Arias, A., Zaera, R., 2006. An experimental method of measuring the confi ned compression strength of high-performance concretes to analyse their ballistic behaviour, in: J. Phys. IV , DYMAT, 134 , 629 – 634 .

Forquin, P., Blasone, M., Georges, D., Dargaud, M., Ando, E., 2019. Modelling of the fragmentation process in brittle solids based on x-ray micro-tomography analysis, in: 24ème Congrès Français de Mécanique, Brest, 26 Au 30 Août.

Forquin, P., Blasone, M., Georges, D., Dargaud, M., Saletti, D., Ando, E., 2020. The Brittle ’ s CODEX chair, in: DYMAT Winter School , Les Houches School of Physics.

Forquin, P., Erzar, B., 2013. Experimental approach and modeling of the dynamic tensile behavior of a micro-concrete, in: Materials under Extreme Loadings – Application to Penetration and Impact.

Forquin, P., Gary, G., Gatuingt, F., 2008b. A testing technique for concrete under confinement at high rates of strain. Int. J. Impact Eng. 35, 425–446. https://doi.org/10.1016/j.ijimpeng.2007.04.007

Forquin, P., Hild, F., 2010. A Probabilistic Damage Model of the Dynamic Fragmentation Process in Brittle Materials, Advances in Applied Mechanics. Elsevier Inc. https://doi.org/10.1016/S0065-2156(10)44001-6

Forquin, P., Hild, F., 2008. Dynamic fragmentation of an ultrahigh-strength concrete during edge-on impact tests. J. Eng. Mech. 134, 302–315. https://doi.org/10.1061/(ASCE)0733-

9399(2008)134:4(302)

Forquin, P., Riedel, W., Weerheijm, J., 2013. Dynamic test devices for analyzing the tensile properties of concrete, Understanding the Tensile Properties of Concrete. Woodhead Publishing Limited. https://doi.org/10.1533/9780857097538.2.137

Forquin, P., Safa, K., Gary, G., 2010. Influence of free water on the quasi-static and dynamic strength of concrete in confined compression tests. Cem. Concr. Res. 40, 321–333. https://doi.org/10.1016/j.cemconres.2009.09.024

Forquin, P., Sallier, L., 2014. Caractérisation expérimentale d'un béton à ultra-hautes performances. 3SR-LEM3 Rep. to Atten. CEA-Gramat, 10/12/2014.

Forquin, P., Sallier, L., Pontiroli, C., 2015. A numerical study on the influence of free water content on the ballistic performances of plain concrete targets. Mech. Mater. 89, 176–189. https://doi.org/10.1016/j.mechmat.2015.02.016

Forquin, P., Zinszner, J., 2017. A pulse-shaping technique to investigate the behaviour of brittle materials subjected to plate-impact tests. Philos. Trans. R. Soc. A Math. Phys. Eng. Sci. 375. https://doi.org/10.1098/rsta.2016.0333

Forquin, P., Zinszner, J., Lukić, B., 2017. Mesoscopic Modelling of Ultra-High Performance Fiber Reinforced Concrete Under Dynamic Loading. In: Casem D., Lamberson L., Kimberley J. (eds) Dynamic Behavior of Materials, 1:123-129, DOI: 10.1007/978-3-319-41132-3_17.

Fujikake, K., Senga, T., Ueda, N., Ohno, T., Katagiri, M., 2006. Effects of strain rate on tensile behavior of reactive powder concrete. J. Adv. Concr. Technol. 4, 79–84. https://doi.org/10.3151/jact.4.79

Gatuingt, F., 1999. Prévision de la rupture des ouvrages en béton sollicités en dynamique rapide.

Gran, Frew, 1996. In-target radial stress measurements from penetration experiments into concrete by ogive-nose steel projectiles. Int. J. Impact Eng. 19(8), 715–726. https://doi.org/10.1016/s0734-743x(97)00008-0

Graybeal A., 2006. Material Property Characterization of Ultra-High Performance Concrete.

Green, B.H., Moser, R.D., Scott, D.A., Long, W.R., 2014. Ultra-High Performance Concrete History and Usage by the Corps of Engineers. Adv. Civ. Eng. Mater. https://doi.org/10.1520/ACEM20140031

Grote, D.L., Park, S.W., Zhou, M., 2001. Experimental characterization of the dynamic failure behavior of mortar under impact loading. J. Appl. Phys. 89, 2115–2123.

https://doi.org/10.1063/1.1340005

Hild, F., Forquin, P., Denoual, C., Brajer, X., 2008. Probabilistic-deterministic transition involved in a fragmentation process of brittle materials: Application to a high performance concrete.

Hong Vu, X., Malecot, Y., Daudeville, L., Buzaud, E., 2013. Experimental Analysis of Concrete Behavior Under High Confinement, in: Materials under Extreme Loadings. John Wiley & Sons, Ltd, pp. 101–119. https://doi.org/10.1002/9781118622612.ch5

Jayatilaca A. D. S., Trustmm K., 1977. Statistical approach to brittle fracture. J. Mat. Sci. 12, 1426–1430.

Kanninen, M.F., Popelar, C.H., McEvily, A.J., 1986. Advanced Fracture Mechanics, Journal of Engineering Materials and Technology. https://doi.org/10.1115/1.3225862

Leal, W.R., Svec, O., Thrane, L.N., Pade, C., 2017. Effect of fibre orientation on the tensile strength of ultra-high performance steel fibre-reinforced self- compacting concrete, in: AFGC-ACI-Fib-RILEM. pp. 191–200.

Li, Q.M., Reid, S.R., Wen, H.M., Telford, A.R., 2005. Local impact effects of hard missiles on concrete targets. Int. J. Impact Eng. 32, 224–284. https://doi.org/10.1016/j.ijimpeng.2005.04.005

Millon, O., Riedel, W., Thoma, K., Fehling, E., Nöldgen, M., 2009. Fiber-reinforced ultra-high performance concrete under tensile loads 671–677. https://doi.org/10.1051/dymat/2009095

Neel, C., 2018. Compaction and Spall of UHPC Concrete Under Shock Conditions. J. Dyn. Behav. Mater. 4, 505–528. https://doi.org/10.1007/s40870-018-0173-3

Nf P 18-710, 2016. Nf P 18-710. Ultra-High Perform. Fiber Reinf. Concr. – Specif. Performance, Prod. Conform. AFNOR 33.

Nöldgen, M., Riedel, W., Thoma, K., Fehling, E., 2013. Properties of Ultra High Performance Concrete (UHPC) in tension at high strain rates. Proc. 8th Int. Conf. Fract. Mech. Concr. Concr. Struct. Fram. 2013 988–1000.

Novikov, S.A., Divnov, I.I., Ivanov, A.G., 1966. The study of fracture of steel, aluminium and copper under explosive loading. Phys. Met. Met. Sci. 21, 608–615.

Orange, G., 1999. A New Generation of UHP Concrete (DUCTAL), Damage Resistance and Micromechanical Analysis. Proc. Third Int. RILEM Work. HPFRCC 101–111.

Ozbolt, J., Li, Y.J., Kozar, I., 2001. Microplane Model for Concrete with Relaxed Kinematic

Constraint. Fract. Mech. Concr. Struct. 38, 609–616.

Ožbolt, J., Sharma, A., Irhan, B., Sola, E., 2014. Tensile behavior of concrete under high loading rates. Int. J. Impact Eng. 69, 55–68. https://doi.org/10.1016/j.ijimpeng.2014.02.005

Piotrowska, E., Forquin, P., 2015. Experimental Investigation of the Confined Behavior of Dry and Wet High-Strength Concrete: Quasi Static Versus Dynamic Loading. J. Dyn. Behav. Mater. 1, 191–200. https://doi.org/10.1007/s40870-015-0017-3

Piotrowska, E., Forquin, P., Malecot, Y., 2016. Experimental study of static and dynamic behavior of concrete under high confinement: Effect of coarse aggregate strength. Mech. Mater. 92, 164–174. https://doi.org/10.1016/j.mechmat.2015.09.005

Plesha, M.E., 2003. Final Report: Discrete Element Method for Modeling Penetration 298.

Pontiroli, C., Erzar, B., Buzaud, E., 2016. Ultra high performance fiber reinforced concrete behavior under static and high velocity impact. Key Eng. Mater. 711, 171–178. https://doi.org/10.4028/www.scientific.net/KEM.711.171

Pyo, S., El-Tawil, S., Naaman, A.E., 2016. Direct tensile behavior of ultra high performance fiber reinforced concrete (UHP-FRC) at high strain rates. Cem. Concr. Res. 88, 144–156. https://doi.org/10.1016/j.cemconres.2016.07.003

Pyo, S., Wille, K., El-Tawil, S., Naaman, A.E., 2015. Strain rate dependent properties of ultra high performance fiber reinforced concrete (UHP-FRC) under tension. Cem. Concr. Compos. 56, 15–24. https://doi.org/10.1016/j.cemconcomp.2014.10.002

Ren, G.M., Wu, H., Fang, Q., Kong, X.Z., 2017. Parameters of Holmquist–Johnson–Cook model for high-strength concrete-like materials under projectile impact. Int. J. Prot. Struct. 8, 352–367. https://doi.org/10.1177/2041419617721552

Richard, P., Cheyrezy, M., 1995. Composition of reactive powder concretes. Cem. Concr. Res. 25, 1501–1511. https://doi.org/10.1016/0008-8846(95)00144-2

Riou, P., Denoual, C., Cottenot, C.E., 1998. Visualization of the damage evolution in impacted silicon carbide ceramics. Int. J. Impact Eng. 21, 225–235. https://doi.org/10.1016/S0734-743X(97)00018-3

Rossi, P., Toutlemonde, F., 1996. Effect of loading rate on the tensile behaviour of concrete : Description of the physical mechanisms. Mater. Struct. Constr. 29, 116–118. https://doi.org/10.1007/bf02486201

Rouquand, A., Mazars, J., 2010. impact . An overview of the PRM model Predicting concrete behaviour from quasi-static loading to hy- pervelocity impact : an overview of the PRM

Model. https://doi.org/10.3166/ejece.14.703-727

Safa, K., 2009. Mise au point d'un essai de compaction dynamique. Application au béton. Thèse Dr. l' Ec. Polytech. Spécialité Mécanique.

Scheydt, J., Muller, H., 2012. Microstructure of Ultrahigh Performance Concrete (UHPC) and Its Impact on Durability, in: Proceeding of 3rd International Symposium on UHPC and Nanotechnology for High Performance Construction Materials. Kassel: Kassel University Press. pp. 349–356.

Schuler, H., Mayrhofer, C., Thoma, K., 2006. Spall experiments for the measurement of the tensile strength and fracture energy of concrete at high strain rates. Int. J. Impact Eng. 32, 1635–1650. https://doi.org/10.1016/j.ijimpeng.2005.01.010

Stamati, O., Andò, E., Roubin, E., Cailletaud, R., Wiebicke, M., Pinzon, G., Couture, C., Hurley, R., Caulk, R., Caillerie, D., Matsushima, T., Bésuelle, P., Bertoni, F., Arnaud, T., Laborin, A., Rorato, R., Sun, Y., Tengattini, A., Okubadejo, O., Colliat, J.-B., Saadatfar, M., Garcia, F., Papazoglou, C., Vego, I., Brisard, S., Dijkstra, J., Birmpilis, G., 2020. spam: Software for Practical Analysis of Materials. J. Open Source Softw. 5, 2286. https://doi.org/10.21105/joss.02286

Strassburger, E., Senf, H., Rothenhaeusler, H., 1994. Fracture propagation during impact in three types of ceramics. J. Phys. IV JP 4. https://doi.org/10.1051/jp4:1994899

Swenson, D. V., Taylor, L.M., 1983. A finite element model for the analysis of tailored pulse stimulation of boreholes. Int. J. Numer. Anal. Methods Geomech. 7, 469–484. https://doi.org/10.1002/nag.1610070408

Tai, Y.S., 2009. Flat ended projectile penetrating ultra-high strength concrete plate target. Theor. Appl. Fract. Mech. 51, 117–128. https://doi.org/10.1016/j.tafmec.2009.04.005

Thomas, R.J., Sorensen, A.D., 2017. Review of strain rate effects for UHPC in tension. Constr. Build. Mater. 153, 846–856. https://doi.org/10.1016/j.conbuildmat.2017.07.168

Toutlemonde, F., Resplendino, J., 2013. Designing and Building with UHPFRC, Designing and Building with UHPFRC. https://doi.org/10.1002/9781118557839

Trainor, K.J., Asce, A.M., Foust, B.W., Asce, A.M., Landis, E.N., Asce, M., 2013. Measurement of Energy Dissipation Mechanisms in Fracture of Fiber-Reinforced Ultrahigh-Strength Cement-Based Composites 771–779. https://doi.org/10.1061/(ASCE)EM.1943-7889.0000545.

Voorn, M., Exner, U., Rath, A., 2013. Computers & Geosciences Multiscale Hessian fracture fi ltering for the enhancement and segmentation of narrow fractures in 3D image data.

Comput. Geosci. 57, 44–53. https://doi.org/10.1016/j.cageo.2013.03.006

Wang, R., Gao, X., Zhang, J., Han, G., 2018. Spatial distribution of steel fibers and air bubbles in UHPC cylinder determined by X-ray CT method. Constr. Build. Mater. 160, 39–47. https://doi.org/10.1016/j.conbuildmat.2017.11.030

Warren, T.L., Forquin, P., 2016. Penetration of common ordinary strength water saturated concrete targets by rigid ogive-nosed steel projectiles. Int. J. Impact Eng. 90, 37–45. https://doi.org/10.1016/j.ijimpeng.2015.11.003

Weerheijm, J., 2013. Understanding the Tensile Properties of Concrete, Understanding the Tensile Properties of Concrete. https://doi.org/10.1533/9780857097538

Williams, E.M., Graham, S.S., Reed, P. a, Rushing, T.S., 2009. Concrete With and Without Steel Fibers Geotechnical and Structures Laboratory Concrete With and Without Steel Fibers. Stress Int. J. Biol. Stress.